Advances in Industrial Control

Qingsong Xu
Kok Kiong Tan

Advanced Control of Piezoelectric Micro-/Nano-Positioning Systems

AIC
Springer

Advances in Industrial Control

Series editors

Michael J. Grimble, Glasgow, UK
Michael A. Johnson, Kidlington, UK

More information about this series at http://www.springer.com/series/1412

Qingsong Xu · Kok Kiong Tan

Advanced Control of Piezoelectric Micro-/Nano-Positioning Systems

Springer

Qingsong Xu
Department of Electromechanical Engineering
University of Macau
Macau
China

Kok Kiong Tan
Department of Electrical and Computer Engineering
National University of Singapore
Singapore
Singapore

ISSN 1430-9491 ISSN 2193-1577 (electronic)
Advances in Industrial Control
ISBN 978-3-319-21622-5 ISBN 978-3-319-21623-2 (eBook)
DOI 10.1007/978-3-319-21623-2

Library of Congress Control Number: 2015944753

Mathematics Subject Classification: 93, 93B12, 93B30, 93B52, 93C10, 93C40, 93C55, 93C57, 93C62, 93C73, 93C83, 93C85, 93C99, 93D05, 93D21, 68T40, 70Q05

Springer Cham Heidelberg New York Dordrecht London
© Springer International Publishing Switzerland 2016
This work is subject to copyright. All rights are reserved by the Publisher, whether the whole or part of the material is concerned, specifically the rights of translation, reprinting, reuse of illustrations, recitation, broadcasting, reproduction on microfilms or in any other physical way, and transmission or information storage and retrieval, electronic adaptation, computer software, or by similar or dissimilar methodology now known or hereafter developed.
The use of general descriptive names, registered names, trademarks, service marks, etc. in this publication does not imply, even in the absence of a specific statement, that such names are exempt from the relevant protective laws and regulations and therefore free for general use.
The publisher, the authors and the editors are safe to assume that the advice and information in this book are believed to be true and accurate at the date of publication. Neither the publisher nor the authors or the editors give a warranty, express or implied, with respect to the material contained herein or for any errors or omissions that may have been made.

MATLAB® and Simulink® are registered trademarks of The MathWorks, Inc., 3 Apple Hill Drive, Natick, MA 01760-2098, USA, http://www.mathworks.com.
LabVIEW™ is a trademark of National Instruments Corporation, 11500 N Mopac Expwy, Austin, TX 78759-3504, USA, http://www.ni.com/.

Printed on acid-free paper

Springer International Publishing AG Switzerland is part of Springer Science+Business Media (www.springer.com)

To Prof. Wei Zhao and my family for the encouragement all the time

Qingsong Xu

To my family

Kok Kiong Tan

Series Editors' Foreword

The series *Advances in Industrial Control* aims to report and encourage technology transfer in control engineering. The rapid development of control technology has an impact on all areas of the control discipline. New theory, new controllers, actuators, sensors, new industrial processes, computer methods, new applications, new philosophies and, new challenges. Much of this development work resides in industrial reports, feasibility study papers, and the reports of advanced collaborative projects. The series offers an opportunity for researchers to present an extended exposition of such new work in all aspects of industrial control for wider and rapid dissemination.

This monograph reports the recent work of Qingsong Xu and Kok Kiong Tan in the field of modelling, design, and control of piezoelectric systems. Qingsong Xu is an Associate Professor in the Department of Electromechanical Engineering at the University of Macau, China. His background is in mechatronics and electromechanical systems. He has been well supported by his university to develop considerable expertise in this field and since 2005 has published regularly in peer-refereed journals on his electromechanical systems work. Author Kok Kiong Tan is a well-established contributor to the *Advances in Industrial Control* monograph series. He is an Associate Professor in the Department of Electrical and Computer Engineering at the National University of Singapore and it is possible to appreciate his extensive expertise and research activities through his monograph contributions to the series:

- *Advances in PID Control*, Kok Kiong Tan, Qing-Guo Wang and Chang Chieh Hang with Tore J. Hägglund (ISBN 978-1-85233-138-2, 1999);
- *Precision Motion Control* (2nd Edition), Kok Kiong Tan, Tong Heng Lee and Sunan Huang (ISBN 978-1-84800-020-9, 2008);
- *Applied Predictive Control*, Sunan Huang, Kok Kiong Tan and Tong Heng Lee (ISBN 978-1-85233-338-6, 2002); and
- *Drives and Control for Industrial Automation*, Kok Kiong Tan and Andi Sudjana Putra (ISBN 978-1-84882-424-9, 2011).

There are clear technical links between these monographs and the work reported in *Advanced Control of Piezoelectric Micro-/Nano-positioning Systems*. This is a work of 11 chapters and after an introductory chapter is partitioned into four parts:

- Part I—Chapters 2 and 3: these two chapters cover hysteresis modelling and look at feedforward controller design, with and without recourse to a hysteresis model;
- Part II—Chapters 4 and 5: the control approaches followed by these two chapters use a fusion of model predictive and discrete sliding-mode control;
- Part III—Chapters 6–9: each chapter in this part investigates variants of sliding-mode control and concludes with a model-reference adaptive control approach; and
- Part IV—Chapters 10 and 11: the last part of the monograph is devoted to micromanipulation and mini-gripper applications.

A full and useful description of the contents of individual chapters can be found in the Preface. There, the reader will find there are some special features of the monograph that make it a distinctive contribution to the piezoelectric control literature. Apart from the wide range of control approaches developed, all the chapters after the introductory chapter contain experimental verification studies and results sections. The range of control approaches, the inclusion of experimental results, and the applications studied makes the monograph an important addition to the literature and to the *Advances in Industrial Control* series.

Recently, piezoelectric control studies have received some exposure in the *Advances in Industrial Control* series and readers will find complementary material to the work of Qingsong Xu and Kok Kiong Tan in the series monograph *Design, Modelling and Control of Nanopositioning Systems* by Andrew J. Fleming and Kam K. Leang (ISBN 978-3-319-06616-5, 2014).

Related studies of the modelling and control applications of "smart materials" can be found in a very novel application described in the forthcoming monograph by R. Ganguli, D. Thakkar, and S.R. Viswamurthy entitled *Smart Helicopter Rotors: Optimization and Piezoelectric Vibration Control* that will appear in the series in the near future.

Industrial Control Centre, Glasgow, Scotland, UK M.J. Grimble
M.A. Johnson

Preface

Micro-/nano-positioning systems are positioning devices that are capable of producing displacement down to micro-/nano-meter resolution and accuracy. As typical ultrahigh-precision positioning devices, piezoelectric micro-/nano-positioning systems are driven by piezoelectric actuators (PEAs). They have found extensive applications in fields involving scanning probe microscopy, lithography manufacturing, and wafer alignment. In addition, these devices have also been applied in precision micro-/nano-manipulation and assembly domains.

Piezoelectric micro-/nano-positioning systems usually exhibit low damping, which causes the structural vibration problem. In addition, PEA introduces nonlinearity into the system in terms of piezoelectric hysteresis and drift effects. The hysteresis is a nonlinear relationship between the applied voltage and output displacement of the PEA and induces a severe open-loop positioning error as high as 10–15 % of the travel range. Thus, the hysteresis has to be suppressed in high precision applications. Moreover, the nonlinearity poses a great challenge in combined position and force control of piezoelectric micro-/nano-positioining devices dedicated to micromanipulation tasks.

This book is focused on enabling technologies in the control implementation of piezoelectric micro-/nano-positioning systems. The book provides a collation of the state of the art of emerging techniques to precision motion control of micro-/nano-positioning systems actuated by PEAs. It covers both feedforward and feedback control strategies for positioning and tracking control of piezoelectric actuation micro-/nano-positioning systems. This book also demonstrates the joint position and force control of piezoelectric micro-/nano-positioning systems in micromanipulation applications. A comprehensive treatment of the subject matter is provided in a manner amenable to readers ranging from researchers to engineers, by providing detailed experimental verifications of the developed approaches.

The book begins with an introduction to piezoelectric micro-/nano-positioning system and provides a brief survey of its development and applications. According to different realizations of the control strategies, the remaining ten chapters are divided into four parts.

Part I consists of Chaps. 2 and 3, which addresses the hysteresis mode-based feedforward control technology. Chapter 2 extends least squares support vector machines (LSSVM) to the domain of rate-dependent piezoelectric hysteresis modeling and compensation. A LSSVM-based rate-dependent hysteresis model is proposed for a PEA by introducing the current input value and input variation rate as one data set to construct a one-to-one mapping. The adoption of the input variation rate allows the capture of the rate dependency of the hysteresis. For comparative studies, the widely used Bouc–Wen and modified Prandtl–Ishlinskii (MPI) hysteresis models are implemented. The hysteresis nonlinearity is suppressed by a hybrid control which employs an LSSVM inverse model-based feedforward controller combined with a proportional-integral-derivative (PID) feedback controller.

Chapter 3 addresses the identification and compensation of the rate-dependent piezoelectric hysteresis using an intelligent hysteresis model, while without modeling the hysteresis inverse. Generally, both a hysteresis model and an inverse hysteresis model are required for hysteresis identification and compensation purposes. In this chapter, an LSSVM-based hysteresis model is established and a feedforward compensator is developed based on a single model, which provides a computationally efficient way in hysteresis compensation.

Chapters 4 and 5 construct Part II, which presents the hysteresis mode-free, state observer-based control schemes. The merit of such schemes lies in that no hysteresis model is required. The unmodeled hysteresis is considered as an uncertainty or a disturbance to the nominal system, which is tolerated by an advanced robust or adaptive controller. Chapter 4 reports on a model predictive discrete-time sliding-mode control (MPDTSMC) to achieve the advantages of both model predictive control (MPC) and discrete-time sliding-mode control (DTSMC). It is shown that the proposed MPDTSMC with proportional-integral (PI) action drives the system state to slide in a vicinity of the sliding surface with a boundary layer of thickness $O(T^3)$ (T is the sampling time), which is much lower than a commonly designed DTSMC with $O(T)$ boundary layer in the sliding mode. In addition, the state tracking error of the order $O(T^2)$ is achieved with the presented control scheme. The theoretical analysis and effectiveness of the PI action in the control scheme are verified by experimental studies carried out on a nanopositioning platform.

Chapter 5 presents the design and implementation of a more desirable output-based DTSMC strategy, called model predictive output integral discrete-time sliding-mode control (MPOIDSMC), for micro-/nano-positioning applications. The presented strategy is capable of improving the system performance by integrating MPC, output integral discrete-time sliding-mode control (OIDSMC), and state observer techniques together. A sliding-mode observer is adopted to estimate the system state and to suppress the spillover effects. It is demonstrated that the integrated scheme eliminates the chattering effect by forcing the system trajectory to a vicinity of the sliding surface with a boundary layer of thickness $O(T^3)$ in an optimal manner, and achieves an output tracking error of the order $O(T^2)$. The theoretical analysis and effectiveness of the proposed strategy are validated by experimental studies.

Part III includes Chaps. 6–9, which addresses the strategy of hysteresis model-free, state observer-free digital feedback control. Generally, the DTSMC can be categorized into state-based and output-based methods. The implementation of either method usually requires the state feedback of the system. A state observer is indispensable for the practical realization of DTSMC, which complicates the control design procedure. In addition, an improperly designed state observer may cause instability of the system. Hence, it is desirable to eliminate the use of state observers. Chapter 6 proposes the design of a digital sliding-mode control (DSMC) for a piezoelectric micro-/nano-positioning system with a simple second-order plant model. The local stability of the closed-loop system is proved theoretically and the effectiveness of the proposed scheme is validated through experimental investigations.

Chapter 7 reports an input–output-based DSMC (IODSMC) algorithm for precision motion tracking of a class of piezoelectric micro-/nano-positioning systems, which can be described by a high-order linear model preceded by disturbances. Its implementation requires an input–output data-based model only, whereas neither a hysteresis model nor a state observer is needed.

Chapter 8 presents a digital sliding-mode prediction control (DSMPC) scheme for precision motion tracking of a class of piezoelectric micro-/nano-positioning systems, which can be represented by a high-order linear model preceded by disturbances. Its implementation does not require the knowledge of system states. The overall control action of the proposed DSMPC scheme involves equivalent control, switching control, and predictive control.

Chapter 9 devises a model-reference adaptive control (MRAC) scheme to compensate for the unmodeled hysteresis effect of a class of PEA-actuated systems which possess a second-order nominal model. By treating the uncertainties as a lumped perturbation to the nominal system, a scheme of MRAC with perturbation estimation (MRACPE) is developed and validated on a micropositioning system. Compared with the existing work, the presented scheme allows the predesign of the maximum tracking error. It is capable of estimating the unmodeled perturbation of the system.

Part IV is composed of Chaps. 10 and 11, which deal with the technique of position and force joint control for micromanipulation applications. As a typical micro-/nano-positioning device, microgripper is a crucial tool to realize the grasp–hold–release operation in micromanipulation tasks. To avoid damaging the grasped fragile microobjects and the microgripper itself, an interaction control is critical to regulate the desired position and contact force simultaneously. Chapter 10 presents an adaptive discrete-time sliding-mode generalized impedance control (ADSMGIC) to realize an interaction control of a piezoelectric microgripper dedicated to micromanipulation and microassembly. The control scheme regulates a desired dynamics relation between the position and contact force. The chattering phenomenon is suppressed by employing an adaptive law for the switching gain. The stability of the closed-loop system is proved theoretically and the effectiveness of the interaction control scheme is validated by conducting experimental studies on a piezo-bimorph microgripper system.

Chapter 11 reports on a scheme of position/force switching control to adjust the gripper tip position and gripping force in an alternate manner. An incremental control framework is developed to achieve a smooth transition between the position and force controls for the gripper system. Specifically, in the closing and opening phases, an incremental digital sliding-mode control is devised to cater for the position control. During the contact phase, an incremental-type digital PID force control is adopted. The proposed control algorithm is deployed to a field-programmable gate array (FPGA)-based digital control platform. The feasibility of the scheme is examined by a typical grasp–hold–release operation of a micro copper wire through experimental studies. Its superiority over the conventional approach is demonstrated through experimental comparisons.

This book provides the state-of-the-art coverage of the methodology and algorithms of precision motion control of piezoelectric micro-/nano-positioning systems in the context of control engineering and soft computing. The control approaches involve feedforward control based on intelligent hysteresis model, discrete-time sliding-mode control, model predictive control, and model-reference adaptive control. The book also touches on the combined position and force control in micromanipulation, which is a typical application of micro-/nano-positioning systems. Detailed examples of their implementations are provided. Readers can expect to learn how to design and apply new control approaches to precision motion control of piezoelectric micro-/nano-positioning systems.

The authors would like to acknowledge the University of Macau (under Grants SRG006-FST11-XQS, MYRG083(Y1-L2)-FST12-XQS, and MYRG078(Y1-L2)-FST13-XQS) and the Science and Technology Development Fund (FDCT) of Macao (under Grants 024/2011/A, 070/2012/A3, and 052/2014/A1) for co-funding the projects. The authors are also grateful for the help provided by Editor Oliver Jackson and Editor Karin de Bie from Springer.

Macau, China — Qingsong Xu
Singapore — Kok Kiong Tan
June 2015

Contents

1 Introduction 1
1.1 Micro-/Nano-positioning Technique. 1
1.2 Actuators and Sensors 2
1.3 Piezoelectric Nonlinearity. 4
1.4 Feedforward Control Based on Hysteresis Models. 5
1.4.1 Conventional Hysteresis Model. 6
1.4.2 Intelligent Hysteresis Model 8
1.4.3 Feedforward Plus Feedback Control 8
1.5 Robust Feedback Control. 9
1.5.1 Sliding-Mode Control 10
1.5.2 Model Predictive Control. 11
1.5.3 Model-Reference Adaptive Control 12
1.5.4 Other Control Strategies 13
1.6 Position/Force Control in Micromanipulation 13
1.6.1 Hybrid Control. 14
1.6.2 Impedance Control 14
1.6.3 Switching Control. 15
1.7 Book Summary 16
References. 16

Part I Hysteresis-Model-Based Feedforward Control

2 Feedforward Control Based on Inverse Hysteresis Models 23
2.1 Introduction 23
2.2 System Description and Hysteresis Characterization 24
2.2.1 Experimental Setup 24
2.2.2 Hysteresis Characterization. 25
2.3 Hysteresis Modeling 28
2.3.1 Hysteresis Modeling with the Bouc–Wen Model. 28

2.3.2 Hysteresis Modeling with the MPI Model 29
2.3.3 Hysteresis Modeling with the LSSVM. 32
2.4 Experimental Studies. 36
2.4.1 Bouc–Wen Model Results 36
2.4.2 MPI Model Results. 37
2.4.3 LSSVM Model Results 40
2.4.4 Model Capability Comparison 42
2.4.5 Generalization Study 44
2.5 Controller Design and Verification 47
2.5.1 Feedforward Controller Design. 47
2.5.2 Feedforward Plus Feedback Controller Design 49
2.5.3 Controller Verification. 49
2.6 Chapter Summary 54
References. 54

3 Feedforward Control Without Modeling Inverse Hysteresis 57
3.1 Introduction 57
3.2 Dynamics Modeling of Hysteretic System 58
3.2.1 Dynamics Modeling with Bouc–Wen Hysteresis. 58
3.2.2 Dynamics Modeling with Intelligent Hysteresis Model 59
3.3 Hysteresis Modeling Using LSSVM 60
3.3.1 Regression Model Establishment. 60
3.3.2 LSSVM Modeling 60
3.4 Experimental Studies on Hysteresis Identification 62
3.4.1 Experimental Setup. 62
3.4.2 Dynamics Model Identification. 63
3.4.3 Bouc–Wen Model Results 64
3.4.4 LSSVM Model Results 67
3.5 Experimental Studies on Hysteresis Compensation 71
3.5.1 Feedforward Compensation 71
3.5.2 Feedforward Plus Feedback Control 73
3.6 Chapter Summary 74
References. 75

Part II Hysteresis-Model-Free, State-Observer-Based Feedback Control

4 Model Predictive Discrete-Time Sliding-Mode Control 79
4.1 Introduction 79
4.2 Problem Formulation. 81
4.2.1 Dynamics Modeling of a Nanopositioning System . . . 81

4.2.2 Sliding-Mode Controller Design 83
4.2.3 Control Gain Design 85
4.3 DTSMC Design 86
4.3.1 Controller Design and Analysis 86
4.3.2 Tracking Error Bound Analysis 88
4.4 MPDTSMC Design 89
4.4.1 MPDTSMC Controller Design 89
4.4.2 Stability Analysis 91
4.4.3 State Observer Design 92
4.4.4 Tracking and Estimation Error Bound Analysis 93
4.5 Experimental Investigation 94
4.5.1 Experimental Setup 94
4.5.2 Hysteresis Characterization 94
4.5.3 Plant Model Identification 95
4.5.4 Controller Parameter Design 96
4.5.5 Simulation Studies 97
4.5.6 Experimental Testing Results 99
4.5.7 Discussion on System Performance 102
4.6 Chapter Summary 103
References 103

5 Model Predictive Output Integral Discrete-Time Sliding-Mode Control 105
5.1 Introduction 105
5.2 Problem Formulation 106
5.3 MPOIDSMC Design 107
5.3.1 OIDSMC Controller Design 107
5.3.2 MPOIDSMC Controller Design 109
5.4 Experimental Investigations 114
5.4.1 Experimental Setup 114
5.4.2 Plant Model Identification 115
5.4.3 Controller Parameter Design 116
5.4.4 Experimental Studies 118
5.4.5 Discussion on Controller Performance 121
5.5 Chapter Summary 122
References 122

Part III Hysteresis-Model-Free, State-Observer-Free Feedback Control

6 Digital Sliding-Mode Control of Second-Order Systems 127
6.1 Introduction 127
6.2 Dynamics Model and Problem Formulation 128

6.3 DSMC Design 130
6.4 Experimental Studies 133
6.4.1 Experimental Setup 133
6.4.2 Plant Model Identification 134
6.4.3 Experimental Results 135
6.4.4 Discussion 145
6.5 Chapter Summary 145
References 146

7 Digital Sliding-Mode Control of High-Order Systems 147
7.1 Introduction 147
7.2 Problem Formulation 148
7.2.1 System Modeling 148
7.2.2 Disturbance Estimation 150
7.3 IODSMC Design 151
7.3.1 Sliding Function Definition 151
7.3.2 Design of IODSMC 152
7.3.3 Robust IODSMC Design 154
7.4 Experimental Setup and Controller Setup 156
7.4.1 Experimental Setup 156
7.4.2 Plant Model Identification 157
7.4.3 Controller Parameter Design 158
7.5 Experimental Results and Discussion 159
7.5.1 Set-Point Positioning Results 159
7.5.2 Sinusoidal Positioning Results 159
7.5.3 Bandwidth Testing Results 161
7.5.4 Robustness Testing Results 162
7.5.5 Further Discussion 164
7.6 Chapter Summary 164
References 165

8 Digital Sliding-Mode Prediction Control 167
8.1 Introduction 167
8.2 Problem Formulation 168
8.2.1 System Modeling 168
8.2.2 Disturbance Estimation 169
8.3 DSMC Design 169
8.3.1 Sliding Function Definition 170
8.3.2 Design of DSMC 170
8.3.3 Error Bound Analysis 172
8.4 DSMPC Design 173
8.4.1 DSMPC Design 173
8.4.2 Stability Analysis 175
8.4.3 Error Bound Analysis 177

8.5 Experimental Studies and Discussion . . . 177
8.5.1 Experimental Setup . . . 177
8.5.2 Plant Model Identification . . . 178
8.5.3 Controller Parameter Design . . . 179
8.5.4 Experimental Studies . . . 179
8.5.5 Further Discussion . . . 183
8.6 Chapter Summary . . . 184
References . . . 184

9 Model-Reference Adaptive Control with Perturbation Estimation . . . 187
9.1 Introduction . . . 187
9.2 Dynamics Modeling and Perturbation Estimation . . . 188
9.2.1 Dynamics Modeling . . . 188
9.2.2 Perturbation Estimation . . . 189
9.3 MRACPE Control Design . . . 190
9.3.1 MRACPE Controller Design . . . 190
9.3.2 Dead-Zone Modification of Adaptive Laws . . . 193
9.3.3 Overview of Control Scheme . . . 193
9.4 Experimental Setup and Controller Setup . . . 194
9.4.1 Experimental Setup . . . 194
9.4.2 Statics Testing and Dynamics Model Identification . . . 196
9.4.3 Controller Setup . . . 197
9.5 Experimental Results and Discussion . . . 198
9.5.1 Set-Point Positioning Testing . . . 198
9.5.2 Sinusoidal Positioning Testing . . . 200
9.5.3 Control Bandwidth Testing . . . 200
9.5.4 Discussion . . . 202
9.6 Chapter Summary . . . 204
References . . . 205

Part IV Applications to Micromanipulation

10 Adaptive Impedance Control of Piezoelectric Microgripper . . . 209
10.1 Introduction . . . 209
10.2 Problem Formulation . . . 211
10.2.1 Dynamics Modeling and Perturbation Estimation . . . 212
10.2.2 Impedance Control Problem . . . 213
10.3 ADSMGIC Scheme Design . . . 214
10.3.1 Sliding Function Definition . . . 214
10.3.2 ADSMGIC Design . . . 215
10.3.3 Stability Analysis . . . 216
10.3.4 Evaluation of Steady-State Errors . . . 218

10.4 Experimental Setup and Controller Setup 219
10.4.1 Experimental Setup 219
10.4.2 Force Observer Design 220
10.4.3 Controller Setup 222
10.5 Experimental Results and Discussion 224
10.5.1 Interaction Control Results 224
10.5.2 Discussion on Control Performance 229
10.6 Chapter Summary 230
References 230

11 Position/Force Switching Control of a Miniature Gripper 233
11.1 Introduction 233
11.2 Experimental Setup and Calibration 234
11.2.1 Working Principle of the Gripper 234
11.2.2 Experimental Setup 236
11.2.3 Calibration of Position and Force Sensors 237
11.2.4 Gripping Range Testing 239
11.2.5 Frequency Response Testing 240
11.3 Position/Force Switching Control Scheme Design 241
11.3.1 Event-Based Switching Control Framework 241
11.3.2 Incremental DSMC Position Controller 242
11.3.3 Incremental PID Force Controller 245
11.3.4 Switching Criterion 245
11.4 Experimental Investigations and Discussion 246
11.4.1 Controller Setup 246
11.4.2 Position/Force Switching Control Results 247
11.4.3 Further Discussion 249
11.5 Chapter Summary 252
References 252

Index 255

Abbreviations

ADSMGIC	Adaptive digital sliding-mode generalized impedance control
ANN	Artificial neural networks
DSMC	Digital sliding-mode control
DSMPC	Digital sliding-mode prediction control
DSP	Digital signal processor
DTSMC	Discrete-time sliding-mode control
EDM	Electrical discharge machining
FEA	Finite-element analysis
FPGA	Field-programmable gate array
GA	Genetic algorithm
GIC	Generalized impedance control
GMVC	Generalized minimum variance control
IODSMC	Input–output-based digital sliding-mode control
LSSVM	Least squares support vector machines
LTI	Linear time-invariant
LVDT	Linear variable differential transformer
MAE	Mean absolute error
MAXE	Maximum error
MPC	Model predictive control
MPDTSMC	Model predictive discrete-time sliding model control
MPI	Modified Prandtl–Ishlinskii
MPOIDSMC	Model predictive output integral discrete-time sliding-mode control
MRAC	Model-reference adaptive control
MRACPE	Model-reference adaptive control with perturbation estimation
OIDSMC	Output integral discrete-time sliding-mode control
PC	Personal computer
PEA	Piezoelectric actuator
PI	Proportional-integral
PID	Proportional-integral-derivative
PRB	Pseudo-rigid-body

PSA	Piezoelectric stack actuator
PSO	Particle swarm optimization
PZT	Pb(Zr, Ti)O_3 crystal
QP	Quadratic programming
QSD	Quasi-sliding domain
RMS	Root-mean-square
RMSE	Root-mean-square error
SISO	Single-input-and-single-output
SMC	Sliding-mode control
SNR	Signal-to-noise ratio
SVM	Support vector machines
Z–N	Ziegler–Nichols
ZOH	Zero-order-hold

Chapter 1
Introduction

This chapter provides an introduction to the piezoelectric micro-/nano-positioning system and the concerned control problems. The hysteresis compensation is solved using both feedforward and feedback control approaches to achieve a precision motion control. As a typical application of micro-/nano-positioning device, the micromanipulation application is also introduced, and the concerned position and force control problem is addressed to facilitate a delicate automated manipulation operation.

1.1 Micro-/Nano-positioning Technique

Micro-/nano-positioning concerns precision motion control with the resolution down to micro-/nanometer scale. Micro-/nano-positioning system refers to a positioning device which is capable of producing displacement down to micro-/nanometer resolution. Such positioning devices have been widely applied in fields including scanning probe microscopy, lithography manufacturing, and wafer alignment. In addition, these devices have also found extensive applications in precision micro-/nano-manipulation and micro-/nano-assembly domains. For instance, in biological cell manipulation or micro-component assembly, micro-/nano-positioning systems are employed to realize a precise positioning of the end-effector, such as micro pipette or gripper, for successful execution of the manipulation or assembly task.

Conventionally, the lead-screw mechanisms are usually employed to achieve a precision positioning motion. However, these traditional mechanisms suffer from the adverse effects of backlash, clearance, friction, and wear, which deteriorate the positioning accuracy of the system. Alternatively, flexure hinge-based-compliant mechanisms can be used to overcome these shortcomings. Different from traditional sliding and rolling mechanisms, compliant mechanisms deliver motions by making use of the elastic deformation of the material. As a consequence, they allow the generation of several attractive merits in terms of no backlash and clearance,

© Springer International Publishing Switzerland 2016

Q. Xu and K.K. Tan, *Advanced Control of Piezoelectric Micro-/Nano-Positioning Systems*, Advances in Industrial Control,
DOI 10.1007/978-3-319-21623-2_1

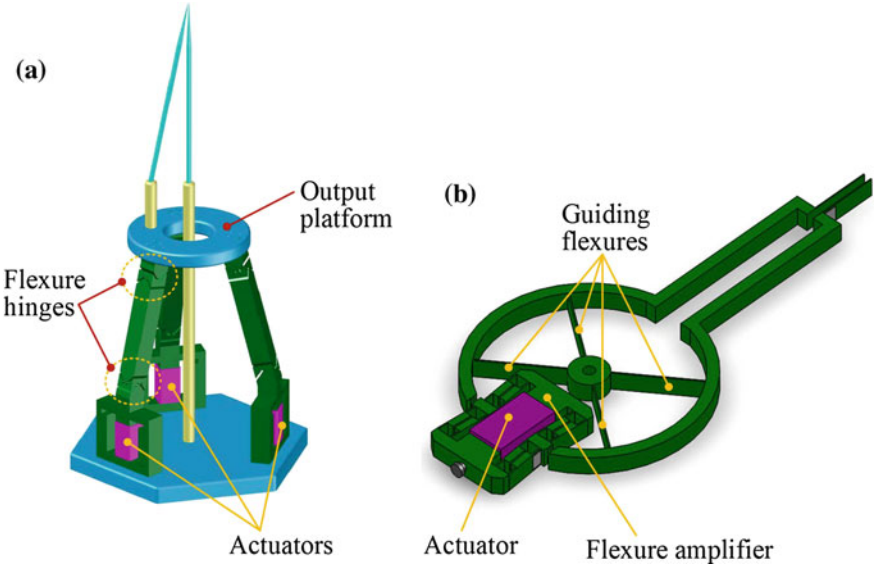

Fig. 1.1 Examples of micro-/nano-positioning devices. **a** A compliant micromanipulator. **b** A compliant microgripper

no friction and wear, no need for lubrication, smooth and continuous motion, inherently infinite resolution, vacuum and cryogenic compatibility, and monolithic manufacturing. Hence, various modern micro-/nano-positioning stages have been devised based on compliant mechanisms. For example, a flexure hinge-based compliant micromanipulator and microgripper are shown in Fig. 1.1a and b, respectively.

1.2 Actuators and Sensors

Different kinds of actuators can be employed to drive the positioning stages, such as piezoelectric actuators, magnetic levitation motors, electromagnetic actuators, and voice coil motors. In particular, smart actuators based on smart materials (e.g., piezoelectric materials, shape memory alloys, magnetostrictive materials, etc.) are popularly employed for the actuation in various precision systems dedicated to micro-/nano-positioning. As a typical smart actuator, piezoelectric actuator (PEA) prevails in many industrial applications thanks to its merits of sub-nanometer positioning resolution, rapid response speed, large blocking force, and compact size.

As a typical flexure-based ultrahigh-precision positioning device, piezoelectric micro-/nano-positioning system is driven by PEAs. Popular PEAs involve the forms of piezo stacks, piezo benders, and piezo diaphragms as shown in Fig. 1.2. Owing to the aforementioned advantages, PEAs are popularly applied in various

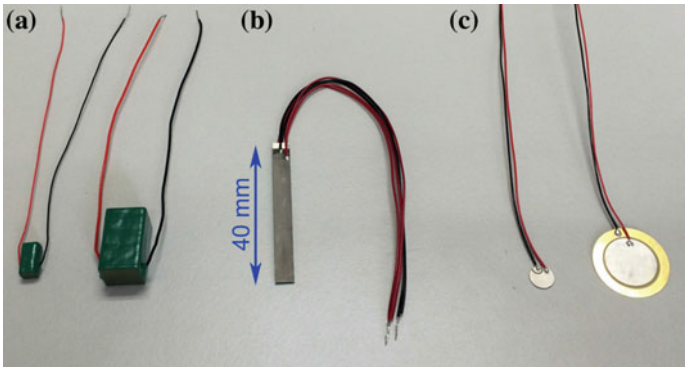

Fig. 1.2 Examples of popular piezoelectric actuators. **a** Piezo stacks. **b** Piezo bender. **c** Piezo diaphragms

micro-/nano-positioning systems such as scanning probe microscopes, precision alignment devices, e-beam lithography systems, and so on.

To measure the output displacement of micro-/nano-positioning stages, sensors based on different principles have been exploited. The popular types of displacement sensors include capacitive sensor, optical sensor, strain sensor, and inductance sensor. As reviewed below, these sensors own different properties and can be employed in different scenarios in accordance with specific requirements.

Capacitive sensors measure the displacement by detecting the capacitance change between two metal plates. Generally, they can provide the sensing resolution down to sub-nanometer level in a small measuring range (typically, tens of micrometers). Optical sensors are capable of high resolution measurement in a large range. Popular optical sensors involve laser interferometers and laser displacement sensors, where the latter are based on the triangulation measurement method. Although these sensors can provide nanometer-level resolution, they are bulky and not suitable for compact system application. In contrast, strain sensors possess a small size and they are most suitable for embedded design of micro-/nano-positioning system. Strain sensors involve metal strain gauges and piezoresistive strain gauges. While the former is capable of a larger strain deformation, the latter is able to deliver a higher sensitivity. Usually, the strain sensors exhibit considerable noises, which require extra signal processing so as to achieve a high sensing resolution. Commonly used inductance sensors involve linear variable differential transformers (LVDT) and eddy-current sensors. These sensors are sensitive to the motion in the axes orthogonal to the measurement axis. Hence, these inductance sensors are more suitable for uniaxial motion measurement to achieve nanometer-level resolution.

In addition, different microscopes in terms of optical microscopes and scanning electron microscopes, etc., have also been adopted as position sensors to detect the output displacement of micro-/nano-positioning devices. Yet, the disadvantage lies in the relatively low sampling frequency of universal image processing unit.

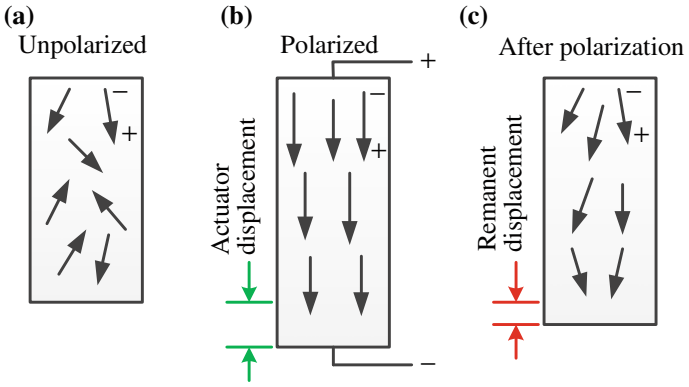

Fig. 1.3 Polarization process for a piezoelectric actuator

1.3 Piezoelectric Nonlinearity

The piezoelectric effect is a fundamental process involving electro-mechanical interactions and represents the conversion of energy. It relates the electric field to the mechanical compression/elongation in a piezoelectric material. This fundamental property of piezoelectricity has therefore led to the utilization of such materials in the fabrication of various piezoelectric transducers including actuators and sensors.

Generally, PEAs are fabricated by piezoelectric ceramic materials such as lead zirconate-titanate $Pb(Zr, Ti)O_3$ crystal, commonly called PZT. Figure 1.3 illustrates the polarization process for a piezoelectric actuator. In Fig. 1.3a, the electric dipoles of ceramic materials are oriented randomly. Without an applied electric field, it does not exhibit the function of piezoelectricity. Once an electric field is applied, the electric dipoles align themselves in a direction close to the applied electric field, and the crystals expand in a direction close to the applied electric field, as shown in Fig. 1.3b. This process is called polarization. However, when the electric field is removed, the electric dipoles will not return to the original position exactly, which results in remanent polarization, as shown in Fig. 1.3c.

PEAs produce mechanical movement by making use of the inverse piezoelectric effect of piezoelectric materials, which causes the shape change under the input of voltage or current. The movement with the resolution of micro-/nanometer level is desirable. At the same time, PEA introduces nonlinearity into the system due to the piezoelectric hysteresis and creep effects. The creep effect causes the drifts of PEA output when the PEA is driven by low-frequency input. Hence, the creep is a low-frequency behavior, which can be modeled, for instance, by a linear transfer function.

The hysteresis nonlinearity has some special features. First, it exhibits multi-valued mapping, as shown in Fig. 1.4. That is, given the same input signal, the outputs are different if the history output states are not identical. In other words, it has the memory of history state. In order to determine the output of the system, both the input

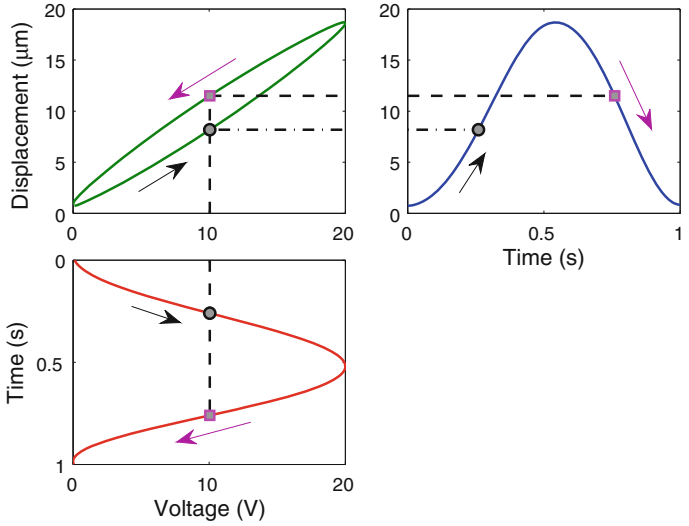

Fig. 1.4 Illustration of the piezoelectric hysteresis. Given the same input voltage, the output displacements are different due to the hysteresis effect

signal and the history state of system should be considered. In addition, when the direction of the input change rate changes, the output signal shows non-differentiable characteristics. The hysteresis nonlinearity induces a severe open-loop positioning error as high as 10–15 % of the stage travel range. Moreover, the output signal is also dependent on the frequency of the input signal. When the rate of the input signal is increased, the error increases accordingly.

Therefore, the hysteresis has to be suppressed to cater for the accuracy requirement of high precision applications. In the past two decades, extensive works have been carried out for the compensation of the hysteretic behaviors. Although the hysteresis can be greatly alleviated if a PEA is driven by a charge source [13], it is at the cost of a reduced stroke. Thus, voltage actuation has been widely adopted in practice.

1.4 Feedforward Control Based on Hysteresis Models

By taking the driving voltage and the produced position as the input and output, respectively, a piezoelectric micro-/nano-positioning system can be described by a block diagram as shown in Fig. 1.5a. As a nonlinear system, the piezoelectric micro-/nano-positioning system can be represented by a Hammerstein cascade model [32, 33], as shown in Fig. 1.5b. The nonlinear hysteresis model $H(.)$ is followed by a linear dynamics model $G(s)$. The dynamics model involves the vibration dynamics and creep effects. The hysteresis nonlinearity can be compensated for by different ways as discussed in the subsequent sections. Generally, the existing hysteresis

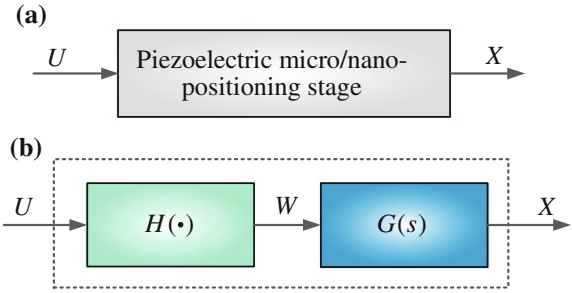

Fig. 1.5 **a** Piezo-actuated stage with voltage input U and position output X. **b** Hammerstein cascade model of a nonlinear hysteresis model $H(.)$ and linear dynamics model $G(s)$. The intermediate variable W is usually unmeasurable

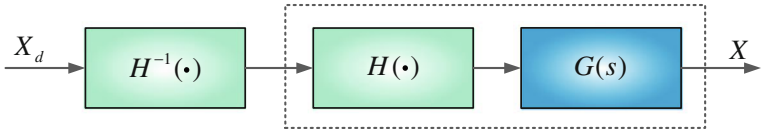

Fig. 1.6 Block diagram of feedforward control to compensate the nonlinear hysteresis effect $H(.)$ using an inverse hysteresis model $H^{-1}(.)$

compensation schemes fall into two categories in terms of hysteresis model-based feedforward control and hysteresis model-free feedback control.

To compensate for the hysteresis nonlinearity, an inverse hysteresis model $H^{-1}(.)$ can be developed and used as a feedforward control, as shown in Fig. 1.6. By this approach, the hysteresis is cancelled and a linear dynamics system is obtained approximately. In order to construct the feedforward controller, a hysteresis model is usually identified and then inverted to generate an inverse hysteresis model. Hence, the establishment of a suitable hysteresis model is required.

1.4.1 Conventional Hysteresis Model

Traditionally, the modeling of hysteresis nonlinearity is a time-consuming problem, and there is no universal model. In the literature, a number of models have been developed for describing the hysteresis nonlinearity, which can be classified into two main types: physics-based models and phenomenological models. A classification diagram is depicted in Fig. 1.7.

Based on the fundamental physical principle of piezoelectric material, physics-based models try to establish the hysteresis model by making use of the relationships of energy, displacement and so on. Generally, it is difficult to build a physics-based model because the physical feature of the hysteretic system is usually very complicated. In addition, the physics-based model of one hysteretic system

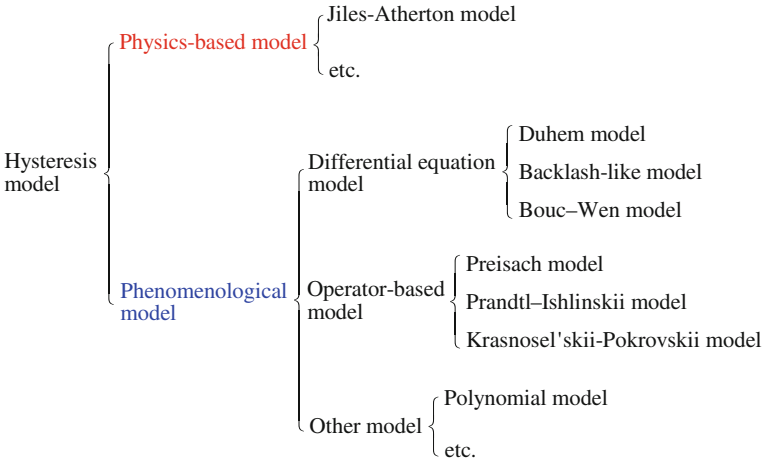

Fig. 1.7 Classification diagram of some popular hysteresis models

usually cannot be applied to another one. Hence, the physics-based model is lack of generalization.

In contrast, starting from the characteristic of hysteresis curve, phenomenological models try to describe the hysteresis effect using effective mathematical model directly [9, 21, 26, 30, 35, 38, 71]. Based on different mathematical interpretations, phenomenological models have been established without considering the physical meanings. These models include differential equation-based and operator-based hysteresis models.

Normally, a hysteresis model is identified using the excitation input and output data of the system. Afterwards, an inverse hysteresis model is constructed and utilized as a feedforward controller to cancel the hysteresis effect. With a perfect cancellation of the hysteresis effect, the resulted linear dynamics system is easy to control.

A majority of the aforementioned models deal with rate-independent hysteresis. Actually, the hysteresis effect is dependent not only on the amplitude but also on the frequency of input signals. Fortunately, the rate-dependent behavior can be described by the cascade of a rate-independent hysteresis followed by a linear dynamics model, i.e., a Hammerstein model as described in Fig. 1.5b. Hence, a two-step process is needed to accurately identify the hysteresis model and dynamics model, respectively.

Alternatively, the entire system can be modeled together using a rate-dependent hysteresis model. However, it is difficult to capture the complicated rate-dependent hysteretic behavior precisely. In addition, a majority of the existing models employ a large number of parameters to describe the rate-dependent hysteresis [4, 78]. As an adverse effect, it may block their applications in high-speed real-time control.

1.4.2 Intelligent Hysteresis Model

Recently, it has been shown that artificial intelligence algorithms pave a promising way to model the complicated hysteresis nonlinearity. In particular, the artificial neural networks (ANN) provide an efficient approach to model the nonlinear hysteresis [15, 76]. Nevertheless, there is no universal method to determine an optimal ANN structure in terms of the number of hidden layers and the number of neurons in each layer. Moreover, ANN exhibit the problems of overfitting and sinking into local optima, which are their major drawbacks in practical implementation.

Alternatively, support vector machines (SVM) are a potential way to estimate nonlinear system models accurately. Based on statistical learning theory and structural risk minimization principle, the SVM approach is capable of modeling nonlinear systems by transforming the regression problem into a convex quadratic programming (QP) problem and then solving it with a QP solver. Compared with conventional ANN, SVM have the major advantages of global optimization and higher generalization capability.

As a variant of SVM, least squares support vector machines (LSSVM) have been introduced in 1999 [60]. LSSVM utilizes equality constraints instead of inequality constraints as in the ordinary SVM. Hence, it simplifies the regression to a problem that can be easily solved from a set of linear equations. As a result, the LSSVM has a relatively low complexity and it is computationally more efficient than the standard SVM [60]. Another advantage of LSSVM is that it has fewer parameters to be tuned. More detailed information about LSSVM can be found in the book [59].

Although SVM techniques have been widely applied to solve classification and regression problems, their applications in the treatment of hysteresis are still limited. To date, the employment of SVM or LSSVM for the modeling and compensation of hysteresis effects has been conducted by only a few works [74]. The major challenge of developing an intelligent model lies in how to establish an effective one-to-one mapping of the hysteresis nonlinearity.

In addition, a review of model-based hysteresis compensation approaches reveals that a majority of the existing works compensate for the hysteresis effect by employing an inverse hysteresis model. Thus, both a hysteresis model and an inverse hysteresis model are required for the hysteresis identification and compensation purposes. In this sense, to reduce the workload of precision control, it is desirable to develop a sole hysteresis model for purposes of both hysteresis description and compensation.

1.4.3 Feedforward Plus Feedback Control

In practice, uncertainties always exist in some degree in the identified hysteresis model and dynamics model. To handle these uncertainties, feedback control is required to make the system robust against the disturbances. Two popular schemes of feedback combined with feedforward control are shown in Fig. 1.8. Figure 1.8a

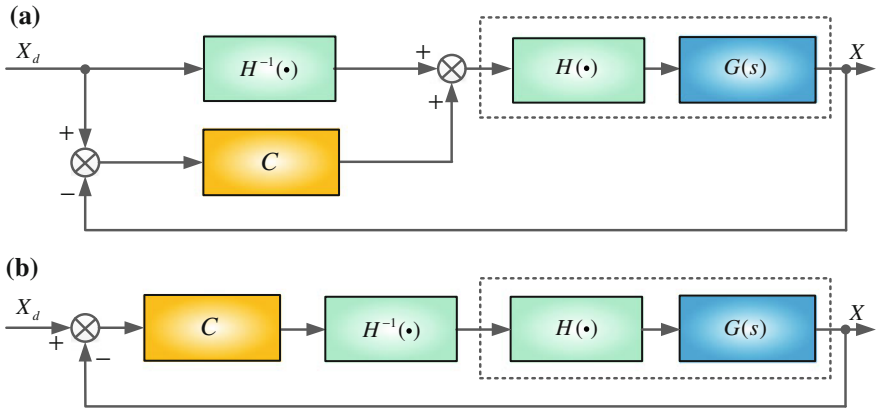

Fig. 1.8 Block diagram of feedforward plus feedback control scheme for precision motion control

illustrates a control scheme where the feedback control C is connected in parallel to the feedforward control term $H^{-1}(.)$ [21, 58], while Fig. 1.8b shows a strategy where the feedback control C is applied once the nonlinear system is linearized by the feedforward control $H^{-1}(.)$ [16]. It is notable that the purpose of the feedforward control in both schemes is to compensate for the hysteresis effect. An alternative scheme is presented in the book [17] (Fig. 9.6, page 259), where an offline feedforward control is employed to compensate for the vibrational dynamics instead.

Targeting at specific applications, different feedback controllers can be designed to realize such a precision motion control system. In the literature, classical feedback controls have been employed, such as proportional-integral-derivative (PID) control, high-gain feedback control, state feedback control, etc., owing to their easy implementation.

1.5 Robust Feedback Control

Considering that hysteresis modeling is usually time-consuming, it is attractive to suppress the hysteresis nonlinearity by implementing a stand-alone feedback control scheme. Hence, the main property of hysteresis model-free control is that no hysteresis model is required. Alternatively, the hysteresis effect is considered as an uncertainty or a disturbance [75] to the nominal dynamics system, which is tolerated by an advanced robust or adaptive controller. For instance, the applications of sliding-mode control [11, 68, 72, 77], H_∞ robust control [63, 65], adaptive control [36], fuzzy logic control [24, 25, 62], and neural network control [49] have been successfully reported in the literature. Three typical nonlinear control methods, namely sliding mode control, model predictive control, and model-reference adaptive control, are discussed as follows.

1.5.1 Sliding-Mode Control

Sliding-mode control (SMC) technique provides an effective and simple way to deal with the model imperfection and uncertainties for nonlinear systems. As a variable structure control, SMC is a nonlinear control approach which drives the nonlinear system's state trajectory onto a specified sliding surface ($s = 0$) and maintains the trajectory on this surface for the subsequent time, as illustrated in Fig. 1.9. Because the control can be as simple as switching between two states, it is not sensitive to parameter variations and uncertainties once entering into the control loop. Thus, the main attractive property of SMC lies in its robustness in the presence of modeling imprecision and uncertainty.

In practice, the control scheme of a micro-/nano-positioning system is usually realized using a sampled-data system, such as a computer or a digital signal processor (DSP). Deploying a continuous-time controller directly to a digital system may cause instability of the control system. In addition, concerning SMC, the digital implementation of a continuous-time control deteriorates the invariance property exhibited by continuous-time SMC. Hence, to implement a reliable control scheme on a sampled-data system, the discrete-time sliding-mode control (DTSMC) can be adopted [7, 19].

Generally, the DTSMC can be categorized into state-based and output-based methods. The former is developed based on system state or state error [1, 66, 73], while the latter is realized on the basis of system output or output error [68, 72]. Usually, the implementation of either method requires the state feedback of the system. However, in the majority of practical situations, only the position information of a piezoelectric micro-/nano-positioning system is provided by the displacement sensor. Hence, a state observer is indispensable for the practical realization of DTSMC, which

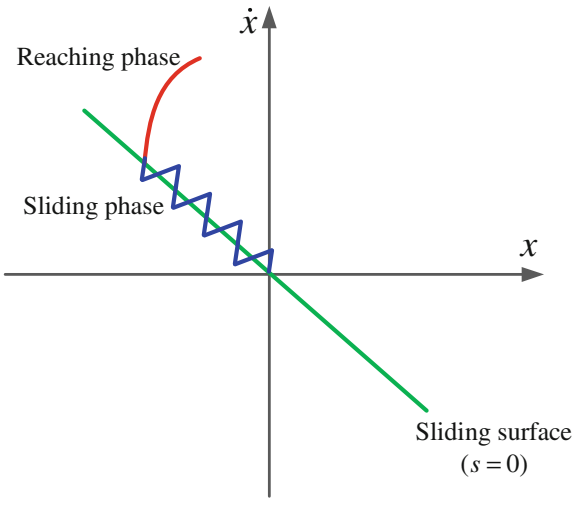

Fig. 1.9 Phase plane of the sliding-mode control (SMC)

complicates the control design procedure. Furthermore, an improperly designed state observer may cause instability of the system. In this sense, it is desirable to eliminate the use of a state observer.

In previous works, an input–output based adaptive DTSMC has been developed in [55], which is based solely on input and output data. However, the controller is dedicated to a first-order model with long dead-time. It is not suitable for a piezoelectric actuation system which typically features a plant model of higher order preceded by complicated nonlinearity. To remove the restriction of the first-order plant model as required in [55], a new input–output based DTSMC control has been figured out for a velocity tracking system [56]. Adaptive coefficients of the switching hyperplane are employed to tolerate the modeling error, and its effectiveness is verified by simulation studies. Nonetheless, due to a relatively long parameter adaptation process, the adaptive control normally leads to a slow transient response before attaining the steady state [11, 70]. On the other hand, the generalized minimum variance control (GMVC) scheme can be employed to develop a DTSMC control without using a state observer. To improve the tracking accuracy, a DTSMC scheme is presented in [45], which is developed based on input/output measurements and the GMVC technique. Nevertheless, the output tracking accuracy is unknown and filtering is required to suppress the induced chattering phenomenon. To eliminate the chattering completely, a fuzzy sliding mode control is demanded [44]. In addition, the multirate output feedback technique has been developed to relax the need of the entire state vector for the realization of DTSMC control scheme [5].

To this end, targeting at easy realization, it is desirable to develop a simple DTSMC scheme without using the complicated hysteresis model and state observer for precise motion control of a piezoelectric micro-/nano-positioning system.

1.5.2 Model Predictive Control

For a discrete-time system, the strategy of model predictive control (MPC) can be employed to predict the system performance in a specified time in the future and to produce an optimal control action with respect to a predefined cost criterion at each time step [64], as illustrated in Fig. 1.10.

By combining the SMC and MPC techniques, the model predictive sliding-mode control has been recently proposed to achieve the advantages of both methods [20, 67]. Although the combined control has been adopted in a few previous works [29, 47] for the control of piezoelectric actuator by suppressing the chattering phenomenon, it remains unclear why the MPC methodology can eliminate the chattering phenomenon in the sliding mode. Hence, more theoretical analysis is required to facilitate better understanding of the combination of SMC and MPC techniques, which is addressed in Chaps. 4, 5, and 8 in this book.

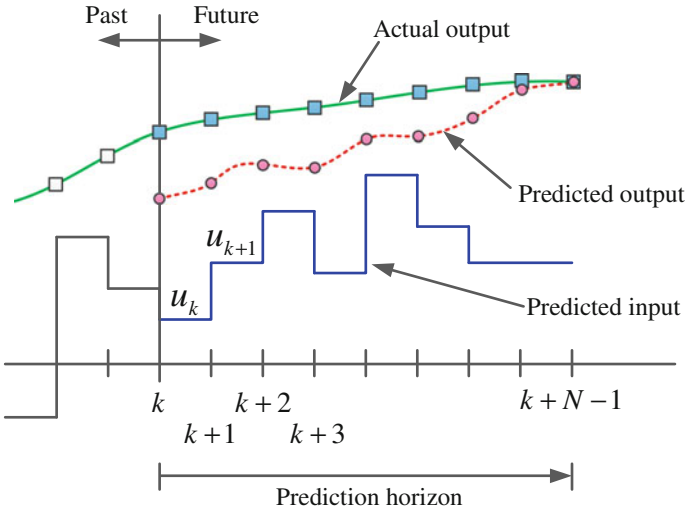

Fig. 1.10 Schematic diagram of the model predictive control (MPC)

1.5.3 Model-Reference Adaptive Control

Compared with the general robust control approach, the adaptive control does not require prior information about the bounds on uncertain or time-varying items. Hence, adaptive control paves a more straightforward way to the precision control of micro-/nano-positioning systems.

In the literature, only limited work has been dedicated to the extension of adaptive controllers to micro-/nano-positioning system control. In addition, uncertainty bounds are usually required to realize the control system. In previous work [34], a model-reference adaptive control (MRAC) strategy is reported to compensate for the hysteresis effect of a micropositioning stage. Although the adaptive controller is realized without modeling the hysteresis effect nor acquiring the uncertainty bounds, a Prandtl–Ishlinskii hysteresis model is required to convert the desired motion trajectory into a voltage input. More recently, a MRAC scheme based on hyperstability theory is presented for a piezoactuated system [39]. Nonetheless, a Bouc–Wen hysteresis model is still employed to identify the dynamics equation of the system.

From a practical point of view, it is preferable to develop a MRAC scheme without modeling the complicated nonlinear effects. By considering the nonlinearity as a perturbation to the system, several perturbation estimation methods have been reported to be integrated with MRAC schemes. To name a few, a MRAC with disturbance rejection strategy is presented for the systems, which can be represented by parabolic or hyperbolic partial differential equations along with known disturbance model or constant disturbance [31]. However, these scenarios are different from the situation in a PEA-driven system where the unmodeled disturbance involving hysteresis nonlinearity is not constant. In addition, an adaptive perturbation approximator is outlined

to estimate the structured perturbations of second-order systems online [14], and a perturbation estimation mechanism is proposed to design a MRAC controller for a class of multiple-input and multiple-output (MIMO) dynamic systems [12]. The aforementioned two methods are implemented on the basis of the assumption that the plant states are all measurable. Nevertheless, this assumption does not always hold for micro-/nano-positioning systems which typically only offer displacement feedback. Moreover, the reference signals used in the preceding literature are all given in terms of voltage. For practical applications, a desired motion trajectory instead of voltage signal is preferable. These issues are overcome in Chap. 9 in the book.

1.5.4 Other Control Strategies

In addition to the aforementioned control schemes, H_∞ robust control, repetitive control, iterative learning control, disturbance observer, neural network control, fuzzy control, etc., have also been extensively explored for piezo-driven micro-/nano-positioning control.

Different control schemes own their specific properties and are suitable for different application scenarios. For example, H_∞ controller is usually of high order, which requires excessive computational burden. Repetitive control and iterative learning control are commonly applicable to the tracking of periodical motion trajectory. Fuzzy control is heavily dependent on the finely tuned rule tables.

1.6 Position/Force Control in Micromanipulation

Micromanipulation and microassembly are important approaches to producing complex micro/nano-systems which are composed of microparts fabricated from different materials [6, 40, 51]. In view of the limitations of human operators in terms of accuracy and efficiency for executing such tasks, automated handling of the objects in micro- and nanometer scales necessitates the development of robotic microassembly systems. As a crucial micro-/nano-positioning device to realize a grasp operation in the aforementioned application, microgripper has gained intensive attention in the literature. Typically, the gripper is employed to execute an automated grasp-hold-release operation for such applications as material characterization, biological sample pick-and-place, and micro-object assembly.

To avoid the damage of the fragile microobjects and microgripper arms which contact each other during microassembly process, the interaction control is critical to regulate the desired position and contact force simultaneously. One of the major challenges stems from the combination method of position and force control. Generally, there are two basic approaches to interaction control, i.e., hybrid control and impedance control, which are presented below.

1.6.1 Hybrid Control

The hybrid position/force control method decomposes the task space of the end-effector into position subspace and force subspace. It allows the generation of compliant motion by controlling the end-effector position in position subspace and the interaction force in force subspace, respectively. Generally, a position control law along the force constrained directions and a force control law along the position constrained directions are designed through the use of selection matrices. However, a switching of the control law is required to implement the position and force control alternately. In addition, this approach usually suffers from robustness problems during the transition between unconstrained and constrained motions [54].

1.6.2 Impedance Control

The impedance control enables compliant motion of the end-effector in a unified framework for both constrained and unconstrained directions [27]. The goal of impedance control is to regulate a desired dynamics relation between the position and contact force. That is, both position and force are indirectly controlled by regulating the predefined dynamics response, i.e., the desired impedance.

Impedance control emerges as a promising approach to interaction control in micro-/nanoscales [23, 42]. For example, a position-based impedance control of a piezoelectric bimorph microgripper is reported in [53], where a state-feedback position controller and a low-pass filtered force feedback controller are implemented. However, the impedance control usually requires an exact dynamics model of the system. Due to the uncertainties in dynamics model, it is practically difficult to achieve the desired impedance. To remedy this shortcoming, adaptive [41] and robust [43] impedance control algorithms have been developed to tolerate the dynamic parameter uncertainties. Nevertheless, the conventional impedance control framework exhibits a drawback of inability of tracking the reference force input. Several schemes have been exploited to overcome this shortcoming. Typically, a generalized impedance control (GIC) scheme has been established based on a generalized desired impedance [10]. It integrates both position and force errors, and enables the force tracking ability.

Recently, intensive efforts have been made toward force-tracking impedance control, which is robust to parameter uncertainties in both dynamics and environment models [28]. Although this robustness property appears attractive, it is at the expense of implementation complication. Considering that the impedance control possesses some inherent robustness to environment model errors [3, 52], a GIC with robustness to dynamics model uncertainties is desirable for precise interaction control.

On the one hand, the control scheme of a practical microassembly system is usually realized on a digital system, e.g., a computer or DSP apparatus. As it is known, applying a continuous-time controller directly to a digital system can induce instability due to the computational delays [8]. This is true for a microassembly system, e.g.,

a visual servoing system [50], which typically has a low sampling rate, typically, of the order of 10 Hz. Hence, to deploy a reliable interaction control to a sampled-data system, a discrete-time impedance controller is more preferable. However, limited work has been conducted on discrete-time sliding-mode impedance control scheme in the literature. It is necessary to devise new discrete-time sliding-mode impedance control to realize an interaction control of a piezoelectric microgripper dedicated to micromanipulation and microassembly tasks.

1.6.3 Switching Control

To use the impedance control framework [37, 69], care must be taken for the position and force trajectory planning to ensure a desired performance. Intuitively, a position/force switching control can be adopted to adjust the gripper tip position and gripping force in an alternate manner [57]. The concerned dominant issue is how to realize a smooth transition when different control variables are switched [48].

In order to achieve a smooth transition between the position and force control, an intermediate brake mode can be added between the two control modes [22, 61]. Furthermore, to accomplish a rapid intermediate control and to reduce the force overshoot in the initial contact, an optimal velocity profile can be used [2]. However, an extra control mode is required, whose execution increases the overall operation time of the gripper. More recently, fuzzy control has been proposed to smooth the transition [18, 46]. However, the membership functions have to be readjusted to adapt to the gripping of different objects, which complicates the practical implementation process. Hence, a simple and efficient approach is desirable to realize a smooth transition between the position and force control.

Chapter 11 reports on a scheme of incremental control to implement a smooth transition of the position/force switching control for a micrograpping system. Specifically, in the closing and opening phases, an incremental digital sliding-mode control (DSMC) is devised to cater for the position control. During the contact phase, an incremental-type digital PID force control is adopted. The incremental controller only solves the change value of the control action at each time step. At the moment of switching between two consecutive control phases, the controller adopts the control action in the previous phase as the base value for the next one. In this way, a smooth transition between two adjacent phases is easily achieved. The feasibility of the scheme is examined by a typical grasp-hold-release operation of a micro copper wire through experimental studies. Moreover, its superiority over the conventional approach is revealed by experimental demonstrations.

1.7 Book Summary

This book mainly concerns hysteresis modeling and compensation of piezoelectric micro-/nano-positioning systems. Both feedforward and feedback controls have been employed in piezoelectric micro-/nano-positioning control. The approaches of piezoelectric system control with and without using hysteresis model are two different ways. By comparing the two approaches, it is observed that the feedforward control is capable of compensating the majority of the piezoelectric nonlinearity effect. Through the combination of a simple feedback control with the feedforward control, better tracking accuracy can be achieved. However, hysteresis or inverse hysteresis modeling is a time-consuming work, which requires extensive experimental testing. In addition, the couplings among hysteresis, creep, and vibration dynamics call for a careful treatment. Such kind of computational burden can be avoided by developing a robust control which considers the unmodeled nonlinearity as a disturbance to the nominal plant model. In this way, the time-consuming procedure of hysteresis modeling is eliminated. At the same time, extensive knowledge of control engineering is needed to design such kind of control strategies. Therefore, these different approaches possess specific advantages and disadvantages. It is suggested to select a suitable control approach based on the control objective and on the background of the reader.

As a typical application of the piezoelectric micro-/nano-positioning devices, micromanipulation tasks have been demonstrated using piezoelectric grippers. When targeting such an application, the implementation of joint position and force control is very important. In this book, the robust impedance control and position/force switching control are carried out to show the effectiveness of the micro-/nano-positioning systems dedicated to micromanipulation and microassembly scenarios.

References

1. Abidi, K., Xu, J.X., Yu, X.: On the discrete-time integral sliding mode control. IEEE Trans. Automat. Control **52**(4), 709–715 (2007)
2. Alkkiomaki, O., Kyrki, V., Kalviainen, H., Liu, Y., Handroos, H.: Smooth transition from motion to force control in robotic manipulation using vision. In: Proceeding of the 9th International Conference on Control, Automation, Robotics and Vision, pp. 1–6 (2006)
3. Almeida, F., Lopes, A., Abreu, P.: Force-impedance control: A new control strategy of robotic manipulators. In: Kaynak, O., Tosunoglu, S., Ang, M. (eds.) Recent Advances in Mechatronics, pp. 126–137 (1999)
4. Ang, W.T., Khosla, P.K., Riviere, C.N.: Feedforward controller with inverse rate-dependent model for piezoelectric actuators in trajectory-tracking applications. IEEE/ASME Trans. Mechatron. **12**(2), 134–142 (2007)
5. Bandyopadhyay, B., Fulwani, D.: High-performance tracking controller for discrete plant using nonlinear sliding surface. IEEE Trans. Ind. Electron. **56**(9), 3628–3637 (2009)
6. Bargiel, S., Rabenorosoa, K., Clévy, C., Gorecki, C., Lutz, P.: Towards micro-assembly of hybrid moems components on a reconfigurable silicon free-space micro-optical bench. J. Micromech. Microeng. **20**(4), 045012 (2010)

7. Bartoszewicz, A.: Discrete-time quasi-sliding-mode control strategies. IEEE Trans. Ind. Electron. **45**(5), 633–637 (1998)
8. Bonitz, R.G., Hsia, T.C.: Internal force-based impedance control for cooperating manipulators. IEEE Trans. Robot. Automat. **12**(1), 78–89 (1996)
9. Boukari, A.F., Carmona, J.C., Moraru, G., Malburet, F., Chaaba, A., Douimi, M.: Piezo-actuators modeling for smart applications. Mechatronics **21**(1), 339–349 (2011)
10. Chen, S.P., Liaw, H.C.: Generalized impedance control of robot for assembly tasks requiring compliant manipulaiton. IEEE Trans. Ind. Electron. **43**(4), 453–461 (1996)
11. Chen, X., Hisayama, T.: Adaptive sliding-mode position control for piezo-actuated stage. IEEE Trans. Ind. Electron. **55**(11), 3927–3934 (2008)
12. Cheng, C.C., Chang, C.C., Su, T.M.: Design of model reference adaptive tracking controllers for mismatch perturbed nonlinear systems with input nonlinearity. In: Proceeding of 17th IFAC World Congress, pp. 5974–5979. Seoul, Korea (2008)
13. Clayton, G.M., Tien, S., Fleming, A.J., Moheimani, S.O.R., Devasia, S.: Inverse-feedforward of charge-controlled piezopositioners. Mechatronics **18**(5–6), 273–281 (2008)
14. Demetriou, M.A., Fahroo, F.: Model reference adaptive control of structurally perturbed second-order distributed parameter systems. Int. J. Robust Nonlinear Control **16**(16), 773–799 (2006)
15. Dong, R., Tan, Y., Chen, H., Xie, Y.: A neural networks based model for rate-dependent hysteresis for piezoelectric actuators. Sens. Actuator A-Phys. **143**(2), 370–376 (2008)
16. Esbrook, A., Tan, X., Khalil, H.K.: Control of systems with hysteresis via servocompensation and its application to nanopositioning. IEEE Trans. Control Syst. Technol. **21**(3), 725–738 (2013)
17. Fleming, A.J., Leang, K.K.: Design. Springer, Modeling and Control of Nanopositioning Systems (2014)
18. Gao, B., Shao, J., Han, G., Sun, G., Yang, X., Wu, D.: Using fuzzy switching to achieve the smooth switching of force and position. Appl. Mech. Mater. **274**, 638–641 (2013)
19. Gao, W., Wang, Y., Homaifa, A.: Discrete-time variable structure control systems. IEEE Trans. Ind. Electron. **42**(2), 117–122 (1995)
20. Garcia-Gabin, W., Zambrano, D., Camacho, E.F.: Sliding mode predictive control of a solar air conditioning plant. Control Eng. Pract. **17**(6), 652–663 (2009)
21. Ge, P., Jouaneh, M.: Tracking control of a piezoceramic actuator. IEEE Trans. Control Syst. Technol. **4**(3), 209–216 (1996)
22. Hara, S., Yamada, Y.: A control method switching from servo automatic transfer to force sensorless impedance control manual positioning. In: Proceeding IECON 2007—33rd Annual Conference of the IEEE Industrial Electronics Society, pp. 292–298 (2007)
23. Huang, H.B., Sun, D., Mills, J.K., Cheng, S.H.: Robotic cell injection system with position and force control: Toward automatic batch biomanipulation. IEEE Trans. Robot. **25**(3), 727–737 (2009)
24. Huang, H.P., Yan, J.L., Cheng, T.H.: Development and fuzzy control of a pipe inspection robot. IEEE Trans. Ind. Electron. **57**(3), 1088–1095 (2010)
25. Hwang, C.L.: Microprocessor-based fuzzy decentralized control of 2-D piezo-driven systems. IEEE Trans. Ind. Electron. **55**(3), 1411–1420 (2008)
26. Janaideh, M.A., Rakheja, S., Su, C.Y.: Experimental characterization and modeling of rate-dependent hysteresis of a piezoceramic actuator. Mechatronics **19**(5), 656–670 (2009)
27. Jung, S., Hsia, T.C., Bonitz, R.G.: Force tracking impedance control for robot manipulators with an unknown environment: Theory, simulation, and experiment. Int. J. Robot. Res. **20**(9), 765–774 (2001)
28. Jung, S., Hsia, T.C., Bonitz, R.G.: Force tracking impedance control of robot manipulators under unknown environment. IEEE Trans. Control Syst. Technol. **12**(3), 474–483 (2004)
29. Kim, B., Washington, G.N.: Nonlinear position control of smart actuators using model predictive sliding mode control. In: Proceeding of ASME Conference on Smart Materials, Adaptive Structures and Intelligent Systems, pp. 511–522 (2008)

30. Kim, J., Kang, B.: Micro-macro linear piezoelectric motor based on self-moving cell. Mechatronics **19**(7), 1134–1142 (2009)
31. Kim, J.Y., Bentsman, J.: Disturbance rejection in robust model reference adaptive control of parabolic and hyperbolic systems. In: Proceeding of 45th IEEE Conference on Decision and Control, pp. 3083–3088. San Diego, CA, USA (2006)
32. Leang, K.K., Zou, Q., Devasia, S.: Feedforward control of piezoactuators in atomic force microscope systems: Inversion-based compensation for dynamics and hysteresis. IEEE Control Syst. Mag. **19**(1), 70–82 (2009)
33. Li, G., Wen, C., Zheng, W.X., Chen, Y.: Identification of a class of nonlinear autoregressive models with exogenous inputs based on kernel machines. IEEE Trans. Signal Process. **59**(5), 2146–2159 (2012)
34. Li, Y., Xu, Q.: Hysteresis modeling and compensation for an XY micropositioning stage with model reference adaptive control. In: Proceeding of 48th IEEE Conference on Decision and Control, pp. 5580–5585. Shanghai, China (2009)
35. Li, Y., Xu, Q.: Adaptive sliding mode control with perturbation estimation and PID sliding surface for motion tracking of a piezo-driven micromanipulator. IEEE Trans. Control Syst. Technol. **18**(4), 798–810 (2010)
36. Liaw, H.C., Shirinzadeh, B.: Enhanced adaptive motion tracking control of piezo-actuated flexure-based four-bar mechanisms for micro/nano manipulation. Sens. Actuator A-Phys. **147**, 254–262 (2008)
37. Liaw, H.C., Shirinzadeh, B.: Robust adaptive constrained motion tracking control of piezo-actuated flexure-based mechanisms for micro/nano manipulation. IEEE Trans. Ind. Electron. **58**(4), 1406–1415 (2011)
38. Lin, C.J., Chen, S.Y.: Evolutionary algorithm based feedforward control for contouring of a biaxial piezo-actuated stage. Mechatronics **19**(6), 829–839 (2009)
39. Liu, Y.T., Chang, K.M., Li, W.Z.: Model reference adaptive control for a piezo-positioning system. Precis. Eng. **34**(1), 62–69 (2010)
40. Lopez-Walle, B., Gauthier, M., Chaillet, N.: Principle of a submerged freeze gripper for microassembly. IEEE Trans. Robot. **24**(4), 897–902 (2008)
41. Lu, W.S., Meng, Q.H.: Impedance control with adaptation for robotic manipulations. IEEE Trans. Robot. Automat. **7**(3), 408–415 (1991)
42. Lu, Z., Chen, P.C.Y., Lin, W.: Force sensing and control in micromanipulation. IEEE Trans. Syst. Man Cybern. Part C, Appl. Rev. 36(6), 713–724 (2006)
43. Lu, Z., Kawamura, S., Goldenberg, A.A.: An approach to sliding-mode based control. IEEE Trans. Robot. Automat. **11**(5), 754–759 (1995)
44. Mitic, D., Milojkovic, M., Antic, D.: Tracking system design based on digital minimum variance control with fuzzy sliding mode. In: Proceeding of 8th International Conference on Telecommunications in Modern Satellite, Cable and Broadcasting Services (TELSIKS 2007), pp. 494–497. Nis, Serbia (2007)
45. Mitic, D., Milosavljevic, C.: Sliding mode-based minimum variance and generalized minimum variance controls with $O(T^2)$ and $O(T^3)$ accuracy. Electr. Eng. **86**(4), 229–237 (2004)
46. Navarro, C., Treesatayapun, C., Baltazar, A.: Determination of the instantaneous initial contact point on a parallel gripper using a multi input fuzzy rules emulated network controller with feedback from ultrasonic and force sensors. In: Batyrshin, I., Gonzalez Mendoza, M. (eds.) Advances in Artificial Intelligence, Lecture Notes in Computer Science, vol. 7629, pp. 261–272. Springer, Berlin (2013)
47. Neelakantan, V.A., Washington, G.N., Bucknor, N.K.: Model predictive control of a two stage actuation system using piezoelectric actuators for controllable industrial and automotive brakes and clutches. J. Intell. Mater. Syst. Struct. **19**(7), 845–857 (2008)
48. Niksefat, N., Wu, Q., Sepehri, N.: Stable control of an electro-hydraulic actuator during contact tasks: Theory and experiments. In: Proceeding of the American Control Conference, pp. 4114–4118 (2000)
49. Orlowska-Kowalska, T., Dybkowski, M., Szabat, K.: Adaptive sliding-mode neuro-fuzzy control of the two-mass induction motor drive without mechanical sensors. IEEE Trans. Ind. Electron. **57**(2), 553–564 (2010)

50. Reddy, A.N., Maheshwari, N., Sahu, D.K., Ananthasuresh, G.K.: Miniature compliant grippers with vision-based force sensing. IEEE Trans. Robot. **26**(5), 867–877 (2010)
51. Sariola, V., Jaaskelainen, M., Zhou, Q.: Hybrid microassembly combining robotics and water droplet self-alignment. IEEE Trans. Robot. **26**(6), 965–977 (2010)
52. Schutter, J.D., Bruyninckx, H., Zhu, W.H., Spong, M.W.: Force control: A bird's eye view. In: Siciliano, B. (ed.) Control Problems in Robotics and Automation: Future Directions, pp. 1–17 (1998)
53. Seki, H.: Modeling and impedance control of a piezoelectric bimorph microgripper. In: Proceeding of IEEE/RSJ International Conference on Intelligent Robots and Systems, vol. 2, pp. 958–965. Raleigh, USA (1992)
54. Seraji, H., Colbaugh, R.: Force tracking in impedance control. Int. J. Robot. Res. **16**(1), 97–117 (1997)
55. Sha, D., Bajic, V.B.: Robust discrete adaptive input-output-based sliding mode controller. Int. J. Syst. Sci. **31**(12), 1601–1614 (2000)
56. Sha, D., Bajic, V.B., Yang, H.: New model and sliding mode control of hydraulic elevator velocity tracking system. Simul. Pract. Theory **9**(6), 365–385 (2002)
57. Shimada, N., Yoshioka, T., Ohishi, K., Miyazaki, T.: Novel force-sensor-less contact motion control for quick and smooth industrial robot motion. In: Proceeding IECON 2011—37th Annual Conference on IEEE Industrial Electronics Society, pp. 4238–4243 (2011)
58. Song, G., Zhao, J., Zhou, X., De Abreu-Garcia, J.: Tracking control of a piezoceramic actuator with hysteresis compensation using inverse preisach model. IEEE/ASME Trans. Mechatron. **10**(2), 198–209 (2005)
59. Suykens, J.A.K., Gestel, T.V., Brabanter, J.D., Moor, B.D., Vandewalle, J.: Least Squares Support Vector Machines. World Scientific Publishing Co., Singapore (2002)
60. Suykens, J.A.K., Vandewalle, J.: Least squares support vector machine classifiers. Neural Process. Lett. **9**(3), 293–300 (1999)
61. Takahashi, T., Tsuboi, T., Kishida, T., Kawanami, Y., Shimizu, S., Iribe, M., Fukushima, T., Fujita, M.: Adaptive grasping by multi fingered hand with tactile sensor based on robust force and position control. In: Proceeding of the International Conference on Robotics and Automation, pp. 264–271 (2008)
62. Wang, C.H., Huang, D.Y.: A new intelligent fuzzy controller for nonlinear hysteretic electronic throttle in modern intelligent automobiles. IEEE Trans. Ind. Electron. **60**(6), 2332–2345 (2013)
63. Wang, R., Liu, G.P., Wang, W., Rees, D., Zhao, Y.B.: H_∞ control for networked predictive control systems based on the switched Lyapunov function method. IEEE Trans. Ind. Electron. **57**(10), 3565–3571 (2010)
64. Wills, A.G., Bates, D., Fleming, A.J., Ninness, B., Moheimani, S.O.R.: Model predictive control applied to constraint handling in active noise and vibration control. IEEE Trans. Control Syst. Technol. **16**(1), 3–12 (2008)
65. Wu, Y., Zou, Q.: Robust-inversion-based 2-DOF control design for output tracking: Piezoelectric actuator example. IEEE Trans. Control Syst. Technol. **17**(5), 1069–1082 (2009)
66. Xi, Z., Hesketh, T.: Discrete time integral sliding mode control for overhead crane with uncertainties. IET Control Theory Appl. **4**(10), 2071–2081 (2010)
67. Xiao, L., Su, H., Chu, J.: Sliding mode prediction tracking control design for uncertain systems. Asian J. Control **9**(3), 317–325 (2007)
68. Xu, J.X., Abidi, K.: Discrete-time output integral sliding-mode control for a piezomotor-driven linear motion stage. IEEE Trans. Ind. Electron. **55**(11), 3917–3926 (2008)
69. Xu, Q.: Adaptive discrete-time sliding mode impedance control of a piezoelectric microgripper. IEEE Trans. Robot. **29**(3), 663–673 (2013)
70. Xu, Q., Jia, M.: Model reference adaptive control with perturbation estimation for a micropositioning system. IEEE Trans. Control Syst. Technol. **22**(1), 352–359 (2014)
71. Xu, Q., Li, Y.: Dahl model-based hysteresis compensation and precise positioning control of an XY parallel micromanipulator with piezoelectric actuation. J. Dyn. Syst. Meas. Control-Trans. ASME **132**(4), 041011 (2010)

72. Xu, Q., Li, Y.: Micro-/nanopositioning using model predictive output integral discrete sliding mode control. IEEE Trans. Ind. Electron. **59**(2), 1161–1170 (2012)
73. Xu, Q., Li, Y.: Model predictive discrete-time sliding mode control of a nanopositioning piezostage without modeling hysteresis. IEEE Trans. Control Syst. Technol. **20**(4), 983–994 (2012)
74. Xu, Q., Wong, P.K.: Hysteresis modeling and compensation of a piezostage using least squares support vector machines. Mechatronics **21**(7), 1239–1251 (2011)
75. Yi, J., Chang, S., Shen, Y.: Disturbance observer-based hysteresis compensation for piezoelectric actuators. IEEE/ASME Trans. Mechatron. **14**(4), 456–464 (2009)
76. Yu, S., Alici, G., Shirinzadeh, B., Smith, J.: Sliding mode control of a piezoelectric actuator with neural network compensating rate-dependent hysteresis. In: Proceeding of IEEE International Conference on Robotics and Automation, pp. 3641–3645 (2005)
77. Yu, X., Kaynak, O.: Sliding mode control with soft computing: A survey. IEEE Trans. Ind. Electron. **56**(9), 3275–3285 (2009)
78. Yu, Y., Xiao, Z., Naganathan, N.G., Dukkipati, R.V.: Dynamic Preisach modelling of hysteresis for the piezoceramic actuator system. Mech. Mach. Theory **37**(1), 75–89 (2002)

Part I
Hysteresis-Model-Based Feedforward Control

Chapter 2
Feedforward Control Based on Inverse Hysteresis Models

This chapter presents the rate-dependent hysteresis compensation of a piezoelectric nanopositioning stage using the feedforward control based on an inverse hysteresis model. Three different controllers are realized and compared, which employ Bouc–Wen model, modified Prandtl–Ishlinskii (MPI) model, and least squares support vector machines (LSSVM)-based intelligent model, respectively. Experimental studies demonstrate the superiority of LSSVM model in hysteresis modeling and compensation tasks.

2.1 Introduction

In order to compensate for the hysteresis effect, the hysteresis behavior is usually modeled by Preisach model [3, 6], Prandtl–Ishlinskii model [7], Bouc–Wen model [11, 12], Maxwell-based model [8], Dahl model [18], polynomial model [9], etc. Then, an inverse hysteresis model is constructed and utilized as a feedforward controller to cancel the hysteresis effect. However, the hysteresis effect is dependent not only on the amplitude but also on the frequency of input signals. It is very difficult to capture the complicated rate-dependent hysteretic behavior precisely. In addition, majority of the existing models employ a large number of parameters to describe the rate-dependent hysteresis [1, 21], which may block their applications in high-speed real-time control as an adverse effect.

Recently, it has been shown that ANN provides an efficient way to model the nonlinear hysteresis [5, 20]. Nevertheless, there is no universal method to determine an optimal ANN structure in terms of the number of hidden layers and number of neurons in each layer. Moreover, ANN exhibits the problems of overfitting and sinking into local optima, which are their major drawbacks in practical implementation. Alternatively, SVM gives a promising way to estimate nonlinear system models accurately. Based on the statistical learning theory and structural risk minimization principle, the SVM approach is capable of modeling nonlinear systems by trans-

© Springer International Publishing Switzerland 2016

Q. Xu and K.K. Tan, *Advanced Control of Piezoelectric Micro-/Nano-Positioning Systems*, Advances in Industrial Control,
DOI 10.1007/978-3-319-21623-2_2

forming the regression problem into a convex quadratic programming (QP) problem and then solving it with a QP solver. As compared with the conventional ANN, SVM exhibits the major advantages of global optimization and higher generalization capability. As a variant of SVM, LSSVM is introduced in 1999 [13]. LSSVM utilizes equality constraints instead of inequality constraints as in the ordinary SVM. Hence, it simplifies the regression to a problem that can be easily solved from a set of linear equations [17]. As a result, the LSSVM has a relatively low complexity and are more computationally efficient than the standard SVM [13]. Another advantage of LSSVM lies in that it has fewer parameters to tune [19]. For more details about LSSVM algorithm, the reader may refer to the book [14].

In this chapter, the LSSVM is introduced to the domain of hysteresis modeling and compensation for a nanopositioning stage, which is driven by piezoelectric stack actuators. A LSSVM model is proposed and trained by introducing the current input value and input variation rate as the input data set to formulate a one-to-one mapping. By adopting the radial basis function (RBF) as kernel function, the LSSVM model only has two free hyperparameters, which are optimally tuned by resorting to Bayesian inference framework. The effectiveness of the presented model is verified by carrying out experimental studies. For a comparison study, two state-of-the-art approaches, namely, Bouc–Wen model and MPI model, are employed. Both Bouc–Wen and MPI models are identified by resorting to a global search approach of particle swarm optimization (PSO).

In addition, a LSSVM inverse model-based feedforward control in combination with a proportional-integral-derivative (PID) feedback control is designed to compensate for the hysteresis nonlinearity. The feasibility of the presented modeling and control approaches are validated by a series of simulation and experimental studies.

2.2 System Description and Hysteresis Characterization

The test bed as employed in this work and its hysteresis properties are described in this section.

2.2.1 Experimental Setup

The experimental setup is shown in Fig. 2.1. A commercial two-axis nanopositioning stage (model: P-734.2CL, from Physik Instrumente Co., Ltd.) is adopted. It is driven by two piezoelectric stack actuators (PSAs) through a high-voltage amplifier (model: E-503.00, from Physik Instrumente Co., Ltd.). The integrated capacitive sensors are used for displacement measurement. The displacement sensors provide the accuracy and repeatability in nanometer and sub-nanometer levels, respectively. The output signals of the two capacitive sensors are processed by a signal conditioner module (model: E-509.C2A, from Physik Instrumente Co., Ltd.). In addition,

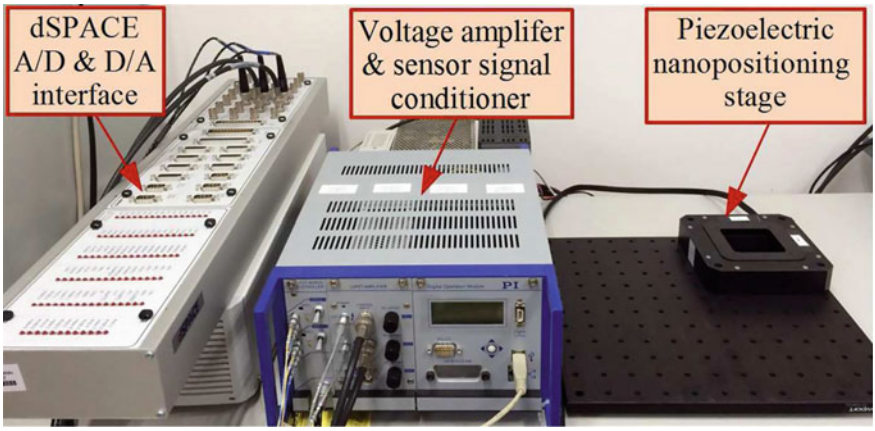

Fig. 2.1 Experimental setup of a piezoelectric nanopositioning system

the control hardware consists of a digital signal processor (DSP)-based real-time controller (model: DS1103, from dSPACE GmbH) with equipped 16-bit A/D and D/A converters. Control algorithms are developed with MATLAB® software and then downloaded to DS1103 board via the ControlDesk interface to implement the real-time control.

2.2.2 Hysteresis Characterization

By applying a triangular-wave voltage with the constant feed-rate and variable amplitudes to PSA #1, the open-loop position responses of the XY nanopositioning stage in the two working axes are shown in Fig. 2.2. It is seen that the cross-talk between the two axes is about 1.17 %, which indicates that the output motions in the two axes are approximately decoupled. Owing to the decoupling property of the two working axes, the motion control in one axis (x-axis) of the system is carried out in the following discussion.

The x-axis hysteresis curves in Fig. 2.2c reveal that the shape of the hysteresis loop is dependent on the amplitude of the input. The larger the amplitude of the input signal, the wider the output hysteresis loop. In addition, by applying sine waves with the same amplitude and varying frequencies (1–10 Hz) as shown in Fig. 2.3a, the x-axis displacement output is depicted in Fig. 2.3b. It can be observed from Fig. 2.3c that the hysteresis shape also relies on the input rate. The higher the frequency of the input signal, the larger the width of the output hysteresis.

The foregoing open-loop testing results indicate that the complicated hysteresis effects are dependent not only on the amplitude but also on the frequency of the input signal. The modeling and compensation of the hysteretic nonlinearity are carried out in the following sections.

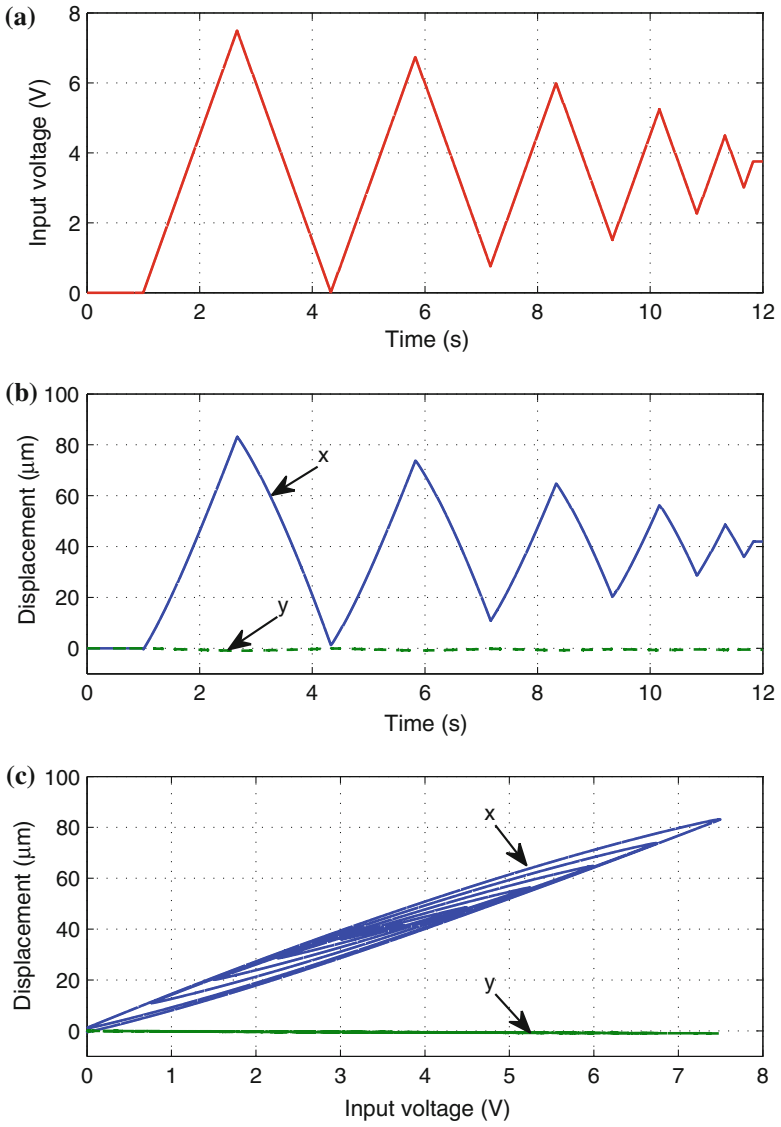

Fig. 2.2 Hysteresis curves of the XY nanopositioning stage with triangular-wave inputs. **a** Input voltage to the voltage amplifier. **b** Time history of the displacements x and y. **c** Output displacements x and y versus input voltage

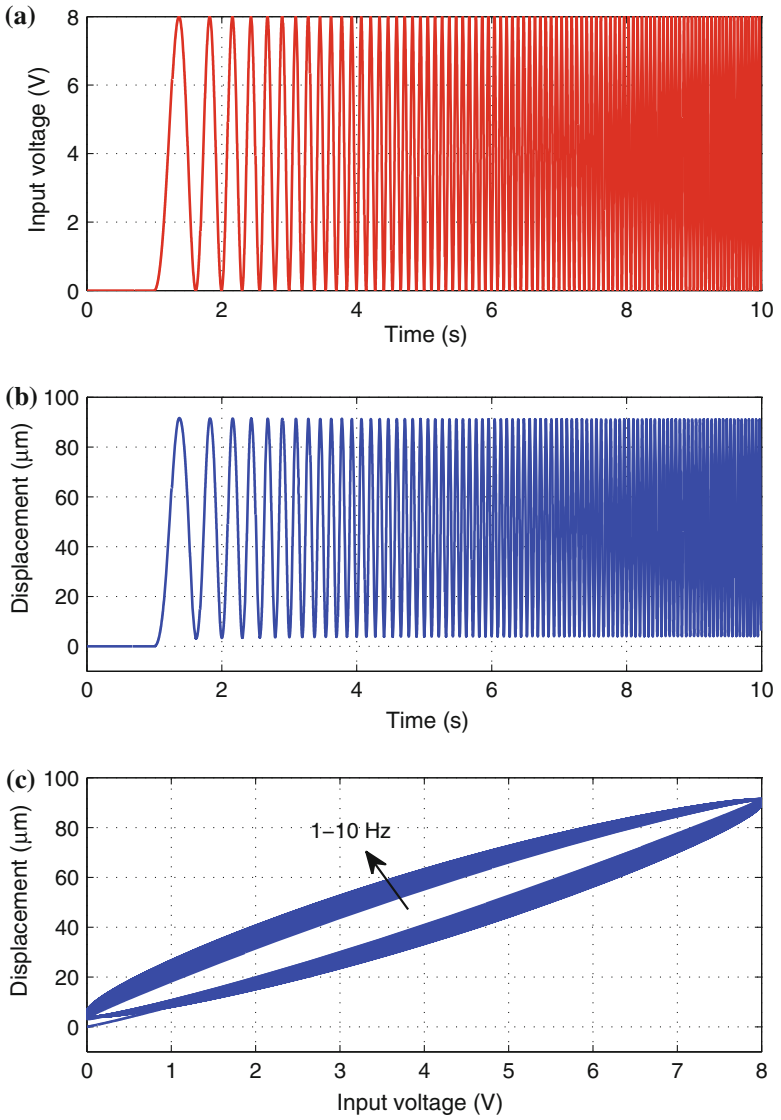

Fig. 2.3 Hysteresis curves of the XY nanopositioning stage with sinusoidal-wave inputs. **a** Input voltage to the voltage amplifier. **b** Time history of the displacement x. **c** Output displacement x versus input voltage

2.3 Hysteresis Modeling

The purpose of hysteresis modeling is to capture the hysteresis behavior of the system. First, the hysteresis is modeled using the popular Bouc–Wen, MPI, and LSSVM models. In addition, the corresponding inverse hysteresis models are also derived for the purpose of hysteresis compensation.

2.3.1 Hysteresis Modeling with the Bouc–Wen Model

Thanks to a fewer number of parameters, Bouc–Wen model has been widely employed in piezoelectric hysteresis modeling. In particular, the entire dynamics model of the piezoelectrically driven system with Bouc–Wen type of hysteresis can be established as follows [11, 12]:

$$m\ddot{y}(t) + b\dot{y}(t) + ky(t) = k[du(t) - h(t)] \tag{2.1}$$

$$\dot{h}(t) = \alpha d\dot{u}(t) - \beta|\dot{u}(t)|h(t)|h(t)|^{n-1} - \gamma\dot{u}(t)|h(t)|^{n} \tag{2.2}$$

where t is the time variable; parameters m, b, k, and y represent the mass, damping coefficient, stiffness, and displacement response of the piezostage, respectively; d is the piezoelectric coefficient; u denotes the input voltage; and h indicates the hysteretic loop in terms of displacement whose magnitude and shape are determined by parameters α, β, γ, and the order n, with n governing the smoothness of the transition from elastic to plastic response. For the elastic structure and material, $n = 1$ is assigned in Eq. (2.2).

To determine the model parameters, the seven parameters ($m, b, k, d, \alpha, \beta$, and γ) of the Bouc–Wen model are identified by minimizing the following fitness function [11]:

$$F(m, b, k, d, \alpha, \beta, \gamma) = \frac{1}{N}\sum_{i=1}^{N}\left(x_i - x_i^{BW}\right)^2 \tag{2.3}$$

where N denotes the total number of samples, and $x_i - x_i^{BW}$ represents the error of the i-th sample which is calculated as the deviation of Bouc–Wen model output (x_i^{BW}) from experimental result (x_i).

The hysteresis model describes the relationship between the input voltage and output displacement of the system. The dynamics model with Bouc–Wen hysteresis model can be realized using MATLAB®/Simulink® blocks as shown in Fig. 2.4. On the other hand, the input voltage used to produce a desired displacement value is solved by the inverse hysteresis model [11]. Specifically, the inverse dynamic model can be derived from Eqs. (2.1) and (2.2). It is realized using MATLAB/Simulink blocks as shown in Fig. 2.5, where the "Bouc–Wen model" subsystem is depicted in Fig. 2.4b.

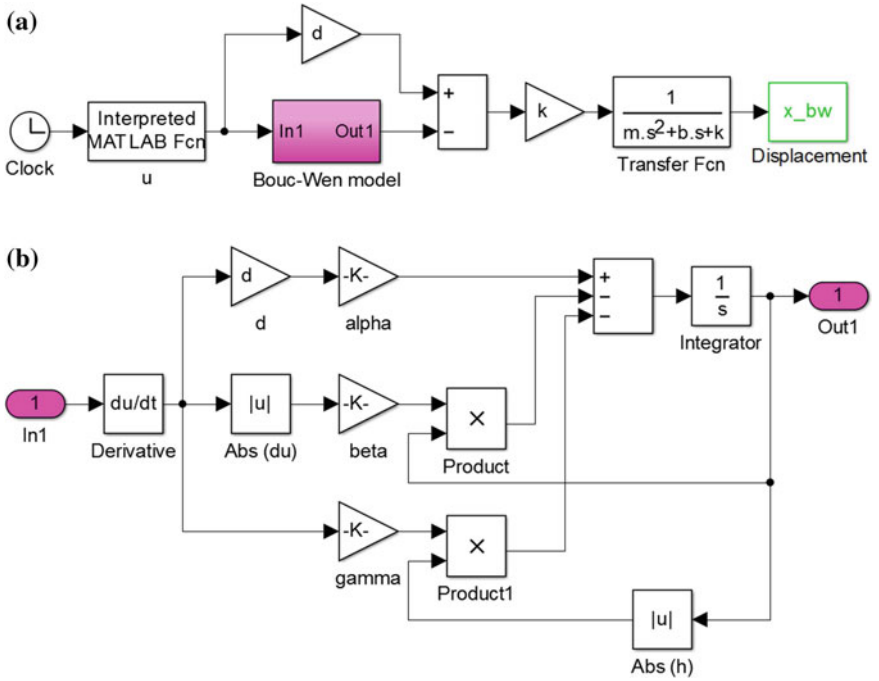

Fig. 2.4 Dynamic model implemented with MATLAB/Simulink blocks. **a** Dynamic model of the entire system. **b** Bouc–Wen hysteresis model

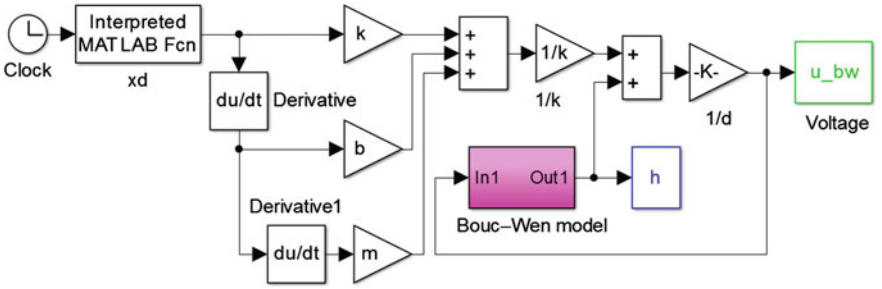

Fig. 2.5 The inverse dynamic model implemented with MATLAB/Simulink blocks

2.3.2 Hysteresis Modeling with the MPI Model

The hysteresis effect is described using MPI model, which has more parameters than the Bouc–Wen model. Then, an inverse hysteresis model is derived to compensate for the hysteresis effect.

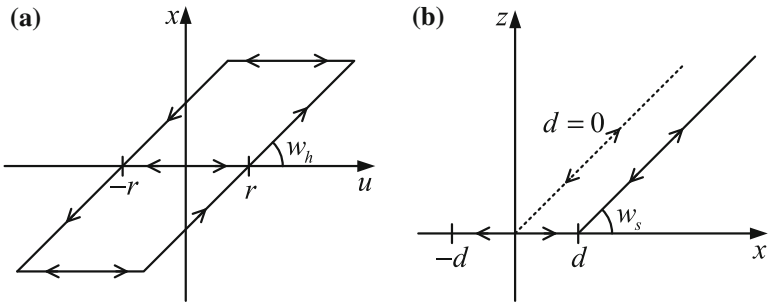

Fig. 2.6 Illustrations of elementary PI operators. **a** Backlash operator H_r. **b** Dead-zone operator S_d

2.3.2.1 PI Model

First, the Prandtl–Ishlinskii (PI) model is described briefly. As a subclass of the Preisach hysteresis model, the PI model is a superposition of elementary backlash or play operators. The backlash operator H_r is illustrated in Fig. 2.6a, which is defined by

$$\begin{aligned} y(t) &= H_r[u, x_0](t) \\ &= \max\{u(t) - r, \min\{u(t) + r, y(t - T)\}\} \end{aligned} \tag{2.4}$$

where u is the voltage control input, y is the displacement response of the stage, r is the control input threshold value or magnitude of the backlash, and T is the sampling time interval.

The initial condition of Eq. (2.4) is given by

$$y(0) = \max\{u(0) - r, \min\{u(0) + r, y_0\}\} \tag{2.5}$$

where y_0 is usually but not necessarily initialized to zero.

A generalized backlash operator can be obtained by multiplying H_r with a weight value w_h, i.e.,

$$y(t) = w_h H_r[u, y_0](t) \tag{2.6}$$

where the weight w_h describes the gain of the backlash operator.

Using a linearly weighted superposition of multiple backlash operators with different thresholds and weights, the complex hysteresis can be modeled by

$$y(t) = \mathbf{w}_h^T \mathbf{H}_r[u, \mathbf{y}_0](t) \tag{2.7}$$

where $\mathbf{w}_h^T = [w_{h0}, w_{h1}, \ldots, w_{hn}]$ is the weight vector, $\mathbf{H}_r[u, \mathbf{y}_0](t) = [H_r[u, y_{00}](t), H_r[u, y_{01}](t), \ldots, H_r[u, y_{0n}](t)]^T$ with the threshold vector $\mathbf{r} = [r_0, r_1, \ldots,$

$r_n]^T$ and the initial state vector $\mathbf{x}_0 = [x_{00}, x_{01}, \ldots, x_{0n}]^T$, for $0 = r_0 < r_1 < \cdots < r_n < +\infty$. The control input thresholds r_i can be chosen as equal intervals between the minimum and maximum voltage control input values of the piezoelectric actuation stage.

2.3.2.2 MPI Model

The PI operator has the same symmetric property as the backlash operator with respect to the center point of the loop formed by the operator. Hence, the model accuracy of PI operator will be reduced for the situations where the hysteresis loops are not symmetric. In order to overcome this issue, a saturation operator is adopted to connect in serial with the hysteresis operator.

Specifically, the saturation operator is a weighted linear superposition of linear-stop or one-sided dead-zone operators given as follows:

$$S_d[y](t) = \begin{cases} \max\{y(t) - d, 0\}, & d > 0 \\ y(t), & d = 0 \end{cases} \tag{2.8}$$

where the dead-zone operator S_d is depicted in Fig. 2.6b.

Based on the aforementioned dead-zone operator, the saturation operator is expressed by

$$z(t) = \mathbf{w}_s^T \mathbf{S}_d[y](t) \tag{2.9}$$

where y is the output of the hysteresis operator, z is the stage response, $\mathbf{w}_s^T = [w_{s0}, w_{s1}, \ldots, w_{sm}]$ is the weight vector, $\mathbf{S}_d[y](t) = [S_{d0}[y](t), S_{d1}[y](t), \ldots, S_{dm}[y](t)]^T$ with the threshold vector $\mathbf{d} = [d_0, d_1, \ldots, d_m]^T$, for $0 = d_0 < d_1 < \cdots < d_m < +\infty$.

Therefore, the modified PI operator is derived as follows:

$$z(t) = \Gamma[u](t) = \mathbf{w}_s^T \mathbf{S}_d\left[\mathbf{w}_h^T \mathbf{H}_r[u, \mathbf{y}_0]\right](t). \tag{2.10}$$

A realization of the MPI model using MATLAB/Simulink blocks is shown in Fig. 2.7.

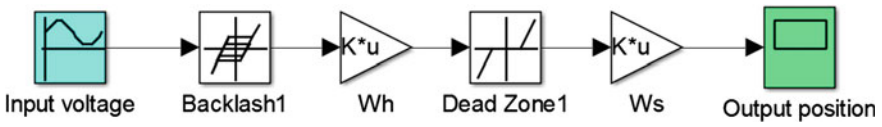

Fig. 2.7 MPI model implemented with MATLAB/Simulink blocks

2.3.2.3 Inverse MPI Model

In order to use the MPI model for the feedforward hysteresis compensation, an inverse model is required to express the voltage as a function of the position.

It has been shown that the inverse MPI model is also PI-type, which can be calculated by

$$u(t) = \Gamma^{-1}[z](t) = \mathbf{w}_h^{*T}\mathbf{H}_r^*\left[\mathbf{w}_s^{*T}\mathbf{S}_d^*[z], \mathbf{y}_0^*\right](t) \tag{2.11}$$

where $\mathbf{w}_h^{*T} = [w_{h0}^*, w_{h1}^*, \ldots, w_{hn}^*]$ and $\mathbf{w}_s^{*T} = [w_{s0}^*, w_{s1}^*, \ldots, w_{sm}^*]$ are the weight vectors, $\mathbf{y}_0^* = [y_{00}^*, y_{01}^*, \ldots, y_{0n}^*]^T$ is the initial state vector, and the threshold vectors are $\mathbf{r}^* = [r_0^*, r_1^*, \ldots, r_n^*]^T$ and $\mathbf{d}^* = [d_0^*, d_1^*, \ldots, d_m^*]^T$, respectively.

The inverse MPI model parameters are given as follows [1, 10]:

$$w_{h0}^* = \frac{1}{w_{h0}} \tag{2.12}$$

$$w_{hi}^* = \frac{-w_{hi}}{\left(\sum_{j=0}^{i} w_{hj}\right)\left(\sum_{j=0}^{i-1} w_{hj}\right)}, \quad i = 1, \ldots, n \tag{2.13}$$

$$r_i^* = \sum_{j=0}^{i} w_{hj}(r_i - r_j), \quad i = 0, 1, \ldots, n \tag{2.14}$$

$$y_{0i}^* = \sum_{j=0}^{i} w_{hj} y_{0i} + \sum_{j=i+1}^{n} w_{hj} y_{0j}, \quad i = 0, 1, \ldots, n \tag{2.15}$$

$$w_{s0}^* = \frac{1}{w_{s0}} \tag{2.16}$$

$$w_{sj}^* = \frac{-w_{sj}}{\left(\sum_{k=0}^{j} w_{sk}\right)\left(\sum_{k=0}^{j-1} w_{sk}\right)}, \quad j = 1, \ldots, m \tag{2.17}$$

$$d_j^* = \sum_{k=0}^{j} w_{sk}(d_j - d_k), \quad j = 0, 1, \ldots, m. \tag{2.18}$$

2.3.3 Hysteresis Modeling with the LSSVM

In this section, the hysteresis modeling is treated as a nonlinear regression problem, and the LSSVM is employed to model the piezoelectric hysteresis for the piezoelectric nanopositioning system. Due to the hysteresis effects, one input voltage can produce multiple values of the output displacements. Thus, one challenge lies in how to convert the one-to-many mapping into a one-to-one mapping. Here, both the current input and input variation rates are introduced to form the input data set, which

determines a unique output value. By making use of the input variation rate, the rate dependency of the hysteretic behavior can be captured.

Specifically, the hysteresis model is identified using the input voltage (u) and voltage variation rate ($\dot{u}$) as the inputs and the displacement (y) as the output to train the LSSVM.

2.3.3.1 LSSVM Modeling

LSSVM maps the input data into a high-dimensional feature space and constructs a linear regression function therein. The unknown hysteresis function is approximated by the equation

$$y(\mathbf{x}) = \mathbf{w}^T \varphi(\mathbf{x}) + b \tag{2.19}$$

with the given training data set $\{\mathbf{x}_i, y_i\}_{i=1}^N$, where N represents the number of training data set, $\mathbf{x}_i = \{u_i, \dot{u}_i\} \in \mathbb{R}^2$ are the input data, and $y_i \in \mathbb{R}$ are the output data. Additionally, the weight vector $\mathbf{w} \in \mathbb{R}^{n_h}$, the nonlinear mapping $\varphi(\cdot) : \mathbb{R}^2 \to \mathbb{R}^{n_h}$ denotes a map from the input space to a feature space, and b is the bias.

The LSSVM approach formulates the regression as an optimization problem in the primal weight space:

$$\min_{\mathbf{w},b,\mathbf{e}} J(\mathbf{w}, \mathbf{e}) = \frac{1}{2}\mathbf{w}^T\mathbf{w} + \frac{1}{2}\gamma \sum_{i=1}^{N} e_i^2 \tag{2.20}$$

subject to the equality constraints

$$y_i = \mathbf{w}^T \varphi(\mathbf{x}_i) + b + e_i, \quad i = 1, 2, \ldots, N \tag{2.21}$$

where e_i is the residual error.

The weight vector $\mathbf{w}$ may be in high dimension, and it cannot be solved directly. In order to solve the optimization problem, a Lagrangian function is defined as follows:

$$L(\mathbf{w}, b, \mathbf{e}; \boldsymbol{\alpha}) = J(\mathbf{w}, \mathbf{e}) - \sum_{i=1}^{N} \alpha_i [\mathbf{w}^T \varphi(\mathbf{x}_i) + b + e_i - y_i] \tag{2.22}$$

where α_i are the Lagrange multipliers which can be either positive or negative values. The conditions for optimality can be obtained by solving the following partial derivatives:

$$\frac{\partial L}{\partial \mathbf{w}} = 0 \to \mathbf{w} = \sum_{i=1}^{N} \alpha_i \varphi(\mathbf{x}_i) \tag{2.23}$$

$$\frac{\partial L}{\partial b} = 0 \rightarrow \sum_{i=1}^{N} \alpha_i = 0 \tag{2.24}$$

$$\frac{\partial L}{\partial e_i} = 0 \rightarrow \alpha_i = \gamma e_i, \quad i = 1, 2, \ldots, N \tag{2.25}$$

$$\frac{\partial L}{\partial \alpha_i} = 0 \rightarrow \mathbf{w}^T \varphi(\mathbf{x}_i) + b + e_i - y_i = 0, \quad i = 1, 2, \ldots, N \tag{2.26}$$

which can be used to construct the dual formulation by eliminating $\mathbf{w}$ and e_i, i.e.,

$$\underbrace{\begin{bmatrix} 0 & \mathbf{1}_N^T \\ \mathbf{1}_N & \Omega + \gamma^{-1}\mathbf{I}_N \end{bmatrix}}_{\boldsymbol{\Phi}} \begin{bmatrix} b \\ \boldsymbol{\alpha} \end{bmatrix} = \begin{bmatrix} 0 \\ \mathbf{y} \end{bmatrix} \tag{2.27}$$

where $\boldsymbol{\alpha} = [\alpha_1, \alpha_2, \ldots, \alpha_N]^T$ is called the support vector, whose support values α_i are proportional to the residual errors e_i by the regularization factor $\gamma \in \mathbb{R}$. In addition, $\mathbf{1}_N = [1, 1, \ldots, 1]^T$, $\mathbf{y} = [y_1, y_2, \ldots, y_N]^T$, and $\mathbf{I}_N$ is an identity matrix.

Besides, the kernel trick is employed to derive that:

$$\Omega_{ij} = \varphi(\mathbf{x}_i)^T \varphi(\mathbf{x}_j) = K(\mathbf{x}_i, \mathbf{x}_j), \quad i, j = 1, 2, \ldots, N \tag{2.28}$$

where K is a predefined kernel function. The purpose of introducing the kernel function is to avoid the explicit computation of the map $\varphi(\cdot)$ in dealing with the high-dimensional feature space.

It is observed that the LSSVM approach utilizes the equality constraints instead of the inequality constraints as in the ordinary SVM. Thus, it simplifies the regression to a problem that can be easily solved from a set of linear equations. Assume that $\boldsymbol{\Phi}$ is invertible, then b and $\boldsymbol{\alpha}$ can be calculated from Eq. (2.27):

$$\begin{bmatrix} b \\ \boldsymbol{\alpha} \end{bmatrix} = \boldsymbol{\Phi}^{-1} \begin{bmatrix} 0 \\ \mathbf{y} \end{bmatrix}. \tag{2.29}$$

Then, in view of Eq. (2.23), the solution for the regression problem can be derived:

$$y(\mathbf{x}) = \sum_{i=1}^{N} \alpha_i K(\mathbf{x}, \mathbf{x}_i) + b \tag{2.30}$$

where K is the kernel function satisfying Mercer's condition, $\mathbf{x}_i$ is the training data, and $\mathbf{x}$ denotes the new input data.

By adopting the RBF kernel function

$$K(\mathbf{x}, \mathbf{x}_i) = \exp\left(-\frac{\|\mathbf{x} - \mathbf{x}_i\|^2}{\sigma^2}\right) \tag{2.31}$$

with $\sigma > 0$ denoting the width parameter (which specifies the kernel sample variance σ^2) and $\|\cdot\|$ representing the Euclidean distance, the LSSVM model for the hysteresis model estimation becomes

$$y(\mathbf{x}) = \sum_{i=1}^{N} \alpha_i \exp\left(-\frac{\|\mathbf{x} - \mathbf{x}_i\|^2}{\sigma^2}\right) + b. \tag{2.32}$$

Once the regularization parameter γ and kernel parameter σ are assigned, a training process is needed to determine the support values α_i and the bias b.

2.3.3.2 Hyperparameters Tuning with Bayesian Inference

The above modeling procedure shows that there are two hyperparameters (γ and σ) to be adjusted. The high generalization ability of the LSSVM model relies on the appropriate tuning of the two parameters. To select the best hyperparameters, the approach of tenfold cross validation is usually adopted. However, it is a very time-consuming method. Alternatively, it has been shown that the Bayesian framework with three levels of inference is an effective way to infer the optimal hyperparameters of the LSSVM regressors [15].

Given a set of training data, Bayesian inference is a robust framework to determine the distribution of the estimated model parameters based on the data sets. Afterward, the optimal model parameters can be predicted. The basic idea of the hyperparameters inference procedure using Bayesian framework arises from a modified version of the LSSVM regression problem as shown below:

$$\min_{\mathbf{w},b,\mathbf{e}} J(\mathbf{w}, \mathbf{e}) = \mu E_W + \zeta E_D \tag{2.33}$$

subject to:

$$e_i = y_i - [\mathbf{w}^T \varphi(\mathbf{x}_i) + b], \quad i = 1, 2, \ldots, N \tag{2.34}$$

with

$$E_W = \frac{1}{2}\mathbf{w}^T\mathbf{w} \tag{2.35}$$

$$E_D = \frac{1}{2}\sum_{i=1}^{N} e_i^2 = \frac{1}{2}\sum_{i=1}^{N}\left\{y_i - [\mathbf{w}^T \varphi(\mathbf{x}_i) + b]\right\}^2 \tag{2.36}$$

where μ is the new regularization factor and ζ denotes the variance of the noise for the residual error e_i.

The dual program of the above optimization problem is the same as Eq. (2.27). The hyperparameter γ is related to μ and ζ by $\gamma = \zeta/\mu$. It is noticeable that, by substituting Eq. (2.35) and the above relationship into Eq. (2.33), the same problem as described by Eq. (2.20) is generated. Given a training data set, the Bayesian inference algorithm for the calculation of the two optimal hyperparameters is presented in [16]. Here, the procedure is implemented by resorting to a MATLAB toolbox [4].

2.4 Experimental Studies

In this section, the hysteresis modeling for a piezo-driven nanopositioning stage using the Bouc–Wen, MPI, and LSSVM models is carried out by experimental studies.

Without loss of generality, the input voltage signal is chosen below in order to identify the hysteresis model:

$$u(t) = 5e^{-0.11t}[\sin(6\pi t e^{-0.345t} - 1.55) + 1.0] \tag{2.37}$$

which is depicted in Fig. 2.8a. In addition, the experimental output data are obtained as depicted in Fig. 2.8b.

2.4.1 Bouc–Wen Model Results

By setting a time interval of 0.02 s, 500 training data sets are obtained as shown in Fig. 2.9a. Then, the Bouc–Wen model is identified off-line by optimizing the seven parameters to minimize the fitness function in Eq. (2.3).

In view of the superior performance of PSO over alternative methods such as the direct search approach and genetic algorithm (GA), the PSO is adopted for the parameter optimization. The optimization is carried out with a PSO toolbox [2] running in MATLAB environment. The identified model parameters are shown in Table 2.1.

The experimental result and the simulated Bouc–Wen model output are compared in Fig. 2.9a. The plots indicate that the Bouc–Wen model cannot exactly represent the complicated hysteresis of the system. A relative large error exists between the identified model output and the experimental result as shown in Fig. 2.9b. Specifically, the maximum model error is 4.70 μm, which accounts for 5.3 % of the concerned travel range of the nanopositioning stage. It is observed that a smaller model error is obtained when the input has lower magnitude and frequency (2–4 s). Hence, the model error varies greatly at different amplitudes and frequencies of the input signal, which indicates that the Bouc–Wen model cannot capture the rate dependency of the hysteresis precisely.

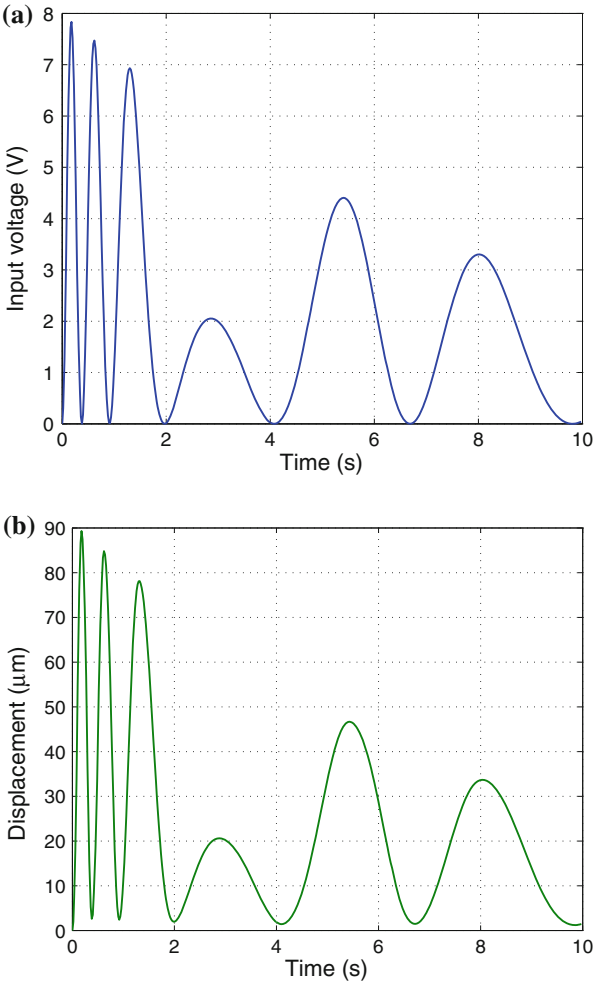

Fig. 2.8 Time history of the training data sets. **a** Input voltage to the high-voltage amplifier. **b** Output displacement of the nanopositioning stage

2.4.2 MPI Model Results

In order to identify the MPI model, the key step lies in the weight parameter determination for matching the model output to the experimental hysteresis data. Based on the input and output data sets, the thresholds r_i and d_i^* are assigned as follows:

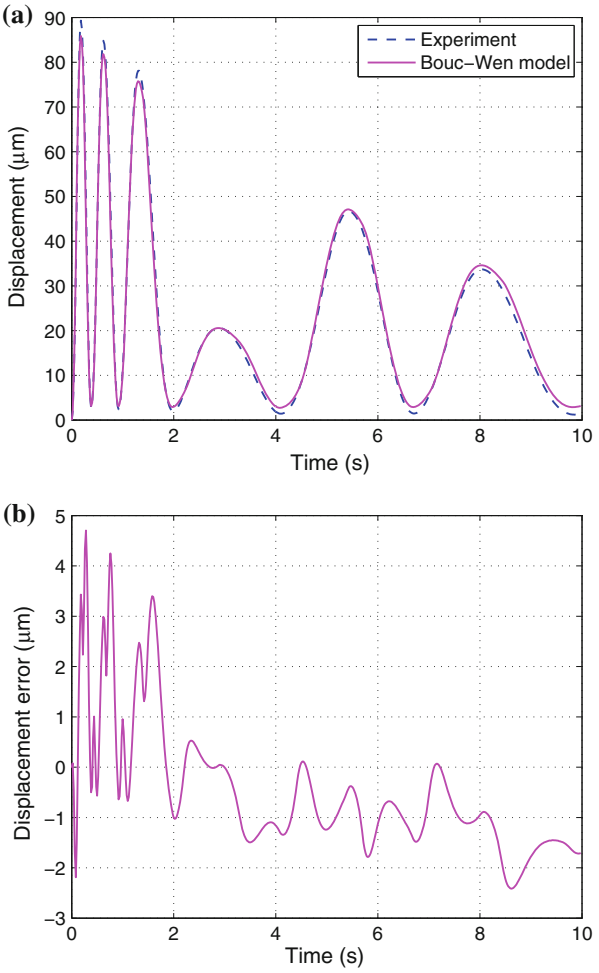

Fig. 2.9 Results of the identified Bouc–Wen model. **a** Experimental result and Bouc–Wen model output. **b** Bouc–Wen model output errors

$$r_i = \frac{i}{n+1} \max |u(t)|, \quad \text{for} \quad i = 0, 1, \ldots, n \tag{2.38}$$

$$d_j^* = \frac{j}{m+1} \max |y(t)|, \quad \text{for} \quad j = 0, 1, \ldots, m \tag{2.39}$$

where u and y denote the voltage input and displacement output data of the piezostage system, respectively. In addition, the initial states are assigned as $y_{0i} = 0, i = 0, 1, \ldots, n$, for simplicity.

Table 2.1 Parameters of the identified Bouc–Wen hysteresis model

Parameter	Search space	Identified value
m	[0, 1]	0.2789 kg
b	$[10^2, 10^6]$	8.9055×10^5 N s/m
k	$[10^3, 10^9]$	3.5244×10^8 N/m
d	[0, 0.1]	1.1351×10^{-5} m/V
α	[0, 1]	0.4754
β	[0, 1]	0.8718
γ	[0, 1]	0.9925

Then, the weights $\mathbf{w}_h$ and $\mathbf{w}_s^*$ are identified by solving an optimization problem of minimizing the model error:

$$E[u, y](\mathbf{w}_h, \mathbf{w}_s^*, t) = \mathbf{w}_h^T \mathbf{H}_r[u, \mathbf{y}_0](t) - \mathbf{w}_s^{*T} \mathbf{S}_d^*[y](t). \tag{2.40}$$

Here, instead of using L_2^2-norm optimization [10], the weight parameters are identified by resorting to the PSO approach. Additionally, $n = 12$ and $m = 6$ are assigned, and the thresholds r_i and d_j^* are allocated according to Eqs. (2.38) and (2.39). Using the same training data sets as shown in Fig. 2.8a, b, the MPI model is identified off-line by optimizing a total of $n + m + 2 = 20$ weight parameters ($\mathbf{w}_h$ and $\mathbf{w}_s^*$) within the search space of [0, 1] using the PSO algorithm [2].

The identified MPI model and inverse MPI model parameters are described in Tables 2.2 and 2.3, respectively. The presence of zero weight values of w_{hi} and w_{sj}^* indicates that the selected n and m are large enough for the modeling process.

The comparisons of the experimental output and simulated MPI model output are illustrated in Fig. 2.10. It is observed from Fig. 2.10a that the MPI model cannot

Table 2.2 Parameters of the identified MPI hysteresis model

i	r_i	w_{hi}	j	d_j	w_{sj}
0	0	0.0677	0	0	99.9999
1	0.6036	0.0228	1	0.1276	-1.0010×10^{-5}
2	1.2072	6.5979×10^{-6}	2	0.2552	-3.3798×10^{-5}
3	1.8108	0.0196	3	0.3827	-1.5611×10^{-5}
4	2.4145	0.0037	4	0.5103	0
5	3.0181	4.0252×10^{-6}	5	0.6379	-2.6054×10^{-4}
6	3.6217	1.0681×10^{-6}	6	0.7655	-6.8291×10^{-5}
7	4.2253	6.7711×10^{-8}			
8	4.8289	6.1372×10^{-8}			
9	5.4325	3.8439×10^{-8}			
10	6.0362	2.9690×10^{-8}			
11	6.6398	8.4374×10^{-9}			
12	7.2434	0			

Table 2.3 Parameters of the inverse MPI hysteresis model

i	r_i^*	w_{hi}^*	j	d_j^*	w_{sj}^*
0	0	14.7797	0	0	0.0100
1	0.0408	−3.7195	1	12.7581	1.0010×10^{-9}
2	0.0954	-8.0705×10^{-4}	2	25.5163	1.3798×10^{-9}
3	0.1500	−1.9672	3	38.2744	1.5611×10^{-9}
4	0.2164	−0.2980	4	51.0326	0
5	0.2850	-3.1129×10^{-4}	5	63.7907	2.6054×10^{-8}
6	0.3537	-8.2597×10^{-5}	6	76.5488	6.8292×10^{-9}
7	0.4223	-5.2362×10^{-6}			
8	0.4909	-4.7460×10^{-6}			
9	0.5596	-2.9725×10^{-6}			
10	0.6282	-2.2959×10^{-6}			
11	0.6969	-6.5247×10^{-7}			
12	0.7655	0			

exactly represent the complicated hysteresis of the nanopositioning system. A relative large error exists between the identified model output and the experimental result as shown in Fig. 2.10b. Specifically, the maximum model error is 6.35 μm which occurs along with the input component of the highest frequency (0–0.38 s). It accounts for 7.1 % of the concerned travel range of the nanopositioning stage. On the other hand, the model error is reduced at lower frequency with smaller amplitude of the input signal, that is, the model errors vary significantly at different frequencies and amplitudes of the input signal, which means that the MPI model cannot capture the rate dependency of the hysteresis either. Due to the existence of zero weights in $\mathbf{w}_h$ and $\mathbf{w}_s^*$, the increases of m and n will not cause significant improvement on the model accuracy. Hence, the capability of the MPI model is limited in modeling the rate-dependent hysteresis.

2.4.3 LSSVM Model Results

To identify the LSSVM model, the 500 sets of input and output data sets as shown in Fig. 2.8 are also adopted to train the LSSVM. To capture the rate dependency behavior, the input rate is numerically calculated by the backward difference equation:

$$\dot{u}(kT) = \frac{u(kT) - u(kT - T)}{T} \tag{2.41}$$

where T is the sampling time and k denotes the index of the time series. The two input variables are shown in Fig. 2.11.

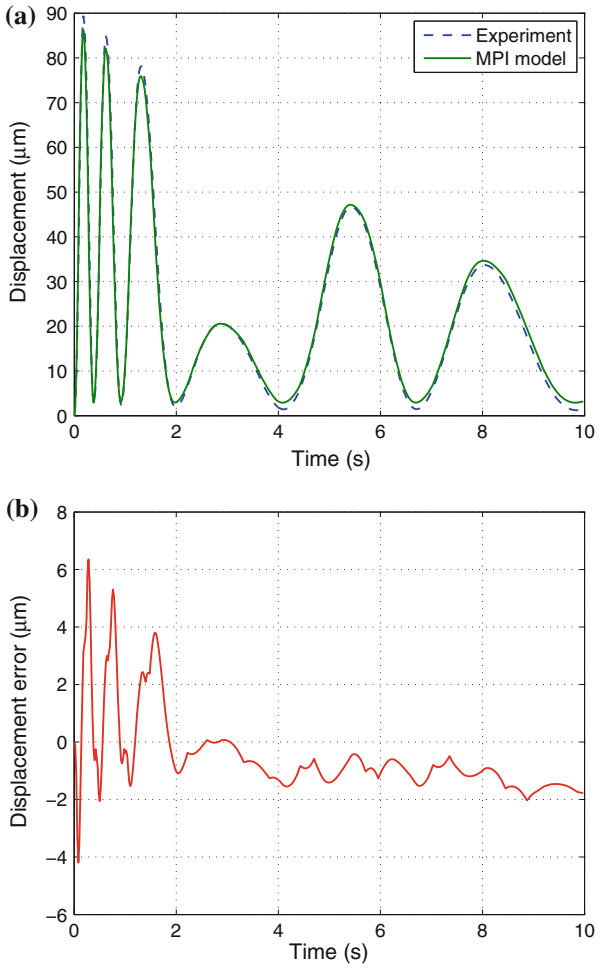

Fig. 2.10 Results of the identified MPI model. **a** Experimental result and MPI model output. **b** MPI model output errors

To facilitate the LSSVM modeling, the data sets are normalized before the training process. Specifically, both the input and output data are normalized within the range of [0, 1] by the following transformation [17]:

$$\mathscr{N}(v) = v^* = \frac{v - v_{\min}}{v_{\max} - v_{\min}} \tag{2.42}$$

where $\mathscr{N}$ represents the normalization operation, and $v_{\min}$ and $v_{\max}$ denote the minimum and maximum values of the input or output data v, respectively. It is notable that, after the training process, the LSSVM output y^* is re-transformed into the actual value y using the inverse normalization operation $\mathscr{N}^{-1}$.

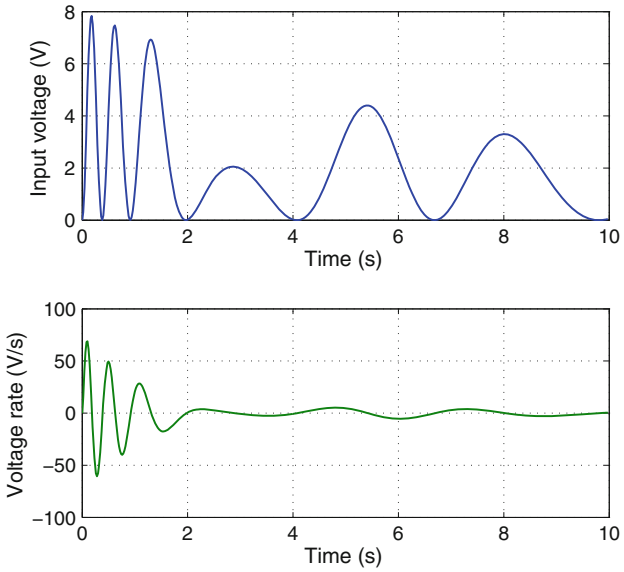

Fig. 2.11 Training data sets of the two input variables for the LSSVM model

Given arbitrary initial values ($\gamma_0 = 100$ and $\sigma_0 = 1$), the optimized LSSVM model hyperparameters are obtained by the Bayesian framework automatically. The optimal hyperparameters are $\gamma = 741.57$ and $\sigma = 7.39$. They are used to train the LSSVM to obtain the values of α_i and b, which minimizes the objection function (2.22).

Once the training process is completed, the LSSVM model produces the outputs as illustrated in Fig. 2.12. It is seen that the maximum model error is only 1.27 μm, i.e., 1.4 % of the motion range. Thus, with the same number of training data sets, the LSSVM model error has been reduced by 79 and 80 % as compared with the Bouc–Wen and MPI model errors, respectively. In addition, Fig. 2.12b exhibits that the LSSVM model errors are more uniformly distributed in comparison with Bouc–Wen and MPI model results as shown in Figs. 2.9b and 2.10b, respectively. Relatively, the LSSVM model errors are not dependent on neither the amplitude nor the frequency of the input signals. Therefore, the trained LSSVM model captures the amplitude- and rate-dependent hysteresis accurately.

2.4.4 Model Capability Comparison

Based on the displacement error $e = y_d - y$, where y_d and y represent the desired and actual displacements, respectively, the mean absolute error (MAE) and root-mean-square error (RMSE) are defined as follows:

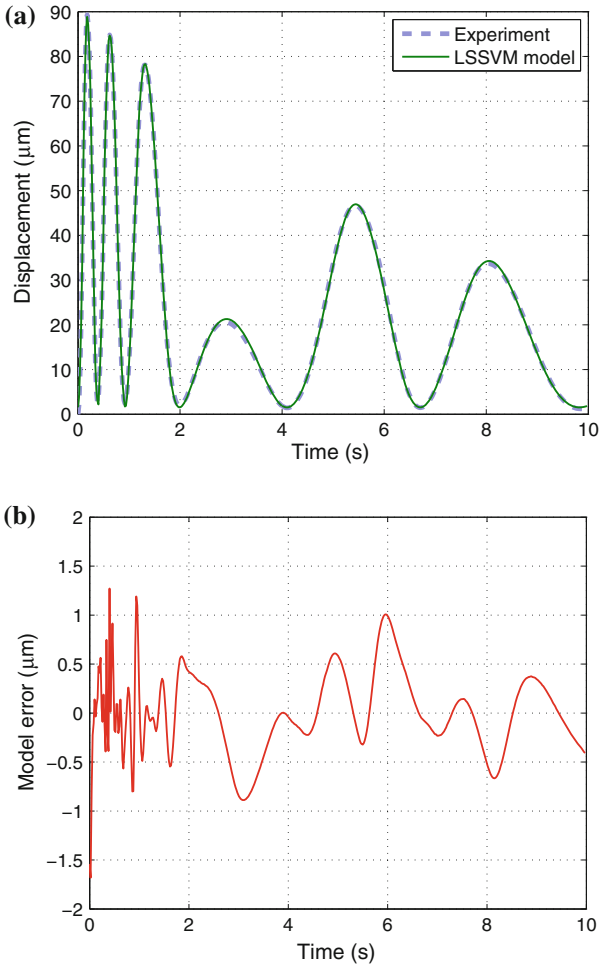

Fig. 2.12 Results of the trained LSSVM model. **a** Experimental result and LSSVM model output. **b** LSSVM model output errors

$$\text{MAE} = \frac{1}{N_t}\sum_{i=1}^{N_t}|e_i| \tag{2.43}$$

$$\text{RMSE} = \sqrt{\frac{1}{N_t}\sum_{i=1}^{N_t}e_i^2} \tag{2.44}$$

where $N_t = 500$ is the number of test data sets in the experiment.

The modeling performances of the three models are tabulated in Table 2.4. Due to the fewer number of parameters, the Bouc–Wen model takes 19.1 % shorter time than

Table 2.4 Modeling performances of Bouc–Wen, MPI, and LSSVM models

Specification	Bouc–Wen	MPI	LSSVM
No. of model parameters	7	20	2
Model identification time (s)	614.89	759.91	2.56
Modeling error			
MAE (%)	1.276	1.358	0.364
RMSE (%)	1.560	1.692	0.470
Generalization error			
MAE (%)	1.253	1.318	0.621
RMSE (%)	1.530	1.621	0.858

the MPI model to identify all the parameters by resorting to the same optimization approach (PSO) in 1500 epoches. On the other hand, the LSSVM model needs a significantly shorter time than both Bouc–Wen and MPI models to identify the model parameters.

Concerning the modeling error, it is observed that the Bouc–Wen model produces 6.0 % lower MAE and 7.8 % lower RMSE than the MPI model. In contrast, the LSSVM model achieves the best results among the three methods. Regarding MAE, the LSSVM has improved the accuracy by 71.5 and 73.2 % in comparison with Bouc–Wen and MPI models, respectively. As far as RMSE is concerned, the LSSVM has enhanced the accuracy by 69.9 and 72.2 % as compared with Bouc–Wen and MPI models, respectively.

2.4.5 Generalization Study

To test the generalization of the obtained models, a new input signal is chosen as follows:

$$u(t) = 5e^{-0.14t}[\cos(3\pi t e^{-0.092t} - 3.15) + 1.0] \tag{2.45}$$

which is depicted in Fig. 2.13a. In addition, the displacement output of the nanopositioning stage is shown in Fig. 2.13b.

The Bouc–Wen, MPI, and LSSVM model outputs are depicted in Fig. 2.14. The model output errors with respect to the actual output obtained by experiments are illustrated in Fig. 2.15. Table 2.4 describes the generalization testing results of the three types of models.

It is found that the Bouc–Wen model produces a MAE of 1.086 μm and a RMSE of 1.326 μm, which accounts for 1.25 and 1.53 % of the motion range, respectively. Using the MPI model, the MAE and RMSE are 1.143 and 1.405 μm, which are equivalent to 1.32 and 1.62 % of the overall motion range, respectively. As compared

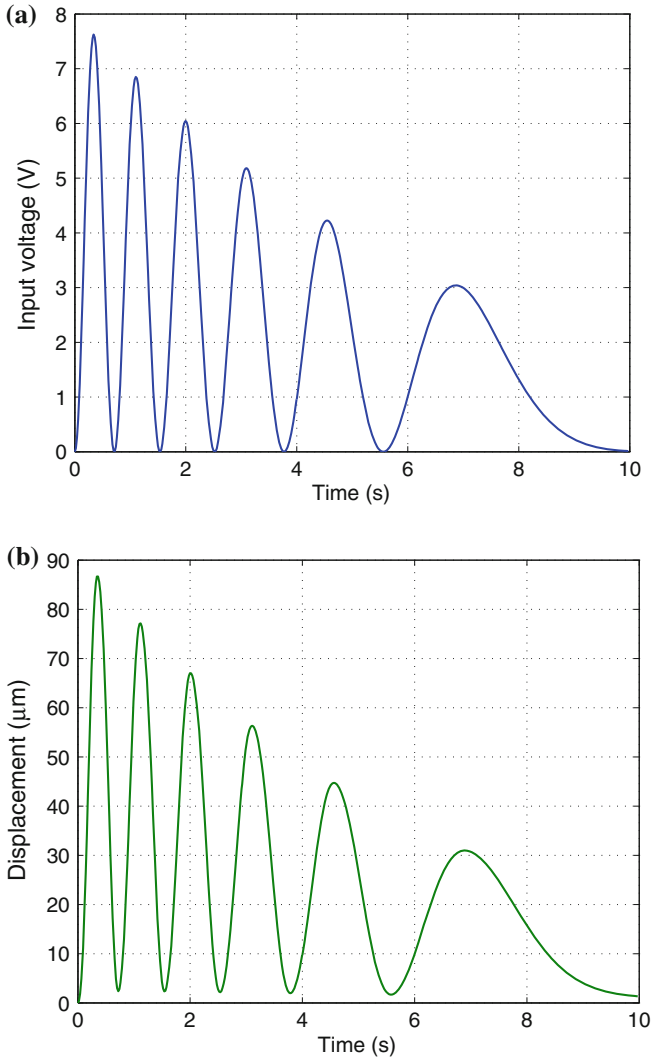

Fig. 2.13 Time history of the testing data sets. **a** Input voltage to the high-voltage amplifier. **b** Output displacement of the nanopositioning stage

with MPI model, the Bouc–Wen model reduces the MAE and RMSE by 4.9 and 5.6 %, respectively. Thus, the generalization ability of the Bouc–Wen model is slightly better than that of the MPI model.

In contrast, the LSSVM model produces a MAE of 0.538 μm and a RMSE of 0.744 μm, i.e., 0.62 and 0.86 % of the overall motion range, which have been reduced by 50.5 and 43.9 % in comparison with the Bouc–Wen model results and by 52.9

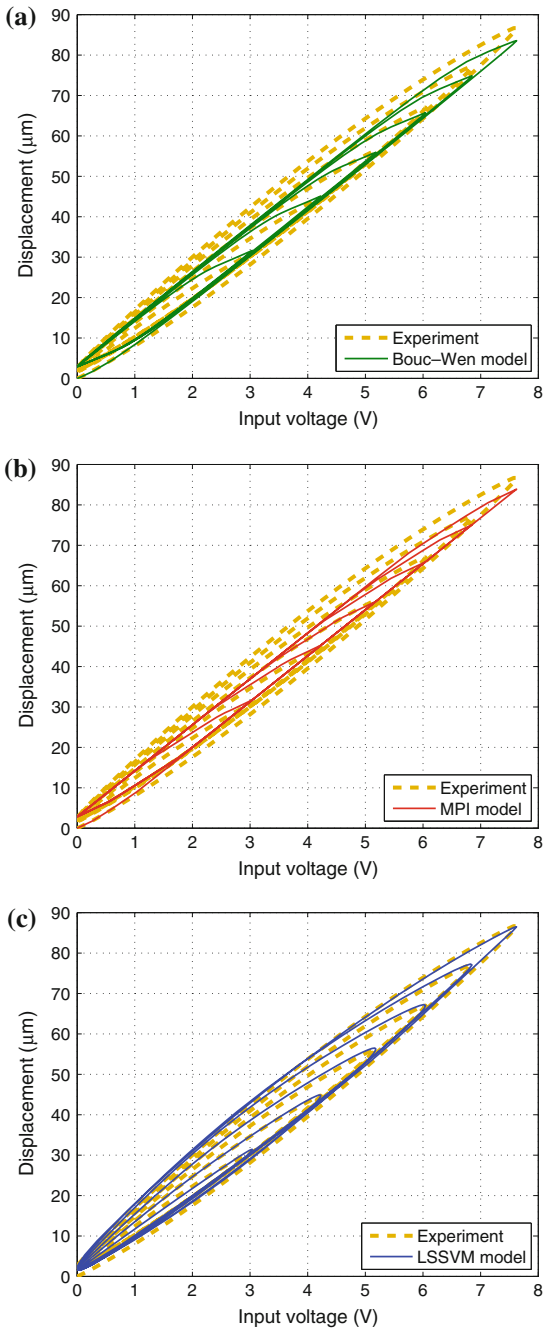

Fig. 2.14 Model generalization testing results. **a** Boun-Wen model output. **b** MPI model output. **c** LSSVM model output

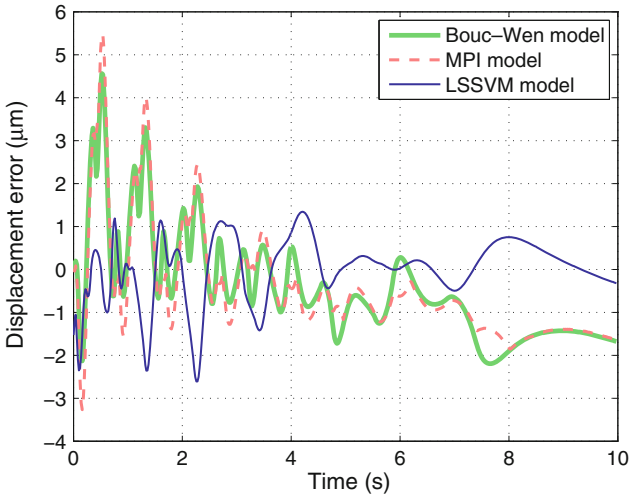

Fig. 2.15 Displacement errors of the Bouc–Wen model, MPI model, and LSSVM model

and 47.0 % in comparison with the MPI model outputs, respectively. Therefore, the experimental results demonstrate a good generalization capacity of the LSSVM hysteresis model.

2.5 Controller Design and Verification

Based on the established hysteresis models, a feedforward plus feedback control scheme is implemented and verified for the hysteresis compensation in this section. Both the inverse Bouc–Wen model and inverse MPI model are adopted for comparisons with the LSSVM inverse model-based control scheme.

2.5.1 Feedforward Controller Design

To compensate for the hysteresis nonlinearity, a feedforward (FF) control based on the inverse hysteresis model can be constructed. The FF control effort u_{FF}^{BW} is created by the inverse Bouc–Wen model. Similarly, the inverse MPI model is used to produce the FF control signal u_{FF}^{MPI}. The overall control scheme is shown in Fig. 2.16a, where the feedback (FB) control u_{FB} is adopted to suppress the residual control error due to the model errors of the identified Bouc–Wen and MPI models.

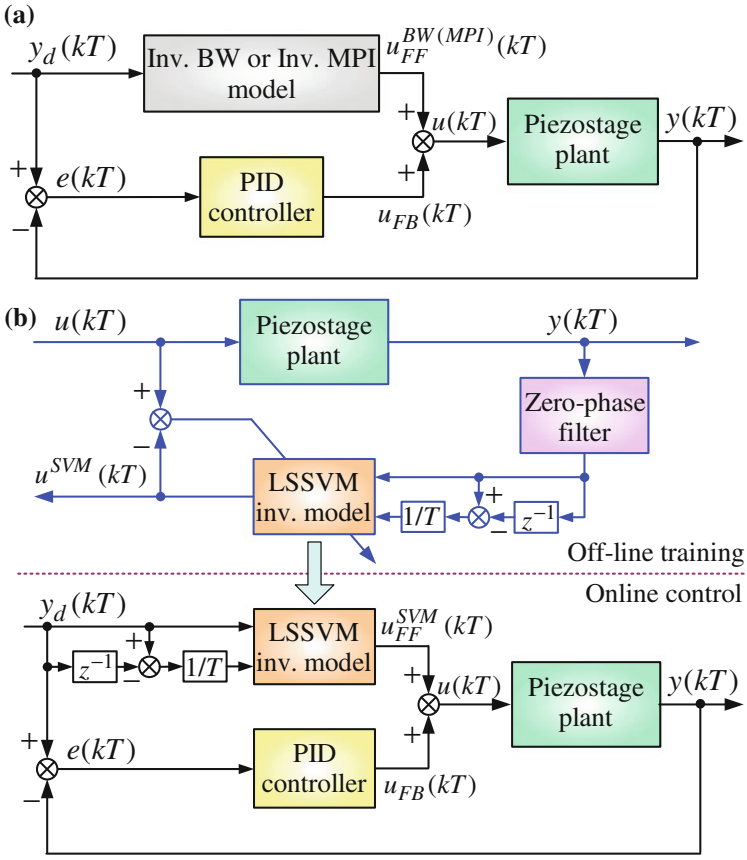

Fig. 2.16 Block diagram of the feedforward (FF) plus feedback (FB) hybrid controller for a piezostage system. **a** Bouc–Wen model or MPI model-based control. **b** LSSVM model-based control

To establish an inverse LSSVM hysteresis model, the displacement (y) and velocity ($\dot{y}$) are selected as the inputs and the corresponding voltage (u) is assigned as the output for the LSSVM training. Preliminary investigations indicate that the noisy sensor readings produce slightly oscillating voltage input by the inverse LSSVM model. Thus, to alleviate the noises in the displacement sensor readings, the displacement data y are filtered by adopting a zero-phase digital filter with 50-Hz cutoff frequency. The filter is implemented with the command "filtfilt" in MATLAB. Afterward, the input data sets are formed by the filtered displacement data and the calculated velocity. Once trained off-line using the scheme as shown in Fig. 2.16b, the LSSVM inverse model provides the online FF control signal u_{FF}^{SVM}.

2.5.2 Feedforward Plus Feedback Controller Design

Due to the presence of modeling error, the hysteresis cannot be completely eliminated by the stand-alone inverse model-based FF compensator. Therefore, a FB control u_{FB} is employed to create a hybrid control as described in Fig. 2.16.

Here, the PID control algorithm is implemented as a FB control due to its robustness and popularity. By adopting an incremental PID algorithm, the overall control input can be derived in the discretized form:

$$\begin{aligned} u(kT) &= u_{FF}(kT) + u_{FB}(kT) \\ &= u_{FF}(kT) + u_{FB}(kT - T) \\ &\quad + K_p\,[e(kT) - e(kT - T)] + K_i\,e(kT) \\ &\quad + K_d\,[e(kT) - 2e(kT - T) + e(kT - 2T)] \end{aligned} \tag{2.46}$$

where e represents the displacement error, $u_{FB}(kT - T)$ is the FB control command in the previous time step, and the FF term $u_{FF}(kT)$ is given by the inverse MPI model or LSSVM inverse hysteresis model. Additionally, K_p, K_i, and K_d are the proportional, integral, and derivative gains, respectively.

2.5.3 Controller Verification

In the control experiments, the sampling time interval is assigned as $T = 0.001$ s. Actually, a PI control is employed. The control gains are tuned as $K_p = 0.0864$, $K_i = 31.1040$, and $K_d = 0$ using the Ziegler–Nichols (Z–N) method.

For a reference displacement as shown in Fig. 2.17a, the Bouc–Wen (BW) and MPI model-based FF control results are both shown in Fig. 2.17. The two FF plus PID FB control results are depicted in Fig. 2.18. In addition, the LSSVM inverse hysteresis model is trained with the hyperparameters $\gamma = 741.82$ and $\sigma = 7.69$, which are optimized by the Bayesian inference framework. Using the same reference input as shown in Fig. 2.17a, the control results and tracking errors of the LSSVM model-based FF and FF+FB control are also shown in Figs. 2.17 and 2.18.

Figure 2.17b reveals that the inverse Bouc–Wen model-based FF gives a MAE of 1.199 % and a RMSE of 1.660 % with respect to the motion range. On the other hand, the FF control using the inverse MPI model produces a MAE of 1.080 % and a RMSE of 1.813 %. It is seen that the Bouc–Wen model and MPI model produce similar results. While the former achieves a slightly better RMSE than the latter, the latter produces a better MAE than the former. By contrast, the LSSVM inverse model-based FF approach further reduces the MAE and RMSE to 0.416 and 0.537 %, respectively, which have been significantly improved by 65.3 and 67.7 % in comparison with the inverse Bouc–Wen model results and by 61.5 and 70.4 % in comparison with the inverse MPI model results, respectively.

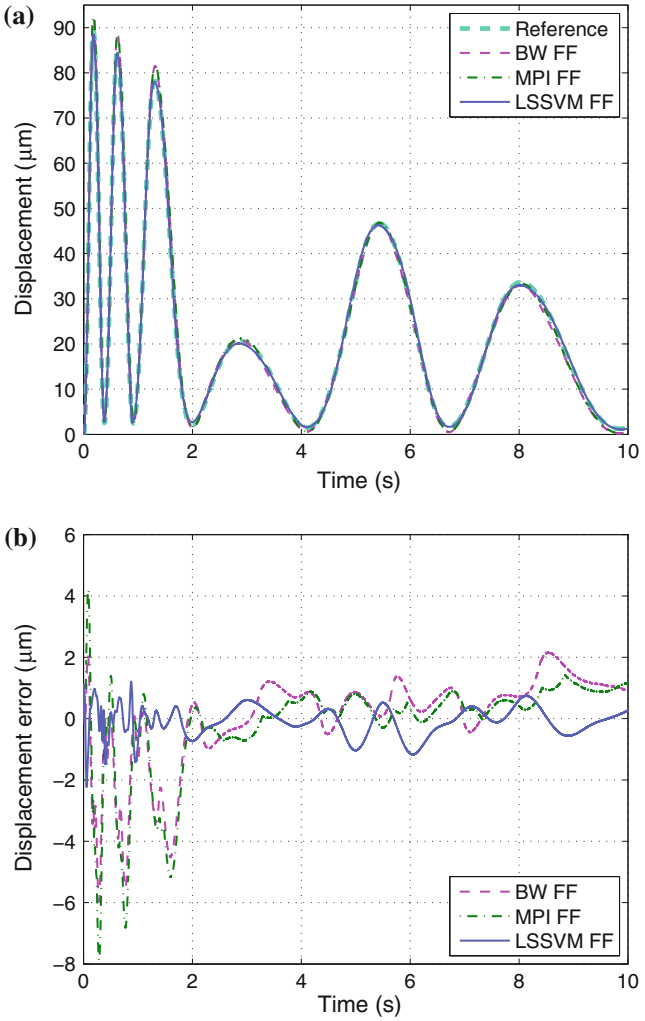

Fig. 2.17 Bouc–Wen, MPI, and LSSVM-based FF control results. **a** Feedforward (FF) control results. **b** Control errors of the three FF methods

Moreover, the hybrid control results as shown in Fig. 2.18b indicate that the inverse Bouc–Wen model-based FF+FB control scheme leads to a MAE of 0.024 % and a RMSE of 0.048 %. In addition, the inverse MPI model-based FF+FB control scheme results in a MAE of 0.023 % and a RMSE of 0.052 %, while the LSSVM-based hybrid control substantially suppresses the MAE to 0.015 % and RMSE to 0.038 %. As compared to the inverse Bouc–Wen hysteresis model, the LSSVM inverse model-based FF+FB control reduces the tracking errors in terms of MAE and RMSE by 37.5 and 20.8 %, respectively. Moreover, the LSSVM inverse model-based FF+FB control

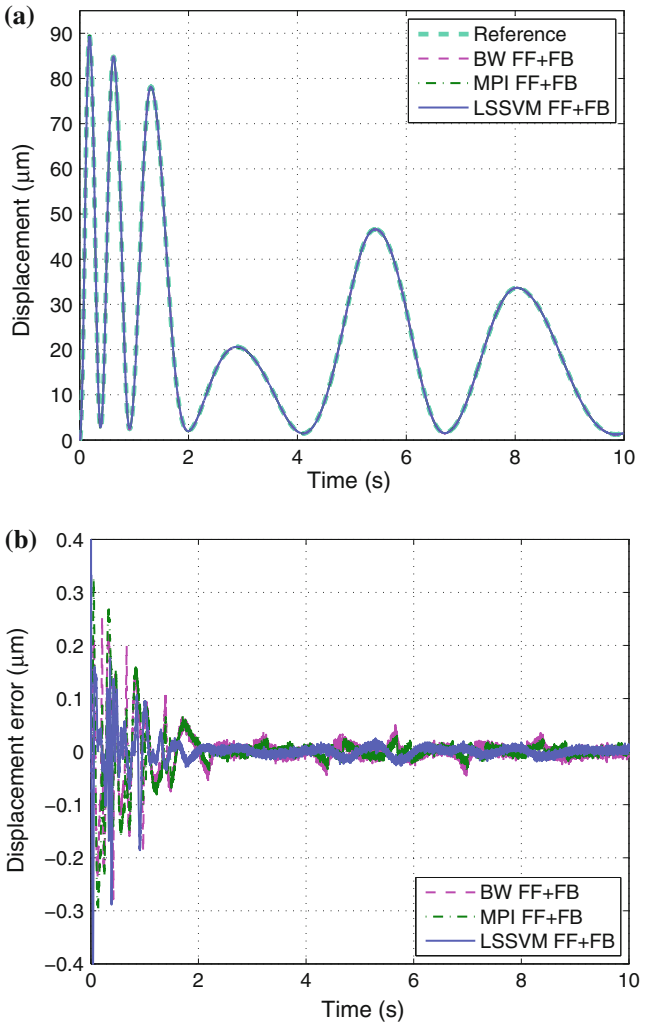

Fig. 2.18 Bouc–Wen, MPI, and LSSVM-based FF plus FB control results. **a** FF plus feedback (FB) control results. **b** Control errors of the three hybrid approaches

suppresses the MAE and RMSE by 34.8 and 26.9 %, respectively, as compared with the inverse MPI model-based control. This is caused by the fact that the model accuracy of LSSVM is superior to that of both Bouc–Wen and MPI models. The effectiveness of the LSSVM-based control is evident from the control results.

In addition, to reveal the efficiency of the hybrid control, the control results of the stand-alone FF and FB and the combined FF+FB control based on the LSSVM model are illustrated in Fig. 2.19. It can be observed from Fig. 2.19b that the FF+FB produces the MAE and RMSE of 0.015 and 0.038 %, respectively, which have been

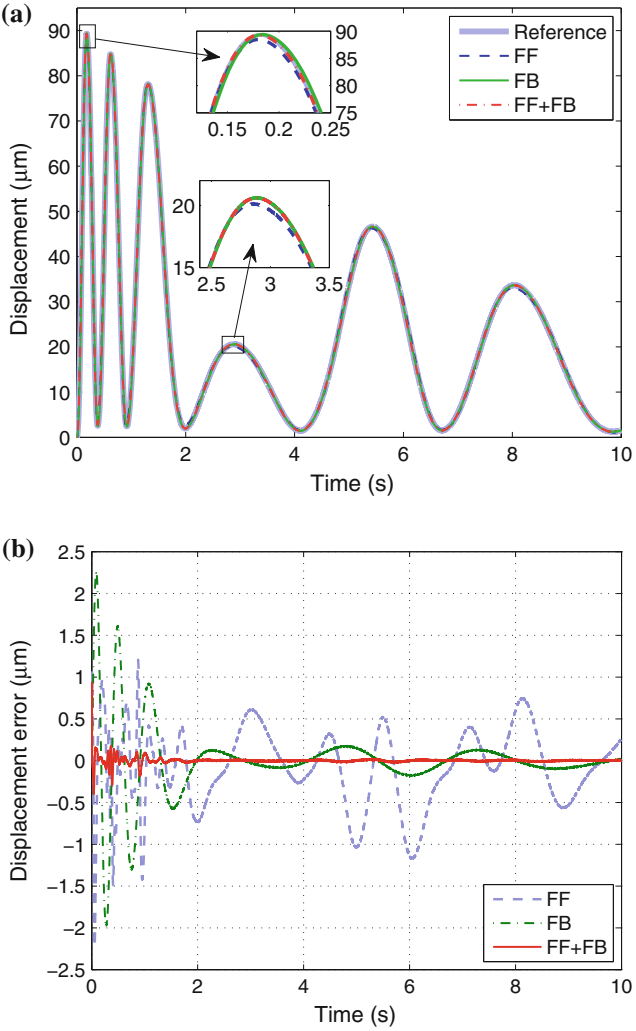

Fig. 2.19 LSSVM-based stand-alone and hybrid control results. **a** FF, FB, and FF+FB results. **b** Tracking errors of the three methods

significantly improved by 96.5 and 92.9 % in comparison with the FF control results, and substantially enhanced by 93.7 and 91.7 % as compared with the stand-alone FB outputs, respectively. As a result, the hysteresis effects have been suppressed by the FF+FB approach to a negligible level as indicated in Fig. 2.20a. Although the PID FB control results can be improved by tuning the control gains larger, it is at the risk of oscillations in the hybrid control results. With the hybrid control, the individual control input components are illustrated in Fig. 2.20b. It is found that the overall control effort is dominated by the FF control, whereas the FB control effort is minor.

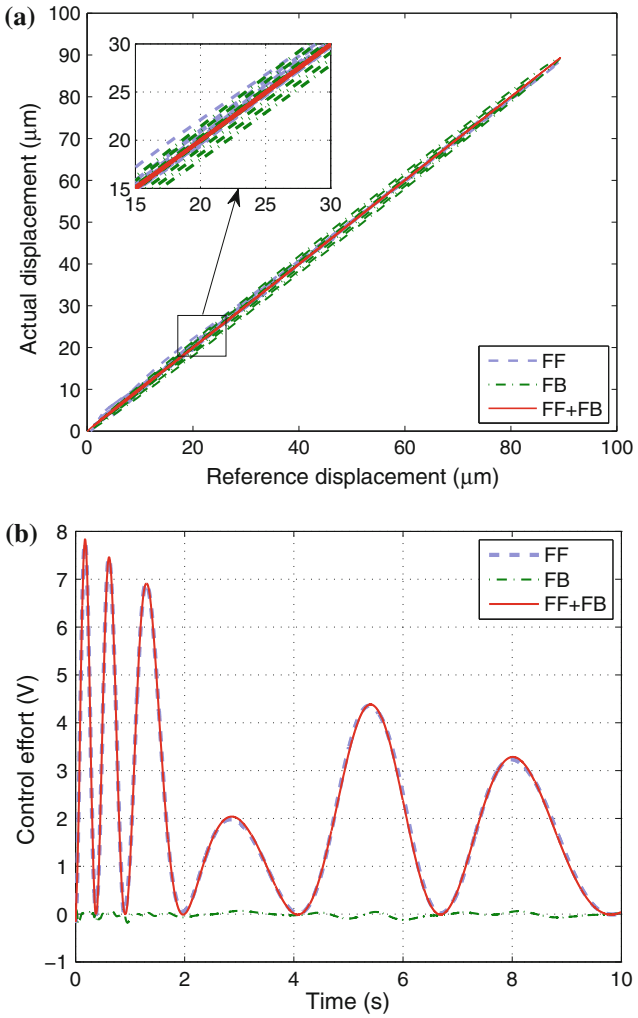

Fig. 2.20 LSSVM-based control results. **a** Actual versus reference displacements obtained by the three approaches. **b** Control signal components of the FF+FB hybrid control

Even so, the FB control is capable of suppressing the residual tracking errors and leading to a better result than the stand-alone FF method, which is verified by the tracking errors as compared in Fig. 2.19b.

For the purpose of comparison, the control results obtained by the Bouc–Wen, MPI, and LSSVM inverse models are tabulated in Table 2.5, where the MAE and RMSE are calculated as percentage values with respect to the motion range. It is obvious that the FF control accuracy of the LSSVM model has been enhanced by over 65 and 60 % as compared with those of the Bouc–Wen and MPI models, respectively.

Table 2.5 Control performances using Bouc–Wen, MPI, and LSSVM models

Controller	Performance (%)	Bouc–Wen	MPI	LSSVM
FF	MAE	1.199	1.080	0.416
	RMSE	1.660	1.813	0.537
FF+FB	MAE	0.024	0.023	0.015
	RMSE	0.048	0.052	0.038

With the FF+FB hybrid control, the LSSVM approach has suppressed the control errors by more than 20 and 25 % in comparison with the Bouc–Wen and MPI models, respectively. Therefore, the superiority of the LSSVM model over the popular Bouc–Wen and MPI models is verified for the hysteresis compensation task.

2.6 Chapter Summary

The results presented in this chapter show that the rate-dependent hysteresis of a piezoelectric nanopositioning stage can be accurately modeled and effectively suppressed by the LSSVM regression model and LSSVM inverse model, respectively. By selecting the input variation rate as an auxiliary input variable, the multi-valued mapping due to the hysteresis nonlinearity is converted into a one-to-one mapping, and the LSSVM is trained to capture the rate-dependent hysteretic behavior. Its superior modeling performance over the popular Bouc–Wen and MPI hysteresis models has been revealed by experimental studies. Results also demonstrate that the hybrid control using the LSSVM inverse model-based feedforward control combined with a PID control is capable of compensating the hysteresis nonlinearity effectively. Due to a simple structure of the presented modeling and control framework, it can be easily extended to the hysteretic systems driven by shape-memory alloy or other types of smart actuators as well. As a future work, an incremental LSSVM model can be established to automatically update the model parameters online once new training data occur.

References

1. Ang, W.T., Khosla, P.K., Riviere, C.N.: Feedforward controller with inverse rate-dependent model for piezoelectric actuators in trajectory-tracking applications. IEEE/ASME Trans. Mechatron. **12**(2), 134–142 (2007)
2. Birge, B.: PSOt—a particle swarm optimization toolbox for use with Matlab. In: Proceedings of IEEE Swarm Intelligence Symposium, pp. 182–186. Indianapolis, Indiana, USA (2003)
3. Boukari, A.F., Carmona, J.C., Moraru, G., Malburet, F., Chaaba, A., Douimi, M.: Piezo-actuators modeling for smart applications. Mechatronics **21**(1), 339–349 (2011)

4. De Brabanter, K., Karsmakers, P., Ojeda, F., Alzate, C., De Brabanter, J., Pelckmans, K., De Moor, B., Vandewalle, J., Suykens, J.A.K.: LS-SVMlab toolbox user's guide version 1.7. Internal Report 10-146, ESAT-SISTA, K.U.Leuven, Leuven, Belgium (2010)
5. Dong, R., Tan, Y., Chen, H., Xie, Y.: A neural networks based model for rate-dependent hysteresis for piezoelectric actuators. Sens. Actuator A-Phys. **143**(2), 370–376 (2008)
6. Ge, P., Jouaneh, M.: Tracking control of a piezoceramic actuator. IEEE Trans. Contr. Syst. Technol. **4**(3), 209–216 (1996)
7. Janaideh, M.A., Rakheja, S., Su, C.Y.: Experimental characterization and modeling of rate-dependent hysteresis of a piezoceramic actuator. Mechatronics **19**(5), 656–670 (2009)
8. Juhasz, L., Maas, J., Borovac, B.: Parameter identification and hysteresis compensation of embedded piezoelectric stack actuators. Mechatronics **21**(1), 329–338 (2011)
9. Kim, J., Kang, B.: Micro-macro linear piezoelectric motor based on self-moving cell. Mechatronics **19**(7), 1134–1142 (2009)
10. Kuhnen, K.: Modeling, identification and compensation of complex hysteretic nonlinearities: a modified Prandtl-Ishlinskii approach. Eur. J. Control **9**(4), 407–421 (2003)
11. Li, Y., Xu, Q.: Adaptive sliding mode control with perturbation estimation and PID sliding surface for motion tracking of a piezo-driven micromanipulator. IEEE Trans. Contr. Syst. Technol. **18**(4), 798–810 (2010)
12. Lin, C.J., Chen, S.Y.: Evolutionary algorithm based feedforward control for contouring of a biaxial piezo-actuated stage. Mechatronics **19**(6), 829–839 (2009)
13. Suykens, J.A.K., Vandewalle, J.: Least squares support vector machine classifiers. Neural Process. Lett. **9**(3), 293–300 (1999)
14. Suykens, J.A.K., Gestel, T.V., Brabanter, J.D., Moor, B.D., Vandewalle, J.: Least Squares Support Vector Machines. World Scientific Publishing Co., Singapore (2002)
15. Van Gestel, T., Suykens, J.A.K., Baestaens, D.E., Lambrechts, A., Lanckriet, G., Vandaele, B., De Moor, B., Vandewalle, J.: Financial time series prediction using least squares support vector machines within the evidence framework. IEEE Trans. Neural Netw. **12**(4), 809–821 (2001)
16. Vong, C.M., Wong, P.K., Li, Y.P.: Prediction of automotive engine power and torque using least squares support vector machines and Bayesian inference. Eng. Appl. Artif. Intell. **19**(3), 277–287 (2006)
17. Wong, P.K., Vong, C.M., Tam, L.M., Li, K.: Data preprocessing and modelling of electronically-controlled automotive engine power performance using kernel principal components analysis and least-square support vector machines. Int. J. Veh. Syst. Model. Test. **3**(4), 312–330 (2008)
18. Xu, Q., Li, Y.: Dahl model-based hysteresis compensation and precise positioning control of an XY parallel micromanipulator with piezoelectric actuation. J. Dyn. Syst. Meas. Control-Trans. ASME **132**(4), 041,011 (2010)
19. Yang, J., Bouzerdoum, A., Phung, S.L.: A training algorithm for sparse LS-SVM using compressive sampling. In: Proceedings of IEEE International Conference on Acoustics Speech and Signal Processing, pp. 2054–2057 (2010)
20. Yu, S., Alici, G., Shirinzadeh, B., Smith, J.: Sliding mode control of a piezoelectric actuator with neural network compensating rate-dependent hysteresis. In: Proc. of IEEE Int. Conf. on Robotics and Automation, pp. 3641–3645 (2005)
21. Yu, Y., Xiao, Z., Naganathan, N.G., Dukkipati, R.V.: Dynamic Preisach modelling of hysteresis for the piezoceramic actuator system. Mech. Mach. Theory **37**(1), 75–89 (2002)

Chapter 3
Feedforward Control Without Modeling Inverse Hysteresis

This chapter presents an approach of hysteresis identification and compensation of piezoelectric actuators by resorting to an intelligent hysteresis model. In particular, a least squares support vector machine (LSSVM)-based hysteresis model is developed and used for both purposes of hysteresis identification and hysteresis compensation. By this way, the inverse hysteresis is not needed in the feedforward hysteresis compensator because the hysteresis model is directly used. The effectiveness of the presented idea is validated by a series of experimental studies on a piezoactuated micro-/nano-positioning system.

3.1 Introduction

Concerning the approach of model-based hysteresis compensation, the hysteresis effect is generally compensated for by employing an inverse hysteresis model. It follows that both a hysteresis model and an inverse hysteresis model are needed for the purposes of hysteresis identification and compensation. Hence, it is desirable to mitigate the hysteresis effect by adopting a hysteresis model directly without using the inverse hysteresis [5].

In addition, it has been shown that the piezoelectric hysteresis effect is rate-dependent [2]. The hysteresis behavior is dependent not only on the amplitude but also on the frequency of input voltage signals. As compared with ANN and SVM, LSSVM is superior in terms of modeling accuracy and computational efficiency. Thus, LSSVM is selected for the hysteresis modeling process. Owing to the hysteresis nonlinearity, one value of input voltage corresponds to multiple position outputs for a piezoactuated device. Therefore, one challenge in identifying the hysteresis behavior with LSSVM lies in how to transfer the multivalued mapping into a single-valued one. In previous work, a one-to-one mapping was established by introducing the current input and input variation rate as one data set [7, 8]. However, in case that the input data are accompanied with noises, the variation rate is non-smooth, which causes

© Springer International Publishing Switzerland 2016

Q. Xu and K.K. Tan, *Advanced Control of Piezoelectric Micro-/Nano-Positioning Systems*, Advances in Industrial Control,
DOI 10.1007/978-3-319-21623-2_3

modeling error. Besides, it is unknown how many orders of the variation rates are sufficient to construct the mapping. Additionally, a regression-type hysteresis model was developed in [6] by employing the current and previous inputs and previous outputs as exogenous inputs. However, this work considered the position and voltage as output and input variables, respectively, and both direct and inverse hysteresis models are required, which implies a time-consuming process.

This chapter presents the identification and compensation of rate-dependent piezoelectric hysteresis using an intelligent hysteresis model without modeling the inverse hysteresis. A LSSVM-based hysteresis model is established, and a feedforward compensator is developed based on the single model, which provides a computationally efficient approach in hysteresis compensation. To establish the LSSVM model, the problem of how to select input variables to convert the multivalued mapping into a single-valued one is addressed in detail. The effectiveness of the idea is verified by a series of experimental studies. It will be shown that the established LSSVM model is more effective than Bouc–Wen model in terms of hysteresis identification as well as hysteresis compensation performances.

3.2 Dynamics Modeling of Hysteretic System

3.2.1 Dynamics Modeling with Bouc–Wen Hysteresis

Owing to a fewer number of parameters, the Bouc–Wen model has been extensively applied in piezoelectric hysteresis modeling. The entire dynamics model of a piezoactuated system can be established as follows [3, 4]:

$$M\ddot{y}(t) + B\dot{y}(t) + Ky(t) = K[Du(t) - H(t)] \tag{3.1}$$

$$\dot{H}(t) = \alpha D\dot{u}(t) - \beta|\dot{u}(t)|H(t) - \gamma\dot{u}(t)|H(t)| \tag{3.2}$$

where t is the time variable; parameters M, B, K, and y represent the mass, damping coefficient, stiffness, and displacement response of the piezoactuated system, respectively; D is the piezoelectric coefficient; u denotes the input voltage; and H indicates the hysteretic loop in terms of displacement whose magnitude and shape are determined by parameters α, β, and γ.

Once the dynamics parameters M, B, and K are determined, the four parameters (D, α, β, and γ) of the Bouc–Wen model can be identified by minimizing an objective function:

$$f(D, \alpha, \beta, \gamma) = \frac{1}{N}\sum_{i=1}^{N}\left(y_i - y_{\mathrm{BW}_i}\right)^2 \tag{3.3}$$

where N denotes the total number of samples, and $y_i - y_{\mathrm{BW}_i}$ represents the residual error of the ith sample which is the discrepancy between Bouc–Wen model output (y_{BW_i}) and experimental result (y_i).

Given the input voltage u and Bouc–Wen hysteresis model H, the output displacement of the system is governed by the model (3.1). On the other hand, given a desired displacement y_d, the required input voltage can be determined via Eq. (3.1):

$$u_{\mathrm{FF}}(t) = \frac{1}{KD}[M\ddot{y}_d(t) + B\dot{y}_d(t) + Ky_d(t) + KH(t)]. \tag{3.4}$$

It is found that the feedforward controller (3.4) is obtained using the hysteresis term H without solving the inverse hysteresis model.

3.2.2 Dynamics Modeling with Intelligent Hysteresis Model

By extending the aforementioned idea of hysteresis compensation using Bouc–Wen model where an inverse hysteresis model is not needed, an intelligent hysteresis model is proposed as follows.

First, the dynamics model (3.1) of the system is rewritten into the following form:

$$\ddot{y}(t) + 2\xi\omega_n\dot{y}(t) + \omega_n^2 y(t) = du(t) + h(t) \tag{3.5}$$

where ξ and ω_n denote the damping ratio and natural frequency of the piezo-actated system, respectively; d is a positive parameter; and h represents the hysteresis effect in terms of acceleration.

Then, in view of Eq. (3.5), the hysteresis term can be generated below:

$$h(t) = \ddot{y}(t) + 2\xi\omega_n\dot{y}(t) + \omega_n^2 y(t) - du(t). \tag{3.6}$$

In practice, the system parameters and output positions are not always available. Under such scenarios, it is necessary to establish an intelligent model to identify and compensate for the hysteresis term h.

Once an intelligent model of the hysteresis term $\hat{h}$ is obtained, a feedforward hysteresis compensator can be developed to create a desired output position y_d:

$$u_{\mathrm{FF}}(t) = \frac{1}{d}[\ddot{y}_d(t) + 2\xi\omega_n\dot{y}_d(t) + \omega_n^2 y_d(t) - \hat{h}(t)] \tag{3.7}$$

which uses the hysteresis model directly without solving the inverse hysteresis model. An intelligent hysteresis model is established based on LSSVM technique in the subsequent section.

3.3 Hysteresis Modeling Using LSSVM

LSSVM maps the input data into a high-dimensional feature space and constructs a linear regression function therein [7]. As is known, the hysteresis exhibits multivalued and non-smooth features [1]. Generally, the LSSVM is only able to estimate high-dimensional smooth functions with a satisfactory accuracy. Therefore, only the multivalued nonlinearity of hysteresis effect is handled here, that is, it is assumed that the signal of input command is smooth. With such a hypothesis, a LSSVM-based regression model is established to represent the piezoelectric hysteresis effect.

3.3.1 Regression Model Establishment

Equation (3.6) indicates that the output variable is the hysteresis term h, whereas input variables include both input voltage u and output position y.

Using LSSVM, a nonlinear regression model is formulated to describe the hysteresis effect as follows:

$$\hat{h}_k = f(\mathbf{x}_k) \tag{3.8}$$

where

$$\mathbf{x}_k = [u_k, \ldots, u_{k-m}, y_k, \ldots, y_{k-n}, h_{k-1}, \ldots, h_{k-l}] \tag{3.9}$$

with $\hat{h}_k$ denoting the hysteresis term predicted by LSSVM at the current time instant k. u_{k-1}, y_{k-1}, and h_{k-1} are the input voltage, output position, and hysteresis term at the previous time instant $k-1$, respectively. In addition, the order of the model is defined by m ($m \geq 0$), n ($n \geq 0$), and l ($l \geq 1$). The problem of how to select these three orders is discussed later.

3.3.2 LSSVM Modeling

Assume that the training data set is given by $\{\mathbf{x}_k, h_k\}_{k=1}^{N}$, where N represents the number of training data set, $\mathbf{x}_k \in \mathbb{R}^{m+n+l+2}$ is an input vector as shown in Eq. (3.9), and $h_k \in \mathbb{R}$ are the output data. The unknown hysteresis function can be approximated by the following equation:

$$\hat{h}(\mathbf{x}) = \mathbf{w}^T \varphi(\mathbf{x}) + b \tag{3.10}$$

where $\mathbf{w}$ is a weight vector, $\varphi(\cdot)$ denotes a nonlinear mapping from the input space to a higher dimensional feature space, and b is the bias.

The LSSVM approach formulates the regression as an optimization problem in the primal weight space. Then, the conditions for optimality are obtained by solving a series of partial derivatives, which are used to construct the dual formulation as follows:

$$\begin{bmatrix} 0 & \mathbf{1}_N^T \\ \mathbf{1}_N & \boldsymbol{\Omega} + \Gamma^{-1}\mathbf{I}_N \end{bmatrix} \begin{bmatrix} b \\ \boldsymbol{\alpha} \end{bmatrix} = \begin{bmatrix} 0 \\ \mathbf{h} \end{bmatrix} \tag{3.11}$$

where $\boldsymbol{\alpha} = [\alpha_1, \alpha_2, \ldots, \alpha_N]^T$ is called the support vector, and $\alpha_k = \Gamma e_k$ are support values with $\Gamma \in \mathbb{R}$ denoting the regularization factor. In addition, $\mathbf{1}_N = [1, 1, \ldots, 1]^T$, $\mathbf{h} = [h_1, h_2, \ldots, h_N]^T$, and $\mathbf{I}_N$ is an identity matrix.

Then, the kernel trick is employed to derive the relationship:

$$\Omega_{kj} = \varphi(\mathbf{x}_k)^T \varphi(\mathbf{x}_j) = K(\mathbf{x}_k, \mathbf{x}_j), \quad k, j = 1, 2, \ldots, N \tag{3.12}$$

where $K(\cdot)$ is a predefined kernel function. The role of the kernel function is to avoid explicit computation of the map $\varphi(\cdot)$ in dealing with the high-dimensional feature space.

Calculating b and $\boldsymbol{\alpha}$ from Eq. (3.11), the solution to the regression problem is obtained below:

$$\hat{h}(\mathbf{x}) = \sum_{k=1}^{N} \alpha_k K(\mathbf{x}, \mathbf{x}_k) + b \tag{3.13}$$

where $K(\cdot)$ is the kernel function satisfying Mercer's condition, $\mathbf{x}_k$ is the training data, and $\mathbf{x}$ denotes the new input data.

By employing the radial basis function (RBF) as kernel function,

$$K(\mathbf{x}, \mathbf{x}_k) = \exp\left(-\frac{\|\mathbf{x} - \mathbf{x}_k\|^2}{\sigma^2}\right) \tag{3.14}$$

where $\sigma > 0$ denotes the width parameter (which specifies the kernel sample variance σ^2) and $\|\cdot\|$ represents the Euclidean distance, and the LSSVM model for the hysteresis model estimation becomes

$$\hat{h}(\mathbf{x}) = \sum_{k=1}^{N} \alpha_k \exp\left(-\frac{\|\mathbf{x} - \mathbf{x}_k\|^2}{\sigma^2}\right) + b. \tag{3.15}$$

Assigning the regularization parameter Γ and kernel parameter σ, the objective of training process is to determine the support values α_k and the bias b. The high generalization ability of the LSSVM model relies on appropriate tuning of these two hyperparameters (Γ and σ). Here, the leave-one-out cross-validation approach is adopted to infer the values of the hyperparameters.

3.4 Experimental Studies on Hysteresis Identification

In this section, the hysteresis identification processes with Bouc–Wen model and LSSVM model are carried out through experimental studies.

3.4.1 Experimental Setup

The experimental setup is depicted in Fig. 3.1. A four-layer piezoelectric bimorph actuator (model: T434-A4-201, from Piezo Systems, Inc.) with the dimension of $28 \times 5 \times 0.86\,\text{mm}^3$ is selected. The actuator is fabricated from the piezo-material of Industry Type 5A (Navy Type II), and its key parameters are shown in Table 3.1. A USB-6259 board (from National Instruments Corp.) equipped with 16-bit D/A and A/D converters is adopted to produce an analog voltage, which is then amplified by a high-voltage amplifier (model: EPA-104, from Piezo Systems, Inc.) to provide a voltage of ±200 V for the drive of the piezoelectric actuator. The output displacement at the end point of piezo-bimorph is measured by a laser displacement sensor (model: LK-H055, from Keyence Corp.). The analog output voltage of the sensor

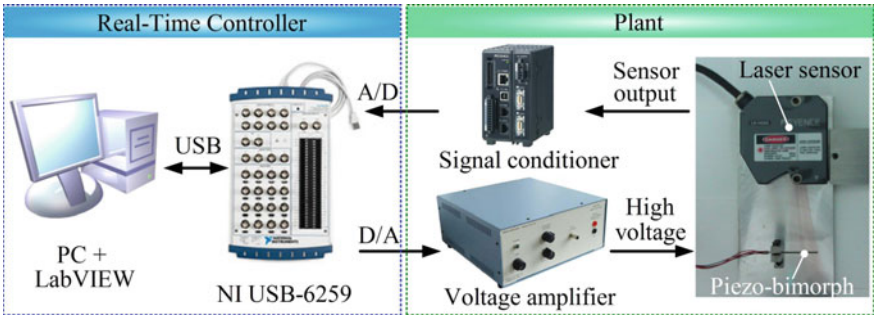

Fig. 3.1 Experimental setup of a piezoactuated system

Table 3.1 Main parameters of the piezoelectric bimorph actuator

Specification	Parameter
Mass	1.8×10^{-3} kg
Stiffness	1.4×10^{3} N/m
Capacitance	77 nF
Maximum voltage	±90 V
Resonant frequency	440 Hz
Free deflection	±262 μm
Blocked force	±0.36 N

signal conditioner is acquired by a PC through one A/D channel of the USB-6259 board. LabVIEW™ software is adopted to implement a real-time control of the piezoactuated system.

3.4.2 Dynamics Model Identification

Prior to the development of hysteresis models, a linear dynamics model of the system plant is identified by the frequency response approach. Specifically, swept-sine waves with an amplitude of 0.5 V and the frequency range of 1–1000 Hz are produced to drive the piezo-bimorph. The position responses of the piezoelectric actuator are recorded using a sampling rate of 2 kHz. The input–output data sets are used to identify the plant transfer function by estimating the model from the frequency response data. Figure 3.2 depicts the results of frequency responses obtained by experiment and the identified model (3.16):

$$G(s) = \frac{1.247 \times 10^7}{s^2 + 1.847s + 6.477 \times 10^6}. \tag{3.16}$$

It is found that the first resonant mode occurs around 404 Hz. The identified second-order model well captures the system dynamics in terms of magnitude and phase at frequencies below 600 and 100 Hz, respectively, that is, the second-order model cannot properly describe the phase behavior about 100 Hz. It implies that a model of much higher order is required to capture the high-frequency dynamics

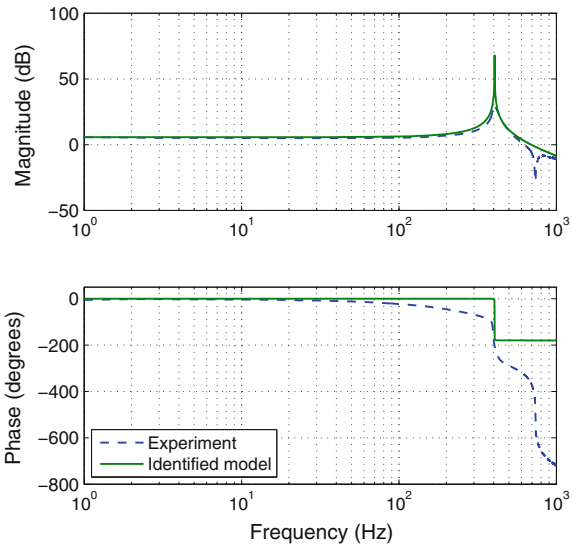

Fig. 3.2 System frequency response obtained by experimental study and the identified second-order model

more accurately. Here, a simple second-order model is employed to demonstrate the effectiveness of the reported hysteresis identification scheme.

3.4.3 Bouc–Wen Model Results

Regarding the dynamics parameters, the mass is taken as the nominal value $M = 1.8 \times 10^{-3}$ kg as shown in Table 3.1. Additionally, by neglecting the nonlinear term H in Eq. (3.1), taking the Laplace transform and comparing the parameters with Eq. (3.16), the damping coefficient and stiffness values are calculated as $B = 3.3 \times 10^{-3}$ N·s/m and $K = 1.1659 \times 10^{4}$ N/m, respectively. Other parameters are identified below.

3.4.3.1 Bouc–Wen Model Identification

To identify the Bouc–Wen hysteresis model, various types of signals can be utilized. Without loss of generality, an input voltage signal as shown in Fig. 3.3a is chosen for the purpose of model identification:

$$u(t) = 50e^{-0.13t}[\cos(3\pi t e^{-0.09t} - 3.15) + 1.0]. \tag{3.17}$$

By applying the signal to the piezoelectric bimorph actuator, the position output is generated as depicted in Fig. 3.3b.

By selecting a time interval of 0.02 s, 500 training data sets are acquired as shown in Fig. 3.3a, b. The Bouc–Wen model is then identified by optimizing the four parameters so as to minimize the objective function (3.3). In particular, the particle swarm optimization (PSO) is adopted for the function minimization, and the optimum parameters are obtained as $D = 2.4373 \times 10^{-6}$ m/V, $\alpha = 0.1947$, $\beta = 3.3626$, and $\gamma = -2.8526$.

It is notable that the optimized piezoelectric coefficient $D = 2.4373$ μm/V deviates a little from the nominal value $D = 2.91$ μm/V calculated from Table 3.1. The discrepancy can be explained by examining the experimental setup as shown in Fig. 3.1. Owing to an offset of the laser measuring point away from the free end of the bimorph, the actual length of the bimorph is less than the nominal value of 28 mm. Thus, the optimized D is slightly less than the nominal value.

3.4.3.2 Modeling Results

The results obtained by experiment and the Bouc–Wen model simulation are compared in Fig. 3.3b–d. It is observed that the Bouc–Wen model cannot describe the complicated hysteresis behavior of the piezoactuated system exactly. A relatively large error exists between the model output and experimental result as shown in

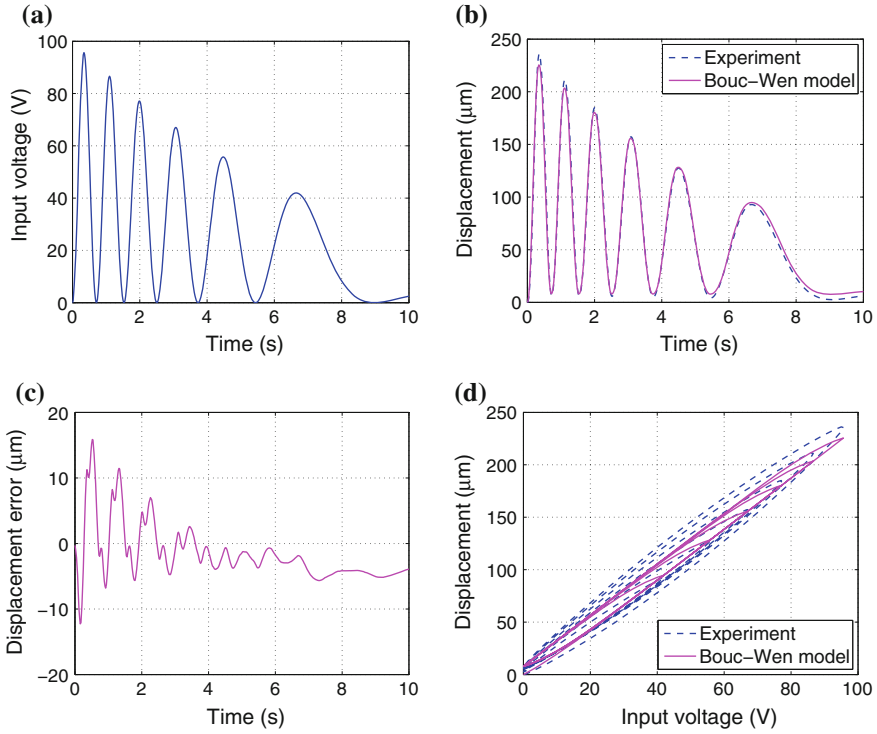

Fig. 3.3 Results of the identified Bouc–Wen model. **a** Input voltage. **b** Experimental result and Bouc–Wen model output. **c** Bouc–Wen model output errors. **d** Displacement–voltage hysteresis loops

Fig. 3.3c. The maximum model error is 15.56 μm, which accounts for 6.6 % of the travel range of the piezoelectric actuator. Based on the displacement error $e = y_d - y$, the root-mean-square error (RMSE) is defined as follows:

$$\text{RMSE} = \sqrt{\frac{1}{N_t}\sum_{i=1}^{N_t} e_i^2} \tag{3.18}$$

where $N_t = 500$ is the number of test data sets.

The identified Bouc–Wen model produces a RMSE of 4.43 μm, which accounts for 1.9 % of the travel range of the piezo-actuator. When the input has lower magnitude and frequency, a smaller model error is produced. Hence, the model error varies greatly at different amplitudes and frequencies of the input signal, which indicates that the Bouc–Wen model cannot capture the rate dependency of the hysteresis.

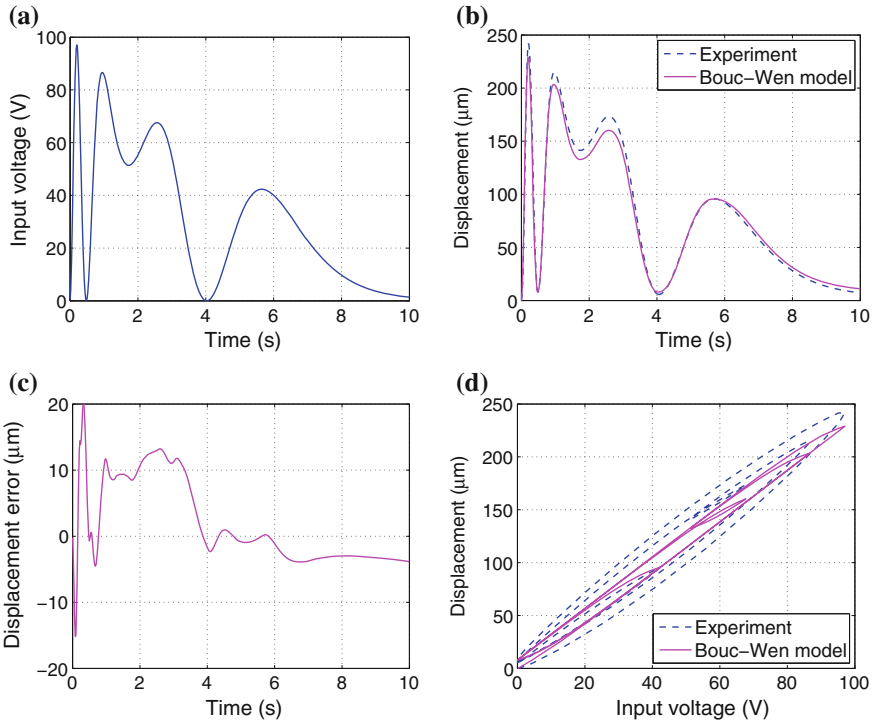

Fig. 3.4 Testing result #1 of the Bouc–Wen model. **a** Input voltage. **b** Experimental result and Bouc–Wen model output. **c** Bouc–Wen model output errors. **d** Displacement–voltage hysteresis loops

3.4.3.3 Generalization Study

In order to test the generalization capability of the Bouc–Wen model, two new input signals are selected as shown in Figs. 3.4a and 3.5a.

For the test signal #1, the model output is depicted in Fig. 3.4b–d. The discrepancy between the model result and the obtained actual output (y_d) by experiment is illustrated in Fig. 3.4c. It is observed that the Bouc–Wen model produces a RMSE of 6.78 μm, which accounts for 2.8 % of the motion range. Hence, as compared with the training error (1.9 %), the Bouc–Wen model gives a much worse testing result even with a simple test signal.

With a more complex test signal #2, the model output is described in Fig. 3.5b–d. It is found that the Bouc–Wen model creates a RMSE of 4.73 μm, i.e., 1.9 % of the motion range. Hence, as compared with the training result, the Bouc–Wen model obtains a slightly larger testing error for the test signal #2.

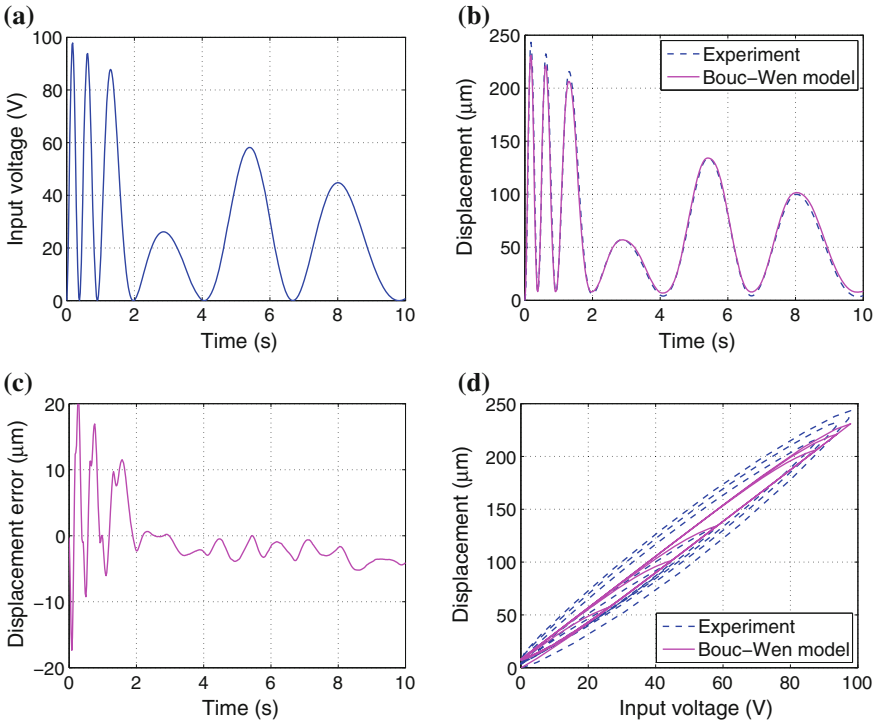

Fig. 3.5 Testing result #2 of the Bouc–Wen model. **a** Input voltage. **b** Experimental result and Bouc–Wen model output. **c** Bouc–Wen model output errors. **d** Displacement–voltage hysteresis loops

3.4.4 LSSVM Model Results

Taking the Laplace transform of Eq. (3.5) and comparing its parameters with Eq. (3.16), the following parameters are obtained: $\omega = 2.5450 \times 10^3$ rad/s, $\xi = 3.6287 \times 10^{-4}$, and $d = 12.47$ m/s^2 − V.

3.4.4.1 LSSVM Modeling

For the training of LSSVM model, the same exciting voltage signal as shown in Eq. (3.17) is employed, which is depicted in Fig. 3.3a. In order to identify the hysteresis behavior accurately based on LSSVM model, a suitable input vector (3.9) requires to be determined.

By selecting three types of input variables with different orders defined by m, n, and l, three LSSVM models are trained using the corresponding input and output variables. The output variable is taken as the hysteresis term as shown in Fig. 3.6a, which is obtained by resorting to Eq. (3.6).

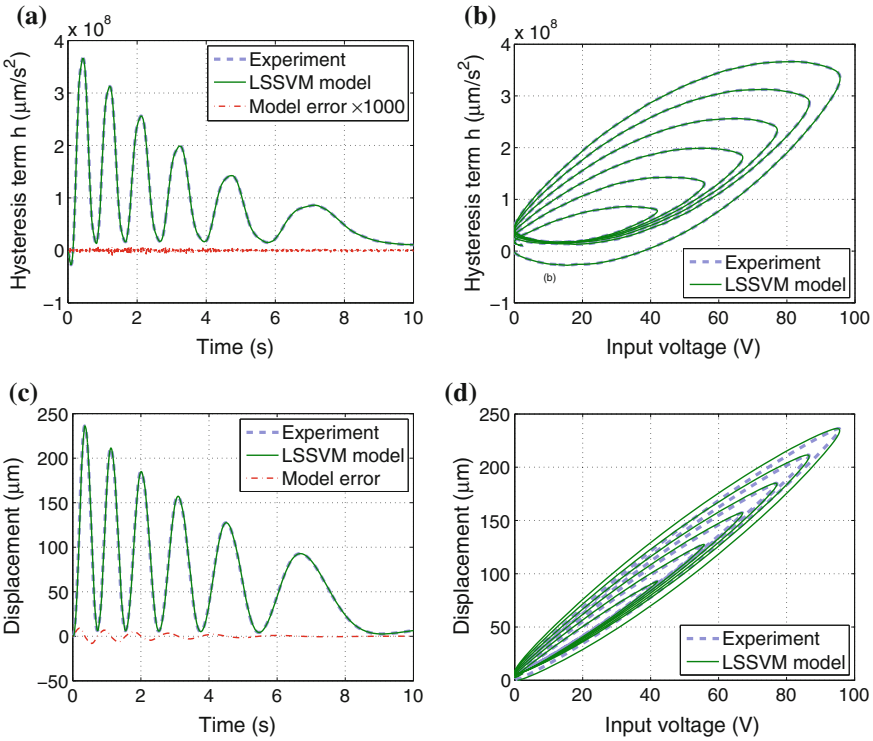

Fig. 3.6 Training result of LSSVM model III. **a** Experimental result and LSSVM model output for hysteresis term h. **b** h versus input voltage. **c** Experimental result and LSSVM model result for displacement y. **d** Displacement y versus input voltage

The LSSVM model I only takes the voltage and hysteresis terms as the input variables with $m = 2$, $n = 0$, and $l = 2$. Similarly, LSSVM model II only considers the position and hysteresis terms as the input variables with $m = 0$, $n = 2$, and $l = 2$. In contrast, by choosing the voltage, position, and hysteresis terms as input variables, LSSVM model III is constructed with $m = 2$, $n = 2$, and $l = 2$. Results show that further increase of the orders does not lead to significant improvement on the modeling accuracy.

For example, the training results of LSSVM model III are shown in Fig. 3.6. Using the test signal #1 as shown in Fig. 3.4a and test signal #2 as shown in Fig. 3.5a, the testing results are depicted in Figs. 3.7 and 3.8, respectively. In addition, the training and testing results of Bouc–Wen model and the three LSSVM models are compared in Table 3.2. Evidently, each LSSVM model achieves a better identification result than the Bouc–Wen model.

By comparing the results of models I and II, it is found that model II produces much better testing results than model I for both test signals. This indicates that the position is better than voltage as input variables. Moreover, among the three

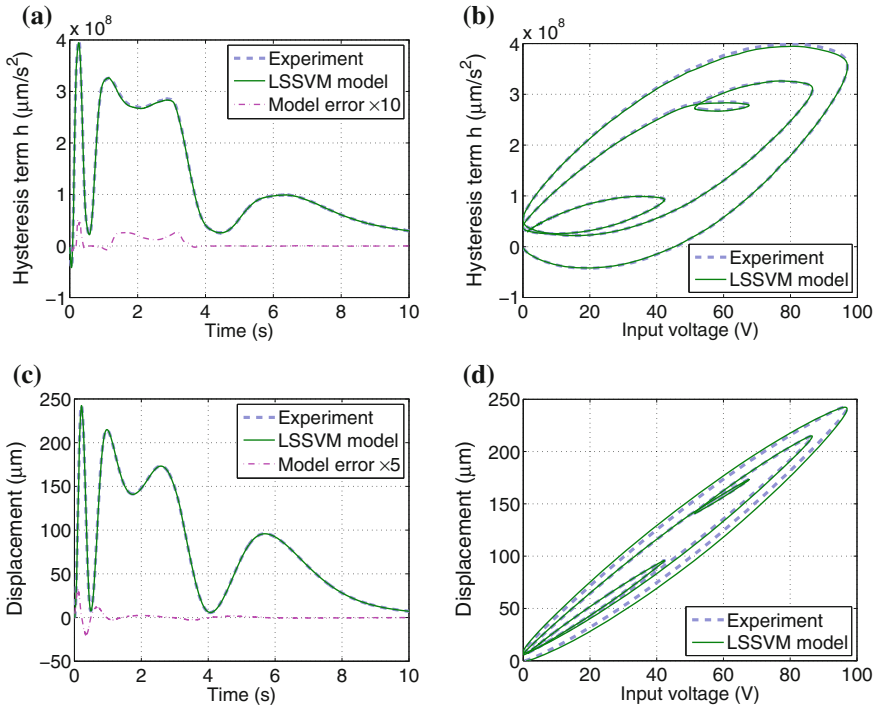

Fig. 3.7 Testing result #1 of LSSVM model III. **a** Experimental result and LSSVM model output for hysteresis term h. **b** h versus input voltage. **c** Experimental result and LSSVM model result for displacement y. **d** Displacement y versus input voltage

LSSVM models, the LSSVM model III produces the best results in terms of lower modeling errors for both hysteresis term h and output position y. Specifically, the model III produces a negligible training RMSE for the hysteresis term h, which leads to a percent RMSE of 1.05 % for the output position y. With the test signal #1, the LSSVM model III gives a RMSE of 0.27 % for h, which results in a 0.35 % RMSE for the output position y. Using the test signal #2, it produces 0.15 % and 0.50 % RMSE for the hysteresis term h and output position y, respectively.

Owing to a better performance, the LSSVM model III is chosen for a further comparison study with respect to the identified Bouc–Wen model. Results show that the LSSVM model has reduced the testing errors of output position by 87.4 % and 74.3 % in comparison with the Bouc–Wen model for the test signals #1 and #2, respectively. Hence, the hysteresis identification results demonstrate the effectiveness of LSSVM model.

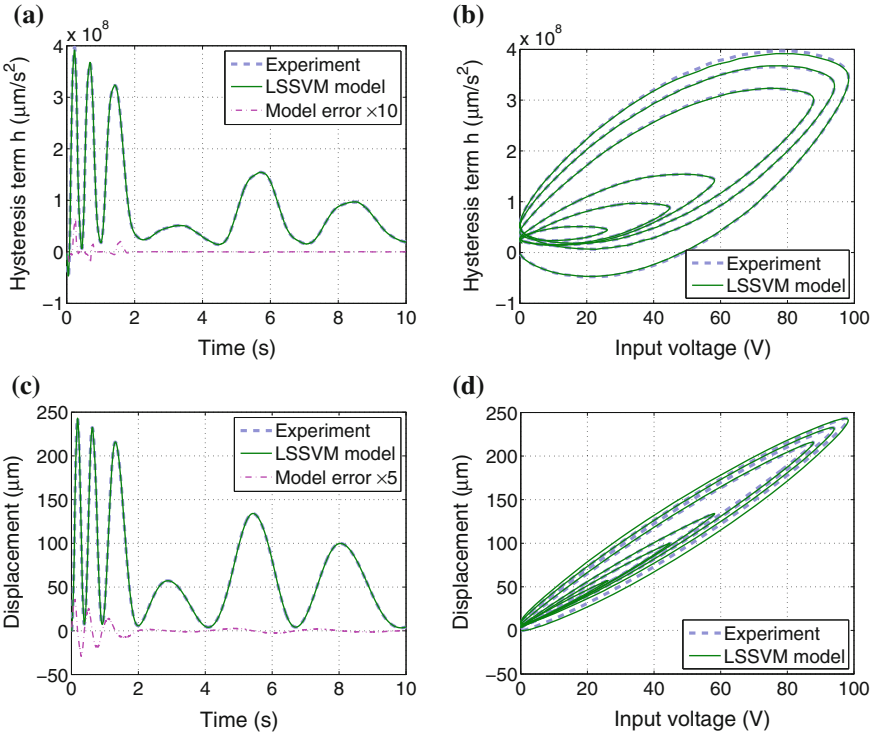

Fig. 3.8 Testing result #2 of LSSVM model III. **a** Experimental result and LSSVM model output for hysteresis term h. **b** h versus input voltage. **c** Experimental result and LSSVM model result for displacement y. **d** Displacement y versus input voltage

Table 3.2 Training and testing results of Bouc–Wen model and LSSVM models

Model	Input variable	Training RMSE (%)		Testing RMSE (%)			
				Trajectory 1		Trajectory 2	
		h	y	h	y	h	y
Bouc–Wen model	–	–	1.88	–	2.80	–	1.95
LSSVM model I	$m = 2$, $n = 0$, $l = 2$	0.0391	1.05	3.62	0.79	3.04	0.62
LSSVM model II	$m = 0$, $n = 2$, $l = 2$	0.0075	1.05	0.19	0.36	0.21	0.51
LSSVM model III	$m = 2$, $n = 2$, $l = 2$	0.0005	1.05	0.27	0.35	0.15	0.50

3.5 Experimental Studies on Hysteresis Compensation

In this section, the control schemes based on the developed Bouc–Wen model and LSSVM model are realized to compensate for the rate-dependent hysteresis effect. The real-time control in the experimental studies is implemented with a sampling time of 0.004 s.

3.5.1 Feedforward Compensation

To compensate for the hysteresis nonlinearity, a feedforward (FF) control (3.4) based on the Bouc–Wen model is first implemented. The block diagram of LSSVM model-based FF control is depicted in Fig. 3.9, where the control signal u_{FF} is obtained by Eq. (3.7). It is seen that only the hysteresis model is needed, whereas no inverse hysteresis model is required to implement the FF compensation.

In order to demonstrate the performances of the Bouc–Wen model and LSSVM model for the purpose of hysteresis compensation, a series of experimental studies are performed. For instance, concerning a desired 2-Hz sinusoidal position trajectory as shown in Fig. 3.10a, the FF control results of Bouc–Wen model and LSSVM model are illustrated in Fig. 3.10a, c, and the tracking errors are compared in Fig. 3.10b. The control actions are shown in Fig. 3.10d. The control results are summarized in Table 3.3, where the hysteresis width is defined as the ratio between the maximum discrepancy of the ascending and descending curves of hysteresis loop and the output motion range.

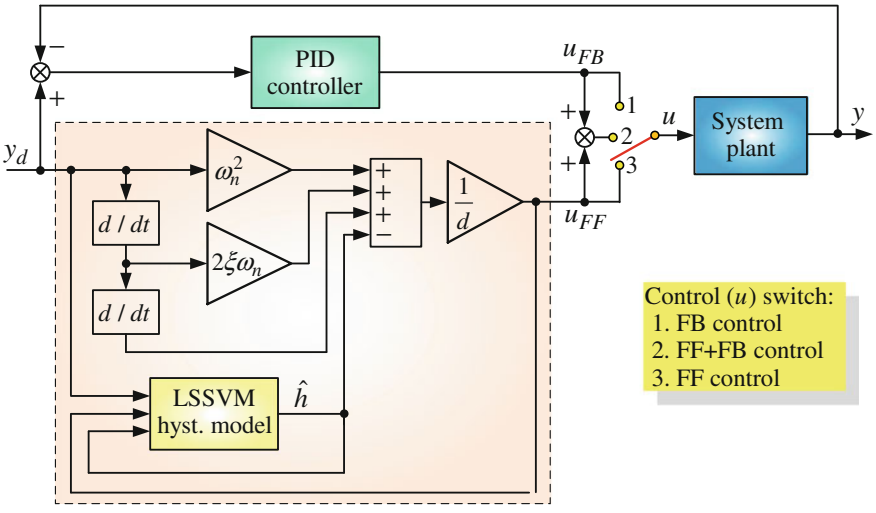

Fig. 3.9 Block diagram of LSSVM hysteresis model-based control schemes

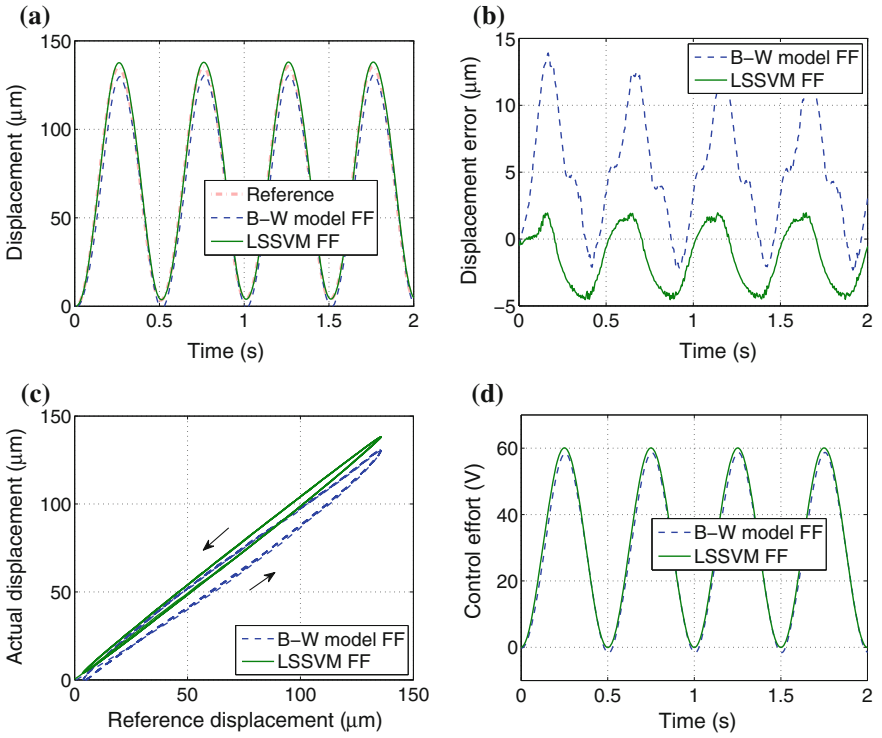

Fig. 3.10 Motion tracking results of the FF compensation. **a** Reference and experimental results of Bouc–Wen and LSSVM models. **b** Tracking errors. **c** Actual–reference displacement hysteresis loops. **d** Control actions

Table 3.3 Hysteresis compensation results of different control schemes

Controller	RMSE		Hysteresis width	RMS control action
	(μm)	(%)	(%)	(V)
PID FB	0.04	1.05	14.29	3.62
Bouc–Wen FF	6.76	4.98	10.20	3.47
LSSVM FF	2.55	1.88	4.29	3.72
Bouc–Wen FF+FB	1.55	1.14	2.23	3.65
LSSVM FF+FB	0.62	0.46	0.45	3.64

Results show that the Bouc–Wen FF control produces a RMSE of 6.76 μm, i.e., 5.0 % of motion range, and the LSSVM-based FF control produces a 2.55-μm RMSE, i.e., 1.9 % of motion range. As compared with Bouc–Wen model, the LSSVM model suppresses the tracking error furthermore by 62 %, which leads to a 58 % reduction

of the hysteresis width. Hence, the superiority of LSSVM over Bouc–Wen model in FF hysteresis compensation is validated by the experimental results. Moreover, the LSSVM model requires 7.2 % higher RMS control action than Bouc–Wen model for FF compensation.

3.5.2 Feedforward Plus Feedback Control

In order to further suppress the residual tracking errors of the feedforward compensation, a FF augmented with feedback (FB) control is realized. Owing to its popularity, the digital PID algorithm is employed as the FB control:

$$u_{\mathrm{FB}_k} = K_p e_k + K_i \sum_{j=0}^{k} e_j + K_d (e_k - e_{k-1}) \tag{3.19}$$

where the displacement error $e_k = y_{d_k} - y_k$ with y_{d_k} and y_k representing the desired and actual system outputs at the kth time step, respectively. In addition, K_p, K_i, and K_d denote the proportional, integral, and derivative gains, respectively. The control gains are tuned by Ziegler–Nichols method through experiments.

Using the LSSVM hysteresis model, the three control schemes of FF, FB, and FF+FB can be switched easily as shown in Fig. 3.9. For the same position reference trajectory as shown in Fig. 3.10a, the tracking results of the Bouc–Wen model and LSSVM model-based FF+FB control are depicted in Fig. 3.11a–c. In addition, the stand-alone PID FB tracking error is also illustrated in Fig. 3.11b, and the control actions of the three schemes are shown in Fig. 3.11d. For a clear comparison, the control results are tabulated in Table 3.3.

Although the Bouc–Wen model-based FF+FB control reduces the tracking error to 1.55 μm (i.e., 1.14 % of motion range) and hysteresis width to 2.23 %, the LSSVM model-based one further suppresses the RMSE and hysteresis to negligible levels of 0.62 μm (i.e., 0.46 % of motion range) and 0.45 %, respectively. Thus, the LSSVM model-based hybrid control has improved the tracking accuracy and hysteresis compensation by 60 % and 80 %, respectively.

Comparing the control actions, the LSSVM model-based FF+FB control needs 0.17 % lower control voltage than the Bouc–Wen model-based one. The slight lower control effort of the former is contributed by the employed PID FB control, which produces a 2.9 % lower control action than the LSSVM model-based FF control approach, as shown in Table 3.3.

The experimental results demonstrate the effectiveness of the LSSVM model over Bouc–Wen model for the task of hysteresis compensation. The performance of the LSSVM model can be improved to achieve a better generalization ability by selecting more comprehensive input signal to excite the piezo-actuator for the model training. Moreover, to further reduce the tracking error for periodic reference inputs, repetitive control or iterative learning control algorithms can be employed.

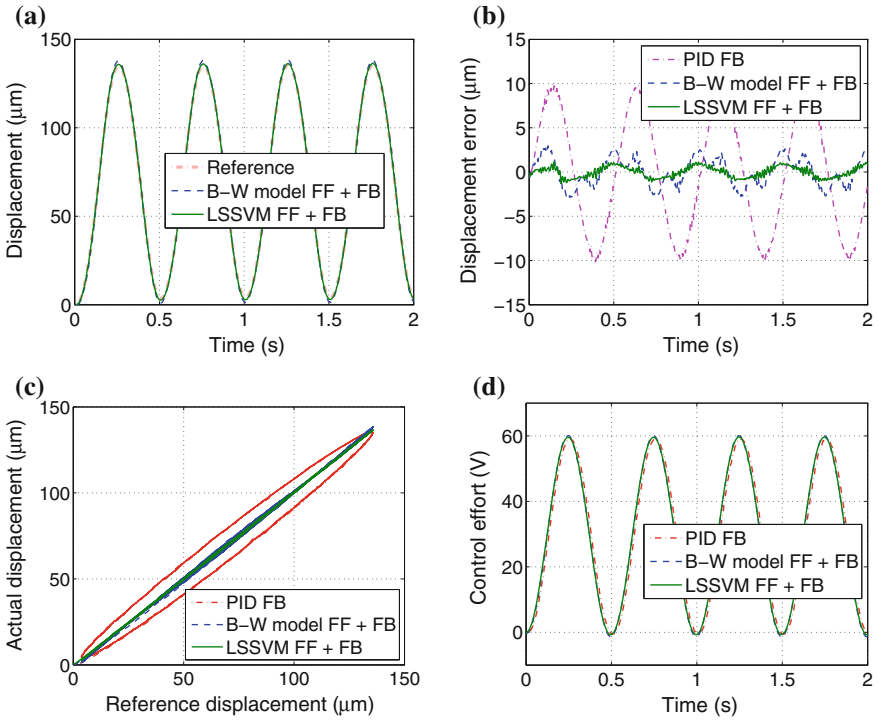

Fig. 3.11 Motion tracking results of the FF plus FB compensation. **a** Reference trajectory. **b** Tracking errors. **c** Actual–reference displacement hysteresis loops. **d** Control actions

3.6 Chapter Summary

This chapter is concentrated on hysteresis identification and compensation of a piezoelectric actuator. The nonlinear hysteresis behavior has been well identified by resorting to a developed LSSVM-based intelligent hysteresis model. It has been shown that the position information is better than voltage information as input variables in hysteresis model development. Moreover, the model can be directly employed to compensate for the hysteresis effect without modeling the inverse hysteresis. This indicates that the established single hysteresis model is used for both hysteresis identification and compensation, which is more computationally efficient than the existing approaches where both a hysteresis model and an inverse hysteresis model are employed. Experimental results demonstrate that the LSSVM model is superior to Bouc–Wen model in terms of both hysteresis identification accuracy and hysteresis compensation effectiveness. The presented idea can also be extended to hysteresis identification and compensation of other types of smart actuators.

References

1. Chen, X., Hisayama, T.: Adaptive sliding-mode position control for piezo-actuated stage. IEEE Trans. Ind. Electron. **55**(11), 3927–3934 (2008)
2. Janaideh, M.A., Rakheja, S., Su, C.Y.: Experimental characterization and modeling of rate-dependent hysteresis of a piezoceramic actuator. Mechatronics **19**(5), 656–670 (2009)
3. Li, Y., Xu, Q.: Adaptive sliding mode control with perturbation estimation and PID sliding surface for motion tracking of a piezo-driven micromanipulator. IEEE Trans. Control Syst. Technol. **18**(4), 798–810 (2010)
4. Lin, C.J., Chen, S.Y.: Evolutionary algorithm based feedforward control for contouring of a biaxial piezo-actuated stage. Mechatronics **19**(6), 829–839 (2009)
5. Rakotondrabe, M.: Bouc-Wen modeling and inverse multiplicative structure to compensate hysteresis nonlinearity in piezoelectric actuators. IEEE Trans. Autom. Sci. Eng. **8**(2), 428–431 (2011)
6. Wong, P.K., Xu, Q., Vong, C.M., Wong, H.C.: Rate-dependent hysteresis modeling and control of a piezostage using online support vector machine and relevance vector machine. IEEE Trans. Ind. Electron. **59**(4), 988–2001 (2012)
7. Xu, Q., Wong, P.K.: Hysteresis modeling and compensation of a piezostage using least squares support vector machines. Mechatronics **21**(7), 1239–1251 (2011)
8. Yu, S., Alici, G., Shirinzadeh, B., Smith, J.: Sliding mode control of a piezoelectric actuator with neural network compensating rate-dependent hysteresis. In: Proceedings of the IEEE International Conference on Robotics and Automation, pp. 3641–3645. Barcelona, Spain (2005)

Part II
Hysteresis-Model-Free, State-Observer-Based Feedback Control

Chapter 4
Model Predictive Discrete-Time Sliding-Mode Control

This chapter presents a scheme of model predictive discrete-time sliding mode control (MPDTSMC) with proportional-integral (PI) sliding function and state observer for the motion tracking control of a nanopositioning system driven by piezoelectric actuators. One distinct advantage of the controller is that its implementation only requires a simple second-order model of the system, whereas it does not need to know the hysteresis model and the bounds on system uncertainties. The reasons why the model predictive control methodology and PI action can eliminate the chattering effects and produce a low level of tracking error are addressed in the state-space framework. Experimental investigations are carried out to verify the feasibility of the control scheme.

4.1 Introduction

Due to the low damping of the piezoelectric micro-/nano-positioning system, a number of vibration modes exist and a high-order model is commonly identified, which results in a high-order controller as a consequence. From the practical point of view, a linear model of low order, e.g., second order, is very desirable for easy implementation of control strategies. However, the adoption of a low-order model means that the residual modes will not be considered in the controller and observer design. The neglect of residual modes may cause both control spillover and observation spillover [17]. Spillover is undesirable because it may induce system instability and performance degradation [20]. In view of these issues, it is a major challenge in piezostate control by employing a low-order model without modeling the complicated hysteresis effects.

In the literature, some pioneer works have been conducted to deal with the piezoelectric micro-/nano-positioning control problem by employing a low-order linear model. For example, by identifying a second-order model of a piezostage, a precise

© Springer International Publishing Switzerland 2016

Q. Xu and K.K. Tan, *Advanced Control of Piezoelectric Micro-/Nano-Positioning Systems*, Advances in Industrial Control,
DOI 10.1007/978-3-319-21623-2_4

control is implemented in [26] based on the integral resonant control method, in which the charge actuation is employed to reduce piezoelectric hysteresis. Although the hysteresis becomes almost negligible if a piezoelectric actuator is driven by a charge source, the stroke will be reduced as the cost. Hence, voltage actuation is still widely adopted in practice. An enhanced adaptive sliding-mode motion tracking control is reported in [15] for a piezoelectrically actuated system, which only uses a second-order dynamics model. However, the sliding-mode control (SMC) is designed based on the continuous-time dynamics model, and the uncertainty bounds are required to implement the controller. Based on the second-order dynamics model of a piezoelectric actuator (PEA), a model predictive sliding-mode control is presented in [9], where a nonlinear, energy-based model is employed to construct an inverse compensator of the hysteresis. The same model predictive-based control is also adopted in [16] for the force control of a piezoelectric actuator. In the previous works, a SMC controller is designed based on a proportional-type sliding function, whereas no stability analysis of the control system is given. Besides, the spillover effects are not treated explicitly. Based on a second-order mass–spring–damper model of a nanopositioning system, this work presents a MPDTSMC with PI type of sliding function, and provide stability analysis of the closed-loop system in detail. The observation spillover is suppressed by designing a proper state observer.

It is known that SMC is a popular nonlinear control approach to deal with disturbance. The discrete-time sliding-mode control (DTSMC) is presented for the implementation on sampled-data systems [3, 7]. For a discrete-time system, the strategy of model predictive control (MPC) can be employed to predict the system performance in a specified time in the future and to produce an optimal control action with respect to a predefined cost criterion at each time step [21]. By combining the SMC and MPC techniques, model predictive sliding-mode control has been recently proposed to achieve the advantages of both methods [8, 23]. Although the combined control has been adopted in a few of previous works [9, 16] for the control of PEA by suppressing the chattering phenomenon, it still remains unclear why the MPC methodology can eliminate the chattering phenomenon in the sliding mode.

This chapter shows that the MPDTSMC with the PI action drives the system state to slide in a vicinity of the sliding surface with a boundary layer of thickness $O(T^3)$ [1], which is much lower than a commonly designed DTSMC with $O(T)$ boundary layer in the sliding mode. In addition, the state tracking error of the order $O(T^2)$ is achieved with the presented control scheme. The theoretical analysis and the effectiveness of the PI action in the control scheme are verified by conducting experimental studies on a nanopositioning platform.

4.2 Problem Formulation

4.2.1 Dynamics Modeling of a Nanopositioning System

The entire dynamics model of a piezoelectric nanopositioning system with nonlinear hysteresis can be established as follows:

$$m\ddot{x}(t) + b\dot{x}(t) + kx(t) = du(t) - f_h(t) \tag{4.1}$$

where t is the time variable, parameters m, b, k, and x represent the mass, damping coefficient, stiffness, and output displacement of the nanopositioning stage, respectively; d is the piezoelectric coefficient, u denotes the input voltage, and f_h describes the hysteretic effect of the system in terms of force which is not modeled in this research.

The dynamics model (4.1) can be expressed in the state-space form:

$$\dot{\mathbf{X}}(t) = \mathbf{A}_c\mathbf{X}(t) + \mathbf{B}_c u(t) + \mathbf{D}_c f_h(t) \tag{4.2}$$

$$\mathbf{Y}(t) = \mathbf{C}\,\mathbf{X}(t) \tag{4.3}$$

where the state vector $\mathbf{X}(t) = [x(t), \dot{x}(t)]^T$, the unmodeled hysteresis effect f_h is considered as a disturbance to the system, and the four matrices are

$$\mathbf{A}_c = \begin{bmatrix} 0 & 1 \\ -\frac{k}{m} & -\frac{b}{m} \end{bmatrix},\ \mathbf{B}_c = \begin{bmatrix} 0 \\ \frac{d}{m} \end{bmatrix},\ \mathbf{D}_c = \begin{bmatrix} 0 \\ -\frac{1}{m} \end{bmatrix},\ \mathbf{C} = [1\ \ 0]\,. \tag{4.4}$$

It is observed that the disturbance f_h satisfies the matching condition, i.e., $\mathbf{D}_c = \delta_d \mathbf{B}_c$ where $\delta_d = -\frac{1}{d}$ is a scalar.

Using a sampling time T, the continuous-time system model given by Eqs. (4.2) and (4.3) can be discretized as:

$$\mathbf{X}_{k+1} = \mathbf{A}\mathbf{X}_k + \mathbf{B}u_k + \mathbf{f}_k \tag{4.5}$$

$$\mathbf{Y}_k = \mathbf{C}\mathbf{X}_k \tag{4.6}$$

where the notation $\mathbf{X}_k = \mathbf{X}(kT)$ and the corresponding matrices are calculated by:

$$\mathbf{A} = e^{\mathbf{A}_c T} \tag{4.7}$$

$$\mathbf{B} = \int_0^T e^{\mathbf{A}_c \tau} d\tau \mathbf{B}_c \tag{4.8}$$

$$\mathbf{f}_k = \int_0^T e^{\mathbf{A}_c \tau} \delta_d \mathbf{B}_c f_h((k+1)T - \tau) d\tau \tag{4.9}$$

which indicate that both $\mathbf{B}$ and $\mathbf{f}_k$ are $O(T)$, i.e., the order of T.

In addition, two useful properties are employed to facilitate the control design [24, 25].

Property 4.1 *$d_k = O(T)$, $d_k - d_{k-1} = O(T^2)$, and $d_k - 2d_{k-1} + d_{k-2} = O(T^3)$.*

Property 4.2 *Assume $E_{k+1} = \Xi E_k + \delta_k$ where matrix Ξ is asymptotically stable ($\|\Xi\| < 1$), and the magnitude of δ_k is of the order $O(T^r)$ where r is an integer. Then the ultimate bound of E_k is of the order $O(T^{r-1})$ when $k \to \infty$.*

The proof of Property 4.2 is given as follows.

Proof Assume that m eigenvalues of Ξ are deadbeat, i.e., Ξ has m poles locating at the origin. Then, Ξ can be written as [1]

$$\Xi = PJP^{-1} \tag{4.10}$$

where P is a transformation matrix and J is the Jordan matrix of the eigenvalues of Ξ.

The matrix J can be expressed as

$$J = \begin{bmatrix} J_1 & 0 \\ 0 & J_2 \end{bmatrix} \tag{4.11}$$

where $J_1 \in R^{m\times m}$ and $J_2 \in R^{(n-m)\times(n-m)}$ taking on the forms:

$$J_1 = \begin{bmatrix} 0 & I_{m-1} \\ 0 & 0 \end{bmatrix} \tag{4.12}$$

$$J_2 = \begin{bmatrix} \lambda_{m+1} & & 0 \\ & \ddots & \\ 0 & & \lambda_n \end{bmatrix} \tag{4.13}$$

where λ_j denote the poles of Ξ.

For simplicity, it is assumed that the nonzero poles are designed to be distinct and their continuous-time counterparts are of the order $O(1)$. Then, the solution of $E_{k+1} = \Xi E_k + \delta_k$ can be derived as:

$$E_k = PJ^kP^{-1}E_0 + P\left(\sum_{i=0}^{k-1} J^iP^{-1}\delta_{k-i-1}\right) \tag{4.14}$$

which can be rewritten as

$$E_k = PJ^kP^{-1}E_0 + P\left(\sum_{i=0}^{k-1}\begin{bmatrix} J_1^i & 0 \\ 0 & 0 \end{bmatrix}P^{-1}\delta_{k-i-1}\right) + P\left(\sum_{i=0}^{k-1}\begin{bmatrix} 0 & 0 \\ 0 & J_2^i \end{bmatrix}P^{-1}\delta_{k-i-1}\right). \tag{4.15}$$

In view of $J_1^i = 0$ for $i \geq m$, Eq. (4.15) can be expressed into the following form for $k \geq m$:

$$E_k = PJ^kP^{-1}E_0 + P\left(\sum_{i=0}^{m}\begin{bmatrix} J_1^i & 0 \\ 0 & 0 \end{bmatrix} P^{-1}\delta_{k-i-1}\right) + P\left(\sum_{i=0}^{k-1}\begin{bmatrix} 0 & 0 \\ 0 & J_2^i \end{bmatrix} P^{-1}\delta_{k-i-1}\right). \tag{4.16}$$

Taking into account $\|J_1\| = 1$ and $\|J_2\| = \lambda_{\max} = \max\{\lambda_{m+1}, \ldots, \lambda_n\}$ with $\|\cdot\|$ denoting $\|\cdot\|_2$, Eq. (4.16) leads to

$$\begin{aligned} \|E_k\| \leq \|P\| \Bigg(& \sum_{i=0}^{m} \left\| \begin{bmatrix} J_1 & 0 \\ 0 & 0 \end{bmatrix} \right\|^i \|P^{-1}\| \, \|\delta_{k-i-1}\| \\ & + \sum_{i=0}^{k-1} \left\| \begin{bmatrix} 0 & 0 \\ 0 & J_2 \end{bmatrix} \right\|^i \|P^{-1}\| \, \|\delta_{k-i-1}\| \Bigg). \end{aligned} \tag{4.17}$$

Considering that the matrix Ξ is asymptotically stable, $\lambda_{\max} < 1$ holds, then

$$\sum_{i=1}^{m} \|J_1\|^i = m, \quad \sum_{i=1}^{\infty} \|J_2\|^i = \frac{1}{1-\lambda_{\max}}. \tag{4.18}$$

Using the Tustin approximation

$$\begin{aligned} \lambda_{\max} &= \frac{2+Tp}{2-Tp} \\ \Rightarrow \frac{1}{1-\lambda_{\max}} &= \frac{1}{1-\frac{2+Tp}{2-Tp}} = \frac{2-Tp}{-2Tp} = O(T^{-1}) \end{aligned} \tag{4.19}$$

where $p = O(1)$ is the corresponding pole in continuous-time.

Assuming that $m = O(1)$ and considering $\|P^{-1}\| = \|P\|^{-1}$, the ultimate bound of E_k can be deduced from Eq. (4.17):

$$\begin{aligned} \lim_{k\to\infty} \|E_k\| &\leq O(1) \cdot O(T^r) + O(T^{-1}) \cdot O(T^r) \\ &\approx O(T^r) + O(T^{r-1}) \\ &\approx O(T^{r-1}). \end{aligned} \tag{4.20}$$

4.2.2 Sliding-Mode Controller Design

Most of the existing works construct a discrete-time sliding-mode controller using a proportional sliding function defined based on the system state only [3, 7, 19],

which leads to the order reduction of the system. A few of previous studies employ the integral term in the sliding surface [1, 24]. In this work, a PI-type sliding surface is defined in order to speed up the system response.

By assigning a vector of state error

$$\mathbf{E}_k = \mathbf{X}_k - \mathbf{X}_k^d \tag{4.21}$$

where $\mathbf{X}_k^d$ denotes the desired system state, a PI-type sliding function is defined as follows:

$$S_k = \mathbf{G}\mathbf{E}_k + \mathbf{K}_I \boldsymbol{\xi}_k \tag{4.22}$$

where

$$S = \{S_k | S_k = 0, \text{ for } k = 0, 1, \dots\} \tag{4.23}$$

represents the sliding surface or sliding hyperplane, and the integral error vector is defined as follows:

$$\boldsymbol{\xi}_k = \mathbf{E}_k + \boldsymbol{\xi}_{k-1}. \tag{4.24}$$

In addition, $\mathbf{G}$ and $\mathbf{K}_I$ are constant proportional and integral gain vectors, which are designed to assign appropriate eigenvalues for the system.

In view of Eqs. (4.21) and (4.5), one gets

$$\begin{aligned} \mathbf{E}_{k+1} &= \mathbf{X}_{k+1} - \mathbf{X}_{k+1}^d \\ &= \mathbf{A}\mathbf{X}_k + \mathbf{B}u_k + \mathbf{f}_k - \mathbf{X}_{k+1}^d \\ &= \mathbf{A}\mathbf{E}_k + \mathbf{B}u_k + \mathbf{f}_k + \mathbf{A}\mathbf{X}_k^d - \mathbf{X}_{k+1}^d \\ &= \mathbf{A}\mathbf{E}_k + \mathbf{B}u_k + \mathbf{d}_k \end{aligned} \tag{4.25}$$

where $\mathbf{d}_k = \mathbf{f}_k + \mathbf{A}\mathbf{X}_k^d - \mathbf{X}_{k+1}^d$ denotes the overall disturbance.

Considering that the equivalent control u_k^{eq} is the solution to $\Delta S = S_{k+1} - S_k = 0$ [6], it can be deduced that

$$\begin{aligned} &\mathbf{G}\mathbf{E}_{k+1} + \mathbf{K}_I \boldsymbol{\xi}_{k+1} = S_k \\ \Rightarrow\ &\mathbf{G}\mathbf{E}_{k+1} + \mathbf{K}_I(\mathbf{E}_{k+1} + \boldsymbol{\xi}_k) = S_k \\ \Rightarrow\ &(\mathbf{G} + \mathbf{K}_I)\mathbf{E}_{k+1} + \mathbf{K}_I \boldsymbol{\xi}_k = S_k \\ \Rightarrow\ &(\mathbf{G} + \mathbf{K}_I)(\mathbf{A}\mathbf{E}_k + \mathbf{B}u_k + \mathbf{d}_k) + \mathbf{K}_I \boldsymbol{\xi}_k = S_k \end{aligned} \tag{4.26}$$

which allows the generation of an equivalent controller:

$$u_k^{eq} = -(\mathbf{G}_a\mathbf{B})^{-1}(-S_k + \mathbf{G}_a\mathbf{A}\mathbf{E}_k + \mathbf{G}_a\mathbf{d}_k + \mathbf{K}_I \boldsymbol{\xi}_k) \tag{4.27}$$

where

$$\mathbf{G}_a = \mathbf{G} + \mathbf{K}_I \tag{4.28}$$

and the disturbance $\mathbf{d}_k$ is estimated by its one-step delayed value $\mathbf{d}_{k-1}$.

Thus, Eq. (4.27) becomes

$$u_k^{eq} = -(\mathbf{G}_a\mathbf{B})^{-1}(-S_k + \mathbf{G}_a\mathbf{A}\mathbf{E}_k + \mathbf{G}_a\mathbf{d}_{k-1} + \mathbf{K}_I\boldsymbol{\xi}_k) \tag{4.29}$$

where

$$\mathbf{d}_{k-1} = \mathbf{E}_k - \mathbf{A}\mathbf{E}_{k-1} + \mathbf{B}u_{k-1} \tag{4.30}$$

is derived by noting Eq. (4.25).

4.2.3 Control Gain Design

To implement the PI sliding function, the gain vectors $\mathbf{G}$ and $\mathbf{K}_I$ should be designed such that $\mathbf{G}_a\mathbf{B}$ is invertible. Moreover, the problem of gain vector design is addressed in the following discussion to guarantee the stability of the closed-loop system.

In the ideal sliding mode, $S_{k+1} = S_k = 0$ holds. Then, Eq. (4.27) reduces to

$$u_k^{eq} = -(\mathbf{G}_a\mathbf{B})^{-1}(\mathbf{G}_a\mathbf{A}\mathbf{E}_k + \mathbf{G}_a\mathbf{d}_k + \mathbf{K}_I\boldsymbol{\xi}_k). \tag{4.31}$$

Substituting Eq. (4.31) into Eq. (4.25) leads to the closed-loop state error dynamics equation:

$$\begin{aligned}\mathbf{E}_{k+1} &= \mathbf{A}\mathbf{E}_k + \mathbf{B}u_k + \mathbf{d}_k \\ &= \mathbf{A}\mathbf{E}_k - \mathbf{B}(\mathbf{G}_a\mathbf{B})^{-1}(\mathbf{G}_a\mathbf{A}\mathbf{E}_k + \mathbf{G}_a\mathbf{d}_k + \mathbf{K}_I\boldsymbol{\xi}_k) + \mathbf{d}_k \\ &= \mathbf{U}\mathbf{E}_k - \mathbf{V}\boldsymbol{\xi}_k + \mathbf{W}\mathbf{d}_k\end{aligned} \tag{4.32}$$

where

$$\mathbf{U} = \left[\mathbf{I} - \mathbf{B}(\mathbf{G}_a\mathbf{B})^{-1}\mathbf{G}_a\right]\mathbf{A} \tag{4.33}$$

$$\mathbf{V} = \mathbf{B}(\mathbf{G}_a\mathbf{B})^{-1}\mathbf{K}_I \tag{4.34}$$

$$\mathbf{W} = \mathbf{I} - \mathbf{B}(\mathbf{G}_a\mathbf{B})^{-1}\mathbf{G}_a \tag{4.35}$$

with $\mathbf{I}$ denoting an identity matrix.

The eigenvalues of the matrices $\mathbf{U}$, $\mathbf{V}$, and $\mathbf{W}$ are the solutions of $\det(z\mathbf{I}-\mathbf{U}) = 0$, $\det(z\mathbf{I}-\mathbf{V}) = 0$, and $\det(z\mathbf{I}-\mathbf{W}) = 0$, respectively, which determine the closed-loop

dynamics behavior. To ensure the stability of the closed-loop system, the eigenvalues of the three matrices should be located inside the unit circle in the complex z-plane.

For example, the eigenvalues of the matrix $\mathbf{U}$ can be calculated as the solutions to the equation [4]:

$$\left|\begin{bmatrix} z-u_{11} & -u_{12} \\ \frac{\rho_1}{\rho_2}u_{11} & z-\frac{\rho_1}{\rho_2}u_{12} \end{bmatrix}\right| = z\left(z-\left[u_{11}-\frac{\rho_1}{\rho_2}u_{12}\right]\right) = 0. \tag{4.36}$$

It is found that there is one fixed pole ($z_1 = 0$) at the origin. The other pole lies on the real axis ($z_2 = u_{11} - \frac{\rho_1}{\rho_2}u_{12}$), whose position can be adjusted by tuning the values of $\mathbf{G}_a = [\rho_1 \ \ \rho_2]$ to make the pole locate inside the unit circle. In theory, a faster response can be produced by placing the pole close to 0 and a better robustness can be obtained by locating the pole near 1 for the controller. Similarly, the values of $\mathbf{G}_a$ and $\mathbf{K}_I$ should also be designed to locate the eigenvalues of the other two matrices inside the unit circle.

4.3 DTSMC Design

The equivalent controller as designed in the previous section takes effect in the sliding mode when the system state trajectory is kept on the sliding surface. However, if the initial state of the system does not lie on the sliding surface S or external disturbances occur during the sliding mode motion, the stand-alone equivalent control cannot drive the state toward the sliding surface. Thus, a switching control is necessary. In the following discussions, a DTSMC with switching control is designed.

4.3.1 Controller Design and Analysis

To devise a robust controller, a commonly used method is to augment the equivalent control with a discontinuous switching control u_k^{sw}. The role of u_k^{sw} is to force the system state to reach the sliding mode. Then, the overall control action is derived as:

$$u_k = u_k^{eq} + u_k^{sw}. \tag{4.37}$$

Theorem 4.1 *For the system (4.5) with the switching function (4.22), if the following controller (4.38) is employed, then the discrete sliding mode will occur after a finite number of steps*

$$u_k = -(\boldsymbol{G_aB})^{-1}[-S_k + \boldsymbol{G_aAE}_k + \boldsymbol{G_ad}_{k-1} + \boldsymbol{K}_I\boldsymbol{\xi}_k + \boldsymbol{G_aK}_s sgn(S_k)] \tag{4.38}$$

where $\boldsymbol{K}_s$ is a positive switching gain vector and the last term in the right-hand side represents the switching control action.

Proof In view of Eqs. (4.26) and (4.28), the following expression can be derived:

$$S_{k+1} = \mathbf{G}_a(\mathbf{A}\mathbf{E}_k + \mathbf{B}u_k + \mathbf{d}_k) + \mathbf{K}_I\boldsymbol{\xi}_k. \tag{4.39}$$

Substituting Eq. (4.38) into Eq. (4.39) yields

$$S_{k+1} = S_k - \mathbf{G}_a\mathbf{K}_s\mathrm{sgn}(S_k) + \mathbf{G}_a\boldsymbol{\varepsilon}_k \tag{4.40}$$

where

$$\begin{aligned}\boldsymbol{\varepsilon}_k &= \mathbf{d}_k - \mathbf{d}_{k-1} \approx \mathbf{f}_k - \mathbf{f}_{k-1} \\ &= \int_0^T e^{\mathbf{A}_c\tau}\int_{kT-\tau}^{(k+1)T-\tau}\delta_d\mathbf{B}_c\dot{f}_h(\sigma)d\sigma d\tau = O(T^2)\end{aligned} \tag{4.41}$$

is the estimation error vector of the disturbance, which has a magnitude of $O(T^2)$ and is assumed to be bounded, i.e.,

$$|\boldsymbol{\varepsilon}_k| = |\mathbf{d}_k - \mathbf{d}_{k-1}| \le \boldsymbol{\Delta}_d. \tag{4.42}$$

The switching control gain vector $\mathbf{K}_s$ is designed to meet the condition:

$$\mathbf{K}_s > \boldsymbol{\Delta}_d + \boldsymbol{\sigma} \tag{4.43}$$

where $\boldsymbol{\sigma}$ is an arbitrary positive constant. Then, in the case of $S_k \ge 0$, one has

$$\begin{aligned}S_{k+1} &= S_k - \mathbf{G}_a\mathbf{K}_s + \mathbf{G}_a\boldsymbol{\varepsilon}_k \\ &< S_k - \mathbf{G}_a[\boldsymbol{\Delta}_d + \boldsymbol{\sigma} - \boldsymbol{\varepsilon}_k] \\ &< S_k.\end{aligned} \tag{4.44}$$

On the other hand, if $S_k < 0$, it can be derived that

$$\begin{aligned}S_{k+1} &= S_k + \mathbf{G}_a\mathbf{K}_s + \mathbf{G}_a\boldsymbol{\varepsilon}_k \\ &> S_k + \mathbf{G}_a[\boldsymbol{\Delta}_d + \boldsymbol{\sigma} + \boldsymbol{\varepsilon}_k] \\ &> S_k.\end{aligned} \tag{4.45}$$

Considering Eqs. (4.44) and (4.45) together, yields

$$|S_{k+1}| < |S_k| \quad \text{for} \quad k \ge k_0 \tag{4.46}$$

which indicates that $|S_k|$ decreases monotonously, and the discrete sliding mode is reached after a finite number (k_0) of steps.

It has been shown in [18] that the relationship (4.46) represents a sufficient condition for the existence of discrete sliding mode.

Remark 4.1 Theorem 4.1 gives a sufficient condition for the existence of the discrete sliding mode. Due to the discontinuity of the signum function $\text{sgn}(s)$, chattering may occur in the control input. To alleviate the chattering phenomenon, the boundary layer technique is adopted by replacing the signum function in Eq. (4.38) with the saturation function:

$$\text{sat}(S_k) = \begin{cases} \text{sgn}(S_k) & \text{if} \quad |S_k| > \delta \\ S_k/\delta & \text{if} \quad |S_k| \leq \delta \end{cases} \tag{4.47}$$

where the positive constant δ denotes the boundary layer thickness, which ensures that S_k is bounded by $\pm\delta$. In the selection of parameter δ, a tradeoff between the chattering and tracking error should be taken.

It is observed from Eq. (4.43) that the selection of the control gain $\mathbf{K}_s$ is dependent on the upper bound of the disturbance estimation error $\boldsymbol{\Delta}_d$. Alternatively, this term is the upper bound of the disturbance in the classical SMC. Generally, the disturbance estimation error is much lower than the disturbance itself. Hence, a much smaller switching gain vector $\mathbf{K}_s$ can be designed in comparison with the classical SMC. This is one of the advantages of the constructed DTSMC with one-step delayed disturbance estimation over the conventional SMC.

4.3.2 Tracking Error Bound Analysis

Taking into account the relationship (4.40) and Property 4.2, it can be deduced that S_k has a magnitude of the order $O(T)$. It means that the ultimate state will stay in the neighborhood of S with a boundary layer of the thickness $O(T)$.

Considering Eq. (4.22), the error dynamics equation (4.32) can be further expressed below after a necessary calculation:

$$\mathbf{E}_{k+1} = \mathbf{P}\mathbf{E}_k - \mathbf{Q}S_k + \mathbf{W}\mathbf{d}_k \tag{4.48}$$

where the three matrices are

$$\mathbf{P} = \mathbf{A} - \mathbf{B}(\mathbf{G}_a\mathbf{B})^{-1}[\mathbf{G}_a\mathbf{A} - \mathbf{G}] \tag{4.49}$$

$$\mathbf{Q} = \mathbf{B}(\mathbf{G}_a\mathbf{B})^{-1} \tag{4.50}$$

$$\mathbf{W} = \mathbf{I} - \mathbf{B}(\mathbf{G}_a\mathbf{B})^{-1}\mathbf{G}_a. \tag{4.51}$$

In view of $S_k = O(T)$ and $\mathbf{d}_k = O(T)$, it can be deduced that $\mathbf{E}_k = O(1)$, i.e., the ultimate state error is of the order $O(1)$.

Due to the existence of unmodeled dynamics of the system including the actuator nonlinearities, sensor noises, and high-frequency dynamics, the switching control constructed above may still induce chattering phenomenon. Chattering is the oscillations of the system states around the sliding surface with a certain amplitude and

frequency [11–14]. As a result, chattering leads to a poor system performance and reduces usable life of the actuator. In the next section, the model predictive control scheme is employed to eliminate the chattering effect.

4.4 MPDTSMC Design

A MPDTSMC scheme, which integraties MPC and DTSMC control strategies, is constructed to handle the nonlinearities and disturbances existing in the system. Specifically, the MPC is used to generate an optimal control (u_k^{mp}) to drive the system state to the sliding surface, and the equivalent control (u_k^{eq}) is employed to maintain the state trajectory on the sliding surface for the subsequent time. It is shown that the system state is forced to reach the sliding mode smoothly in an optimal manner without chattering effects.

4.4.1 MPDTSMC Controller Design

Substituting the overall control action

$$u_k = u_k^{eq} + u_k^{mp} \tag{4.52}$$

into Eq. (4.39) and noting Eq. (4.29) gives

$$\begin{aligned} S_{k+1} &= \mathbf{G}_a \left[\mathbf{A}\mathbf{E}_k + \mathbf{B}(u_k^{eq} + u_k^{mp}) + \mathbf{d}_k\right] + \mathbf{K}_I \boldsymbol{\xi}_k \\ &= S_k + \mathbf{G}_a \mathbf{B} u_k^{mp} + \mathbf{G}_a \boldsymbol{\varepsilon}_k \end{aligned} \tag{4.53}$$

which describes the dynamics of the sliding mode and also represents a one-step prediction of the sliding-mode dynamics.

Based on Eq. (4.53), an N-step prediction of the sliding-mode dynamics can be obtained as follows:

$$\begin{aligned} S_{k+N} = S_k + \mathbf{G}_a \mathbf{B}(u_k^{mp} + u_{k+1}^{mp} + \cdots + u_{k+N-1}^{mp}) + \\ (\mathbf{G}_a \boldsymbol{\varepsilon}_{k+N-1} + \cdots + \mathbf{G}_a \boldsymbol{\varepsilon}_{k+1} + \mathbf{G}_a \boldsymbol{\varepsilon}_k) \end{aligned} \tag{4.54}$$

where N is called the prediction horizon.

The N prediction functions can be stacked together into the form:

$$\mathbf{S}_k = \boldsymbol{\Lambda} S_k + \boldsymbol{\Phi} \mathbf{u}_{k-1}^{mp} + \boldsymbol{\Gamma} \boldsymbol{\zeta}_{k-1} \tag{4.55}$$

where the vectors for the sliding surface, future control, and disturbance estimation errors are:

$$\mathbf{S}_k = \begin{bmatrix} S_{k+1} \\ S_{k+2} \\ \vdots \\ S_{k+N} \end{bmatrix}, \ \mathbf{u}_{k-1}^{mp} = \begin{bmatrix} u_k^{mp} \\ u_{k+1}^{mp} \\ \vdots \\ u_{k+N-1}^{mp} \end{bmatrix}, \ \boldsymbol{\zeta}_{k-1} = \begin{bmatrix} \boldsymbol{\varepsilon}_k \\ \boldsymbol{\varepsilon}_{k+1} \\ \vdots \\ \boldsymbol{\varepsilon}_{k+N-1} \end{bmatrix}. \tag{4.56}$$

Additionally, the matrices take on the following forms:

$$\boldsymbol{\Lambda} = \begin{bmatrix} \mathbf{I} \\ \mathbf{I} \\ \vdots \\ \mathbf{I} \end{bmatrix} \tag{4.57}$$

$$\boldsymbol{\Phi} = \begin{bmatrix} \mathbf{G}_a\mathbf{B} & 0 & \dots & 0 \\ \mathbf{G}_a\mathbf{B} & \mathbf{G}_a\mathbf{B} & \dots & 0 \\ \vdots & \vdots & \ddots & \vdots \\ \mathbf{G}_a\mathbf{B} & \mathbf{G}_a\mathbf{B} & \dots & \mathbf{G}_a\mathbf{B} \end{bmatrix} \tag{4.58}$$

$$\boldsymbol{\Gamma} = \begin{bmatrix} \mathbf{G}_a & 0 & \dots & 0 \\ \mathbf{G}_a & \mathbf{G}_a & \dots & 0 \\ \vdots & \vdots & \ddots & \vdots \\ \mathbf{G}_a & \mathbf{G}_a & \dots & \mathbf{G}_a \end{bmatrix}. \tag{4.59}$$

Using the above notations, a cost function for minimization can be expressed by:

$$J = \mathbf{S}_k^T \mathbf{S}_k + \lambda \left(\mathbf{u}_{k-1}^{mp}\right)^T \mathbf{u}_{k-1}^{mp} \tag{4.60}$$

where λ is the weighting parameter to limit the partial control effort. It is notable that $\mathbf{u}_{k-1}^{mp}$ approaches to zero as $\mathbf{S}_k$ tends to zero. Thus, the cost function J will vanish at the steady state.

Substituting Eq. (4.55) into the cost function (4.60) and applying the optimization criterion by setting the condition:

$$\frac{\partial J}{\partial \mathbf{u}_{k-1}^{mp}} = 0 \tag{4.61}$$

yields

$$\mathbf{u}_{k-1}^{mp} = -(\boldsymbol{\Phi}^T\boldsymbol{\Phi} + \lambda\,\mathbf{I})^{-1}\boldsymbol{\Phi}^T(\boldsymbol{\Lambda} S_k + \boldsymbol{\Gamma}\boldsymbol{\zeta}_{k-1}) \tag{4.62}$$

where the future disturbance values in $\boldsymbol{\zeta}_{k-1}$ are unknown. Thus, they are estimated as follows

$$\hat{\boldsymbol{\zeta}}_{k-1} = [\boldsymbol{\varepsilon}_{k-1}^T \ \boldsymbol{\varepsilon}_{k-1}^T \ \cdots \ \boldsymbol{\varepsilon}_{k-1}^T]^T. \tag{4.63}$$

Considering that only the first value of the predicted control sequence is used, the optimal control action is obtained as:

$$u_k^{mp} = -\mathbf{c}(\boldsymbol{\Phi}^T\boldsymbol{\Phi} + \lambda\,\mathbf{I})^{-1}\boldsymbol{\Phi}^T(\boldsymbol{\Lambda}S_k + \boldsymbol{\Gamma}\hat{\boldsymbol{\zeta}}_{k-1}) \tag{4.64}$$

where the vector $\mathbf{c} = [1, 0, 0, \cdots, 0]$.

Therefore, the total control action can be expressed as:

$$\begin{aligned} u_k &= u_k^{eq} + u_k^{mp} \\ &= -(\mathbf{G}_a\mathbf{B})^{-1}[-S_k + \mathbf{G}_a\mathbf{A}\mathbf{E}_k + \mathbf{G}_a\mathbf{d}_{k-1} + \mathbf{K}_I\boldsymbol{\xi}_k] \\ &\quad -\mathbf{c}(\boldsymbol{\Phi}^T\boldsymbol{\Phi} + \lambda\,\mathbf{I})^{-1}\boldsymbol{\Phi}^T(\boldsymbol{\Lambda}S_k + \boldsymbol{\Gamma}\hat{\boldsymbol{\zeta}}_{k-1}). \end{aligned} \tag{4.65}$$

4.4.2 Stability Analysis

Theorem 4.2 *For the system (4.5) with the switching function (4.22), if the disturbance change rate is limited, i.e., the inequality (4.42) is satisfied, then the controller (4.65) leads to a stable closed-loop control system.*

Proof Substituting Eq. (4.65) into Eq. (4.39) results in Eq. (4.53). Then, inserting Eq. (4.62) into the stacked equation (4.55) yields

$$\mathbf{S}_k = \boldsymbol{\Lambda}S_k - \boldsymbol{\Phi}(\boldsymbol{\Phi}^T\boldsymbol{\Phi} + \lambda\,\mathbf{I})^{-1}\boldsymbol{\Phi}^T(\boldsymbol{\Lambda}S_k + \boldsymbol{\Gamma}\hat{\boldsymbol{\zeta}}_{k-1}) + \boldsymbol{\Gamma}\boldsymbol{\zeta}_{k-1} \tag{4.66}$$

where λ is defined in the cost function (4.60) to restrict the control input. For simplicity, it is assumed that there is no penalty for the control effort, i.e., $\lambda = 0$.

Then, Eq. (4.66) reduces to

$$\begin{aligned} \mathbf{S}_k &= \boldsymbol{\Lambda}S_k - (\boldsymbol{\Lambda}S_k + \boldsymbol{\Gamma}\hat{\boldsymbol{\zeta}}_{k-1}) + \boldsymbol{\Gamma}\boldsymbol{\zeta}_{k-1} \\ &= \boldsymbol{\Gamma}(\boldsymbol{\zeta}_{k-1} - \hat{\boldsymbol{\zeta}}_{k-1}). \end{aligned} \tag{4.67}$$

Considering only the first value of the predicted sliding hyperplane vector in Eq. (4.67) and taking into account Eqs. (4.56) and (4.63) yields

$$\begin{aligned} S_{k+1} &= \mathbf{G}_a(\boldsymbol{\varepsilon}_k - \boldsymbol{\varepsilon}_{k-1}) \\ &= \mathbf{G}_a(\mathbf{d}_k - 2\mathbf{d}_{k-1} + \mathbf{d}_{k-2}) = O(T^3) \end{aligned} \tag{4.68}$$

which indicates that the ultimate magnitude of S_{k+1} is of the order $O(T^3)$.

Because the disturbance change rate $\boldsymbol{\varepsilon}_k$ is bounded as supposed in Eq. (4.42), it is reasonable to deduce that the rate of $\boldsymbol{\varepsilon}_k$ is also limited:

$$|\boldsymbol{\varepsilon}_k - \boldsymbol{\varepsilon}_{k-1}| \leq \boldsymbol{\Delta}_\varepsilon. \tag{4.69}$$

Thus, it can be generated that

$$|S_{k+1}| \leq |\mathbf{G}_a \boldsymbol{\Delta}_\varepsilon| = \Delta_S \tag{4.70}$$

where $2\Delta_S$ is defined as the quasi-sliding mode band width.

According to Definition 1 and Definition 2 in [3], it can be concluded that the system (4.5) satisfies the reaching condition of the quasi-sliding mode in the Δ_S vicinity of the sliding surface S in a finite number of steps. Therefore, the closed-loop control system is stable.

Remark 4.2 The essence of the presented MPDTSMC is to drive the system state to a quasi-sliding mode as shown in Eq. (4.70). One advantage of this quasi-sliding model [3] lies in that it does not require the system state to cross the sliding hyperplane S in each successive control step as in [7]. Therefore, the chattering phenomenon is eliminated. As a result, it leads to a reduction of the control effort and improved control performance [3].

Remark 4.3 It is observed from Eq. (4.68) that S_{k+1} has an ultimate magnitude of the order $O(T^3)$. Therefore, the controller (4.65) drives the system state to slide in the vicinity of S with a boundary layer of thickness $O(T^3)$, whose magnitude is much lower than the $O(T)$ thickness achieved by the DTSMC controller designed earlier. Therefore, a much lower tracking error is expected for the proposed MPDTSMC controller.

4.4.3 State Observer Design

The controller equation (4.65) reveals that its implementation needs the full state ($\mathbf{X}_k$) feedback of the system. However, only partial states are available in practice. Thus, a state observer is designed to estimate the full state by making use of the only measurable position information of the nanopositioning system.

Although various methods are available [10], a Luenberger-like observer is adopted here owing to its simplicity. The state observer takes on the form:

$$\hat{\mathbf{X}}_{k+1} = \mathbf{A}\hat{\mathbf{X}}_k + \mathbf{B}\mathbf{u}_k + \mathbf{L}(\mathbf{Y}_k - \hat{\mathbf{Y}}_k) + \hat{\mathbf{f}}_k \tag{4.71}$$

$$\hat{\mathbf{Y}}_k = \mathbf{C}\hat{\mathbf{X}}_k \tag{4.72}$$

where the notation $\hat{\mathbf{X}}_k$ represents the estimate of $\mathbf{X}_k$, and the value of the disturbance $\mathbf{f}_k$ in Eq. (4.5) is obtained by its one-step delayed estimation:

$$\hat{\mathbf{f}}_k = \mathbf{f}_{k-1} = \hat{\mathbf{X}}_k - \mathbf{A}\hat{\mathbf{X}}_{k-1} - \mathbf{B}\mathbf{u}_{k-1}. \tag{4.73}$$

Subtracting Eq. (4.71) from Eq. (4.5) allows the derivation of

$$\widetilde{\mathbf{X}}_{k+1} = (\mathbf{A} - \mathbf{L}\mathbf{C})\widetilde{\mathbf{X}}_k + (\mathbf{f}_k - \mathbf{f}_{k-1}) \tag{4.74}$$

where $\widetilde{\mathbf{X}}_k = \mathbf{X}_k - \hat{\mathbf{X}}_k$ denotes the estimation error of the state $\mathbf{X}_k$. It is seen that the state observer is independent of the controller. To guarantee the stability of the observation unit, the observer gain $\mathbf{L}$ should be designed to make all the eigenvalues of the matrix $\mathbf{A} - \mathbf{L}\mathbf{C}$ locate inside the unit circle.

Remark 4.4 The convergence speed of the observer relies on the location of the poles of the matrix $\mathbf{A} - \mathbf{L}\mathbf{C}$. The poles can be arbitrarily placed by the gain vector $\mathbf{L}$. Generally, small pole value will give rapid convergence, and the convergence speed of the observer should be faster than the system response so that the observer dynamics is insignificant as compared to the system dynamics. However, too small pole produces instability of the system, which arises from the noise and spillover effect of the neglected system dynamics. Hence, a trial-and-error approach is usually required to place the poles appropriately.

4.4.4 Tracking and Estimation Error Bound Analysis

In order to evaluate the tracking error bound, noting that $S_k = O(T^3)$ and $\mathbf{d}_k = O(T)$, it is deduced from Eq. (4.48) that $\mathbf{E}_k = O(1)$, i.e., the ultimate state error is of the order $O(1)$.

In the case of $m = n$, $\mathbf{G}_a$ and $\mathbf{B}$ are nonsingular, i.e., the number of inputs is equal to the number of system states, the matrix $\mathbf{W}$ as shown in Eq. (4.51) will vanish. In such a situation, Eq. (4.48) reduces to

$$\mathbf{E}_{k+1} = \mathbf{P}\mathbf{E}_k - \mathbf{Q}S_k. \tag{4.75}$$

Then, by noting $S_k = O(T^3)$ as shown in Eq. (4.68) and Property 4.2, it can be derived that $\mathbf{E}_k = O(T^2)$, which is much lower than the $O(1)$ tracking error obtained with the DTSMC designed earlier.

Furthermore, considering that $\mathbf{f}_k - \mathbf{f}_{k-1}$ is of the order $O(T^2)$, it can be deduced from Eq. (4.74) that the ultimate bound of $\widetilde{\mathbf{X}}_k$ is $O(T)$. For the systems with relative degrees greater than 1, it has been shown that the state estimation error will be reduced to $O(T^2)$ for the closed-loop system [24] .

4.5 Experimental Investigation

The designed controllers are validated by a series of simulations and experimental studies in this section.

4.5.1 Experimental Setup

The experimental setup is depicted in Fig. 4.1. A flexure-based nanopositioning stage is fabricated from a plate of Al-7075 alloy by the wire electrical discharge machining (EDM) process. Driven by a piezoelectric stack actuator (PSA) with the stroke of 14.5 μm (model: TS18-H5-202, from Piezo Systems, Inc.), the stage delivers an amplified translational motion through elastic deformations of the bridge-type displacement amplifier. The output displacement is measured by a capacitive sensor (model: D-510.050, from Physik Instrumente Co., Ltd.). A dSPACE DS1103 (from dSPACE GmbH) rapid prototyping system equipped with 16-bit A/D and D/A converters are employed to implement the controller. The D/A channel produces a voltage control signal which is then amplified by a high-voltage amplifier (model: EPA-104, from Piezo Systems, Inc.) to provide a voltage ranging between −100 and 100 V for driving the PSA. In addition, the sensor output voltage signal is passed through a signal conditioner (model: E-852, from Physik Instrumente Co., Ltd.) and then acquired by the A/D channel. Control algorithms are developed with MATLAB®/Simulink® software and downloaded to the DS1103 board to realize the real-time control.

4.5.2 Hysteresis Characterization

By applying a 0.5-Hz sinusoidal wave with the amplitude of 10 V to the PSA, the output versus input curve is generated as shown in Fig. 4.2, which exhibits a nonlinear relationship between the output displacement and input voltage. The maximum

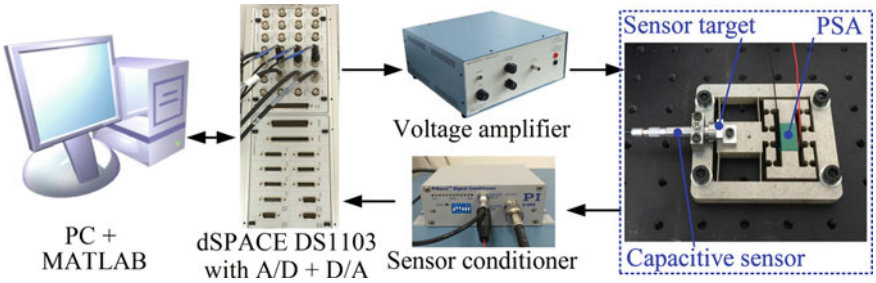

Fig. 4.1 Experimental setup of a flexure-based nanopositioning stage driven by a piezoelectric stack actuator (PSA)

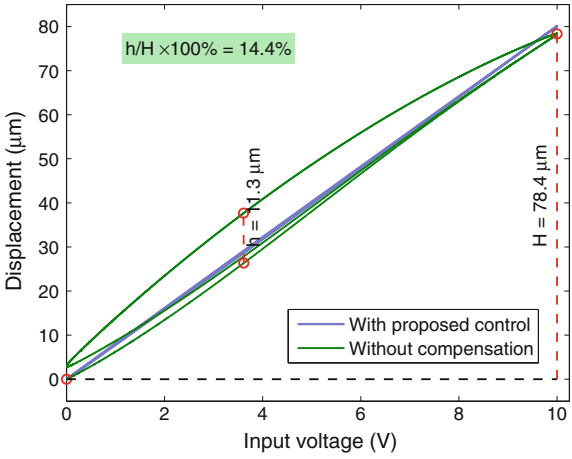

Fig. 4.2 The output versus input hysteresis loops which are obtained by applying a 0.5-Hz sine wave input

output displacement is 78.4 µm, and the maximum deviation between the ascending and descending curves is 11.3 µm. Hence, the output hysteresis accounts of 14.4 % of the travel range, which reveals a big challenge to the controller design task.

In this work, the hysteresis is treated as a bounded disturbance to the nanopositioning system, which is considered as a second-order linear system as described in Eq. (4.1).

4.5.3 Plant Model Identification

The linear plant model is identified by the frequency response approach through experimental study. Specifically, swept sine waves with the amplitude of 0.1 V and frequency range of 1–2000 Hz are produced by the D/A channel to drive the PSA through the high-voltage amplifier. The position responses of the nanopositioning stage is recorded using a sampling rate of 5 kHz.

The input–output data sets are used to identify the plant transfer function by estimating a model from the frequency response data. The frequency responses obtained from the experimental data and the identified model are compared in Fig. 4.3. It is observed that the nanopositioning system exhibits two main resonant modes. The first resonant mode occurs around 522 Hz, and the identified second-order model matches the system dynamics well in the frequencies up to 600 Hz. The identified transfer function of the plant model is:

$$G(s) = \frac{5.876 \times 10^7}{s^2 + 183.7s + 1.076 \times 10^7}. \tag{4.76}$$

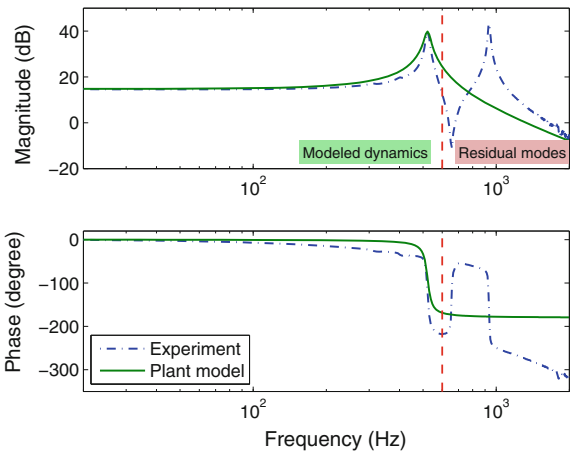

Fig. 4.3 Frequency responses of system plant obtained by experiment and identified second-order model

It is notable that in order to capture the high-frequency dynamics accurately, a much higher order model is required to be identified. Here, a simple second-order model is employed to demonstrate the effectiveness of the control scheme.

4.5.4 Controller Parameter Design

Comparing the transfer function (4.1) with Eq. (4.76) yields the mass–spring–damper system parameters, which allows the calculation of the discrete-time system model (4.5) with a sampling time of 0.5 ms. That is,

$$\mathbf{A} = \begin{bmatrix} -0.0388 & 0.0003 \\ -3126.6906 & -0.0921 \end{bmatrix}, \ \mathbf{B} = \begin{bmatrix} 5.6729 \\ 17075.5580 \end{bmatrix}, \ \mathbf{C} = [1 \ \ 0]. \tag{4.77}$$

First, the state observer is constructed by the pole placement technique for the closed-loop observer system. Simulation study shows that small pole values lead to rapid convergence in that a high bandwidth is achieved by the observer. However, experiments reveal that too small pole produces instability of the system, which may arise from the sensor noises and spillover effects of the neglected dynamics. Thus, the poles are assigned as $(-0.15, -0.15)$, which are selected to guarantee the stability of the observer in the presence of unmodeled high-frequency dynamics. The corresponding gains are obtained as $\mathbf{L} = [0.1691, 0.0003]^T$.

Next, the sliding function is designed by selecting appropriate proportional and integral gain vectors $\mathbf{G} = [g_1, g_2]$ and $\mathbf{K}_I = [k_1, k_2]$. It is found that the matrix $\mathbf{W}$ has two constant eigenvalues of 0 and 1. Each of the other two matrices $\mathbf{U}$ and $\mathbf{V}$ has an eigenvalue fixed at 0. Thus, the gains are chosen to guarantee that the free

eigenvalues λ_u and λ_v of $\mathbf{U}$ and $\mathbf{V}$, respectively, locate inside the unit circle. Noting that $\mathbf{G}_a = [\rho_1, \rho_2] = [g_1 + k_1, g_2 + k_2]$, the eigenvalues can be expressed by:

$$\lambda_u = \frac{u_1 \frac{\rho_1}{\rho_2} - u_2}{u_1 \frac{\rho_1}{\rho_2} + u_2}, \quad \lambda_v = \frac{v_1 \frac{k_1}{k_2} + v_2}{v_1 \frac{k_1}{k_2} + v_2} \tag{4.78}$$

where u_1, u_2, v_1, and v_2 are all constants. It is seen that the ratios $\frac{\rho_1}{\rho_2}$ and $\frac{k_1}{k_2}$ are related to the two eigenvalues λ_u and λ_v, respectively. The eigenvalues are assigned as $\lambda_u = 0.2$ and $\lambda_v = 0.4$ to ensure a quick response of the closed-loop control system. Then, by selecting $k_2 = 1$, extensive simulations show that $g_2 < k_2$ does not improve the performance. It is found that $g_2 = 10000$ results in a better tracking result, whereas further increase of g_2 does not make more contribution. Thus, the gain vectors can be calculated as $\mathbf{G} = [344418.5, 10000]$ and $\mathbf{K}_I = [20293358.5, 1]$.

After some trials, the weighting parameter $\lambda = 10^{19}$ is chosen for the MPDTSMC, and parameters $\mathbf{K}_s = [1\ \ 50]$ and $\delta = 10^8$ are selected for the DTSMC controller to generate better results. In addition, the control action is constrained between -2 to 10 V, which will be produced by the D/A channel and then amplified by the high-voltage amplifier with a gain of 10 to provide the driving voltage range of -20 to 100 V.

4.5.5 Simulation Studies

First, the performance of the implemented controllers are tested by conducting simulation studies. By defining the tracking error $e = x_d - x$, the root-mean-square (RMS) error is defined as follows:

$$e_{\text{rms}} = \sqrt{\frac{1}{N} \sum_{i=1}^{N} e_i^2}. \tag{4.79}$$

For a sinusoidal reference input as shown in Fig. 4.4a, the DTSMC tracking errors and control actions with different parameter δ are shown in Fig. 4.4b, c, respectively. With a larger value of $\delta = 10^{10}$, it is observed from Eq. (4.47) that $\text{sat}(S_k) = S_k/\delta$ always holds. As a result, a smooth control action is produced as shown in Fig. 4.4c. On the contrary, using a smaller value of $\delta = 10^6$, $\text{sat}(S_k) = \text{sgn}(S_k)$ when $|S_k| > \delta$. Hence, slight oscillations are produced in the tracking results as shown in Fig. 4.4b. Correspondingly, slight oscillation phenomenon occurs in the control action, as revealed in Fig. 4.4c.

The RMS error versus the parameter δ is depicted in Fig. 4.4d. To generate a better tracking result for the DTSMC scheme, $\delta = 10^8$ is selected, which produces a RMS error of 0.043 μm.

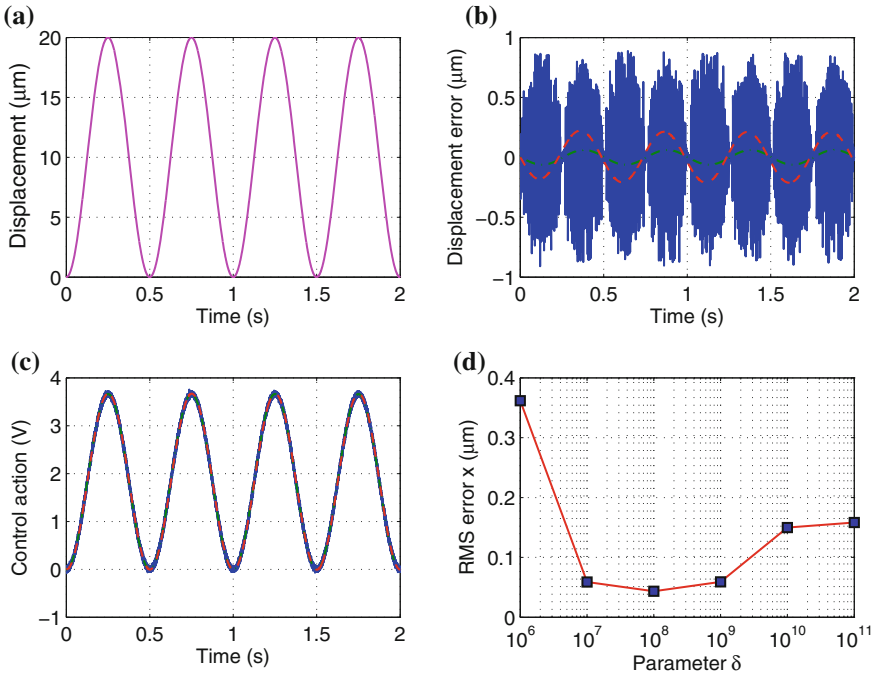

Fig. 4.4 Simulation results of DTSMC controller. **a** Desired position input. **b** Tracking errors of DTSMC with $\delta = 10^6$ (*solid line*), 10^8 (*dash-dot line*), and 10^{10} (*dashed line*). **c** Control actions of DTSMC with $\delta = 10^6$ (*solid line*), 10^8 (*dash-dot line*), and 10^{10} (*dashed line*). **d** RMS error of DTSMC versus the parameter δ

Regarding the MPDTSMC, it is necessary to choose the suitable prediction horizon N. Simulations are carried out to disclose the relationship between the steady-state tracking error and the prediction horizon N. For a sinusoidal reference input as shown in Fig. 4.5a, the RMS error versus the prediction horizon N is obtained as shown in Fig. 4.5d. It is found that the larger the prediction horizon N, the smaller the tracking error. However, the larger the prediction horizon N, the heavier the calculation burden.

It is further observed from Fig. 4.5d that no significant improvement on the tracking result is achieved when $N > 12$. Hence, $N = 12$ is selected to make a compromise between the tracking accuracy and the computation load. With $N = 12$, the tracking error and control action of the MPDTSMC are shown in Fig. 4.5b, c, respectively. Obviously, no chattering phenomenon exists in the control action. Simulation result shows that the MPDTSMC achieves a RMS error of 0.044 μm, which is comparable to the DTSMC simulation result.

The performances of the MPDTSMC and DTSMC controllers are validated through experimental studies as conducted in the following discussion.

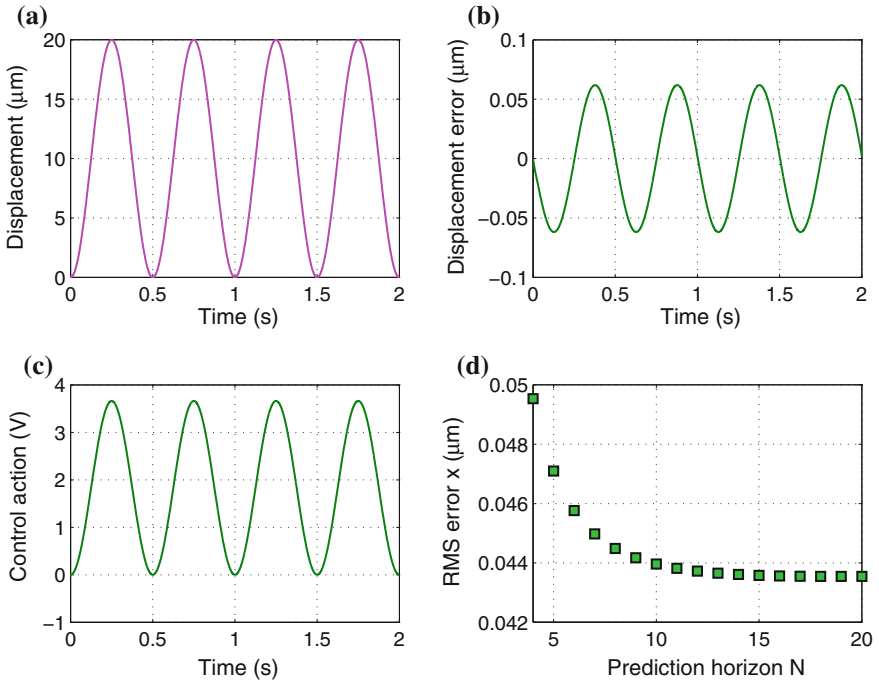

Fig. 4.5 Simulation results of MPDTSMC controller. **a** Desired position input. **b** Tracking errors of MPDTSMC with $N = 12$. **c** Control actions of MPDTSMC with prediction horizon N. **d** RMS error of MPDTSMC versus the prediction horizon N

4.5.6 Experimental Testing Results

The performance testing of the designed controllers is carried out through several experimental studies. For comparisons, the maximum tracking error and percent RMS error are defined as:

$$e_{\max}(\%) = \frac{\max(|e|)}{\max(x_d) - \min(x_d)} \times 100\,\% \tag{4.80}$$

$$e_{\text{rms}}(\%) = \left(\frac{\sqrt{\frac{1}{N}\sum_{i=1}^{N} e_i^2}}{\max(x_d) - \min(x_d)} \right) \times 100\,\%. \tag{4.81}$$

First, in order to conduct a comparison with the simulation results, the 2-Hz reference signal with 20-μm amplitude as shown in Fig. 4.6a is used. The tracking errors of the DTSMC and MPDTSMC schemes are illustrated in Fig. 4.6b. It is observed that the maximum error $e_{\max}$ and RMS error e_{rms} of the DTSMC controller are 0.81 and 0.52 %, respectively. In contrast, the MPDTSMC scheme further reduces

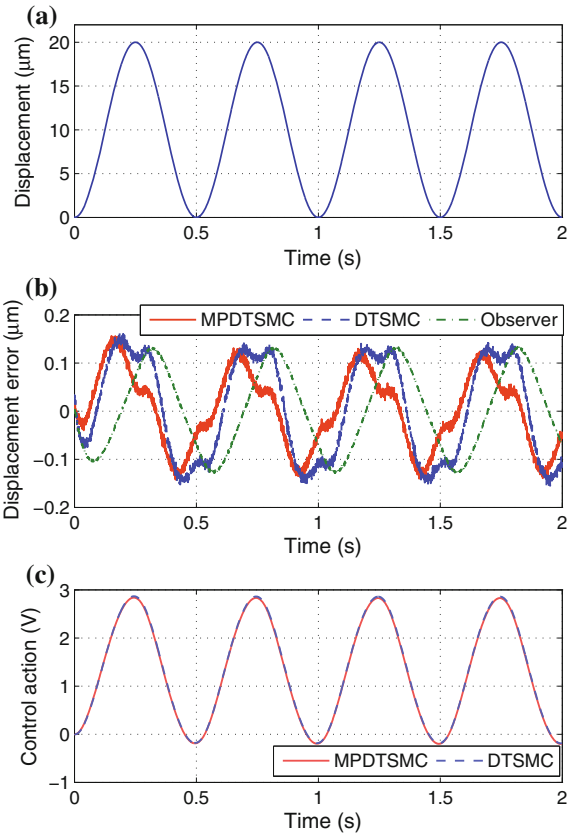

Fig. 4.6 Experimental results of DTSMC and MPDTSMC controller. **a** Reference position input. **b** Experimental results of the DTSMC and MPDTSMC tracking errors, and the state observer estimation errors

the errors to $e_{\max} = 0.77\,\%$ and $e_{\text{rms}} = 0.39\,\%$, respectively. In comparison with the DTSMC results, the MPDTSMC reduces the maximum error by 5 % and RMS error by 25 %, respectively. In addition, Fig. 4.6b also indicates that the state observer estimates the position value with the maximum error below 0.67 %.

Additionally, by comparing the experimental results as shown in Fig. 4.6b with simulation results as shown in Fig. 4.5b, it can be observed that the actual tracking errors are worse than the simulation results of both DTSMC and MPDTSMC controllers. The differences mainly arise from the noises and high-frequency dynamics, which are not captured by the second-order model as employed in the simulation study. The presence of high-frequency dynamics degrades the performance of the controllers as indicated by the experimental results.

Second, the dynamic resolution of the nanopositioning stage is tested. It is known that the resolution can be well presented using the sensitivity and noise variance of the sensing system [2, 5]. However, such approach is more suitable for evaluating the static resolution of the system. In order to exhibit the dynamic resolution and demonstrate the effectiveness of the state observer, sinusoidal signals with small

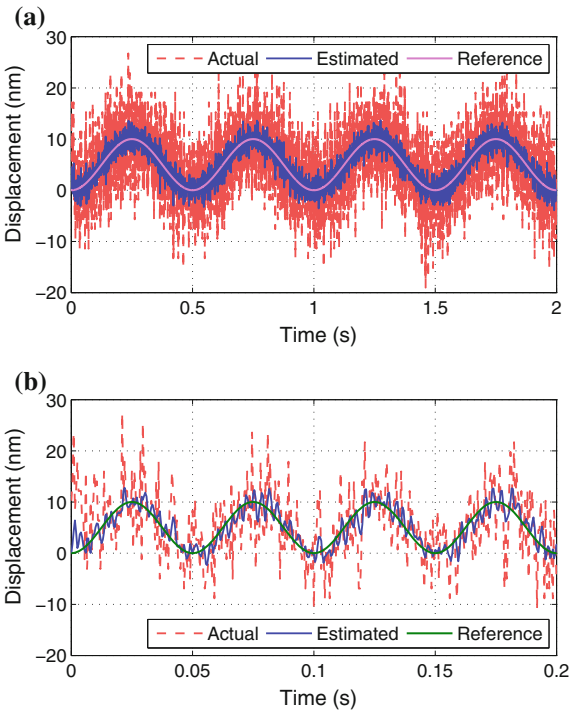

Fig. 4.7 Dynamic resolution test results of the nanopositioning stage using a 2-Hz (**a**) and a 20-Hz (**b**) sinusoidal wave inputs with 10 nm peak-to-peak amplitude

amplitudes are used as inputs in the experimental testing. For instance, Fig. 4.7a, b depict the results which are obtained using reference inputs of 10-nm amplitude along with the frequencies of 2 and 20 Hz, respectively. The sine waves can be clearly identified even with a 20-Hz higher frequency input. It indicates that the resolution of the positioning system is better than 10 nm. Furthermore, the results also illustrate that the implemented state observer acts as a low-pass filter with the extra functions of filtering the noisy sensor readings and suppressing the residual modes of high-frequency dynamics.

Next, with the proposed MPDTSMC controller, the hysteresis effects are tested by applying a 0.5-Hz reference input with the amplitude of 80 μm. Scaling the output displacement with the maximum input voltage value yields the results as illustrated in Fig. 4.2. It is observed that the closed-loop hysteresis is significantly suppressed to 0.56 %. As compared with the open-loop hysteresis width (14.4 %), it has been substantially reduced by 96.1 % owing to the effectiveness of the MPDTSMC strategy. Actually, the proposed scheme significantly mitigates the tracking errors to $e_{\max} = 0.33\,\%$ and $e_{\text{rms}} = 0.19\,\%$, respectively.

Moreover, the bandwidth of the closed-loop system with the MPDTSMC control is tested by applying a sinusoidal reference input with the amplitude of 0.2-μm and varying frequencies of 1–900 Hz. The Bode diagrams are plotted in Fig. 4.8. It is observed that the −3 dB bandwidth is 413 Hz, which is equivalent to 79 % of the first

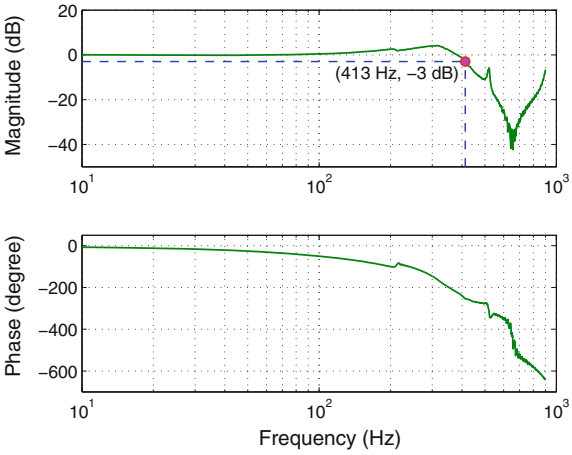

Fig. 4.8 Frequency responses of the closed-loop system with the MPDTSMC controller

resonant frequency (522 Hz). It is notable that the above bandwidth is tested using a small amplitude of the input command where the hysteresis can be neglected. As the motion range increases, the bandwidth decreases due to the effect of the hysteresis. Even so, it demonstrates the effectiveness of the implemented controller as compared with the open-loop testing result as depicted in Fig. 4.3, which is also obtained using a low-amplitude input.

4.5.7 Discussion on System Performance

The foregoing experimental studies confirm the feasibility and effectiveness of the proposed control strategy. Moreover, it is observed that the resonant mode is suppressed by the implemented MPDTSMC control. The observation spillover is successfully eliminated by the state observer at the cost of a lower response speed as reflected by the assigned pole values. On the other hand, the noise in sensor readings requires a further treatment to enhance the positioning resolution of the system.

By adopting a closed-loop sampling rate of 2 kHz, which is sufficient for the investigated plant, the above simulations and experiments demonstrate the effectiveness of the reported control approaches. The controller parameters are not optimally designed, and the current amplitudes of steady-state errors as shown in Fig. 4.6 indicate that the performance of the MPDTSMC may be improved to further reduce the tracking error down to the positioning resolution. For instance, an iterative control [22] may be employed to compensate for the periodic errors.

In addition, the conducted investigations demonstrate an enhancement of the positioning accuracy for the nanopositioning system with the MPDTSMC over the conventional DTSMC control. The results validate the effectiveness of the MPDTSMC control scheme with PI sliding function and displays a great potential for the future research.

4.6 Chapter Summary

This chapter shows that a nanopositioning stage with piezoelectric actuation can be precisely controlled by using only a second-order mass–spring–damper system model without modeling the hysteresis effects. Such a simple framework is very attractive for its easy implementation characteristics, which is enabled by the MPDTSMC with PI sliding function. It is found that the MPC strategy forces the system state to slide in the vicinity of the sliding surface with an $O(T^3)$ boundary layer in an optimal manner, which eliminates the chattering phenomenon. The PI action in the MPDTSMC drives the state tracking error to a boundary layer of $O(T^2)$ in the sliding mode, which indicates a much lower tracking error in comparison with a commonly designed DTSMC controller. The experimental results confirm that the MPDTSMC controller improves the tracking performance as compared with the DTSMC approach. In addition, the hysteresis has been substantially reduced to 0.56 % and a 10-nm dynamic resolution is achieved by the nanopositioning stage. Because the implementation of the controller does not require any bounds on the uncertainties and unknown parameters of the system, the MPDTSMC scheme can be easily extended to the control of micro-/nanopositioning stages driven by other types of actuators as well.

References

1. Abidi, K., Xu, J.X., Yu, X.: On the discrete-time integral sliding mode control. IEEE Trans. Automat. Control **52**(4), 709–715 (2007)
2. Aphale, S.S., Bhikkaji, B., Moheimani, S.O.R.: Minimizing scanning errors in piezoelectric stack-actuated nanopositioning platforms. IEEE Trans. Nanotechnol. **7**(1), 79–90 (2008)
3. Bartoszewicz, A.: Discrete-time quasi-sliding-mode control strategies. IEEE Trans. Ind. Electron. **45**(5), 633–637 (1998)
4. Dannehl, J., Fuchs, F.W.: Discrete sliding mode current control of three-phase grid-connected pwm converters. In: Proceeding of the 13th European Conference on Power Electronics and Applications, pp. 1–10 (2009)
5. Dong, J., Salapaka, S.M., Ferreira, P.M.: Robust control of a parallel-kinematic nanopositioner. J. Dyn. Syst. Meas. Control **130**(4), 041007 (2008)
6. Furuta, K.: Sliding mode control of a discrete system. Syst. Control Lett. **14**(2), 145–152 (1990)
7. Gao, W., Wang, Y., Homaifa, A.: Discrete-time variable structure control systems. IEEE Trans. Ind. Electron. **42**(2), 117–122 (1995)
8. Garcia-Gabin, W., Zambrano, D., Camacho, E.F.: Sliding mode predictive control of a solar air conditioning plant. Control Eng. Pract. **17**(6), 652–663 (2009)
9. Kim, B., Washington, G.N.: Nonlinear position control of smart actuators using model predictive sliding mode control. In: Proceeding of ASME Conference on Smart Materials, Adaptive Structures and Intelligent Systems, pp. 511–522 (2008)
10. Koshkouei, A.J., Zinober, A.S.I.: Sliding mode state observers for discrete-time linear systems. Int. J. Syst. Sci. **33**(9), 751–758 (2002)
11. Liaw, H.C., Shirinzadeh, B.: Enhanced adaptive motion tracking control of piezo-actuated flexure-based four-bar mechanisms for micro/nano manipulation. Sens. Actuator A-Phys. **147**, 254–262 (2008)

12. Liaw, H.C., Shirinzadeh, B.: Robust generalised impedance control of piezo-actuated flexure-based four-bar mechanisms for micro/nano manipulation. Sens. Actuator A-Phys. **148**, 443–453 (2008)
13. Liaw, H.C., Shirinzadeh, B., Smith, J.: Enhanced sliding mode motion tracking control of piezoelectric actuators. Sens. Actuator A-Phys. **138**, 194–202 (2007)
14. Liaw, H.C., Shirinzadeh, B., Smith, J.: Robust motion tracking control of piezo-driven flexure-based four-bar mechanism for micro-nano manipulation. Mechatronics **18**, 111–120 (2008)
15. Liaw, H.C., Shirinzadeh, B., Smith, J.: Sliding-mode enhanced adaptive motion tracking control of piezoelectric actuation systems for micro/nano manipulation. IEEE Trans. Control Syst. Technol. **16**(4), 826–833 (2008)
16. Neelakantan, V.A., Washington, G.N., Bucknor, N.K.: Model predictive control of a two stage actuation system using piezoelectric actuators for controllable industrial and automotive brakes and clutches. J. Intell. Mater. Syst. Struct. **19**(7), 845–857 (2008)
17. Pai, M.C., Sinha, A.: Sliding mode control of vibration in a flexible structure via estimated states and H_∞/μ techniques. In: Proceeeding of American Control Conference, pp. 1118–1123 (2000)
18. Sarpturk, S., Istefanopulos, Y., Kaynak, O.: On the stability of discrete-time sliding mode control systems. IEEE Trans. Automat. Control **32**(10), 930–932 (1987)
19. Su, W.C., Drakunov, S.V., Ozguner, U.: An $O(T^2)$ boundary layer in sliding mode for sampled-data systems. IEEE Trans. Automat. Control **45**(3), 482–485 (2000)
20. Wang, D.A., Huang, Y.M.: Application of discrete-time variable structure control in the vibration reduction of a flexible structure. J. Sound Vibr. **261**(3), 483–501 (2003)
21. Wills, A.G., Bates, D., Fleming, A.J., Ninness, B., Moheimani, S.O.R.: Model predictive control applied to constraint handling in active noise and vibration control. IEEE Trans. Control Syst. Technol. **16**(1), 3–12 (2008)
22. Wu, Y., Zou, Q.: Iterative control approach to compensate for both the hysteresis and the dynamics effects of piezo actuators. IEEE Trans. Control Syst. Technol. **15**(5), 936–944 (2007)
23. Xiao, L., Su, H., Chu, J.: Sliding mode prediction tracking control design for uncertain systems. Asian J. Control **9**(3), 317–325 (2007)
24. Xu, J.X., Abidi, K.: A discrete-time integral sliding mode control approach for output tracking with state estimation. In: Proceeding of the 17th IFAC World Congress, pp. 14,199–14,204 (2008)
25. Xu, J.X., Abidi, K.: Discrete-time output integral sliding-mode control for a piezomotor-driven linear motion stage. IEEE Trans. Ind. Electron. **55**(11), 3917–3926 (2008)
26. Yong, Y.K., Aphale, S., Moheimani, S.O.R.: Design, identification and control of a flexure-based XY stage for fast nanoscale positioning. IEEE Trans. Nanotechnol. **8**(1), 46–54 (2009)

Chapter 5
Model Predictive Output Integral Discrete-Time Sliding-Mode Control

This chapter presents a control scheme termed model predictive output integral discrete-time sliding-mode control (MPOIDSMC) to achieve a precise positioning for a piezoelectric actuation stage. The controller features an integral type of sliding function based on the output error along with a sliding-mode state observer. The model predictive control methodology and the integral item are introduced to eliminate the chattering phenomenon and to achieve a low tracking error. The feasibility and effectiveness of the MPOIDSMC scheme is verified by conducting several experimental studies on a piezoelectric nanopositioning stage.

5.1 Introduction

In the last Chap. 4, a DTSMC scheme has been developed based on the full state feedback approach. In a typical micro-/nano-positioning system, only the output is available from the displacement sensor. Therefore, it is more attractive to design an output-based DTSMC strategy [4, 8]. In addition, the sliding function is commonly designed as a proportional action based on the output or output error. Recent works [6, 15, 16] show that an integral action in the sliding function is capable of improving the performance of the conventional DTSMC. At the same time, the strategy of model predictive control (MPC) can be employed to enhance the performance of a discrete-time system [12]. By combining the SMC and MPC concepts, model predictive sliding-mode control has been recently proposed to achieve the advantages of both methods [3, 14].

In this chapter, a scheme of MPOIDSMC with a sliding-mode state observer is presented for micro-/nano-positioning applications. The presented strategy is capable of improving the system performance by integrating MPC, output integral discrete-time sliding-mode control (OIDSMC), and state observer techniques together. Specifically, the MPC generates an optimal control to drive the system output to the sliding

© Springer International Publishing Switzerland 2016

Q. Xu and K.K. Tan, *Advanced Control of Piezoelectric Micro-/Nano-Positioning Systems*, Advances in Industrial Control,
DOI 10.1007/978-3-319-21623-2_5

surface, and the OIDSMC maintains the output trajectory on the sliding surface for the subsequent time. Moreover, a sliding mode observer is adopted to estimate the system state and to suppress the spillover effects. It is demonstrated that the integrated scheme eliminates the chattering effect by forcing the system trajectory to a vicinity of the sliding surface with a boundary layer of thickness $O(T^3)$ in an optimal manner, and achieves an output tracking error of the order $O(T^2)$. The produced ultimate error has a much lower magnitude than those reported in most of the previous works [15]. The theoretical analysis and the effectiveness of the proposed strategy are validated by experimental studies conducted on a piezo-driven nanopositioning system.

5.2 Problem Formulation

The dynamics model of a piezo-driven micro-/nano-positioning system can be described by a linear time-invariant (LTI) model accompanied by disturbance:

$$\dot{\mathbf{X}}(t) = \mathbf{A}_c\mathbf{X}(t) + \mathbf{B}_c\mathbf{u}(t) + \mathbf{D}_c\mathbf{f}(t) \tag{5.1}$$

$$\mathbf{Y}(t) = \mathbf{C}\mathbf{X}(t) \tag{5.2}$$

where the state vector $\mathbf{X} \in R^n$, the output $\mathbf{Y} \in R^p$, the control input $\mathbf{u} \in R^m$, the disturbance vector $\mathbf{f} \in R^q$ is supposed to be smooth and bounded, and $m \leq p < n$. The system matrices $\mathbf{A}_c$, $\mathbf{B}_c$, $\mathbf{D}_c$, and $\mathbf{C}$ are constant with approximate dimensions.

The disturbance $\mathbf{f}$ describes the combined effects of unmodeled nonlinear hysteresis, higher order dynamics, and external perturbations. It is assumed that $\mathbf{f}$ satisfies the matching condition, i.e., $\mathbf{D}_c = \mathbf{B}_c\delta_d$ where δ_d is a scalar.

Using a sampling time T, the continuous-time system model (5.1) can be discretized as:

$$\mathbf{X}_{k+1} = \mathbf{A}\mathbf{X}_k + \mathbf{B}\mathbf{u}_k + \mathbf{d}_k \tag{5.3}$$

$$\mathbf{Y}_k = \mathbf{C}\mathbf{X}_k \tag{5.4}$$

where $\mathbf{X}_k = \mathbf{X}(kT)$ and

$$\mathbf{A} = e^{\mathbf{A}_c T} \tag{5.5}$$

$$\mathbf{B} = \int_0^T e^{\mathbf{A}_c\tau} d\tau\, \mathbf{B}_c \tag{5.6}$$

$$\mathbf{d}_k = \int_0^T e^{\mathbf{A}_c\tau}\mathbf{B}_c\delta_d\mathbf{f}((k+1)T - \tau)d\tau. \tag{5.7}$$

It is observed that both $\mathbf{B}$ and $\mathbf{d}_k$ are of the order $O(T)$ with respect to the sampling time T. Additionally, the Properties 4.1 and 4.2 are employed to facilitate the control design. In addition, it is assumed that the triplet ($\mathbf{A}$, $\mathbf{B}$, $\mathbf{C}$) of the nominal system is

both controllable and observable with the matrices **B** and **C** being of full rank. In addition, the matrix **CB** is supposed to be invertible.

For a single-input and single-output (SISO) piezoelectric actuation system (i.e., $m = p = 1$), the concerned motion control problem is how to make the output (Y_k) precisely track a command reference input. A discrete-time sliding mode-based controller is presented in the next section.

5.3 MPOIDSMC Design

The design procedure of a MPOIDSMC control scheme is outlined in this section. First, the OIDSMC is designed based on an integral sliding function. Then, an integrated MPOIDSMC scheme is presented. The stability and tracking accuracy of the control algorithm are evaluated in detail.

5.3.1 OIDSMC Controller Design

The output tracking error is defined as:

$$E_k = Y_k - R_k \tag{5.8}$$

where R_k denotes the desired system output.

Based on the output error (5.8), a PI-type sliding function is defined as follows:

$$S_k = GE_k + K_I\xi_k \tag{5.9}$$

where

$$S = \{S_k | S_k = 0, \text{ for } k = 0, 1, \dots\} \tag{5.10}$$

represents the sliding surface or sliding hyperplane, and the integral error is

$$\xi_k = E_k + \xi_{k-1}. \tag{5.11}$$

In addition, G and K_I are constant positive proportional and integral gains, which are specified to assign appropriate eigenvalues for the system.

Considering that the equivalent control u_k^{eq} is the solution of $\Delta S = S_{k+1} - S_k = 0$ [2], it can be deduced that

$$\begin{aligned} & GE_{k+1} + K_I\xi_{k+1} = S_k \\ \Rightarrow\ & GE_{k+1} + K_I(E_{k+1} + \xi_k) = S_k \\ \Rightarrow\ & (G + K_I)E_{k+1} + K_I\xi_k = S_k \\ \Rightarrow\ & (G + K_I)[\mathbf{C}(\mathbf{A}\mathbf{X}_k + \mathbf{B}u_k + \mathbf{d}_k) - R_{k+1}] + K_I\xi_k = S_k \end{aligned} \tag{5.12}$$

which allows the derivation of the equivalent controller:

$$u_k^{eq} = -(\Omega \mathbf{CB})^{-1}(-S_k + \Omega \mathbf{CAX}_k + \Omega \mathbf{Cd}_k + K_I \xi_k - \Omega R_{k+1}) \quad (5.13)$$

where

$$\Omega = G + K_I. \quad (5.14)$$

However, the controller (5.13) is not realizable because it contains the unknown disturbance term $\mathbf{d}_k$ at the current time step. To solve this problem, the disturbance $\mathbf{d}_k$ is obtained by its one-step delayed estimation:

$$\hat{\mathbf{d}}_k = \mathbf{d}_{k-1} = \mathbf{X}_k - \mathbf{AX}_{k-1} - \mathbf{B}u_{k-1} \quad (5.15)$$

which is derived by noting (5.3).

Thus, Eq. (5.13) becomes

$$u_k^{eq} = -(\Omega \mathbf{CB})^{-1}(-S_k + \Omega \mathbf{CAX}_k + \Omega \mathbf{Cd}_{k-1} + K_I \xi_k - \Omega R_{k+1}). \quad (5.16)$$

5.3.1.1 Stability Analysis

Substituting Eq. (5.16) into Eq. (5.3) along with a necessary calculation, yields the closed-loop system state dynamics:

$$\mathbf{X}_{k+1} = \mathbf{UX}_k + \mathbf{Vd}_{k-1} + \mathbf{d}_k - \mathbf{d}_{k-1} + \mathbf{B}(\Omega \mathbf{CB})^{-1}(\Omega R_{k+1} - G R_k) \quad (5.17)$$

with

$$\mathbf{U} = \mathbf{A} - \mathbf{B}(\Omega \mathbf{CB})^{-1}(\Omega \mathbf{CA} - G\mathbf{C}) \quad (5.18)$$

$$\mathbf{V} = \mathbf{I} - \mathbf{B}(\Omega \mathbf{CB})^{-1}\Omega \mathbf{C} \quad (5.19)$$

where $\mathbf{I}$ denotes an identity matrix.

The eigenvalues of the matrices $\mathbf{U}$ and $\mathbf{V}$ are the solutions of $\det(z\mathbf{I} - \mathbf{U}) = 0$ and $\det(z\mathbf{I} - \mathbf{V}) = 0$, respectively, which determine the closed-loop state dynamics behavior. To ensure the stability of the closed-loop system, the eigenvalues of the two matrices should locate inside the unit circle in the complex z-plane.

5.3.1.2 Tracking Error Analysis

In view of Eqs. (5.12) and (5.14), the following expression can be obtained:

$$S_{k+1} = \Omega[\mathbf{C}(\mathbf{AX}_k + \mathbf{B}u_k + \mathbf{d}_k) - R_{k+1}] + K_I \xi_k. \quad (5.20)$$

Substituting Eq. (5.16) into Eq. (5.20), yields

$$S_{k+1} = S_k + \Omega \mathbf{C}\boldsymbol{\varepsilon}_k \tag{5.21}$$

where

$$\begin{aligned}\boldsymbol{\varepsilon}_k &= \mathbf{d}_k - \mathbf{d}_{k-1} \\ &= \int_0^T e^{\mathbf{A}_c \tau} \int_{kT-\tau}^{(k+1)T-\tau} \mathbf{B}_c \delta_d \dot{\mathbf{f}}(\sigma) d\sigma d\tau = O(T^2).\end{aligned} \tag{5.22}$$

Thus, in consideration of Property 4.2, it can be deduced from Eq. (5.21) that S_k has a magnitude of the order $O(T)$, i.e., the sliding surface has an ultimate bound of $O(T)$.

By noting Eqs. (5.8) and (5.9), the one-step forward error equation can be expressed as:

$$\begin{aligned}E_{k+1} &= Y_{k+1} - R_{k+1} \\ &= \mathbf{C}(\mathbf{A}\mathbf{X}_k + \mathbf{B}u_k + \mathbf{d}_k) - R_{k+1}.\end{aligned} \tag{5.23}$$

Substituting Eq. (5.16) into Eq. (5.23), yields

$$\begin{aligned}E_{k+1} &= \mathbf{C}(\mathbf{d}_k - \mathbf{d}_{k-1}) - \Omega^{-1}(K_I \xi_k - S_k) \\ &= \mathbf{C}\boldsymbol{\varepsilon}_k + \Omega^{-1} G E_k.\end{aligned} \tag{5.24}$$

Then, in view of Eq. (5.24) and Property 4.2, it is derived that the ultimate bound of the output tracking error E_k is of the order $O(T)$.

The error dynamics equation (5.24) also indicates that the gains should be designed to satisfy the condition:

$$|\Omega^{-1} G| < 1 \tag{5.25}$$

so that the closed-loop system is stable.

The equivalent controller as designed above takes effect in the sliding mode when the system trajectory is kept on the sliding surface. However, if the initial state of the system does not lie on the sliding surface S or external disturbances occur during the sliding-mode motion, the equivalent control alone cannot drive the trajectory toward S. Thus, an augmented controller is designed in the following discussion.

5.3.2 MPOIDSMC Controller Design

A common method to design a robust controller is to augment the equivalent control with a discontinuous switching control term, whose role is to force the system trajectory to reach the sliding mode. However, the common switching control may induce unwanted chattering phenomenon [17].

Here, an integrated MPC and OIDSMC control scheme is established to handle the nonlinearities and disturbances existed in the system. Specifically, the MPC is used to generate an optimal control (u_k^{mp}) to drive the system output to the sliding surface, and the OIDSMC (u_k^{eq}) is employed to maintain the output trajectory on the sliding surface for the subsequent time. In addition, a sliding-mode observer is designed to estimate the system state and to eliminate the spillover effects.

5.3.2.1 Controller Design

Substituting the augmented control

$$u_k = u_k^{eq} + u_k^{mp} \tag{5.26}$$

into Eq. (5.20) and noting Eq. (5.16), gives

$$S_{k+1} = S_k + \Omega \mathbf{C}\mathbf{B} u_k^{mp} + \Omega \mathbf{C}\boldsymbol{\varepsilon}_k \tag{5.27}$$

which describes the dynamics of the sliding mode and also represents a one-step future prediction of the sliding-mode dynamics.

Based on Eq. (5.27), an N-step prediction of the sliding-mode dynamics can be obtained as follows:

$$\begin{aligned} S_{k+N} = S_k &+ \Omega \mathbf{C}\mathbf{B}(u_k^{mp} + u_{k+1}^{mp} + \cdots + u_{k+N-1}^{mp}) \\ &+ (\Omega \mathbf{C}\boldsymbol{\varepsilon}_{k+N-1} + \cdots + \Omega \mathbf{C}\boldsymbol{\varepsilon}_{k+1} + \Omega \mathbf{C}\boldsymbol{\varepsilon}_k) \end{aligned} \tag{5.28}$$

where the positive integer N is known as the prediction horizon.

The N prediction functions can be stacked together into the form:

$$\mathbf{S}_k^a = \boldsymbol{\Lambda} S_k + \boldsymbol{\Phi} \mathbf{u}_{k-1}^a + \boldsymbol{\Gamma} \boldsymbol{\zeta}_{k-1} \tag{5.29}$$

where the vectors for the future sliding function, control effort, and disturbance estimation errors are:

$$\mathbf{S}_k^a = \begin{bmatrix} S_{k+1} \\ S_{k+2} \\ \vdots \\ S_{k+N} \end{bmatrix}, \ \mathbf{u}_{k-1}^a = \begin{bmatrix} u_k^{mp} \\ u_{k+1}^{mp} \\ \vdots \\ u_{k+N-1}^{mp} \end{bmatrix}, \ \boldsymbol{\zeta}_{k-1} = \begin{bmatrix} \boldsymbol{\varepsilon}_k \\ \boldsymbol{\varepsilon}_{k+1} \\ \vdots \\ \boldsymbol{\varepsilon}_{k+N-1} \end{bmatrix}. \tag{5.30}$$

Additionally, the three matrices take on the following forms:

$$\boldsymbol{\Lambda} = \begin{bmatrix} \mathbf{I} \\ \mathbf{I} \\ \vdots \\ \mathbf{I} \end{bmatrix} \tag{5.31}$$

$$\boldsymbol{\Phi} = \begin{bmatrix} \Omega\mathbf{CB} & 0 & \dots & 0 \\ \Omega\mathbf{CB} & \Omega\mathbf{CB} & \dots & 0 \\ \vdots & \vdots & \ddots & \vdots \\ \Omega\mathbf{CB} & \Omega\mathbf{CB} & \dots & \Omega\mathbf{CB} \end{bmatrix} \tag{5.32}$$

$$\boldsymbol{\Gamma} = \begin{bmatrix} \Omega\mathbf{C} & 0 & \dots & 0 \\ \Omega\mathbf{C} & \Omega\mathbf{C} & \dots & 0 \\ \vdots & \vdots & \ddots & \vdots \\ \Omega\mathbf{C} & \Omega\mathbf{C} & \dots & \Omega\mathbf{C} \end{bmatrix}. \tag{5.33}$$

Using the above notations, a cost function for minimization can be expressed by:

$$J = (\mathbf{S}_k^a)^T \mathbf{S}_k^a + w \left(\mathbf{u}_{k-1}^a\right)^T \mathbf{u}_{k-1}^a \tag{5.34}$$

where w is the weighting to limit the partial control effort. It is notable that $\mathbf{u}_{k-1}^a$ approaches to zero as $\mathbf{S}_k^a$ tends to zero. Thus, the cost function J will vanish at the steady state.

Substituting Eq. (5.29) into the cost function (5.34) and applying the optimization criterion by setting $\frac{\partial J}{\partial \mathbf{u}_{k-1}^a} = 0$, yields

$$\mathbf{u}_{k-1}^a = -(\boldsymbol{\Phi}^T\boldsymbol{\Phi} + w\mathbf{I})^{-1}\boldsymbol{\Phi}^T(\boldsymbol{\Lambda} S_k + \boldsymbol{\Gamma}\boldsymbol{\zeta}_{k-1}) \tag{5.35}$$

where the future disturbance values in $\boldsymbol{\zeta}_{k-1}$ are unknown. Thus, they are estimated by

$$\hat{\boldsymbol{\zeta}}_{k-1} = [\boldsymbol{\varepsilon}_{k-1}^T \ \boldsymbol{\varepsilon}_{k-1}^T \ \cdots \ \boldsymbol{\varepsilon}_{k-1}^T]^T. \tag{5.36}$$

Because only the first value of the predicted control sequence is used, the optimal control effort can be obtained as:

$$u_k^{mp} = -\mathbf{e}(\boldsymbol{\Phi}^T\boldsymbol{\Phi} + wI)^{-1}\boldsymbol{\Phi}^T(\boldsymbol{\Lambda} S_k + \boldsymbol{\Gamma}\hat{\boldsymbol{\zeta}}_{k-1}) \tag{5.37}$$

where the selection vector $\mathbf{e} = [1, 0, 0, \dots, 0]$.

Therefore, the total control action can be expressed as:

$$\begin{aligned} u_k &= u_k^{eq} + u_k^{mp} \\ &= -(\Omega\mathbf{CB})^{-1}[-S_k + \Omega\mathbf{CA}X_k + \Omega\mathbf{C}\mathbf{d}_{k-1} + K_I\xi_k - \Omega R_{k+1}] \\ &\quad -\mathbf{e}(\boldsymbol{\Phi}^T\boldsymbol{\Phi} + w\mathbf{I})^{-1}\Phi^T(\Lambda S_k + \boldsymbol{\Gamma}\hat{\boldsymbol{\zeta}}_{k-1}). \end{aligned} \tag{5.38}$$

5.3.2.2 Stability Analysis

Substituting Eq. (5.35) into the stacked equation (5.29) yields

$$\mathbf{S}_k^a = \boldsymbol{\Lambda} S_k - \boldsymbol{\Phi}(\boldsymbol{\Phi}^T\boldsymbol{\Phi} + w\mathbf{I})^{-1}\boldsymbol{\Phi}^T(\boldsymbol{\Lambda} S_k + \boldsymbol{\Gamma}\hat{\boldsymbol{\zeta}}_{k-1}) + \boldsymbol{\Gamma}\boldsymbol{\zeta}_{k-1} \tag{5.39}$$

where w is defined in the cost function (5.34) to limit the partial control input. For the convenience of analysis, it is assumed that there is no penalty for the partial control effort u_k^{mp}, i.e., $w = 0$.

Then, Eq. (5.39) becomes

$$\begin{aligned}\mathbf{S}_k^a &= \boldsymbol{\Lambda} S_k - (\boldsymbol{\Lambda} S_k + \boldsymbol{\Gamma}\hat{\boldsymbol{\zeta}}_{k-1}) + \boldsymbol{\Gamma}\boldsymbol{\zeta}_{k-1} \\ &= \boldsymbol{\Gamma}(\boldsymbol{\zeta}_{k-1} - \hat{\boldsymbol{\zeta}}_{k-1}).\end{aligned} \tag{5.40}$$

Considering only the first value of the predicted sliding hyperplane vector (5.40) and taking into account Eqs. (5.30) and (5.36), yields

$$\begin{aligned}S_{k+1} &= \Omega\mathbf{C}(\boldsymbol{\varepsilon}_k - \boldsymbol{\varepsilon}_{k-1}) \\ &= \Omega\mathbf{C}(\mathbf{d}_k - 2\mathbf{d}_{k-1} + \mathbf{d}_{k-2}) = O(T^3)\end{aligned} \tag{5.41}$$

which indicates that the magnitude of S_{k+1} is of the order $O(T^3)$ with the consideration of Property 4.1.

It is assumed that the change rate of ε_k is limited:

$$|S_{k+1}| = |\Omega\mathbf{C}(\boldsymbol{\varepsilon}_k - \boldsymbol{\varepsilon}_{k-1})| \leq \Delta_S \tag{5.42}$$

where $2\Delta_S$ is defined as the quasi-sliding mode bandwidth.

According to Definition 1 and Definition 2 in [1], it can be concluded that the system (5.3) satisfies the reaching condition of the quasi-sliding mode in the Δ_S vicinity of the sliding surface S in a finite number of steps. Therefore, the closed-loop control system is stable.

Remark 5.1 The essence of the presented MPOIDSMC is to drive the system trajectory to a quasi-sliding mode as shown in Eq. (5.42). One advantage of this quasi-sliding model [1] lies in that it does not require the system state to cross the sliding hyperplane S in each successive control step. Therefore, the chattering phenomenon is eliminated. This further results in a reduction of the control effort and improved control performance [1].

Remark 5.2 It is observed that S_{k+1} has the magnitude of order $O(T^3)$ as shown in Eq. (5.41). Therefore, the MPOIDSMC controller (5.38) drives the system trajectory to slide in the vicinity of S with an ultimate boundary layer of thickness $O(T^3)$, whose magnitude is much lower than the $O(T)$ thickness achieved by the OIDSMC controller. Therefore, a much lower control error is expected from the MPOIDSMC scheme, which will be proved later.

5.3.2.3 Sliding-Mode Observer Design

An insight into the controller (5.38) reveals that its implementation needs the state feedback $\mathbf{X}_k = [x_k, \dot{x}_k]^T$ of the system. However, only the displacement x_k is available in practice. In addition, a low-order linear model is usually employed as a nominal system model. Thus, the higher order dynamics is neglected in the controller design. However, the neglect of residual modes may result in both control spillover and observation spillover [9], which are undesirable because they may induce system instability and performance degradation [11]. It has been shown [5] that the sliding-mode observer is capable of eliminating the observation spillover effects in the vibration control of flexible structures.

Although various types of state observers are available [13], it is found that a second-order sliding-mode observer [7] is better than the ordinary first-order sliding-mode observer [10] in terms of chattering reduction. Hence, a second-order discrete sliding-mode state observer [7] is designed in this work to suppress the spillover effects and to estimate the full state by making use of the only measurable position information of the nanopositioning system.

The second-order discrete-time sliding-mode observer takes on the form:

$$\hat{\mathbf{X}}_{k+1} = \mathbf{A}\hat{\mathbf{X}}_k + \mathbf{B}u_k + \mathbf{H}\tilde{Y}_k + \mathbf{d}_{k-1} + \mathbf{K}_o \text{sat}(\frac{\tilde{Y}_k}{\delta_o}) \tag{5.43}$$

$$\hat{Y}_k = \mathbf{C}\hat{\mathbf{X}}_k \tag{5.44}$$

where $\tilde{Y}_k = Y_k - \hat{Y}_k$ is the sliding function, $\hat{\mathbf{X}}_k$ represents the estimate of $\mathbf{X}_k$, $\mathbf{H}$ is the observer gain vector, and δ_o denotes the boundary layer. The switching gain vector $\mathbf{K}_o$ is designed as:

$$\mathbf{K}_o \geq |\mathbf{d}_k - \mathbf{d}_{k-1}|. \tag{5.45}$$

Subtracting Eq. (5.43) from Eq. (5.3) allows the derivation of

$$\tilde{\mathbf{X}}_{k+1} = (\mathbf{A} - \mathbf{HC})\tilde{\mathbf{X}}_k + \mathbf{d}_k - \mathbf{d}_{k-1} - \mathbf{K}_o \text{sat}(\frac{\tilde{Y}_k}{\delta_o}) \tag{5.46}$$

where $\tilde{\mathbf{X}}_k = \mathbf{X}_k - \hat{\mathbf{X}}_k$ denotes the estimation error of the state $\mathbf{X}_k$. It is observed that the state observer is independent of the controller. To guarantee the stability of the observation unit, the observer gain $\mathbf{H}$ should be designed to make all the eigenvalues of the matrix $\mathbf{A} - \mathbf{HC}$ locate inside the unit circle.

Remark 5.3 The convergence speed of the observer relies on the location of the poles of the matrix $\mathbf{A} - \mathbf{HC}$. The poles can be arbitrarily placed by the gain vector $\mathbf{H}$. Generally, small pole value will give rapid convergence, and the convergence speed of the observer should be faster than the system response so that the observer dynamics is insignificant compared to the system dynamics. However, too small pole

produces instability of the system, which comes from the noise and spillover effects of the neglected system dynamics. Hence, a trial-and-error approach is needed for an appropriate pole placement.

5.3.2.4 Tracking Accuracy Analysis

In view of the convergence of the second-order sliding-mode observer, the following equation can be deduced at the ultimate steady state:

$$\widetilde{\mathbf{X}}_{k+1} \approx (\mathbf{A} - \mathbf{HC})\widetilde{\mathbf{X}}_k + \mathbf{d}_k - \mathbf{d}_{k-1}. \tag{5.47}$$

Considering that $\mathbf{d}_k - \mathbf{d}_{k-1}$ is of the order $O(T^2)$, it can be observed from Eq. (5.47) that the ultimate bound of the estimation error $\widetilde{\mathbf{X}}_k$ is of the order $O(T)$.

To evaluate the tracking error bound, Eq. (5.38) is substituted into Eq. (5.23). Then, a necessary calculation leads to

$$E_{k+1} = \mathbf{C}\boldsymbol{\varepsilon}_k + \Omega^{-1}GE_k - \mathbf{CBe}(\boldsymbol{\Phi}^T\boldsymbol{\Phi} + w\mathbf{I})^{-1}\boldsymbol{\Phi}^T(\boldsymbol{\Lambda}S_k + \boldsymbol{\Gamma}\hat{\boldsymbol{\xi}}_{k-1}). \tag{5.48}$$

To facilitate the analysis, it is assumed that there is no penalty for the partial control effort u_k^{mp}, i.e., $w = 0$. Then, Eq. (5.48) reduces to

$$\begin{aligned} E_{k+1} &= \mathbf{C}\boldsymbol{\varepsilon}_k + \Omega^{-1}GE_k - \mathbf{CBe}\Phi^{-1}(\boldsymbol{\Lambda}S_k + \boldsymbol{\Gamma}\hat{\boldsymbol{\xi}}_{k-1}) \\ &= \mathbf{C}\boldsymbol{\varepsilon}_k + \Omega^{-1}GE_k - \mathbf{CB}(\Omega\mathbf{CB})^{-1}(S_{k+1} + \Omega\mathbf{C}\boldsymbol{\varepsilon}_k) \\ &= \Omega^{-1}GE_k - \Omega^{-1}S_{k+1}. \end{aligned} \tag{5.49}$$

Taking into accout that S_{k+1} is of the order $O(T^3)$ as shown in Eq. (5.41), it can be deduced from Eq. (5.49) that $E_k = O(T^2)$. That is, the ultimate bound of the output tracking error is $O(T^2)$, which is much lower than the $O(T)$ tracking error obtained with the OIDSMC designed earlier.

5.4 Experimental Investigations

In this section, the designed controller is verified by a series of experimental studies conducted on a piezo-driven nanopositioning system.

5.4.1 Experimental Setup

The experimental setup employed in this work is depicted in Fig. 4.1. The piezostage is composed of a flexure-based compliant mechanism driven by a PSA with the stroke of 14.5 μm (model: TS18-H5-202, from Piezo Systems, Inc.). The stage output

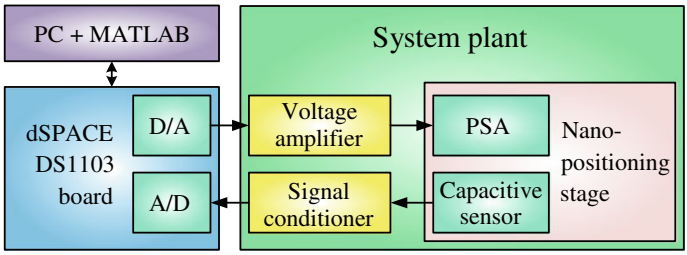

Fig. 5.1 Experimental setup for a nanopositioning stage

platform delivers a one-axis translational motion by making use of elastic deformations of the flexure hinges, and the output displacement is measured by a capacitive sensor (model: D-510.050, from Physik Instrumente Co., Ltd.). A dSPACE DS1103 (from dSPACE GmbH) rapid prototyping system equipped with 16-bit A/D and D/A converters are employed to implement the controller. The D/A channel produces an analog voltage output which is then amplified by a high-voltage amplifier (model: EPA-104, from Piezo Systems, Inc.) to provide a voltage ranging from −100 to 100 V for driving the PSA. In addition, the sensor output voltage signal is passed through a signal conditioner (model: E-852, from Physik Instrumente Co., Ltd.) and then acquired by the A/D channel. Control algorithms are developed with MATLAB® software and downloaded to DS1103 board via the ControlDesk interface to realize the real-time control. A block diagram of the hardware is shown in Fig. 5.1.

5.4.2 Plant Model Identification

The nanopositioning system is viewed as a linear system with bounded disturbances as described in (5.1). The linear plant model is identified by the frequency response approach via experiments. Specifically, swept sine waves with the amplitude of 0.1 V and frequency range of 1–2000 Hz are applied to the voltage amplifier to drive the PSA. The displacement responses of the nanopositioning stage are recorded using a sampling rate of 5 kHz.

The input–output data sets are used to identify the plant model by estimating a transfer function from the frequency response data. The frequency responses obtained by the experiment and the identified model are compared in Fig. 5.2. The first resonant mode occurs around 522 Hz, and the identified second-order model matches the system dynamics well in the frequencies below 600 Hz. The identified second-order transfer function is described by Eq. (5.50)

$$G(s) = \frac{5.876 \times 10^7}{s^2 + 183.7s + 1.076 \times 10^7}. \tag{5.50}$$

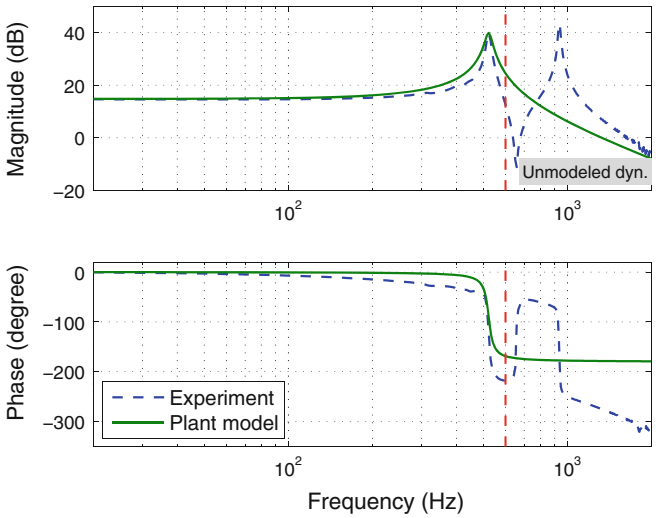

Fig. 5.2 Plant frequency responses obtained by experiments and the identified second-order model

In order to capture the high-frequency dynamics accurately, the identification of a much higher order model is required. Here, a simple second-order model is employed to demonstrate the effectiveness of the control scheme.

5.4.3 Controller Parameter Design

By comparing the state-space model (5.1) with (5.50) allows the generation of the system parameters, which can be converted into the discrete-time system model (5.3) with a sampling time T. In order to select a suitable T, the influences of the sampling rate selection on the controllability and observability of the discrete-time system are investigated.

As quantitative measures, the minimum singular values of the controllability matrix ($\mathscr{C}$) and observability matrix ($\mathscr{O}$):

$$\mathscr{C} = \begin{bmatrix} \mathbf{C} \\ \mathbf{CA} \end{bmatrix}, \quad \mathscr{O} = [\mathbf{B}\ \mathbf{AB}] \tag{5.51}$$

are employed as the controllability index and observability index, respectively. They serve as the indicators of how far the system is from being uncontrollable and unobservable. As the sampling frequency increases from 1000 to 5000 Hz, the two indices are generated as shown in Fig. 5.3.

It is observed that the magnitude of the observability index is about 10^4 times lower than that of the controllability index. Hence, the system is prone to be unobservable

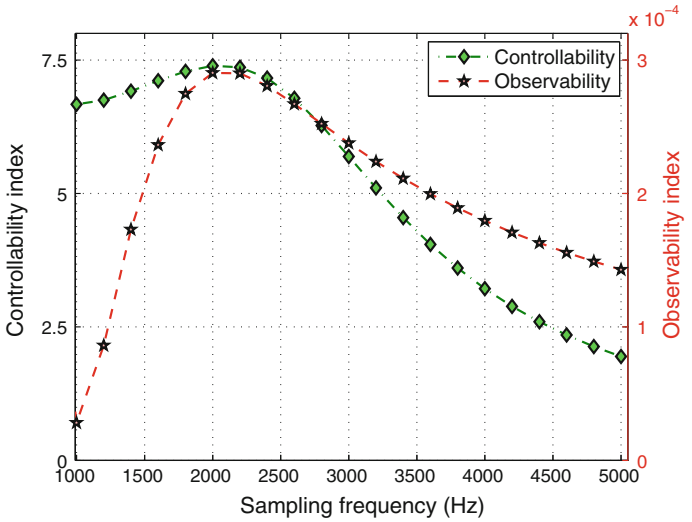

Fig. 5.3 The controllability index and observability index versus the sampling frequency

rather than uncontrollable. Both of the two indices arrive at the maximum value under the sampling frequency around 2000 Hz, and they decay as the increasing of the sampling rate. Additionally, in order to capture the system behavior precisely, a sampling frequency larger than the first resonant frequency (522 Hz) of the system is preferred. Considering the above issues, a sampling rate of 2000 Hz is adopted.

With $T = 0.0005$ s, the discrete-time system is represented by:

$$\mathbf{A} = \begin{bmatrix} -0.0388 & 0.0003 \\ -3126.6906 & -0.0921 \end{bmatrix}, \ \mathbf{B} = \begin{bmatrix} 5.6729 \\ 17075.5580 \end{bmatrix}, \ \mathbf{C} = [1 \ \ 0]. \tag{5.52}$$

Based on the obtained linear model, a sliding-mode observer is then constructed. The observer gain vector H is designed by the pole placement technique. Simulations suggest that small pole values produce rapid convergence in that a high bandwidth is achieved by the observer. However, experiments reveal that too small pole leads to instability of the system, which arises from the sensor noises and spillover effects of the neglected dynamics. To make a tradeoff, the two poles are assigned as $(-0.15, -0.15)$, which are chosen to guarantee a relatively quicker convergence as well as robustness of the observer in the presence of unmodeled dynamics. The corresponding gains are calculated as $\mathbf{H} = [0.1691, 0.0003]^T$. In addition, the switching gain vector is selected as $\mathbf{K}_o = [0.1, 0.1]^T$ and the boundary layer is chosen as $\delta_o = 50$ for the observer.

Next, the sliding function is designed by assigning appropriate proportional and integral gains G and K_I. It is found that the matrix $\mathbf{U}$ has a fixed eigenvalue of $\lambda_{u1} = -0.9669$ and the matrix $\mathbf{V}$ has two constant eigenvalues of 0 and 1. Thus, the gains are chosen to ensure that the free eigenvalue λ_{u2} of the matrix $\mathbf{U}$ locates inside

the unit circle. Moreover, it is found that as the increasing of sampling rate, the fixed eigenvalue moves more closely to the boundary of the unit circle, which drives the closed-loop system to unstable as a consequence. Noting that $\Omega = G + K_I$, the eigenvalue can be obtained as:

$$\lambda_{u2} = \frac{G}{\Omega} \tag{5.53}$$

which allows the calculation of

$$K_I = \frac{G}{\lambda_{u2}} - G. \tag{5.54}$$

By selecting $G = 1$, K_I can be considered as a function of the eigenvalue λ_{u2}. The influences of the selection of λ_{u2} on the controller performances are investigated in the subsequent section. In addition, to obtain better results, the prediction horizon $N = 10$ and weighting parameter $w = 2 \times 10^5$ are chosen for the MPOIDSMC after some trials.

5.4.4 Experimental Studies

The performance of the designed controller is verified by conducting several experimental studies.

First, a 10-μm step positioning is carried out to discover the effects of the assignment of the free eigenvalue λ_{u2}. For instance, with three different λ_{u2} of 0.80, 0.90 and 0.95, the corresponding K_I values are calculated as 0.25, 0.11 and 0.05, respectively. The positioning results are shown in Fig. 5.4. It is observed that as the increasing of the eigenvalue λ_{u2}, the integral action in the sliding function is weakened as the gain K_I is decreased. As a result, the speed of the system transient response becomes slow. The experimental result also demonstrates the effectiveness of the integral effect in the controller. To make a compromise between the overshoot and the response speed, $\lambda_{u2} = 0.90$ corresponding to $K_I = 0.11$ is selected for the set-point positioning.

Next, a consecutive step positioning with a step size of 10 nm is performed and the results are shown in Fig. 5.5. The steps can be identified from the results, which indicates that the positioning resolution of the system is about 10 nm. Additionally, the observer output indicates that the sliding-mode observer is capable of estimating the state from the noisy sensor readings.

Then, the motion tracking performance of the implemented controller is tested using a 5-Hz sinusoidal reference input as shown in Fig. 5.6a. In order to obtain a better result, the integral gain is selected as $K_I = 0.6667$ which corresponds to $\lambda_{u2} = 0.60$. The influence of the weighting parameter w selection is investigated by carrying out a sinusoidal motion tracking task. The 5-Hz reference input is shown in Fig. 5.6a. The tracking errors of the MPOIDSMC with different w values are shown in Fig. 5.6b. It is found that a larger weighting parameter $w = 2.5 \times 10^5$ results in

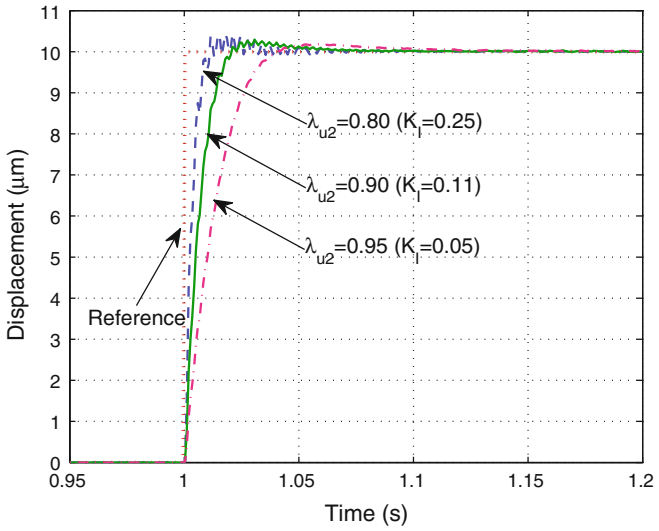

Fig. 5.4 The 10-μm step positioning results with different integral gains K_I

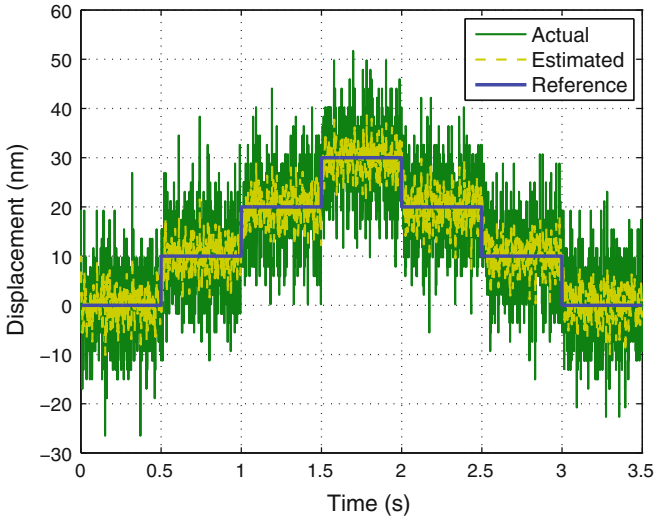

Fig. 5.5 The 10-nm consecutive step positioning results

a larger RMS tracking error of 0.0327 μm. By reducing the weighting parameter to $w = 2.0 \times 10^5$, a smaller RMS error of 0.0288 μm is obtained. However, further reduction of the weighting parameter to $w = 1.5 \times 10^5$ leads to the oscillation in the control result, which causes a larger RMS error of 0.1660 μm. The reason lies in that a smaller weighting parameter imposes less suppression on the MPC control action. To generate a better control result, $w = 2.0 \times 10^5$ is selected in this work.

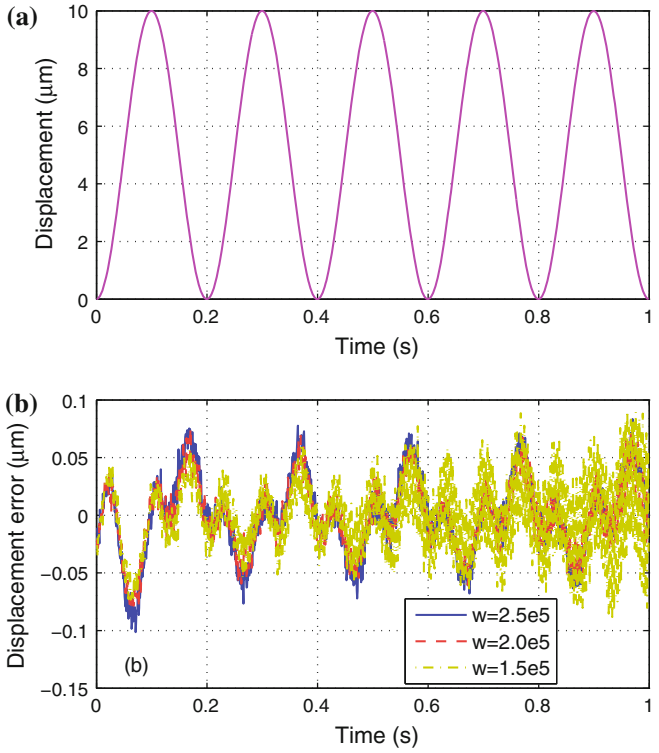

Fig. 5.6 Sinusoidal tracking results of MPOIDSMC with different parameters *w*

For a comparison study, the OIDSMC controller is also implemented. The control results of the OIDSMC and MPOIDSMC controllers are illustrated in Fig. 5.7. Due to the ummodeled hysteresis effect, the OIDSMC control produces the maximum peak-to-peak (PP) tracking error of 0.3117 μm and RMS error of 0.0731 μm, i.e., 3.12 and 0.73 % of the concerned motion range, respectively. In contrast, the MPOIDSMC scheme leads to the maximum PP error of 0.1586 μm and RMS error of 0.0288 μm, which accounts of 1.59 and 0.29 % of the motion range, respectively. As compared to the OIDSMC, the MPOIDSMC controller substantially reduces the PP and RMS errors by 49 and 60 %, respectively. The effectiveness of the proposed control is clearly revealed.

In addition, the position estimated by the sliding-mode observer is also illustrated in Fig. 5.7a, and the error of the observer output with respect to the reference input is depicted in Fig. 5.7b. The error has PP and RMS values of 1.27 and 0.44 % relative to the reference motion range, which demonstrates the efficiency of the sliding-mode observer.

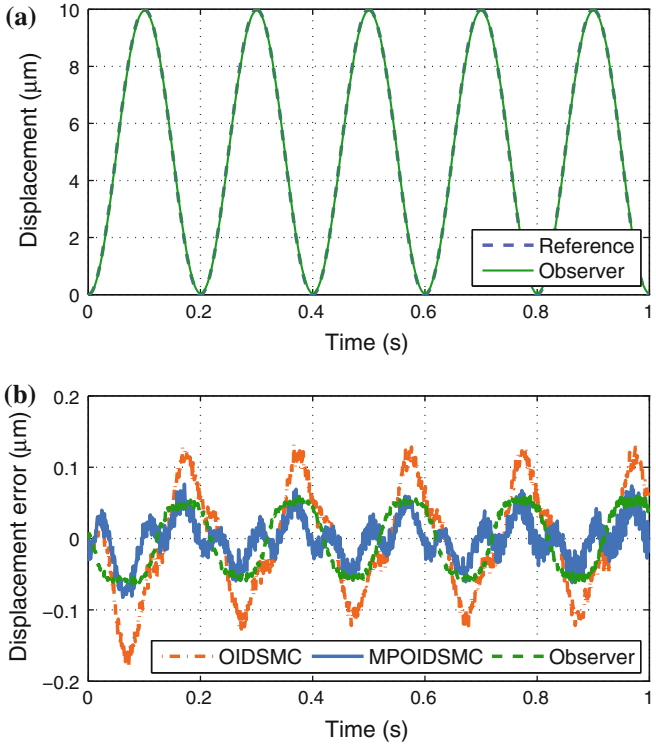

Fig. 5.7 Comparison of sinusoidal tracking results. **a** The reference position input and the position estimated by the sliding mode observer. **b** OIDSMC and MPOIDSMC control errors and the observer output error

5.4.5 Discussion on Controller Performance

The foregoing experimental results show that the observation spillover is successfully eliminated by the designed sliding-mode observer. A precise positioning with a resolution around 10 nm is achieved, and a fine motion tracking superior to OIDSMC result is obtained, which indicates that the hysteresis effects have been alleviated effectively. It is notable that the positioning resolution of the system can be enhanced by filtering the noises in the sensor readings.

The controller parameters are not optimally designed, and the current amplitudes of steady-state errors indicate that the performance of the MPOIDSMC may be improved to further reduce the control error down to the positioning resolution. Although there is plenty of room for performance improvement of the proposed controller, the enhancement of positioning precision for the micro-/nano-positioning system over OIDSMC control as elaborated by the conducted investigations demonstrates the effectiveness of the MPOIDSMC control scheme with integral sliding function and displays great potential for the future research.

As an output-based DTSMC, the major restriction of the proposed control scheme lies in that it is only applicable to minimum phase systems. In addition, it is found that the selection of the sampling frequency is limited by the observability of the discretized system. How to extend the controller to nonminimum phase systems and how to improve the system observability remain to be explored in the future work.

5.5 Chapter Summary

This chapter shows that a piezoelectrically driven micro-/nano-positioning system can be precisely controlled with the MPOIDSMC controller. The OIDSMC, MPC, and state observer are integrated together to improve the system performance, and the accuracy and stability of the control algorithm are analyzed in detail. Experimental results confirm that the unmodeled hysteresis has been effectively suppressed. A 10-nm resolution is achieved by the nanopositioning stage, and the MPOIDSMC scheme substantially improves the tracking performance as compared to the traditional OIDSMC control. Because the implementation of the controller does not require any bounds on uncertainties and unknown parameters of the system, the reported controller can be easily extended to other types of micro-/nano-positioning systems. Future works may be conducted in terms of the extension of the controller to nonminimum phase systems and the enhancement of the observability for discretized systems.

References

1. Bartoszewicz, A.: Discrete-time quasi-sliding-mode control strategies. IEEE Trans. Ind. Electron. **45**(5), 633–637 (1998)
2. Furuta, K.: Sliding mode control of a discrete system. Syst. Control Lett. **14**(2), 145–152 (1990)
3. Garcia-Gabin, W., Zambrano, D., Camacho, E.F.: Sliding mode predictive control of a solar air conditioning plant. Control Eng. Pract. **17**(6), 652–663 (2009)
4. Ha, Q.P., Trinh, H., Nguyen, H.T., Tuan, H.D.: Dynamic output feedback sliding-mode control using pole placement and linear functional observers. IEEE Trans. Ind. Electron. **50**(5), 1030–1037 (2003)
5. Kim, M.H., Inman, D.J.: Reduction of observation spillover in vibration suppression using a sliding mode observer. J. Vib. Control **7**(7), 1087–1105 (2001)
6. Li, Y.F., Wikander, J.: Model reference discrete-time sliding mode control of linear motor precision servo systems. Mechatronics **14**(7), 835–851 (2004)
7. Mihoub, M., Nouri, A.S., Ben Abdennour, R.: A chattering free second order discrete sliding mode observer: an experimentation on a chemical reactor. In: Proceedings of the 18th Mediterranean Conference on Control and Automation, pp. 739–744 (2010)
8. Nguyen, T., Su, W.C., Gajic, Z.: Singular perturbation analysis of discrete-time output feedback sliding mode control with disturbance attenuation. In: Proceedings of the American Control Conference, pp. 757–762 (2009)
9. Pai, M.C., Sinha, A.: Sliding mode control of vibration in a flexible structure via estimated states and H_∞/μ techniques. In: Proceedings of the American Control Conference, pp. 1118–1123 (2000)

10. Thein, M.W.L.: A discrete time variable structure observer with overlapping boundary layers. In: Proceedings of the American Control Conference, pp. 2633–2638 (2002)
11. Wang, D.A., Huang, Y.M.: Application of discrete-time variable structure control in the vibration reduction of a flexible structure. J. Sound Vib. **261**(3), 483–501 (2003)
12. Wills, A.G., Bates, D., Fleming, A.J., Ninness, B., Moheimani, S.O.R.: Model predictive control applied to constraint handling in active noise and vibration control. IEEE Trans. Control Syst. Technol. **16**(1), 3–12 (2008)
13. Wu, L., Gao, H., Wang, C.: Quasi sliding mode control of differential linear repetitive processes with unknown input disturbance. IEEE Trans. Ind. Electron. **58**(7), 3059–3068 (2011)
14. Xiao, L., Su, H., Chu, J.: Sliding mode prediction tracking control design for uncertain systems. Asian J. Control **9**(3), 317–325 (2007)
15. Xu, J.X., Abidi, K.: A discrete-time integral sliding mode control approach for output tracking with state estimation. In: Proceedings of the 17th IFAC World Congress, pp. 14,199–14,204 (2008)
16. Xu, J.X., Abidi, K.: Discrete-time output integral sliding-mode control for a piezomotor-driven linear motion stage. IEEE Trans. Ind. Electron. **55**(11), 3917–3926 (2008)
17. Zhu, Z., Xia, Y., Fu, M.: Adaptive sliding mode control for attitude stabilization with actuator saturation. IEEE Trans. Ind. Electron. **58**(10), 4898–4907 (2011)

Part III
Hysteresis-Model-Free, State-Observer-Free Feedback Control

Chapter 6
Digital Sliding-Mode Control of Second-Order Systems

This chapter presents the precision motion control of a piezoelectric bimorph actuator without using a hysteresis model and a state observer. A digital sliding-mode control (DSMC) scheme is developed based on a second-order plant model of the system. The nonlinearity effect is considered as a lumped perturbation, which is estimated by resorting to a one-step delayed estimation technique. The effectiveness of the approach without using state observer and hysteresis model has been validated by experimental investigations.

6.1 Introduction

Generally, discrete-time sliding-mode control (DTSMC) can be categorized into state-based and output-based methods. The former is developed based on the system state or state error [1, 17, 21], while the latter is implemented on the base of the system output or output error [18, 20]. Usually, the implementation of both methods requires the state feedback of the system. However, in majority of practical situations, only the position information of a piezoelectric actuator system is provided by the displacement sensor. Hence, a state observer is indispensable for the practical realization of DSMC [1, 18, 20, 21], which complicates the control design procedure. Furthermore, an improperly designed state observer may cause instability of the system. In this sense, it is desirable to eliminate the use of state observer. A DTSMC whose implementation does not need a state observer is termed a DSMC scheme.

In the literature, a few efforts have been made toward the DSMC strategy. For example, an input–output-based adaptive DSMC has been developed in [13], which is based solely on input and output data. However, the controller is dedicated to a first-order model with long dead time. It is not suitable for a piezoelectric actuation system which typically features a plant model of higher order preceded by complicated nonlinearity. To relax the restriction of the first-order plant model as required in

© Springer International Publishing Switzerland 2016

Q. Xu and K.K. Tan, *Advanced Control of Piezoelectric Micro-/Nano-Positioning Systems*, Advances in Industrial Control,
DOI 10.1007/978-3-319-21623-2_6

[13], a new input–output-based DSMC control has been figured out for a velocity tracking system [14]. Adaptive coefficients of the switching hyperplane are employed to tolerate the modeling error, and the effectiveness is verified by simulation studies. Nonetheless, due to a relatively long parameter adaptation process, the adaptive control normally leads to a slow transient response before attaining the steady state [4, 19]. On the other hand, the generalized minimum variance control (GMVC) scheme can be employed to develop a DSMC control without using a state observer. To improve the tracking accuracy, a DSMC scheme is presented in [10] to achieve the $O(T^2)$ and $O(T^3)$ accuracy of the sliding hypersurface. This scheme is developed based on input/output measurements and the GMVC technique. Nevertheless, the output tracking accuracy is unknown and filtering is required to suppress the induced chattering phenomenon. To eliminate the chattering completely, a fuzzy sliding mode control is demanded [9]. In addition, the multirate output feedback technique has been developed to release the need of the entire state vector for the realization of DSMC control scheme [2].

This chapter presents the design of a simple DSMC scheme without using the complicated hysteresis model and state observer for precision motion control of a piezoelectric actuator. Specifically, the unmodeled nonlinearity effects are treated as a lumped perturbation and the perturbation is estimated by resorting to a one-step delayed estimation technique. Furthermore, the avoidance of state observer is realized by developing a new DSMC based on a discrete-time second-order dynamics model of the system. The local stability of the closed-loop system is proved theoretically, and the effectiveness of the proposed scheme is validated through experimental investigations.

6.2 Dynamics Model and Problem Formulation

Piezoelectric bimorph actuators are popularly employed to construct microgrippers for performing delicate manipulation tasks. A multi-layer piezoelectric bimorph actuator is illustrated in Fig. 6.1, which consists of a central layer of metal and four layers of piezoelectric materials. Driven by an excitation voltage u, the free end of the

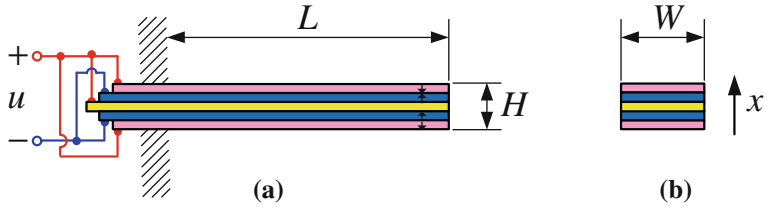

Fig. 6.1 Illustration of a four-layer piezoelectric bimorph with a brass-reinforced inner layer. **a** Front view. **b** Side view

cantilever undergoes an output displacement x. In order to achieve a precise positioning, both piezoelectric nonlinearities and external disturbances call for a suitable control technique.

The dynamics model of a piezoelectric actuator driven by an input voltage can be established as follows:

$$M\ddot{x}(t) + B\dot{x}(t) + Kx(t) = Du(t) + P(t) \tag{6.1}$$

where t is the time variable; parameters M, B, K, and x represent the mass, damping coefficient, stiffness, and output displacement of the actuator, respectively; D is the piezoelectric coefficient; and u denotes the input voltage. In addition, it is assumed that the parameters M, B, K, and D are known by the approach of system identification. The perturbation term $P(t)$ describes the lumped effect of piezoelectric hysteresis, creep, external force, parameter uncertainties, and other disturbances. It is notable that when the driving voltage is $u = 0$, P does not include the piezoelectric hysteresis and creep effects.

To devise a DSMC control scheme, a discrete-time dynamics model is developed. Specifically, dividing both sides of Eq. (6.1) by M results in

$$m\ddot{x}(t) + b\dot{x}(t) + kx(t) = du(t) + p(t) \tag{6.2}$$

where $m = 1, b = \frac{B}{M}, k = \frac{K}{M}, d = \frac{D}{M}$, and $p(t) = \frac{P(t)}{M}$.

Then, the continuous-time model (6.2) is discretized by adopting a small sampling time T. For the purpose of discretization, several approaches are available, e.g., the zero-order hold. In particular, the Euler backward difference is employed owing to its simplicity [7, 15, 16]:

$$\dot{x}(t) \approx \frac{1}{T}[x(kT) - x(kT - T)] \tag{6.3}$$

$$\ddot{x}(t) \approx \frac{1}{T^2}[x(kT) - 2x(kT - T) + x(kT - 2T)] \tag{6.4}$$

where k denotes the kth time step.

Thus, the continuous-time dynamics model (6.2) is converted into an equivalent discrete-time form:

$$\bar{m}x_{k-2} + \bar{b}x_{k-1} + \bar{k}x_k = \bar{d}u_k + p_k \tag{6.5}$$

where $x_{k-2} = x(kT - 2T)$ and

$$\bar{m} = \frac{1}{T^2},\ \bar{b} = -\frac{b}{T} - \frac{2}{T^2},\ \bar{k} = k + \frac{b}{T} + \frac{1}{T^2},\ \bar{d} = d. \tag{6.6}$$

It is notable that the backward difference equations (6.3) and (6.4) are employed to discretize the continuous-time model (6.2), and the discretization noises are not considered here. The discrete-time model (6.5) includes the delayed versions x_{k-2}

and x_{k-1} of the plant output x_k. Similar to other approaches such as zero-order hold, the main problem of the discretization is the generated time delay about $T/2$. The time delay causes slow response in transient behavior of the closed-loop control system [3]. Here, the time delay is neglected because a small sampling time T is selected.

Based on the perturbation estimation technique [5], the perturbation term p_k can be generated by its one-step delayed estimation:

$$\hat{p}_k = p_{k-1} = -\bar{d}u_{k-1} + \bar{m}x_{k-3} + \bar{b}x_{k-2} + \bar{k}x_{k-1}. \tag{6.7}$$

Hence, the dynamics model (6.5) can be rewritten as

$$\bar{m}x_{k-2} + \bar{b}x_{k-1} + \bar{k}x_k = \bar{d}u_k + \hat{p}_k - \tilde{p}_k \tag{6.8}$$

where $\tilde{p}_k = \hat{p}_k - p_k$ is the perturbation estimation error, which can be further expressed as

$$\tilde{p}_k = p_{k-1} - p_k \approx -\dot{p}(t)T = -\frac{T}{M}\dot{P}(t). \tag{6.9}$$

Assumption 6.1 The first derivative of the lumped perturbation $P(t)$ is bounded, i.e., $|\dot{P}(t)| \leq \delta$.

In view of Eq. (6.9) and Assumption 6.1, it can be deduced that $\tilde{p}_k$ is also bounded, i.e.,

$$|\tilde{p}_k| \leq \frac{T\delta}{M}. \tag{6.10}$$

In order to overcome the error term $\tilde{p}_k$ and to achieve a precise position control, a DSMC scheme is devised in the next section.

6.3 DSMC Design

A DSMC with integral action is developed in this section. First, substituting the estimated perturbation term (6.7) into the dynamics model (6.8) allows the calculation of the position:

$$x_k = \frac{1}{\bar{k}}[\bar{d}(u_k - u_{k-1}) + \bar{m}x_{k-3} + (\bar{b} - \bar{m})x_{k-2} + (\bar{k} - \bar{b})x_{k-1} - \tilde{p}_k]. \tag{6.11}$$

Based on the position error $e_k = x_k - x_{d,k}$ where $x_{d,k}$ is the desired position trajectory, a proportional-integral (PI) type of sliding function is defined as follows:

$$s_k = \lambda_P e_k + \lambda_I \varepsilon_k \tag{6.12}$$

where λ_P and λ_I are the proportional and integral gains, respectively.

In addition, the integral error is defined as

$$\varepsilon_k = \sum_{i=1}^{k} e_i = e_k + \varepsilon_{k-1}. \tag{6.13}$$

Concerning the reaching law, there are two different definitions as summarized in [11, 22]. Here, the following definition is adopted [6]:

$$\Delta s_k = s_k - s_{k-1} = 0. \tag{6.14}$$

Considering that the equivalent control u_k^{eq} is the solution to Eq. (6.14), the following deductions hold:

$$\lambda_P e_k + \lambda_I \varepsilon_k = s_{k-1} \tag{6.15}$$

$$\Rightarrow (\lambda_P + \lambda_I) e_k + \lambda_I \varepsilon_{k-1} = s_{k-1} \tag{6.16}$$

$$\Rightarrow (\lambda_P + \lambda_I)(x_k - x_{d,k}) + \lambda_I \varepsilon_{k-1} = s_{k-1}. \tag{6.17}$$

Then, substituting Eq. (6.11) into Eq. (6.17) and ignoring the estimation error $\tilde{p}_k$ lead to the equivalent control:

$$\begin{aligned} u_k^{\text{eq}} = u_{k-1} &+ \frac{1}{\bar{d}}\left[\frac{\bar{k}}{\lambda_A} s_{k-1} - \frac{\bar{k}}{\lambda_A}\lambda_I \varepsilon_{k-1} + \bar{k} x_{d,k}\right] \\ &- \frac{1}{\bar{d}}\left[\bar{m} x_{k-3} + (\bar{b} - \bar{m}) x_{k-2} + (\bar{k} - \bar{b}) x_{k-1}\right] \end{aligned} \tag{6.18}$$

where the gain $\lambda_A = \lambda_P + \lambda_I$.

The equivalent control (6.18) represents the control action for the case of perfect disturbance estimation, i.e., $\tilde{p}_k = 0$. It takes effect in the sliding phase when the position trajectory is kept on the sliding surface ($s_k = 0$). However, if a large error $\tilde{p}_k$ occurs during the sliding phase, the stand-alone equivalent control cannot drive the position toward the sliding surface. Thus, the equivalent control is augmented by a switching control u_k^{sw} to give the total control action:

$$u_k = u_k^{\text{eq}} + u_k^{\text{sw}} \tag{6.19}$$

i.e.,

$$\begin{aligned} u_k = u_{k-1} &+ \frac{1}{\bar{d}}\left[\frac{\bar{k}}{\lambda_A} s_{k-1} - \frac{\bar{k}}{\lambda_A}\lambda_I \varepsilon_{k-1} + \bar{k} x_{d,k}\right] \\ &- \frac{1}{\bar{d}}\left[\bar{m} x_{k-3} + (\bar{b} - \bar{m}) x_{k-2} + (\bar{k} - \bar{b}) x_{k-1}\right] - \frac{\lambda_S}{\bar{d}} \text{sgn}(s_{k-1}) \end{aligned} \tag{6.20}$$

where λ_S is a positive control gain and $\text{sgn}(\cdot)$ denotes the signum function.

Theorem 6.1 *For the system (6.8) with Assumption 6.1 and sliding function (6.12), if the controller (6.20) with gain $\lambda_S \geq |\tilde{p}_k|$ is employed, then the discrete sliding mode will occur with a quasi-sliding domain width of QSD $= \frac{\lambda_A \lambda_S}{\bar{k}} + \frac{\lambda_A}{\bar{k}}|\tilde{p}_k|$ after a finite number of steps.*

Proof Substituting Eq. (6.20) into the expression of the sliding function (6.12), a necessary algebra operation gives

$$\begin{aligned} s_k &= \lambda_A(x_k - x_{d,k}) + \lambda_I \varepsilon_{k-1} \\ &= \lambda_A\{\frac{1}{\bar{k}}[\bar{d}(u_k - u_{k-1}) + \bar{m}x_{k-3} + (\bar{b} - \bar{m})x_{k-2} \\ &\quad +(\bar{k} - \bar{b})x_{k-1} - \tilde{p}_k] - x_{d,k}\} + \lambda_I \varepsilon_{k-1} \\ &= s_{k-1} - \frac{\lambda_A}{\bar{k}}[\lambda_S \mathrm{sgn}(s_{k-1}) - \tilde{p}_k]. \end{aligned} \tag{6.21}$$

It is notable that the parameters $\bar{k}$, λ_A, and λ_S are all positive. In the case of $s_{k-1} \geq 0$, it can be derived that

$$s_k \leq s_{k-1} \quad \text{if} \quad \lambda_S \geq |\tilde{p}_k|. \tag{6.22}$$

Otherwise, if $s_{k-1} < 0$, then

$$s_k \geq s_{k-1} \quad \text{if} \quad \lambda_S \geq |\tilde{p}_k|. \tag{6.23}$$

Hence, in view of Eqs. (6.22) and (6.23), the following conclusion is derived:

$$|s_k| \leq |s_{k-1}| \quad \text{if} \quad \lambda_S \geq |\tilde{p}_k|. \tag{6.24}$$

Considering Eq. (6.10), it is deduced from Eq. (6.24) that s_k decreases monotonously, and the discrete sliding mode is reached after a finite number of steps.

According to Eq. (6.21), the change value of the sliding function can be expressed into the form:

$$\begin{aligned} s_k - s_{k-1} &= -\frac{\lambda_A}{\bar{k}}[\lambda_S \mathrm{sgn}(s_{k-1}) - \tilde{p}_k] \\ &= \mp\frac{\lambda_A \lambda_S}{\bar{k}} + \frac{\lambda_A}{\bar{k}}\tilde{p}_k \neq 0. \end{aligned} \tag{6.25}$$

Hence, the quasi-sliding domain, which represents the variation of the sliding function change, can be determined as

$$|s_k - s_{k-1}| \leq \frac{\lambda_A \lambda_S}{\bar{k}} + \frac{\lambda_A}{\bar{k}}|\tilde{p}_k| = \mathrm{QSD}. \tag{6.26}$$

Remark 6.1 It is notable that only the local convergence is obtained in Theorem 6.1 due to the lack of knowledge of the bound value for $\tilde{p}_k$. In addition, the relationship (6.24) represents a sufficient condition for the existence of discrete sliding mode [12]. The selection of parameter λ_S has no direct relation to the initial conditions. Generally, λ_S as well as λ_P and λ_I can be assigned in consideration of the quasi-sliding domain width as represented by Eq. (6.26).

Remark 6.2 It has been shown that the relationship of $|s_k| \leq |s_{k-1}|$ can be decomposed into two inequalities [12]:

$$(s_k - s_{k-1})\,\mathrm{sgn}(s_{k-1}) \leq 0 \tag{6.27}$$

$$(s_k + s_{k-1})\,\mathrm{sgn}(s_{k-1}) > 0 \tag{6.28}$$

which are called sliding condition and convergence condition, respectively. Because the condition (6.27) itself may cause instability and divergence, the convergence on the sliding surface is assured by the condition (6.28).

Remark 6.3 Due to the discontinuity of the signum function $\mathrm{sgn}(\cdot)$, chattering may occur in the control input. To alleviate the chattering phenomenon, the boundary layer technique is adopted by replacing the signum function in Eq. (6.20) with the saturation function [21]:

$$\mathrm{sat}(s_k) = \begin{cases} \mathrm{sgn}(s_k) & \text{if} \quad |s_k| > \varepsilon \\ s_k/\varepsilon & \text{if} \quad |s_k| \leq \varepsilon \end{cases} \tag{6.29}$$

where the boundary layer thickness ε ensures that s_k is bounded by $\pm\varepsilon$. In practice, a tradeoff between the chattering and tracking error is needed to assign the parameter ε.

6.4 Experimental Studies

In this section, the DSMC controller is validated by conducting a series of experimental studies on a prototype system.

6.4.1 Experimental Setup

The experimental setup of a piezoelectric microgripper prototype is depicted in Fig. 6.2. The gripper is composed of two four-layer piezoelectric bimorph actuators with dimension of $L \times H \times W = 26 \times 5 \times 0.86\,\mathrm{mm}^3$, as shown in Fig. 6.1. In this work, only one actuator is used which is driven by a high-voltage amplifier (model: EPA-104, from Piezo Systems, Inc.). The output displacement at the free end of the actuator is measured by a laser displacement sensor (model: LK-H055, from Keyence Corp.), which has a resolution of 25 nm within a measuring range

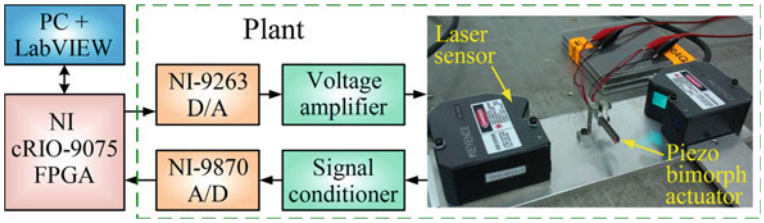

Fig. 6.2 Experimental setup of a piezoelectric bimorph actuator system

of 20 mm. In addition, a National Instruments (NI) cRIO-9075 real-time controller (from National Instruments Corp.) equipped with NI-9263 D/A module and NI-9870 A/D module is adopted to produce excitation voltage signals and acquire the sensor readings, respectively. The NI cRIO-9075 combines a real-time processor and a reconfigurable field-programmable gate array (FPGA) within the same chassis. The chassis is connected to a computer via Ethernet port for communication. Moreover, LabVIEW™ software is employed to realize a deterministic real-time control of the piezoelectric actuator system.

6.4.2 Plant Model Identification

By applying an input sine wave with the amplitude of 0.5 V and varying frequency of 1–1000 Hz to the actuator, the output position responses are recorded. The input–output data sets are then used to identify the plant model by estimating a transfer function G from the frequency response data. The identified second-order model is shown below:

$$G(s) = \frac{1.141 \times 10^8}{s^2 + 126.8\,s + 5.943 \times 10^6}. \tag{6.30}$$

The frequency responses obtained from the experimental data and the identified model G in Eq. (6.30) are compared in Fig. 6.3.

Here, the simple second-order model is employed to demonstrate the effectiveness of the control scheme. By comparing Eq. (6.2) and inverse Laplace transform of Eq. (6.30), the dynamics model parameters can be derived as $b = 126.8$ N s/μm, $k = 5.943 \times 10^6$ N/μm, and $d = 1.141 \times 10^8$ μm/V.

The dominant time constant of the plant is calculated as $\tau = 0.0158$ s. Generally, for the digital control implementation, it has been suggested to select a sampling time less than $\tau/3$ (i.e., 0.0053 s) of the plant [23]. In this work, a sampling time is chosen as $T = 0.004$ s. With such a sampling time, the discrete-time model parameters are obtained by resorting to Eq. (6.6).

The influence of the sampling time T on the performance of sliding-mode control systems has been investigated in the literature [7]. It has been shown that the smaller

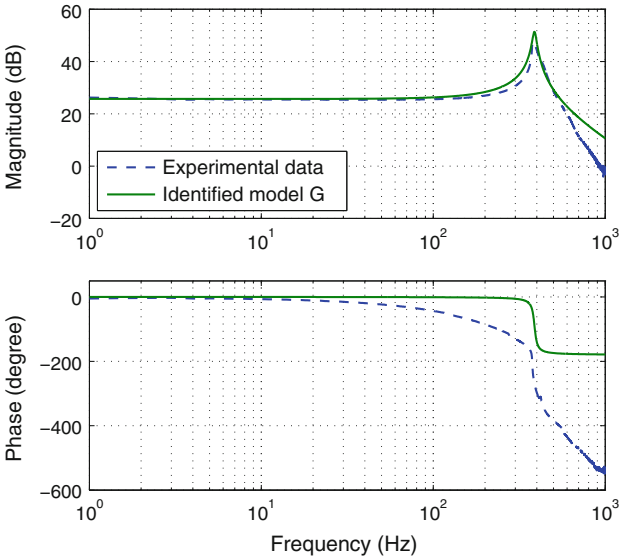

Fig. 6.3 Frequency responses of the system obtained by experiment and identified second-order model

the sampling time interval, the better the control performance. Therefore, a smaller sampling time can be adopted to further improve the control results.

6.4.3 Experimental Results

For the purpose of comparison, a traditional PID controller is also implemented:

$$u_k^{\text{PID}} = K_p e_k + K_i \sum_{j=0}^{k} e_j + K_d (e_k - e_{k-1}) \tag{6.31}$$

where the position error $e_k = x_{d,k} - x_k$ with $x_{d,k}$ and x_k representing the desired and actual system output at the kth time step, respectively. K_p, K_i, and K_d denote the proportional, integral, and derivative gains, respectively. In this work, the control gains are tuned by the trial-and-error approach to obtain a small tracking error.

6.4.3.1 Set-Point Positioning Results

First, the set-point positioning performance of the designed controller is examined. The parameters of the DSMC and PID controllers are tuned by several trials to generate a rapid response with the same magnitude of overshoot. By assigning

Table 6.1 Control parameters of the PID and DSMC controllers

Controller	Parameters			
	K_p	K_i	K_d	
PID #1	0.017	0.534	2×10^{-4}	
PID #2	0.032	1.011	8×10^{-5}	
	λ_P	λ_I	λ_S	ε
DSMC #1	30	1	1×10^{4}	100
DSMC #2	0.5	1	8×10^{5}	10

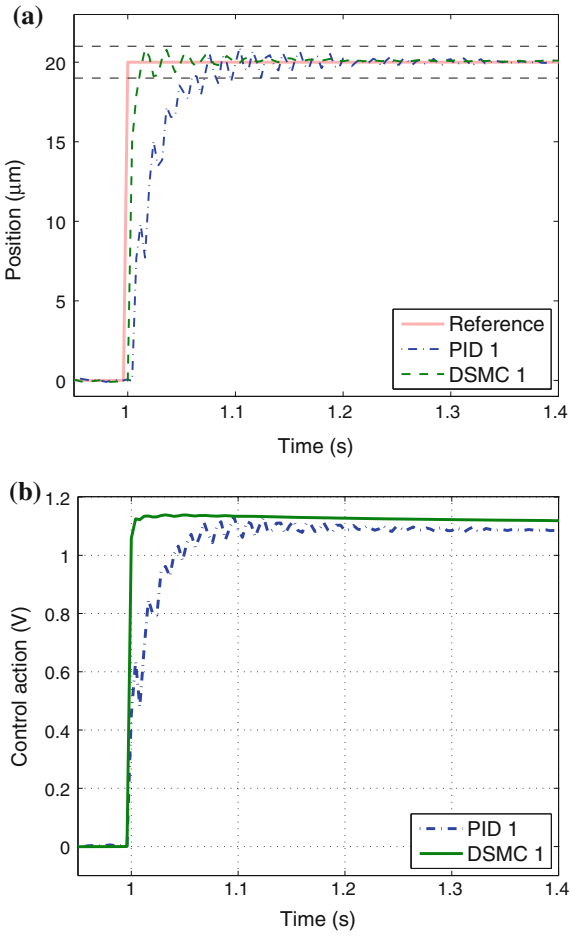

Fig. 6.4 Set-point positioning results of PID #1 and DSMC #1. **a** Positioning results. **b** Control actions

$\lambda_P = 30$, $\lambda_I = 1$, $\lambda_S = 1\times10^4$, and $\varepsilon = 100$ as shown in Table 6.1, the positioning result of the DSMC #1 is depicted in Fig. 6.4. In addition, the parameters of PID controller #1 are tuned as shown in Table 6.1. The comparison of the two

Table 6.2 Positioning results and performance improvement of DSMC with respect to PID controller

Performance	PID	DSMC	Improvement (%)
Set-point positioning			
5 % settling time (s)	0.095	0.048	49.5
Steady-state RMSE (μm)	0.042	0.031	26.2
Sinusoidal motion tracking			
MAXE%	7.26	1.48	79.6
RMSE%	4.00	0.62	84.5
Arbitrary motion tracking			
MAXE%	18.86	2.86	84.8
RMSE%	9.99	1.29	87.1

controller results is tabulated in Table 6.2, where the steady-state root-mean-square error (RMSE) is calculated from the data of the last one second.

From the positioning results as shown in Fig. 6.4, it is observed that both controllers produce no explicit overshoot. Moreover, the DSMC achieves a shorter settling time and a lower steady-state error, which indicates the improvements of 49.5 and 26.2 %, respectively, over the PID control. The control actions are depicted in Fig. 6.4b, which shows that no chattering effect exists in DSMC. However, a further decrease of the control gain λ_P or increase of λ_S will produce a quicker transient response with clear overshoot effect. Therefore, a compromise between the transient speed and overshoot is required to adjust the control gains in practice.

Concerning the DSMC scheme, the time histories of the sliding function s_k and its variation Δs_k are depicted in Fig. 6.5a. The perturbation estimation error is shown in Fig. 6.5b, which reveals an initial value around 1.2×10^8. Fig. 6.5a exhibits that Δs_k is well constrained within the quasi-sliding domain, which confirms the QSD as predicted by (6.26) for the given parameters and the perturbation estimation error. Additionally, in the controller DSMC #1, $\lambda_S = 1\times10^4$ is selected, which is less than the initial value of $|\tilde{p}_k|$. This means that it is not necessary to assign λ_S as the initial value of $|\tilde{p}_k|$. Actually, the initial value of $|\tilde{p}_k|$ is not always available in practice. Thus, λ_S can be assigned by the trial-and-error approach.

In addition, Fig. 6.5a indicates that when the sliding mode is arrived, the sliding function s_k is kept within the interval between -15 and -4. Hence, s_k is well constrained by the boundary thickness parameter $\varepsilon = 100$. On the other hand, the sliding function variation Δs_k varies between -3 and 3, but it does not arrive at zero due to the inherent property of discrete sliding mode. Anyway, Δs_k is more close to zero than s_k. This phenomenon confirms the effectiveness of the selected reaching law (6.14).

Moreover, the data points that do not satisfy the condition of $\lambda_S \geq |\tilde{p}_k|$ in Eq. (6.24) are marked by circles in Fig. 6.5b. The time histories of the sliding condition (6.27) and the convergence condition (6.28) are shown in Fig. 6.5c, d, respectively. Fig. 6.5d illustrates that all of the circle points meet the convergence condition except

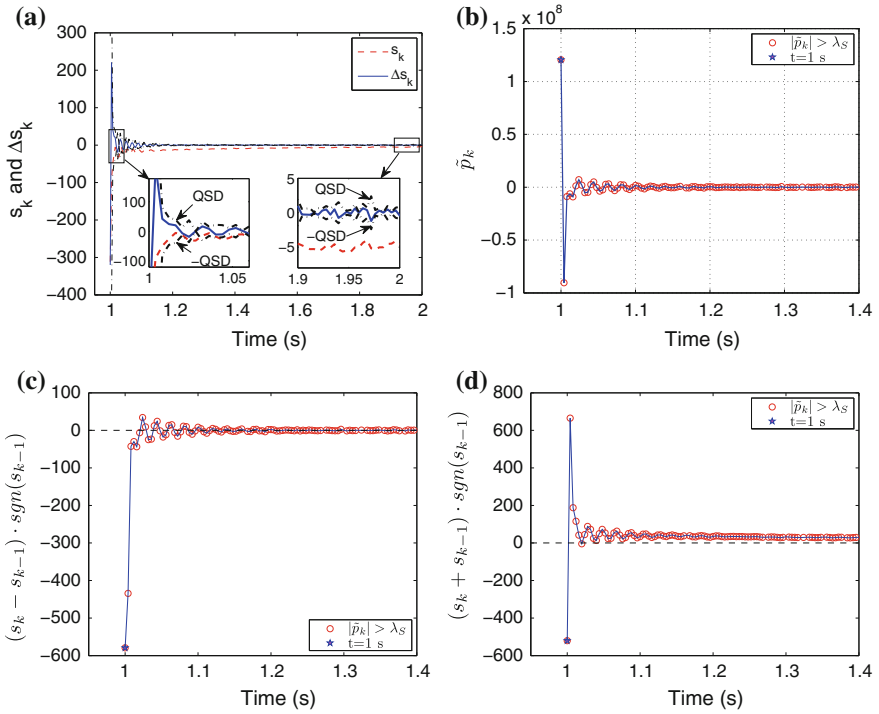

Fig. 6.5 Set-point positioning results of DSMC #1. **a** Time evolutions of s_k and Δs_k. **b** Perturbation estimation error $\tilde{p}_k$. **c** Evolution of sliding condition. **d** Evolution of convergence condition

for the initial one at the time of 1 s. On the other hand, this initial point satisfies the sliding condition as revealed in Fig. 6.5c. It means that the convergence on the sliding manifold is reached in one sampling period. Hence, all of the points meet either the sliding condition or the convergence condition. This explain the reason why the control system still converges even though the relationship of $\lambda_S \geq |\tilde{p}_k|$ is not satisfied (Fig. 6.5).

6.4.3.2 Sinusoidal Tracking Results

Next, the tracking performance of the designed controller for a 1.25-Hz sinusoidal motion, as shown in Fig. 6.6a, is verified. Although the motion tracking can be implemented by employing the foregoing PID #1 and DSMC #1 controllers directly, relatively large tracking errors are produced. In order to achieve better tracking accuracy for the sinusoidal input, PID #2 and DSMC #2 controllers are adopted by finely tuning the parameters through several trials. Specifically, the control parameters of the two controllers are shown in Table 6.1. The positioning errors of PID #2 and DSMC #2 are depicted in Fig. 6.6b.

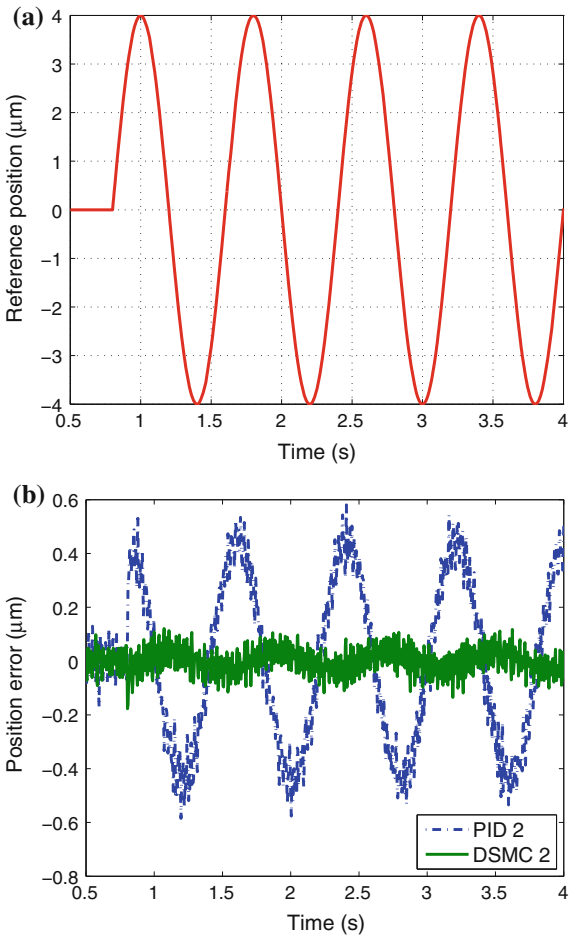

Fig. 6.6 Sinusoidal tracking results of PID #2 and DSMC #2. **a** Reference input. **b** Position errors

For comparison purpose, one-cycle (2.4–3.2 s) positioning results of both controllers are calculated as shown in Table 6.2, where the percent maximum error (MAXE) and RMSE are calculated as follows:

$$\text{MAXE}\% = \frac{\max(|e_k|)}{\max(x_{d,k}) - \min(x_{d,k})} \times 100\,\% \tag{6.32}$$

$$\text{RMSE}\% = \frac{\sqrt{\frac{1}{N}\sum_{k=1}^{N} e_k^2}}{\max(x_{d,k}) - \min(x_{d,k})} \times 100\,\%. \tag{6.33}$$

It is observed that the DSMC scheme produces smaller tracking errors than the PID controller. Specifically, the DSMC approach achieves the MAXE and RMSE of 0.118 and 0.049 μm, respectively, which are almost the noise level of the sensor.

These results indicate significant enhancements of 79.6 and 84.5 % in comparison with the PID results, respectively.

In addition, Fig. 6.7a, b depicts the time histories of s_k, Δs_k, and the perturbation estimation error $\tilde{p}_k$ of DSMC #2. It is observed that Δs_k is well restricted within the QSD band. By selecting a larger value of $\lambda_S = 8\times10^5$, $|\tilde{p}_k| \leq \lambda_S$ holds for this motion trajectory except for one point at the time of 0.8 s, i.e., the initial point of the sinusoidal trajectory. In addition, both s_k and Δs_k vary in the vicinity of zero as shown in Fig. 6.7a. Moreover, Δs_k is one order of magnitude lower than s_k, which also demonstrates the effectiveness of the adopted reaching law (6.14).

The sliding condition and convergence condition of the discrete sliding mode are depicted in Fig. 6.7c, d, respectively. It is seen that the point at 0.8 s meets the sliding condition as denoted by a circle in Fig. 6.7c. In addition, almost all the data points satisfy the convergence condition except for the four points marked by diamonds as shown in Fig. 6.7d. Figure 6.7c reveals that these four points meet the sliding condition instead, that is, the controller converges because all of the points in the trajectory satisfy either the sliding or the convergence condition.

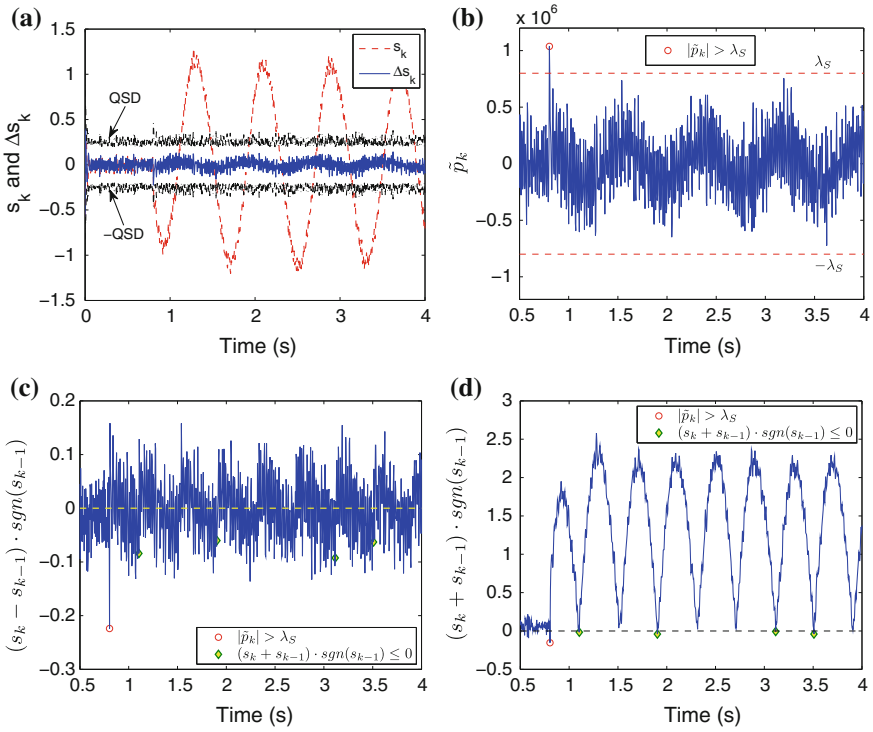

Fig. 6.7 Sinusoidal tracking results of DSMC #2. **a** Time evolutions of s_k and Δs_k. **b** Perturbation estimation error $\tilde{p}_k$. **c** Evolution of sliding condition. **d** Evolution of convergence condition

6.4.3.3 Arbitrary Motion Tracking Results

Then, the tracking performance of the proposed control scheme for an arbitrary reference input is tested. Particularly, by applying an arbitrary input as shown in Fig. 6.8a, the tracking errors of the aforementioned PID #2 and DSMC #2 controllers are shown in Fig. 6.8b. The errors are calculated as shown in Table 6.2. As compared with PID, the DSMC has reduced the MAXE and RMSE by 84.8 and 87.1 %, respectively. Hence, the superiority of DSMC over PID is evident from the experimental results.

For this arbitrary trajectory, the sliding function and perturbation estimation error of the DSMC are shown in Fig. 6.9a, b, respectively. Fig. 6.9a reveals that Δs_k is well constrained by the width of QSD. It is seen that a large estimation error of

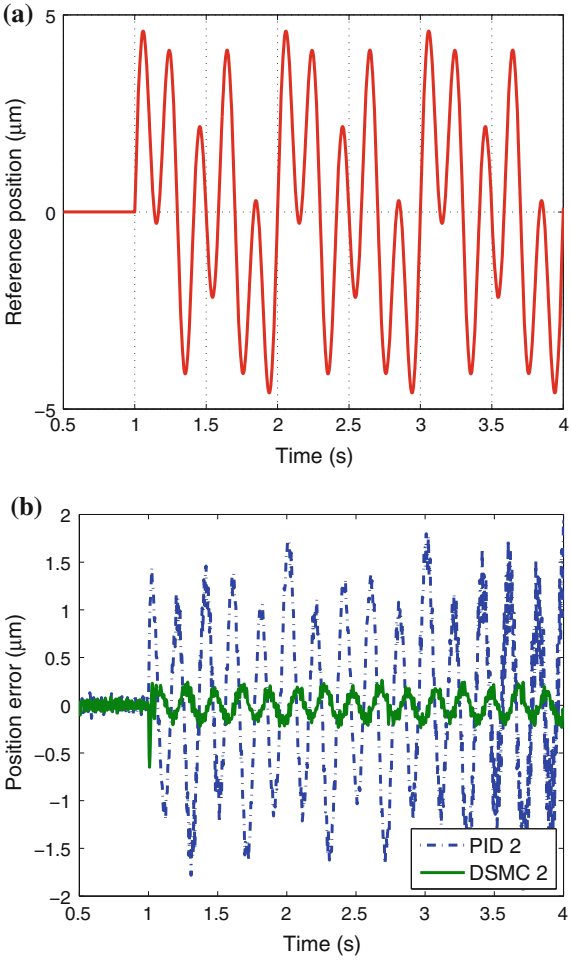

Fig. 6.8 Arbitrary motion tracking results of PID #2 and DSMC #2. **a** Reference input. **b** Position errors

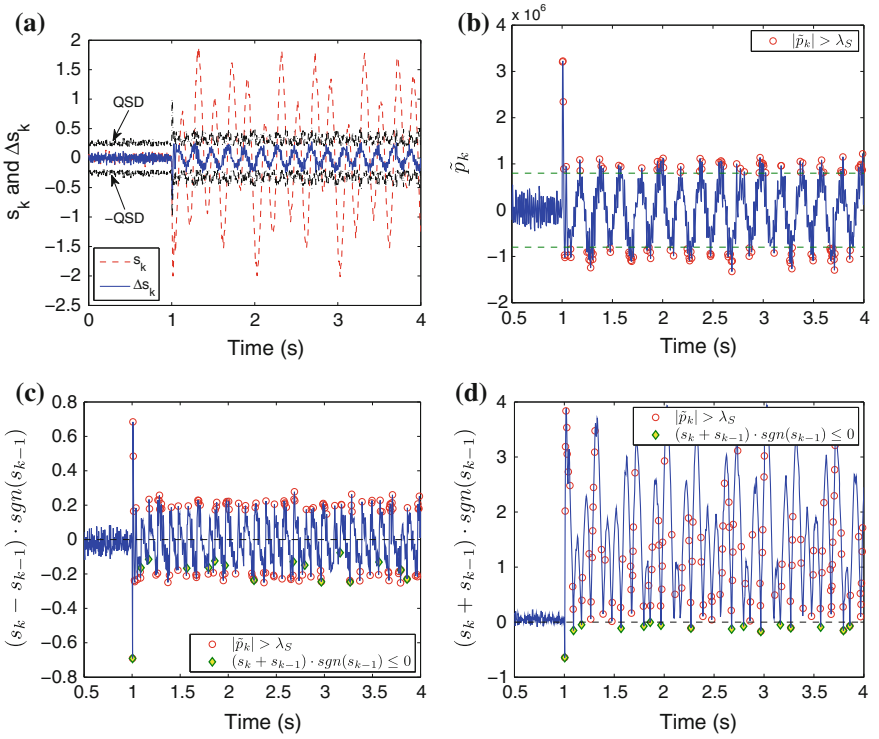

Fig. 6.9 Arbitrary motion tracking results of DSMC #2. **a** Time evolutions of s_k and Δs_k. **b** Perturbation estimation error $\tilde{p}_k$. **c** Evolution of sliding condition. **d** Evolution of convergence condition

$\tilde{p}_k = 3.2\times10^6$ occurs at the time of 1 s. This indicates a sudden change of $\dot{p}(t)$, which is mainly caused by the sharp transition of $\dot{x}(t)$ at 1 s.

In addition, Fig. 6.9b shows that the assigned $\lambda_S = 8\times10^5$ is smaller than the maximum value of $|\tilde{p}_k|$. The data points that violate the condition of $|\tilde{p}_k| \leq \lambda_S$ are denoted by circles in Fig. 6.9b. For these points, the corresponding sliding and convergence conditions are marked by circles in Fig. 6.9c, d, respectively. Fig. 6.9d illustrates that almost all the points satisfy the convergence condition expect for a few points which are marked by diamonds. Alternatively, these points meet the sliding condition as represented in Fig. 6.9c. Therefore, the closed-loop system still converges because the data points that violate the condition of $|\tilde{p}_k| \leq \lambda_S$ satisfy either the sliding or the convergence condition of the discrete sliding mode. The experimental results reveal that the relationship (6.24) is not a necessary condition for the existence of discrete sliding mode.

6.4.3.4 Robustness Resting Results

The forgoing experiments verify the robustness of the DSMC control with respect to internal disturbances in terms of model uncertainties and parameter perturbations. The robustness against external disturbance is examined by applying an external force on the piezoelectric actuator during the motion tracking task.

Specifically, an external force is applied by hanging a weight of 25 mN on the piezoelectric bimorph during the sinusoidal motion tracking. By exerting the force as shown in Fig. 6.10a, the tracking result of DSMC #2 is described in Fig. 6.10b. In addition, the time histories of s_k and Δs_k are plotted in Fig. 6.10c, and the tracking errors are depicted in Fig. 6.10d. In addition, by applying the same external force, the tracking result of the PID #2 controller is depicted in Fig. 6.11a, and the tracking error is shown in Fig. 6.11b.

It is observed that the external force causes an increase of the tracking error at its moment of occurrence around 1.7 s for both PID and DSMC control schemes.

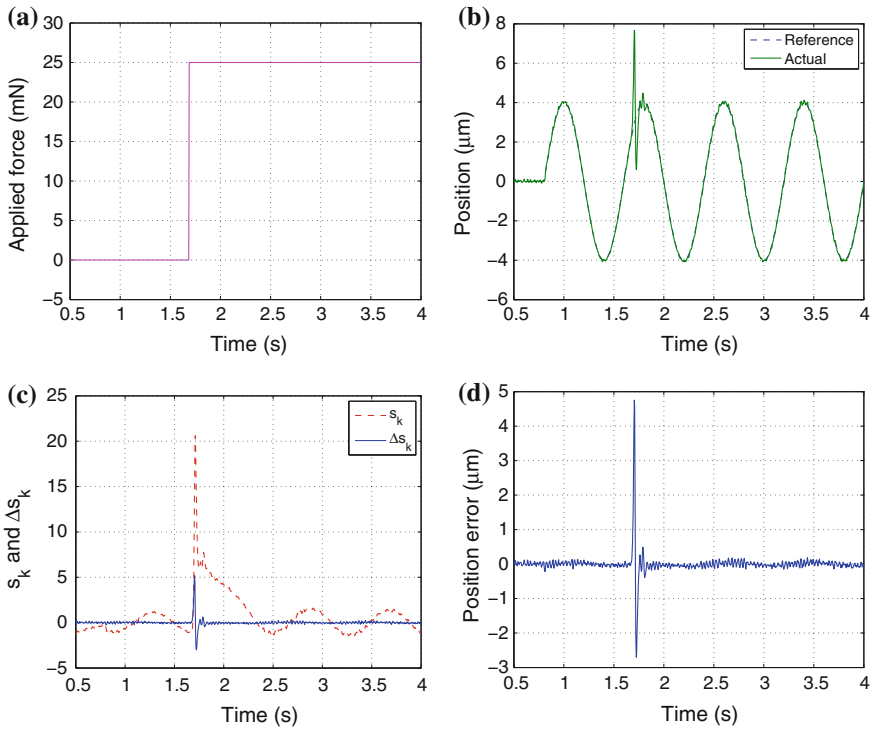

Fig. 6.10 Robustness testing results of DSMC #2 for a sinusoidal motion tracking. **a** Time history of the applied external force. **b** Tracking results. **c** Sliding function s_k and its variation Δs_k. **d** Tracking errors

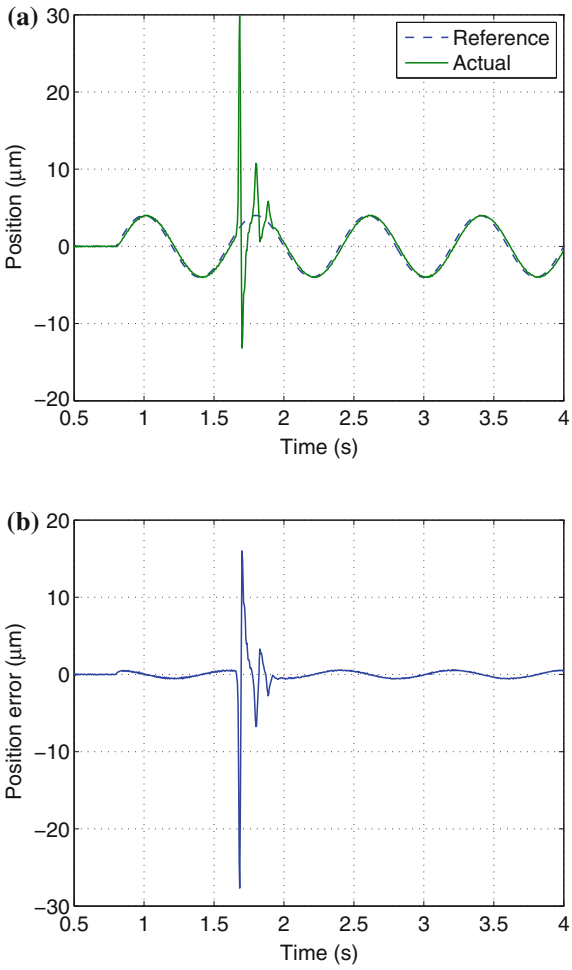

Fig. 6.11 Robustness testing results of PID #2 for a sinusoidal motion tracking. **a** The tracking results. **b** Tracking errors

The PID and DSMC controllers produce the maximum errors of 27.67 and 4.75 μm, respectively. Therefore, as compared with the PID result, the DSMC has reduced the maximum error by 83 %. Moreover, after the occurrence of the external disturbance, the tracking accuracy of DSMC is recovered quickly within 0.18 s, while the result of PID is restored after 0.30 s. Thus, in comparison with PID, the DSMC shortens the recovery time by 40 %. The results demonstrate that the DSMC possesses a much better robustness property than PID against external disturbances.

6.4.4 Discussion

The foregoing experimental investigations validate the effectiveness of the DSMC scheme with Assumption 6.1. Actually, the perturbation estimation errors $\tilde{p}_k$ as plotted in Figs. 6.5b, 6.7b and 6.9b are obtained by Eq. (6.9), i.e., $\tilde{p}_k = p_{k-1} - p_k$. Experimental results also demonstrate the superiority of the DSMC over PID strategy in terms of transient-state response time and steady-state positioning error. The reason why the finely tuned PID controller is still not able to achieve satisfactory positioning results mainly attributes to the nonlinear hysteresis effect of the piezoelectric actuator. In contrast, the fact that a rapid and precise positioning is accomplished by the DSMC controller demonstrates the effectiveness of the DSMC scheme without modeling the hysteresis effect.

It is observed from Fig. 6.3 that the second-order model matches the magnitude response of system well at low frequencies up to 500 Hz. To capture the dynamics behavior accurately, a higher-order model is required to be identified. Here, a simple second-order model is employed and the higher-frequency dynamics is involved in the lumped disturbance p_k. The achieved experimental results demonstrate the effectiveness of the reported control scheme using a lower-order plant model.

The obtained experimental results illustrate that the relationship (6.24) is a sufficient but not necessary condition for the existence of discrete sliding mode. A necessary and sufficient condition is expected to be deduced in the next step. In addition, only a local stability of the closed-loop system is proved in this work. The issue of deriving a simple control scheme with global asymptotic stability is a topic of further work. Additionally, the adaptive mechanism [4, 8, 19] can be employed to adjust the controller parameters online in the future work.

In addition, the quantization errors are not considered in the discretization approach in the current work. It has been shown in [16] that the quantization errors will increase the width of quasi-sliding domain. Hence, the influence of the quantization errors on the performance of the presented control deserves an investigation for potential applications using 8- or 16-bit microcontrollers.

6.5 Chapter Summary

Instead of using a state observer, a DSMC scheme has been developed based on a second-order plant model of the system in this chapter. The unmodeled nonlinearity effect is considered as a lumped perturbation, which is estimated by resorting to the one-step delayed estimation technique. The effectiveness of the presented approach without using state observer and hysteresis model has been validated by experimental investigations. Both set-point positioning and sinusoidal tracking results confirm the superiority of the DSMC over PID control in terms of response speed, positioning accuracy, and robustness property. The presented idea can be extended to precision control of other systems that can be described using a discrete-time plant model preceded by disturbances.

References

1. Abidi, K., Xu, J.X., Yu, X.: On the discrete-time integral sliding mode control. IEEE Trans. Autom. Control **52**(4), 709–715 (2007)
2. Bandyopadhyay, B., Fulwani, D.: High-performance tracking controller for discrete plant using nonlinear sliding surface. IEEE Trans. Ind. Electron. **56**(9), 3628–3637 (2009)
3. Bibian, S., Jin, H.: Time delay compensation of digital control for DC switchmode power supplies using prediction techniques. IEEE Trans. Power Electron. **15**(5), 835–842 (2000)
4. Chen, X., Hisayama, T.: Adaptive sliding-mode position control for piezo-actuated stage. IEEE Trans. Ind. Electron. **55**(11), 3927–3934 (2008)
5. Elmali, H., Olgac, N.: Implementation of sliding mode control with perturbation estimation (SMCPE). IEEE Trans. Control Syst. Technol. **4**(1), 79–85 (1996)
6. Furuta, K.: Sliding mode control of a discrete system. Syst. Control Lett. **14**(2), 145–152 (1990)
7. Galias, Z., Yu, X.: Euler's discretization of single input sliding-mode control systems. IEEE Trans. Autom. Control **52**(9), 1726–1730 (2007)
8. Huang, S., Tan, K.K., Lee, T.H.: Adaptive sliding-mode control of piezoelectric actuators. IEEE Trans. Ind. Electron. **56**(9), 3514–3522 (2009)
9. Mitic, D., Milojkovic, M., Antic, D.: Tracking system design based on digital minimum variance control with fuzzy sliding mode. In: Proceedings of the 8th International Conference on Telecommunications in Modern Satellite, Cable and Broadcasting Services (TELSIKS 2007), pp. 494–497. Nis, Serbia (2007)
10. Mitic, D., Milosavljevic, C.: Sliding mode-based minimum variance and generalized minimum variance controls with $O(T^2)$ and $O(T^3)$ accuracy. Electr. Eng. **86**(4), 229–237 (2004)
11. Monsees, G.: Discrete-time sliding mode control. Ph.D. thesis, Delft University of Technology (2002)
12. Sarpturk, S., Istefanopulos, Y., Kaynak, O.: On the stability of discrete-time sliding mode control systems. IEEE Trans. Autom. Control **32**(10), 930–932 (1987)
13. Sha, D., Bajic, V.B.: Robust discrete adaptive input-output-based sliding mode controller. Int. J. Syst. Sci. **31**(12), 1601–1614 (2000)
14. Sha, D., Bajic, V.B., Yang, H.: New model and sliding mode control of hydraulic elevator velocity tracking system. Simul. Pr. Theory **9**(6), 365–385 (2002)
15. Tarokh, M.: A discrete-time adaptive control scheme for robot manipulators. J. Robot. Syst. **7**(2), 145–166 (1990)
16. Veselic, B., Perunicic-Drazenovic, B., Milosavljevic, C.: Improved discrete-time sliding-mode position control using Euler velocity estimation. IEEE Trans. Ind. Electron. **57**(11), 3840–3847 (2010)
17. Xi, Z., Hesketh, T.: Discrete time integral sliding mode control for overhead crane with uncertainties. IET Control Theory Appl. **4**(10), 2071–2081 (2010)
18. Xu, J.X., Abidi, K.: Discrete-time output integral sliding-mode control for a piezomotor-driven linear motion stage. IEEE Trans. Ind. Electron. **55**(11), 3917–3926 (2008)
19. Xu, Q., Jia, M.: Model reference adaptive control with perturbation estimation for a micropositioning system. IEEE Trans. Control Syst. Technol. **22**(1), 352–359 (2014)
20. Xu, Q., Li, Y.: Micro-/nanopositioning using model predictive output integral discrete sliding mode control. IEEE Trans. Ind. Electron. **59**(2), 1161–1170 (2012)
21. Xu, Q., Li, Y.: Model predictive discrete-time sliding mode control of a nanopositioning piezostage without modeling hysteresis. IEEE Trans. Control Syst. Technol. **20**(4), 983–994 (2012)
22. Young, K.D., Utkin, V.I., Ozguner, U.: A control engineer's guide to sliding mode control. IEEE Trans. Control Syst. Technol. **7**(3), 328–342 (1999)
23. Zhu, Y.: Multivariable System Identification for Process Control. Elsevier Science Inc., New York (2001)

Chapter 7
Digital Sliding-Mode Control of High-Order Systems

This chapter presents the design and implementation of an input–output-based digital sliding-mode control (IODSMC) algorithm to suppress the nonlinearity and disturbance in piezoelectric micro-/nano-positioning systems. It is applicable to precision motion tracking of a class of micro-/nano-positioning systems, which can be described by a high-order linear model preceded by disturbances. The stability of the control system is proved and its effectiveness is validated through experimental investigations on a piezo-driven micropositioning system.

7.1 Introduction

The DSMC scheme as presented in Chap. 6 is applicable to a second-order system. In practice, majority of piezoelectric micro-/naon-positioning systems exhibit a plant mode of higher order. Hence, it is necessary to extend the control strategy to higher order systems. To this end, an input–output-based DSMC (IODSMC) is developed in this chapter. Unlike the DSMC algorithms as devised in the previous chapters, the presented IODSMC exhibits the following three advantages simultaneously, which are particularly attractive for practical applications.

1. Its implementation requires an input–output data-based model only, whereas the hysteresis model and the state observer are not needed.
2. It is capable of suppressing the model disturbance and achieving an $O(T^2)$ accuracy of the output position tracking.
3. It eliminates the chattering phenomenon by means of boundary layer technique.

© Springer International Publishing Switzerland 2016

Q. Xu and K.K. Tan, *Advanced Control of Piezoelectric Micro-/Nano-Positioning Systems*, Advances in Industrial Control,
DOI 10.1007/978-3-319-21623-2_7

7.2 Problem Formulation

7.2.1 System Modeling

A piezo-driven micro-/nano-positioning system can be described by a linear time-invariant (LTI) model preceded by disturbance:

$$\dot{\mathbf{X}}(t) = \mathbf{A}_c\mathbf{X}(t) + \mathbf{B}_c\mathbf{u}(t) + \mathbf{D}_c\mathbf{f}(t) \tag{7.1}$$

$$\mathbf{Y}(t) = \mathbf{C}\mathbf{X}(t) \tag{7.2}$$

where the state vector $\mathbf{X} \in R^{n_0}$, the output $\mathbf{Y} \in R^{p_0}$, the control input $\mathbf{u} \in R^{m_0}$, the disturbance vector $\mathbf{f} \in R^{q_0}$ is supposed to be smooth and bounded, and $m_0 \leq p_0 < n_0$. The system matrices $\mathbf{A}_c$, $\mathbf{B}_c$, $\mathbf{D}_c$, and $\mathbf{C}$ are constants with approximate dimensions.

The disturbance $\mathbf{f}$ represents the lumped effect of the unmodeled nonlinear hysteresis, residual dynamics, and external perturbations. It is assumed that $\mathbf{f}$ satisfies the matching condition, i.e., $\mathbf{D}_c = \mathbf{B}_c\delta_d$ where δ_d is a scalar.

Adopting a sampling time T, the continuous-time system model (7.1) can be discretized by the zero-order-hold (ZOH) sampling:

$$\mathbf{X}_{k+1} = \mathbf{A}\mathbf{X}_k + \mathbf{B}\mathbf{u}_k + \mathbf{d}_k \tag{7.3}$$

$$\mathbf{Y}_k = \mathbf{C}\mathbf{X}_k \tag{7.4}$$

where the notation $\mathbf{X}_k = \mathbf{X}(kT)$, and

$$\mathbf{A} = e^{\mathbf{A}_c T} \tag{7.5}$$

$$\mathbf{B} = \int_0^T e^{\mathbf{A}_c\tau} d\tau\, \mathbf{B}_c \tag{7.6}$$

$$\mathbf{d}_k = \int_0^T e^{\mathbf{A}_c\tau}\mathbf{B}_c\delta_d\mathbf{f}((k+1)T - \tau)d\tau. \tag{7.7}$$

It is observed that both $\mathbf{B}$ and $\mathbf{d}_k$ are of the order $O(T)$ with respect to the sampling time T.

Majority of the existing DSMC schemes have been developed based on the discrete-time model as represented by Eqs. (7.3) and (7.4). Therefore, the full state information is required and various state observers are usually needed. To eliminate the use of state observer, a control scheme is devised in the following discussion.

First, for a SISO system (i.e., $m_0 = p_0 = 1$), the discrete-time model is expressed into the z-domain form [1]:

$$Y(z) = \frac{z^{-1}M(z^{-1})}{N(z^{-1})}U(z) + \frac{z^{-1}L(z^{-1})}{N(z^{-1})}D(z) \tag{7.8}$$

with

$$M(z^{-1}) = z^{-n+1}\mathbf{C}\,\mathrm{adj}(z\mathbf{I} - \mathbf{A})\mathbf{B} \tag{7.9}$$

$$L(z^{-1}) = z^{-n+1}\mathbf{C}\,\mathrm{adj}(z\mathbf{I} - \mathbf{A}) \tag{7.10}$$

$$N(z^{-1}) = z^{-n}\,\det(z\mathbf{I} - \mathbf{A}) \tag{7.11}$$

where $Y(z)$, $U(z)$, and $D(z)$ are the z-transforms of Y_k, u_k, and d_k, respectively. In addition, z^{-1} represents a unit delay.

Assume that the linear part of the plant model (7.8) can be represented as follows:

$$\frac{Y(z)}{U(z)} = \frac{z^{-1}M(z^{-1})}{N(z^{-1})} = \frac{b_1 z^{-1} + b_2 z^{-2} + \cdots + b_m z^{-m}}{1 + a_1 z^{-1} + a_2 z^{-2} + \cdots + a_n z^{-n}} \tag{7.12}$$

where a_i and b_i are the nominal model parameters, and $n \geq m$ holds. Then, the discrete-time model (7.8) can be expanded into the following form:

$$x_k = \sum_{i=1}^{n} a_i x_{k-i} + \sum_{i=1}^{m} b_i u_{k-i} + p_k \tag{7.13}$$

where $x_k = Y_k$ is the output position, p_k denotes the nonlinear disturbance term in the system model (7.8), and Property 4.1 applies to the disturbance p_k.

Subsequently, a controllable canonical form of the plant model (7.13) can be derived as follows:

$$\bar{\mathbf{X}}_{k+1} = \mathbf{G}\bar{\mathbf{X}}_k + \mathbf{H}u_k + \mathbf{Q}\mathbf{V}_k + \mathbf{P}_k \tag{7.14}$$

$$\bar{Y}_k = \bar{\mathbf{C}}\bar{\mathbf{X}}_k \tag{7.15}$$

where

$$\bar{\mathbf{X}}_k = \begin{bmatrix} x_{k-n+1} \\ \vdots \\ x_{k-1} \\ x_k \end{bmatrix} \in R^{n\times 1} \tag{7.16}$$

$$\mathbf{V}_k = \begin{bmatrix} u_{k-m+1} \\ \vdots \\ u_{k-2} \\ u_{k-1} \end{bmatrix} \in R^{(m-1)\times 1} \tag{7.17}$$

$$\mathbf{P}_k = \begin{bmatrix} 0 \\ \vdots \\ 0 \\ p_k \end{bmatrix} \in R^{n\times 1} \tag{7.18}$$

$$\mathbf{G} = \begin{bmatrix} 0 & 1 & \cdots & 0 \\ \vdots & \vdots & \ddots & \vdots \\ 0 & 0 & \cdots & 1 \\ -a_n & -a_{n-1} & \cdots & -a_1 \end{bmatrix} \in R^{n\times n} \tag{7.19}$$

$$\mathbf{H} = \begin{bmatrix} 0 \\ \vdots \\ 0 \\ b_1 \end{bmatrix} \in R^{n\times 1} \tag{7.20}$$

$$\mathbf{Q} = \begin{bmatrix} 0 & 0 & \cdots & 0 \\ \vdots & \vdots & \ddots & \vdots \\ 0 & 0 & \cdots & 0 \\ b_m & b_{m-1} & \cdots & b_2 \end{bmatrix} \in R^{n\times(m-1)} \tag{7.21}$$

$$\bar{\mathbf{C}} = \begin{bmatrix} 0 \cdots 0 \ 1 \end{bmatrix} \in R^{1\times n}. \tag{7.22}$$

It is observed that the models (7.14) and (7.15) are constructed using the history data of the system input and output only. Hence, this state-space model is called an input–output model.

7.2.2 Disturbance Estimation

Based on the perturbation estimation technique, the disturbance term $\mathbf{P}_k$ in Eq. (7.14) can be estimated by its one-step delayed value as follows:

$$\hat{\mathbf{P}}_k = \mathbf{P}_{k-1} = \bar{\mathbf{X}}_k - G\bar{\mathbf{X}}_{k-1} - \mathbf{H}u_{k-1} - \mathbf{Q}\mathbf{V}_{k-1}. \tag{7.23}$$

Then, the system models (7.14) and (7.15) become

$$\bar{\mathbf{X}}_{k+1} = \mathbf{G}\bar{\mathbf{X}}_k + \mathbf{H}u_k + \mathbf{Q}\mathbf{V}_k + \hat{\mathbf{P}}_k - \tilde{\mathbf{P}}_k \tag{7.24}$$

$$\bar{Y}_k = \bar{\mathbf{C}}\bar{\mathbf{X}}_k \tag{7.25}$$

where $\tilde{\mathbf{P}}_k = \hat{\mathbf{P}}_k - \mathbf{P}_k$ is the disturbance estimation error, which can be further expressed as:

$$\begin{aligned} \tilde{\mathbf{P}}_k &= \mathbf{P}_{k-1} - \mathbf{P}_k \\ &= \mathbf{G}(\bar{\mathbf{X}}_k - \bar{\mathbf{X}}_{k-1}) + \mathbf{H}(u_k - u_{k-1}) + \mathbf{Q}(\mathbf{V}_k - \mathbf{V}_{k-1}) - (\bar{\mathbf{X}}_{k+1} - \bar{\mathbf{X}}_k) \end{aligned} \tag{7.26}$$

where $\mathbf{G}$, $\mathbf{H}$, and $\mathbf{Q}$ are constant matrices.

For a piezo-driven micro-/nano-positioning system, the input voltage u_k and output position x_k are limited in practice. Hence, $\bar{\mathbf{X}}_k$ and $\mathbf{V}_k$ are also limited. Then, it is reasonable to assume that $\tilde{\mathbf{P}}_k$ as expressed by Eq. (7.26) is bounded. In view of Eq. (7.18), it can be deduced that only the last element $\tilde{p}_k$ of $\tilde{P}_k$ is nonzero. To facilitate the control design, the following assumption is proposed:

Assumption 7.1 The estimation error $\tilde{p}_k$ of the lumped disturbance p_k is bounded, i.e., $|\tilde{p}_k| \leq \sigma$.

The objective of the motion tracking control is to force the system output ($\bar{Y}_k = x_k$) to precisely follow a desired reference input under the influence of the lumped disturbance P_k. To accomplish this goal, a control algorithm is developed in the next section.

7.3 IODSMC Design

The design procedure of an IODSMC control scheme is outlined in this section. First, the equivalent controller is devised based on an incremental proportional-integral-derivative (PID)-type sliding function. Then, an augmented IODSMC scheme is constructed. The stability and tracking error bound of the control system are also evaluated.

7.3.1 Sliding Function Definition

First, the output tracking error is defined as follows:

$$e_k = \bar{Y}_k - r_k \tag{7.27}$$

where r_k is the desired output position of the system.

Based on the output error in Eq. (7.27), an incremental PID type of sliding function is defined:

$$s_k = s_{k-1} + K_p(e_k - e_{k-1}) + K_i e_k + K_d(e_k - 2e_{k-1} + e_{k-2}) \tag{7.28}$$

where K_p, K_i, and K_d represent the proportional, integral, and derivative gains, respectively.

After a fundamental algebra operation, the sliding function (7.28) is simplified into the form:

$$s_k = s_{k-1} + K_3 e_{k-2} + K_2 e_{k-1} + K_1 e_k \tag{7.29}$$

where

$$K_1 = K_p + K_i + K_d \tag{7.30}$$
$$K_2 = -K_p - 2K_d \tag{7.31}$$
$$K_3 = K_d. \tag{7.32}$$

7.3.2 Design of IODSMC

In the literature, there are different definitions of the reaching law. In particular, the IODSMC algorithm is developed on the basis of the following reaching law:

$$s_{k+1} = 0 \tag{7.33}$$

so that the sliding surface is reached in one sampling instant.

According to Eq. (7.33), the following deduction is generated

$$s_k + K_3 e_{k-1} + K_2 e_k + K_1(\bar{Y}_{k+1} - r_{k+1}) = 0. \tag{7.34}$$

Then, solving the expression of $\bar{Y}_{k+1}$ from Eq. (7.25) and substituting it into Eq. (7.34) leads to

$$s_k + K_3 e_{k-1} + K_2 e_k + K_1[\bar{\mathbf{C}}(\mathbf{G}\bar{\mathbf{X}}_k + \mathbf{H}u_k + \mathbf{Q}\mathbf{V}_k + \hat{\mathbf{P}}_k - \tilde{\mathbf{P}}_k) - r_{k+1}] = 0. \tag{7.35}$$

Considering that the equivalent control u_k^{eq} is the solution to Eq. (7.33), u_k^{eq} is derived from Eq. (7.35) by neglecting the disturbance estimation error $\tilde{P}_k$:

$$u_k^{\text{eq}} = (K_1\bar{\mathbf{C}}\mathbf{H})^{-1}(-s_k - K_3 e_{k-1} - K_2 e_k + K_1 r_{k+1} - K_1\bar{\mathbf{C}}\mathbf{G}\bar{\mathbf{X}}_k - K_1\bar{\mathbf{C}}\mathbf{Q}\mathbf{V}_k - K_1\bar{\mathbf{C}}\hat{\mathbf{P}}_k) \tag{7.36}$$

where the one-step forward reference position r_{k+1} is required to realize the controller. In micro-/nano-positioning applications, the trajectory to be tracked is usually predefined. Hence, it is reasonable to assume that r_{k+1} is known.

7.3.2.1 Stability Analysis

Substituting Eq. (7.36) into Eq. (7.14), the following expression is produced after a necessary calculation

$$\bar{\mathbf{X}}_{k+1} = \mathbf{R}\bar{\mathbf{X}}_k + \mathbf{W}\mathbf{P}_{k-1} + (\mathbf{P}_k - \mathbf{P}_{k-1}) + \mathbf{E} \tag{7.37}$$

where

$$\mathbf{R} = \mathbf{G} - \mathbf{H}(K_1\bar{\mathbf{C}}\mathbf{H})^{-1}[K_2\bar{\mathbf{C}} + K_1\bar{\mathbf{C}}\mathbf{G}] \tag{7.38}$$

$$\mathbf{W} = \mathbf{I} - \mathbf{H}(K_1\bar{\mathbf{C}}\mathbf{H})^{-1}K_1\bar{\mathbf{C}} \tag{7.39}$$

$$\mathbf{E} = \mathbf{H}(K_1\bar{\mathbf{C}}\mathbf{H})^{-1}(-K_3e_{k-1} + K_2r_k + K_1r_{k+1} - K_1\bar{\mathbf{C}}\mathbf{Q}\mathbf{V}_k) \tag{7.40}$$

with $\mathbf{I}$ denoting an identity matrix.

The eigenvalues of the matrices $\mathbf{R}$ and $\mathbf{W}$ are the solutions of $\det(z\mathbf{I} - \mathbf{R}) = 0$ and $\det(z\mathbf{I} - \mathbf{W}) = 0$, respectively, which govern the closed-loop state dynamics behavior. To ensure the stability of the closed-loop system, the eigenvalues of the two matrices are designed to locate inside the unit circle in the z-plane.

7.3.2.2 Tracking Error Bound Analysis

Once given Eqs. (7.14), (7.15), and (7.29), the expression of s_{k+1} can be derived as follows

$$\begin{aligned} s_{k+1} &= s_k + K_3e_{k-1} + K_2e_k + K_1e_{k+1} \\ &= s_k + K_3e_{k-1} + K_2e_k + K_1(\bar{Y}_{k+1} - r_{k+1}) \\ &= s_k + K_3e_{k-1} + K_2e_k + K_1[\bar{\mathbf{C}}(\mathbf{G}\bar{\mathbf{X}}_k + \mathbf{H}u_k + \mathbf{Q}\mathbf{V}_k + \mathbf{P}_k) - r_{k+1}]. \end{aligned} \tag{7.41}$$

Substituting Eq. (7.36) into Eq. (7.41), a fundamental computation leads to

$$s_{k+1} = K_1\bar{\mathbf{C}}(\mathbf{P}_k - \mathbf{P}_{k-1}). \tag{7.42}$$

Then, in view of Property 4.1, the following deduction is generated from Eq. (7.42):

$$s_k = O(T^2). \tag{7.43}$$

Hence, s_k has a magnitude of the order $O(T^2)$. That is, the sliding surface has an ultimate bound of $O(T^2)$.

In addition, by noting Eqs. (7.14), (7.15), and (7.27), the one-step forward error equation can be expressed as:

$$\begin{aligned} e_{k+1} &= \bar{Y}_{k+1} - r_{k+1} \\ &= \bar{\mathbf{C}}(\mathbf{G}\bar{\mathbf{X}}_k + \mathbf{H}u_k + \mathbf{Q}\mathbf{V}_k + \mathbf{P}_k) - r_{k+1}. \end{aligned} \tag{7.44}$$

Then, substituting Eq. (7.36) into Eq. (7.44) gives

$$e_{k+1} = \bar{\mathbf{C}}(\mathbf{P}_k - 2\mathbf{P}_{k-1} + \mathbf{P}_{k-2}) - K_1^{-1}(K_2e_k + K_3e_{k-1}). \tag{7.45}$$

According to Property 4.1, the relation $\mathbf{P}_k - 2\mathbf{P}_{k-1} + \mathbf{P}_{k-2} = O(T^3)$ can be derived. Then, in consideration of Eq. (7.45) and Property 4.2, it is derived that

$$e_k = O(T^2) \tag{7.46}$$

which indicates that the ultimate bound of the output tracking error e_k is of the order $O(T^2)$.

The error dynamics equation (7.45) suggests that the control gains should be designed to satisfy the following conditions so as to make the closed-loop system stable

$$|K_1^{-1}K_2| < 1 \tag{7.47}$$

$$|K_1^{-1}K_3| < 1. \tag{7.48}$$

The equivalent controller (7.36) is designed based on the assumption of zero disturbance estimation error, i.e., $\tilde{\mathbf{P}}_k = 0$. The controller takes effect in the sliding phase when the system trajectory is kept on the sliding surface. Actually, $\tilde{\mathbf{P}}_k \neq 0$. Furthermore, if the initial state of the system does not lie on the sliding surface $s_k = 0$ or external disturbances emerge during the sliding phase motion, the equivalent control alone cannot drive the trajectory toward the sliding surface. In this sense, a robust IODSMC controller is designed in the following section.

7.3.3 Robust IODSMC Design

To design a robust IODSMC controller, the equivalent control is augmented with a discontinuous switching control action. The role of the switching control is to force the system trajectory to reach the sliding mode by overcoming external disturbances.

Here, the switching control is designed as follows:

$$u_k^{\text{sw}} = -b_1^{-1}K_s \,\text{sign}\{s_k\} \tag{7.49}$$

where K_s is a positive control gain and $\text{sign}\{\cdot\}$ denotes the signum function.

The equivalent control u_k^{eq} is then augmented by the switching control u_k^{sw} to give the overall control action:

$$u_k = u_k^{\text{eq}} + u_k^{\text{sw}}. \tag{7.50}$$

That is,

$$\begin{aligned} u_k = {} & (K_1\bar{\mathbf{C}}\mathbf{H})^{-1}(-s_k - K_3e_{k-1} - K_2e_k + K_1r_{k+1} - K_1\bar{\mathbf{C}}\mathbf{G}\bar{\mathbf{X}}_k - K_1\bar{\mathbf{C}}\mathbf{Q}\mathbf{V}_k - K_1\bar{\mathbf{C}}\hat{\mathbf{P}}_k) \\ & -b_1^{-1}K_s \,\text{sign}\{s_k\}. \end{aligned} \tag{7.51}$$

Theorem 7.1 *For the system described by Eqs. (7.24) and (7.25) along with the sliding function (7.52) and Assumption 7.1, if the controller (7.51) is employed, then the quasi-sliding mode will occur in a finite number of steps.*

Proof Substituting Eq. (7.51) into the expression of the sliding function (7.52), a necessary algebra operation gives:

$$\begin{aligned} s_{k+1} &= -K_1\bar{\mathbf{C}}\mathbf{H}b_1^{-1}K_s\,\mathrm{sign}\{s_k\} + K_1\bar{\mathbf{C}}(\mathbf{P}_k - \mathbf{P}_{k-1}) \\ &= -K_1[K_s\,\mathrm{sign}\{s_k\} + (p_{k-1} - p_k)] \\ &= -K_1(K_s\,\mathrm{sign}\{s_k\} + \tilde{p}_k) \end{aligned} \tag{7.52}$$

where both K_1 and K_s are positive gains.

Assigning $K_s = |\tilde{p}_k| + \varepsilon$ where ε denotes an arbitrary positive constant, the following conclusion can be derived from Eq. (7.52):

$$K_1\varepsilon \le |s_{k+1}| \le K_1(2|\tilde{p}_k| + \varepsilon). \tag{7.53}$$

Recalling Assumption 7.1, i.e., $\tilde{p}(k)$ is bounded, it can be obtained that

$$K_1\varepsilon \le |s_{k+1}| \le K_1(2\sigma + \varepsilon). \tag{7.54}$$

Hence, it is deduced from Eq. (7.54) that the quasi-sliding mode in the vicinity of the sliding plane $s_k = 0$ is reached within a finite number of steps.

Remark 7.1 The essence of the switching control action u_k^{sw} of the IODSMC is to overcome the estimation error $\tilde{P}_k$ by driving the system trajectory to a quasi-sliding domain as indicated by Eq. (7.54). Afterwards, the equivalent control action u_k^{eq} takes effect to keep the trajectory sliding in the $O(T^2)$ vicinity of the sliding surface as revealed in Eq. (7.43).

Remark 7.2 Chattering may be induced due to the discontinuity of the signum function $\mathrm{sign}\{\cdot\}$. To alleviate the chattering phenomenon, the boundary layer technique is adopted to replace the signum function in Eq. (7.51) with the saturation function:

$$\mathrm{sat}\{s_k\} = \begin{cases} \mathrm{sign}\{s_k\} & \text{if} \quad |s_k| > \varepsilon \\ s_k/\epsilon & \text{if} \quad |s_k| \le \varepsilon. \end{cases} \tag{7.55}$$

In practice, a compromise between the chattering effect and tracking accuracy is made to assign the parameter ϵ.

By substituting Eq. (7.23) into Eq. (7.51) and replacing the $\mathrm{sign}\{\cdot\}$ function with the saturation function (7.55) results in the overall robust controller:

$$\begin{aligned} u_k = u_{k-1} - (K_1\bar{\mathbf{C}}\mathbf{H})^{-1}[&s_k + K_3e_{k-1} + K_2e_k - K_1r_{k+1} + K_1\bar{\mathbf{C}}\mathbf{G}(\bar{\mathbf{X}}_k - \bar{\mathbf{X}}_{k-1}) \\ &+K_1\bar{\mathbf{C}}\mathbf{Q}(\mathbf{V}_k - \mathbf{V}_{k-1}) + K_1\bar{Y}_k] - b_1^{-1}K_s\,\mathrm{sat}\{s_k\}. \end{aligned} \tag{7.56}$$

Remark 7.3 It is notable that only a linear input–output model of the system is needed, whereas neither a state observer nor a hysteresis model is required for the realization of the controller (7.56). Hence, as compared with the existing DSMC algorithms [4–6], one advantage of the reported IODSMC control is that it is easy to implement.

In the following sections, the performance of the IODSMC controller is verified by conducting a collection of experimental studies on a piezo-driven micropositioning system.

7.4 Experimental Setup and Controller Setup

7.4.1 Experimental Setup

The experimental setup is depicted in Fig. 7.1. A custom-built piezoelectric actuation compliant microgripper is fabricated using Al-7075 alloy and actuated by a piezo-stack actuator (PSA) (model: TS18-H5-202, from Piezo Systems, Inc.). To measure the gripper tip position, four strain gages (model: SGD-3/350-DY13, from Omega Engineering Ltd.) are employed to construct a full-bridge circuit. In addition, for measuring the grasping force, one strain gage (model: SGD-3/350-LY13, from Omega Engineering Ltd.) is adopted to form a quarter-bridge circuit. The control hardware is realized using a National Instruments (NI) cRIO-9022 real-time controller combined with cRIO-9118 reconfigurable chassis (from National Instruments Corp.). The chassis is equipped with NI-9263 D/A module and NI-9237 A/D module for producing analog voltage signals and acquiring the strain gage sensor readings, respectively. The analog excitation signal is amplified by a high-voltage amplifier (model: EPA-104 from Piezo Systems, Inc.) with an adjustable gain of then before being fed into the PSA. LabVIEW™ software is employed to realize a deterministic real-time control for the micropositioning system.

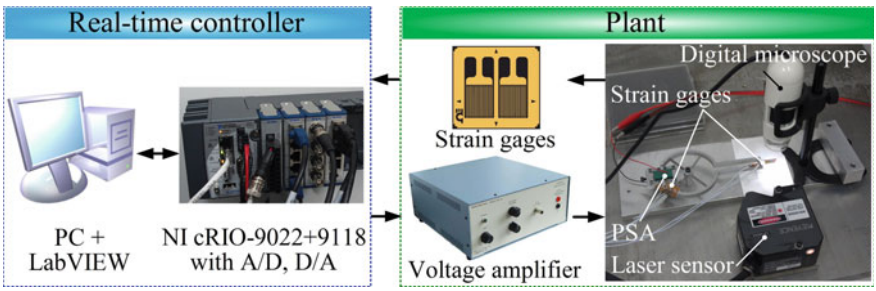

Fig. 7.1 Experimental setup of a piezo-actuated micropositioning system

For the calibration of the position strain gages, the tip position of the gripper is measured by a laser displacement sensor (model: LK-H055, from Keyence Corp.) with a resolution of 25 nm. After calibration, the position and force strain gage sensors offer the three standard deviation resolutions of 0.34 μm and 1.50 mN, respectively. In addition, a digital microscope with a magnification ratio of 200 is employed to monitor the gripper tips and the grasped object during the micropositioning process.

7.4.2 Plant Model Identification

The dynamics model parameters of the micropositioning system are identified by resorting to the frequency response approach. Specifically, swept sine waves with the amplitude of 0.1 V and frequency range of 1–500 Hz are produced by the NI-9263 module to drive the PSA. Without an contact force exerted, the position response is measured by the position strain gage sensor. Then, a spectral analysis is conducted to obtain the frequency responses as depicted in Fig. 7.2.

It is observed from Fig. 7.2 that the system exhibits a resonant peak around 244 Hz. Based on the experimental data, a fourth-order plant model is identified. Figure 7.2 reveals that the identified model well approximates the system behavior up to 300 Hz. Using a sampling time of $T = 0.0005$ s, the model is discretized as follows:

$$G_x(z) = \frac{-0.9373z^{-1} + 5.474z^{-2} - 6.101z^{-3} + 5.513z^{-4}}{1 - 2.126z^{-1} + 2.613z^{-2} - 1.591z^{-3} + 0.621z^{-4}}. \tag{7.57}$$

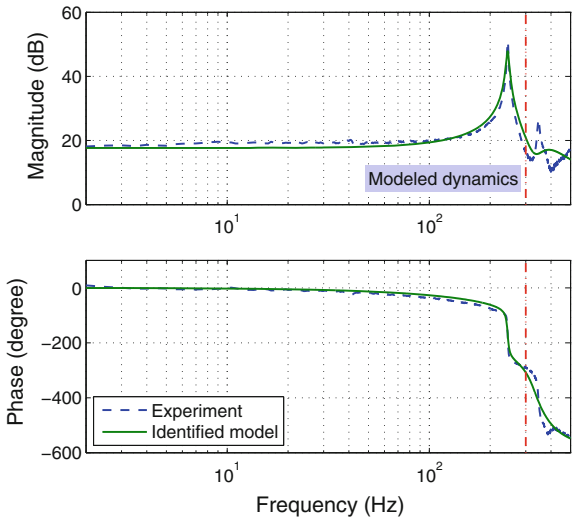

Fig. 7.2 Open-loop frequency response of the micropositioning system generated by experiment and the identified model

Then, the parameters of the nominal dynamics models (7.14) and (7.15) are obtained by comparing Eq. (7.12) with Eq. (7.57).

It is notable that a model of higher order can be identified to better describe the high-frequency dynamics. In the present work, a fourth-order model is employed to make a tradeoff between the model accuracy and complexity, and to demonstrate the effectiveness of the control scheme.

7.4.3 Controller Parameter Design

As a model-free controller, PID solves the control command using the tracking error only. For the purpose of comparison, a PID control is employed due to its popularity. An incremental-type PID algorithm is expressed as follows

$$u_k^{\text{PID}} = u_{k-1} + K_P(e_k - e_{k-1}) + K_I e_k + K_D(e_k - 2e_{k-1} + e_{k-2}) \quad (7.58)$$

where u_{k-1} is the control command in the previous time step. K_P, K_I, and K_D represent the proportional, integral, and derivative gains, respectively. Here, the PID gains are tuned by the trial-and-error approach to achieve a quicker response without overshoot phenomenon.

In addition, the tuned PID gains are adopted to determine the control gains K_1, K_2 and K_3 of the IODSMC using Eqs. (7.30)–(7.32), respectively. As compared with PID algorithm, IODSMC has an additional switching gain K_s, which is introduced to suppress the disturbance estimation error $\tilde{p}_k$. In practice, the switching gain K_s and the boundary layer thickness ϵ are tuned by several trials through experimental testings. The controller parameters are summarized in Table 7.1, which satisfy the conditions as specified by Eqs. (7.38), (7.39), (7.47) and (7.48).

Table 7.1 Parameters of the PID and IODSMC controllers

Controller	Parameter	Value
PID	K_P	0.0040
	K_I	0.0060
	K_D	0.0005
IODSMC	K_1	0.0105
	K_2	−0.0050
	K_3	0.0005
	K_s	5
	ϵ	1

7.5 Experimental Results and Discussion

Using the developed controllers, several experimental studies are conducted to verify the performance of the micropositioning system.

7.5.1 Set-Point Positioning Results

First, a 40-μm set-point positioning is carried out. The experimental results of the PID and IODSMC controllers are shown in Fig. 7.3. The positioning results exhibit that similar steady-state RMSE of 0.018 and 0.020 μm are generated by the PID and IODSMC controllers, respectively.

In addition, the PID and IODSMC schemes produce the 5 % settling time of 0.0638 and 0.0141 s, respectively. As compared with PID, the IODSMC algorithm enables a fourfold more rapid transient response while at the expense of a 8 % overshoot.

It is notable that the control gains K_1, K_2, and K_3 of IODSMC are directly calculated from the PID gains, as shown in Table 7.1. The overshoot magnitude can be reduced by finely tuning the control gains of the IODSMC controller.

7.5.2 Sinusoidal Positioning Results

Next, the sinusoidal motion tracking performance of the controllers is tested using a 5-Hz, 40 μm-amplitude sinusoidal reference input as shown in Fig. 7.4a. The tracking errors of the PID and IODSMC controllers are illustrated in Fig. 7.4b.

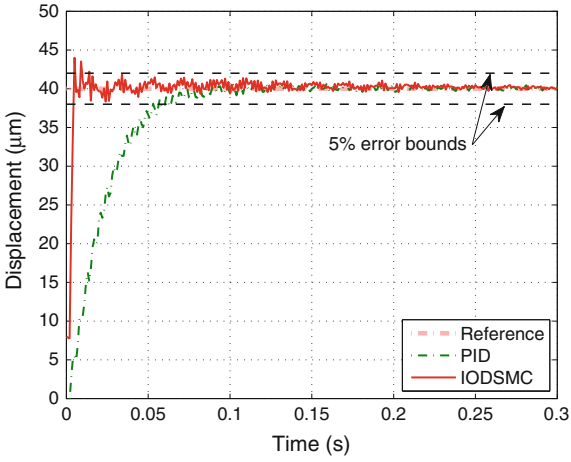

Fig. 7.3 The 40-μm set-point positioning results of PID and IODSMC controllers

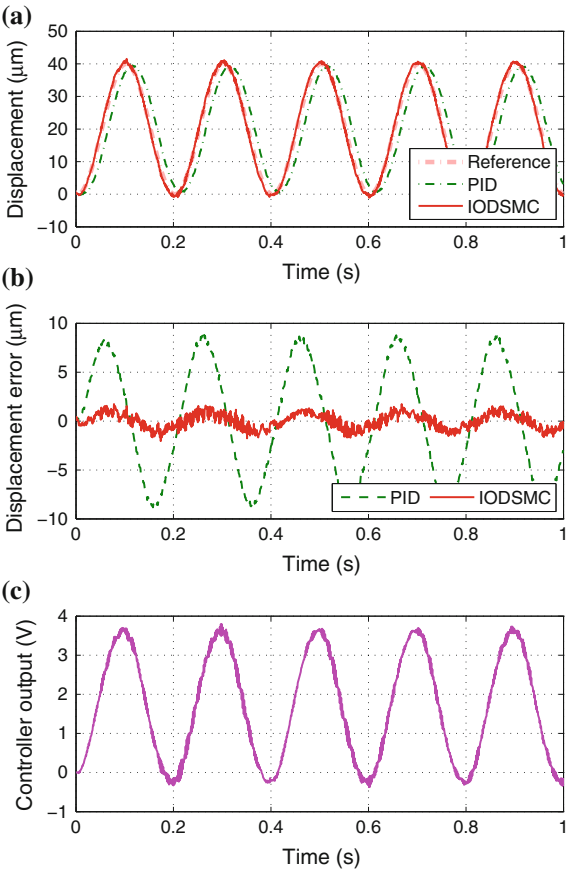

Fig. 7.4 Sinusoidal tracking results of PID and IODSMC controllers. **a** The tracking results. **b** PID and IODSMC tracking errors. **c** IODSMC controller output

It is observed that the PID control produces the maximum peak-to-peak error (PPE) and RMSE of 17.773 and 5.882 μm, i.e., 44.43 and 14.71 % of the motion range, respectively. By contrast, the IODSMC scheme induces the maximum PPE of 3.782 μm and RMSE of 0.802 μm, which are equivalent to 9.46 and 2.01 % of the total range, respectively. As compared with PID, the IODSMC controller substantially reduces the PPE and RMSE by 78.7 and 86.3 %, respectively. The reason why the PID produces a worse result is mainly attributed to its bandwidth limit and the presence of piezoelectric hysteresis effect.

The control action u_k of the IODSMC scheme is depicted in Fig. 7.4c, which exhibits no chattering phenomenon. The time histories of the perturbation estimation error $\tilde{p}_k$ and the sliding function s_k are shown in Fig. 7.5a, b, respectively. It is observed from Fig. 7.5a that the error $\tilde{p}_k$ is constrained by $|\tilde{p}_k| \leq \sigma = 2.65$, which confirms the effectiveness of Assumption 7.1. In addition, the magnitude of the sliding function s_k is well constrained by the assigned boundary layer thickness $\epsilon = 1$ as depicted in Fig. 7.5b.

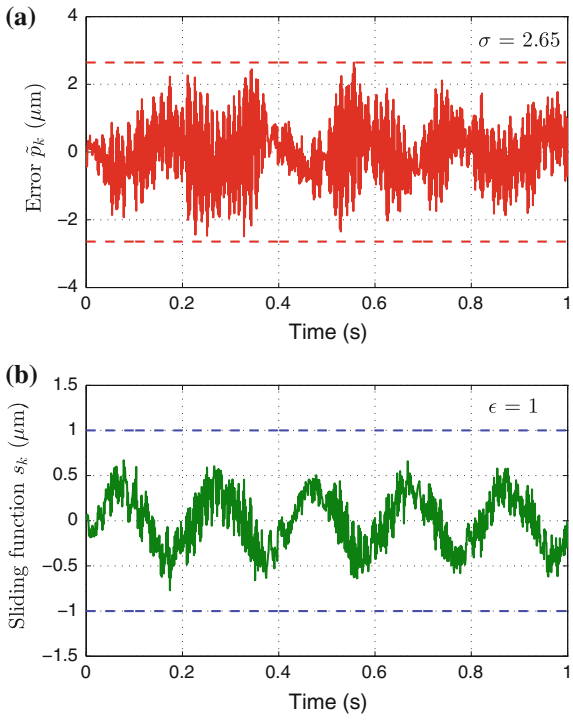

Fig. 7.5 Experimental results of IODSMC controller. **a** The perturbation estimation error $\tilde{p}_k$. **b** Time history of IODSMC sliding function

7.5.3 Bandwidth Testing Results

In order to examine the control bandwidth of the piezoelectric micropositioning system, the motion tracking testing of the 40-μm sinusoidal signal with the frequency varying from 1 to 80 Hz is undertaken. The closed-loop frequency responses of the system are shown in Fig. 7.6.

It is found that the ordinary −3 dB bandwidth corresponds to a large phase lag. Hence, the closed-loop control bandwidth is defined as the frequency at which the phase is lagged 30°. Using the PID and IODSMC controllers, the 30°-lag bandwidths of 6.1 and 40.4 Hz are achieved, which equal to 2.5 and 16.6 % of the resonant frequency, respectively. These cutoff frequencies correspond to magnitude errors of −0.7 and 2.8 dB of the PID and IODSMC responses, respectively. As compared with PID algorithm, the IODSMC scheme creates an over sixfold improvement on the control bandwidth for the micropositioning system.

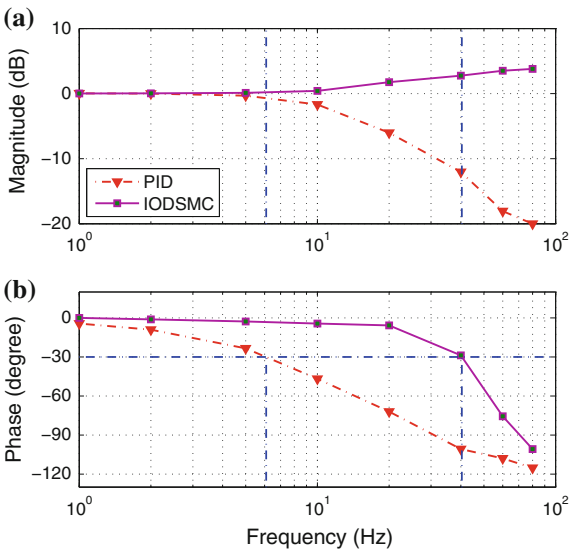

Fig. 7.6 Control bandwidth results of the micropositioning system with PID and IODSMC controllers

7.5.4 Robustness Testing Results

In order to verify the robustness property of the IODSMC controller against internal and external disturbances, two case studies are conducted.

First, the motion tracking of a 1-Hz, 110 μm-amplitude sinusoidal trajectory as shown in Fig. 7.7a is evaluated. The tracking error is plotted in Fig. 7.7c without force exerted. It is observed that a PPE of 4.230 μm and a RMSE of 0.693 μm are produced, which account for 3.85 and 0.63 % of the motion range, respectively. It is notable that such a low tracking error is achieved under the influence of piezoelectric hysteresis effect.

The closed-loop and open-loop hysteresis curves are compared in Fig. 7.8. As compared with the significant open-loop hysteresis of 14.1 %, the IODSMC scheme greatly mitigates the hysteresis to a low level of 1.2 %. Hence, the IODSMC controller has reduced the open-loop hysteresis by over tenfold. The experimental results demonstrate the robustness of the IODSMC control in front of internal disturbance, i.e., unmodeled piezoelectric nonlinearity effect.

Second, the robustness of the IODSMC controller in the presence of external disturbance is evaluated for the micropositioning system. Specifically, the microgripper is commanded to grasp a copper microwire of 300 μm diameter. To realize this task, the gripper arms are controlled to track a 1-Hz, 110 μm-amplitude sinusoidal trajectory, as shown in Fig. 7.7a. Figure 7.7b illustrates the signal of the grasping force, where the peak force occurs when the gripper is closed to grasp the object and zero force means that the gripper is opened. The motion tracking experiments have been carried out under two situations, i.e., without and with grasping the copper wire. The tracking errors for the two situations are shown in Fig. 7.7c.

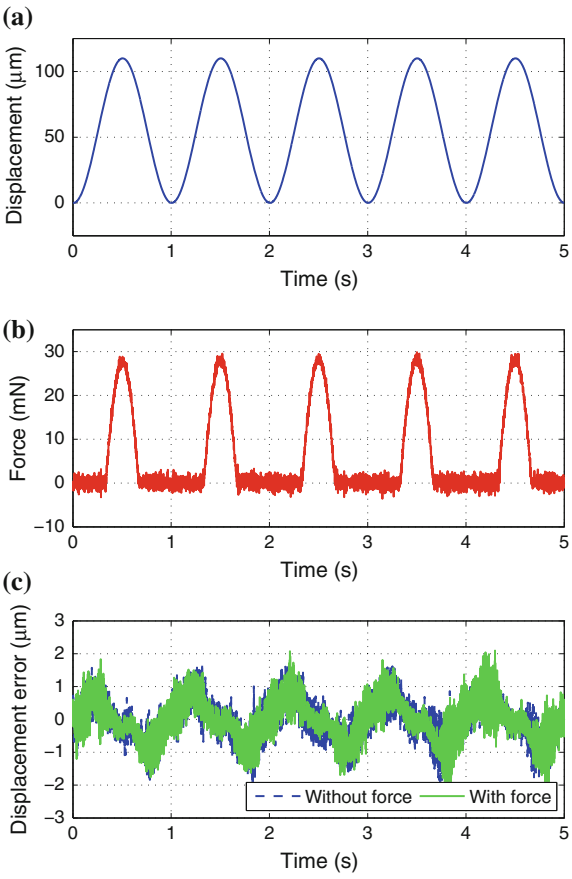

Fig. 7.7 **a** The reference displacement trajectory. **b** Signal of the grasping force. **c** IODSMC tracking errors without and with grasping the copper wire

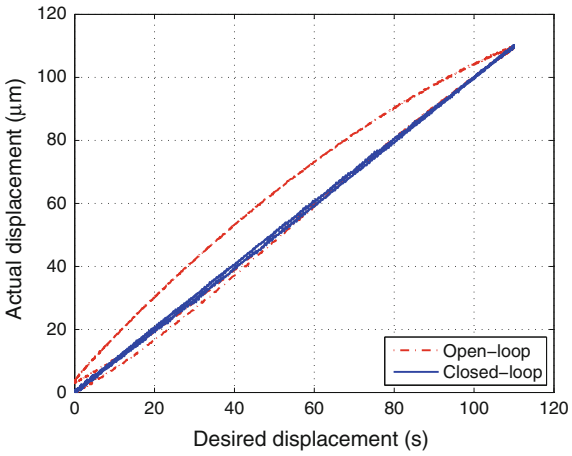

Fig. 7.8 Open-loop and closed-loop hysteresis curves. The open-loop curve is generated by scaling the driving voltage with the motion range

It is found that by exerting an external force with the peak value of 28-mN, the IODSMC scheme is still capable of tracking the predefined trajectory precisely. As a consequence, the experimental results without and with the grasping force applied are very similar in that the RMSEs are calculated as 0.693 and 0.689 μm, respectively. The small discrepancy between the two tracking errors demonstrates the robustness property of the IODSMC control scheme under the influence of external disturbances.

7.5.5 Further Discussion

The generated experimental results validate the effectiveness of the IODSMC control scheme for a piezo-actuated micropositioning system. Because the scheme has been implemented without modeling the hysteresis nonlinearity, the results reveal the efficiency of the reported idea for the model disturbance suppression. Considering that the nominal input–output model has been employed to construct the disturbance estimator for the estimate of the unmodeled dynamics and uncertainties in the control design, the results also demonstrate the feasibility of the identified lower order model for precise positioning applications.

As the frequency of the reference input increases, Fig. 7.6 indicates that the performance of PID control drops more quickly than that of the IODSMC control. Indeed, it is one of the reasons why a 5-Hz sinusoidal reference input is adopted in the comparative study. Actually, the IODSMC achieves a less than 10 % RMSE for a higher speed tracking of 20-Hz reference input trajectory.

It is notable that the control gains of IODSMC have not been optimally tuned. An optimal tuning of the four control gains is a possible solution to further improve the positioning results. In addition, similar to existing work [2, 3], the IODSMC scheme is targeted at minimum-phase plants. The issue of extending the control scheme to nonminimum-phase systems deserves a further investigation.

As compared with the existing DSMC schemes, the reported IODSMC only requires a linear input–output model for its implementation without using a state observer. It is able to accomplish an $O(T^2)$ output tracking accuracy using a chattering-free control action. Moreover, the motion tracking ability is robust against both internal and external disturbances. The design process of the control parameters is as simple as that of a PID control. Comparatively, the IODSMC performs much better than the PID as demonstrated by the aforementioned experimental results.

7.6 Chapter Summary

This chapter presents an IODSMC control algorithm dedicated to precision positioning control of a piezoelectric actuation system. Its novelty lies in the achievement of three advantages when applied to the piezoelectric positioning system control. The tracking accuracy of the controller has been analyzed and the stability in the

presence of model disturbances has been proved. The effectiveness and robustness of the presented control have been validated on a piezo-driven microgripper system. Results show that the IODSMC scheme is superior to the popular PID control in terms of both transient response speed and motion tracking accuracy, which is enabled by an enlarged control bandwidth. Because the implementation of the reported input–output model based control does not require any hysteresis model and state observer, it can be easily extended to other types of micro-/nano-positioning systems. One possible future work is to extend the control scheme to nonminimum-phase systems.

References

1. Mitic, D., Milosavljevic, C.: Sliding mode-based minimum variance and generalized minimum variance controls with $O(T^2)$ and $O(T^3)$ accuracy. Electr. Eng. **86**(4), 229–237 (2004)
2. Sha, D., Bajic, V.B.: Robust discrete adaptive input-output-based sliding mode controller. Int. J. Syst. Sci. **31**(12), 1601–1614 (2000)
3. Sha, D., Bajic, V.B., Yang, H.: New model and sliding mode control of hydraulic elevator velocity tracking system. Simul. Pract. Theory **9**(6), 365–385 (2002)
4. Xu, J.X., Abidi, K.: Discrete-time output integral sliding-mode control for a piezomotor-driven linear motion stage. IEEE Trans. Ind. Electron. **55**(11), 3917–3926 (2008)
5. Xu, Q., Li, Y.: Micro-/nanopositioning using model predictive output integral discrete sliding mode control. IEEE Trans. Ind. Electron. **59**(2), 1161–1170 (2012)
6. Xu, Q., Li, Y.: Model predictive discrete-time sliding mode control of a nanopositioning piezostage without modeling hysteresis. IEEE Trans. Control Syst. Technol. **20**(4), 983–994 (2012)

Chapter 8
Digital Sliding-Mode Prediction Control

This chapter presents the design and verification of a digital sliding-mode prediction control (DSMPC) scheme for precise position control of piezoelectric micro-/nanopositioning systems. Its implementation only needs input/output measurements, whereas the burdens on hysteresis modeling and state observer design are released. As compared with DSMC, the DSMPC is capable of further attenuating the positioning error through an optimal control, which is provided by the predictive control strategy. Its stability is proved, and the ultimate tracking error bounds are evaluated analytically. The feasibility of the control scheme is validated by experimental investigations on a piezo-driven micropositioning device.

8.1 Introduction

This chapter presents the implementation of a scheme of DSMPC for the precision motion tracking of a class of piezoelectric micro-/nanopositioning systems, which can be represented by a linear model preceded by disturbances. As compared with the controllers developed in Chaps. 4 and 5, the control scheme exhibits the following characteristics:

1. It is established based on an input/output data-based model. Hence, its implementation does not require the knowledge on the system states.
2. The design of a state observer is not required. Instead, only the past and current values of the input and output of the system are needed.
3. An incremental PID-type sliding function is employed, which is more flexible than the PI-type sliding function used before.
4. The overall control action of the DSMPC scheme involves the equivalent control, switching control, and predictive control, while the robust switching control action is not involved in the previous work. Hence, the presented control is more robust than the previous algorithms against the disturbances.

© Springer International Publishing Switzerland 2016

Q. Xu and K.K. Tan, *Advanced Control of Piezoelectric Micro-/Nano-Positioning Systems*, Advances in Industrial Control,
DOI 10.1007/978-3-319-21623-2_8

5. The sampling frequency is limited by the controllability and observability indices in previous works. In contrast, the presented DSMPC does not impose such a limitation, and the sampling rate is constrained by the hardware limit only.

8.2 Problem Formulation

8.2.1 System Modeling

A piezo-driven micro-/nanopositioning system can be described by a discrete-time dynamics model preceded by disturbance:

$$x_k = \sum_{i=1}^{n} a_i x_{k-i} + \sum_{i=1}^{m} b_i u_{k-i} + p_k \tag{8.1}$$

where x_k is the output position, u_k is the input voltage, and p_k represents the disturbance term. The disturbance p_k describes the combined effect of the unmodeled nonlinear hysteresis, residual dynamics, and external perturbations.

Then, a controllable canonical form of SISO plant model (8.1) can be derived as follows:

$$\mathbf{X}_{k+1} = \mathbf{G}\mathbf{X}_k + \mathbf{H}u_k + \mathbf{Q}\mathbf{V}_k + \mathbf{P}_k \tag{8.2}$$

$$Y_k = \mathbf{C}\mathbf{X}_k \tag{8.3}$$

where

$$\mathbf{X}_k = \left[x_{k-n+1},\ \ldots,\ x_{k-1},\ x_k\right]^T \tag{8.4}$$

$$\mathbf{V}_k = \left[u_{k-m+1},\ \ldots,\ u_{k-2},\ u_{k-1}\right]^T \tag{8.5}$$

$$\mathbf{P}_k = [0,\ \ldots,\ 0,\ p_k]^T \tag{8.6}$$

$$\mathbf{H} = [0,\ \ldots,\ 0,\ b_1]^T \tag{8.7}$$

$$\mathbf{G} = \begin{bmatrix} 0 & 1 & \cdots & 0 \\ \vdots & \vdots & \ddots & \vdots \\ 0 & 0 & \cdots & 1 \\ -a_n & -a_{n-1} & \cdots & -a_1 \end{bmatrix} \tag{8.8}$$

$$\mathbf{Q} = \begin{bmatrix} 0 & 0 & \cdots & 0 \\ \vdots & \vdots & \ddots & \vdots \\ 0 & 0 & \cdots & 0 \\ b_m & b_{m-1} & \cdots & b_2 \end{bmatrix} \tag{8.9}$$

$$\mathbf{C} = [0, \ \ldots, \ 0, \ 1]^T . \tag{8.10}$$

It is notable that the state-space models (8.2) and (8.3) are constructed using the history data of the system input and output only. This chapter develops an efficient control scheme based on this input/output data-based model.

8.2.2 Disturbance Estimation

According to the perturbation estimation technique [2], the disturbance term P_k in Eq. (8.2) can be estimated by its one-step delayed value as follows:

$$\hat{\mathbf{P}}_k = \mathbf{P}_{k-1} = \mathbf{X}_k - \mathbf{G}\mathbf{X}_{k-1} - \mathbf{H}u_{k-1} - \mathbf{Q}\mathbf{V}_{k-1}. \tag{8.11}$$

Then, the system models (8.2) and (8.3) become

$$\mathbf{X}_{k+1} = \mathbf{G}\mathbf{X}_k + \mathbf{H}u_k + \mathbf{Q}\mathbf{V}_k + \hat{\mathbf{P}}_k - \tilde{\mathbf{P}}_k \tag{8.12}$$

$$Y_k = \mathbf{C}\mathbf{X}_k \tag{8.13}$$

where $\tilde{\mathbf{P}}_k = \hat{\mathbf{P}}_k - \mathbf{P}_k$ is the disturbance estimation error, which can be further expressed as

$$\tilde{\mathbf{P}}_k = \mathbf{P}_{k-1} - \mathbf{P}_k \approx -\dot{\mathbf{P}}(t)T \tag{8.14}$$

where T is the sampling time.

Assumption 8.1 The first-order derivative of the lumped disturbance $\mathbf{P}(t)$ is bounded, i.e., $|\dot{\mathbf{P}}(t)| \leq \Delta$, which means that the norm of $\dot{\mathbf{P}}(t)$ is not larger than a positive constant Δ.

In view of Assumption 8.1 as well as (8.14), it can be deduced that $\tilde{P}_k$ is also bounded, i.e.,

$$|\tilde{\mathbf{P}}_k| = |\mathbf{P}_{k-1} - \mathbf{P}_k| \leq \Delta T. \tag{8.15}$$

The goal of the motion tracking control is to make the system output follow a desired reference input precisely under the influence of the lumped disturbance $\mathbf{P}_k$, more specifically, the bounded disturbance estimation error $\tilde{\mathbf{P}}_k$.

8.3 DSMC Design

First, the design procedure of a DSMC control scheme is outlined in this section.

8.3.1 Sliding Function Definition

The output tracking error is defined as

$$e_k = Y_k - r_k \tag{8.16}$$

where r_k is the desired position output of the system.

Based on the output error (8.16), an incremental PID type of sliding function is defined as follows:

$$s_k = s_{k-1} + K_p(e_k - e_{k-1}) + K_i e_k + K_d(e_k - 2e_{k-1} + e_{k-2}) \tag{8.17}$$

where K_p, K_i, and K_d represent the proportional, integral, and derivative gains, respectively.

After a fundamental algebraic operation, the sliding function (8.17) is simplified as

$$s_k = s_{k-1} + K_3 e_{k-2} + K_2 e_{k-1} + K_1 e_k \tag{8.18}$$

where

$$K_1 = K_p + K_i + K_d \tag{8.19}$$
$$K_2 = -K_p - 2K_d \tag{8.20}$$
$$K_3 = K_d. \tag{8.21}$$

8.3.2 Design of DSMC

Theorem 8.1 *For the system described by Eqs. (8.12) and (8.13) with the sliding function (8.18), if the following controller (8.22) is employed, then the discrete sliding mode will occur within a finite number of steps:*

$$\begin{aligned} u_k^{sm} = (K_1\boldsymbol{CH})^{-1}(&-K_3 e_{k-1} - K_2 e_k + K_1 r_{k+1} \\ &-K_1\boldsymbol{CG}X_k - K_1\boldsymbol{CQ}V_k - K_1\boldsymbol{CP}_{k-1}) - (\boldsymbol{CH})^{-1}K_s sign(s_k) \end{aligned} \tag{8.22}$$

where K_s is a positive switching gain and sign$(\cdot)$ denotes the signum function.

Proof Taking into account the definition (8.18), the one-step forward value of the sliding function is derived as follows

$$\begin{aligned} s_{k+1} &= s_k + K_3 e_{k-1} + K_2 e_k + K_1 e_{k+1} \\ &= s_k + K_3 e_{k-1} + K_2 e_k + K_1(Y_{k+1} - r_{k+1}) \\ &= s_k + K_3 e_{k-1} + K_2 e_k + K_1[\mathbf{C}(\mathbf{G}\mathbf{X}_k + \mathbf{H}u_k + \mathbf{Q}\mathbf{V}_k + \mathbf{P}_k) - r_{k+1}] \end{aligned} \tag{8.23}$$

which is deduced using Eqs. (8.12) and (8.13).

Substituting Eq. (8.22) into Eq. (8.23), a fundamental calculation yields

$$s_{k+1} = s_k - K_1[K_s \text{sign}(s_k) - \mathbf{C}(\mathbf{P}_k - \mathbf{P}_{k-1})]. \tag{8.24}$$

In consideration of Eq. (8.15), it is obtained that

$$|\mathbf{C}(\mathbf{P}_k - \mathbf{P}_{k-1})| \leq \mathbf{C}\Delta T. \tag{8.25}$$

In addition, it is assumed that the switching gain is designed to meet the condition

$$K_s \geq \mathbf{C}\Delta T + \delta \tag{8.26}$$

where δ is an arbitrary positive constant.

In view of the attribute of the discrete sliding-mode system [3], i.e., starting from the initial state, the trajectory will move monotonically toward the switching plane, it is supposed that s_k is a positive sequence or negative sequence in the reaching phase [4]. Actually, if s_k and s_{k+1} have opposite signs, it means that the system state crosses the sliding hyperplane.

If s_k is a positive sequence, i.e., $s_k \geq 0$, then the following deduction holds:

$$\begin{aligned} s_{k+1} &\leq s_k - K_1[\mathbf{C}\Delta T + \delta - \mathbf{C}(\mathbf{P}_k - \mathbf{P}_{k-1})] \\ &\leq s_k. \end{aligned} \tag{8.27}$$

Otherwise, if s_k is a negative sequence, i.e., $s_k < 0$, then

$$\begin{aligned} s_{k+1} &> s_k + K_1[\mathbf{C}\Delta T + \boldsymbol{\delta} + \mathbf{C}(\mathbf{P}_k - \mathbf{P}_{k-1})] \\ &> s_k. \end{aligned} \tag{8.28}$$

Taking into account Eqs. (8.27) and (8.28) together yields

$$|s_{k+1}| \leq |s_k| \quad \text{for} \quad k \geq k_0 \tag{8.29}$$

which implies that s_k decreases monotonously and the discrete sliding mode is reached within a finite number (k_0) of steps. It has been shown that the relationship (8.29) is a sufficient condition for the existence of discrete sliding mode [6].

Remark 8.1 Due to the discontinuity of the signum function sign(·), chattering may occur in the control action. To alleviate the chattering phenomenon, the signum function in (8.22) is replaced with the saturation function:

$$\text{sat}(s_k) = \begin{cases} \text{sign}(s_k) & \text{if} \quad |s_k| > \varepsilon \\ s_k/\varepsilon & \text{if} \quad |s_k| \leq \varepsilon \end{cases}. \tag{8.30}$$

Actually, a tradeoff between the chattering effect and tracking error is needed to assign the parameter ε.

8.3.3 Error Bound Analysis

The DSMC controller (8.22) consists of the equivalent and switching control actions. The essence of the switching control u^{sw}, i.e., the last term in Eq. (8.22), is to overcome the disturbance $\tilde{P}_k$ and to drive the system trajectory toward the sliding surface. The trajectory is then kept on the sliding surface by the equivalent control action. Hence, the ultimate tracking error is attributed to the equivalent control u^{eq}, i.e., controller (8.22) without the last term, which is employed in the following error bound analysis.

Substituting the equivalent controller into Eq. (8.23), a fundamental algebraic operation gives

$$s_{k+1} = s_k + K_1\mathbf{C}(\mathbf{P}_k - \mathbf{P}_{k-1}). \tag{8.31}$$

According to Property 4.1, $\mathbf{P}_k - \mathbf{P}_{k-1} = O(T^2)$ can be derived. Then, in view of Property 4.2, it is deduced from Eq. (8.31):

$$s_k = O(T). \tag{8.32}$$

Thus, s_k has a magnitude of the order $O(T)$, which indicates that the sliding surface has an ultimate bound of $O(T)$.

In view of Eqs. (8.2), (8.3), and (8.16), the one-step forward error equation can be expressed as

$$\begin{aligned} e_{k+1} &= Y_{k+1} - r_{k+1} \\ &= \mathbf{C}(\mathbf{G}\mathbf{X}_k + \mathbf{H}u_k + \mathbf{Q}\mathbf{V}_k + \mathbf{P}_k) - r_{k+1}. \end{aligned} \tag{8.33}$$

Then, substituting the controller expression (8.22) into Eq. (8.33) yields

$$e_{k+1} = \mathbf{C}(\mathbf{P}_k - \mathbf{P}_{k-1}) - K_1^{-1}(K_2 e_k + K_3 e_{k-1}). \tag{8.34}$$

Taking into account Property 4.2 and $\mathbf{P}_k - \mathbf{P}_{k-1} = O(T^2)$, it can be derived from Eq. (8.34) that

$$e_k = O(T). \tag{8.35}$$

The error dynamics equation (8.34) also indicates that the control gains should be designed to satisfy the following conditions so that the closed-loop system is stable:

$$|K_1^{-1}K_2| \leq 1 \tag{8.36}$$

$$|K_1^{-1}K_3| \leq 1. \tag{8.37}$$

In addition, substituting the controller equation (8.22) into Eq. (8.2), a necessary calculation gives the closed-loop system state equation:

$$\mathbf{X}_{k+1} = \mathbf{R}\mathbf{X}_k + \mathbf{W}\mathbf{P}_{k-1} + (\mathbf{P}_k - \mathbf{P}_{k-1}) + \mathbf{E} \tag{8.38}$$

in which

$$\mathbf{R} = \mathbf{G} - \mathbf{H}(K_1\mathbf{C}\mathbf{H})^{-1}[K_2\mathbf{C} + K_1\mathbf{C}\mathbf{G}] \tag{8.39}$$

$$\mathbf{W} = \mathbf{I} - \mathbf{H}(K_1\mathbf{C}\mathbf{H})^{-1}K_1\mathbf{C} \tag{8.40}$$

$$\mathbf{E} = H(K_1\mathbf{C}\mathbf{H})^{-1}(-s_k - K_3e_{k-1} + K_2r_k + K_1r_{k+1} - K_1C\mathbf{Q}\mathbf{V}_k) \tag{8.41}$$

with $\mathbf{I}$ denoting an identity matrix.

The eigenvalues of the matrices $\mathbf{R}$ and $\mathbf{W}$ are the solutions of $\det(z\mathbf{I} - \mathbf{R}) = 0$ and $\det(z\mathbf{I} - \mathbf{W}) = 0$, respectively, which determine the closed-loop state dynamics behavior. To ensure the stability of the closed-loop system, the eigenvalues of the two matrices ($\mathbf{R}$ and $\mathbf{W}$) should locate inside the unit circle in the complex plane.

8.4 DSMPC Design

The DSMC controller developed in the previous section is able to produce a tracking error bound of $O(T)$ order. To further reduce the error bound and to attenuate the chattering effect, a DSMPC control scheme is developed in this section.

8.4.1 DSMPC Design

The MPC is used to generate an optimal control (u_k^{pc}) to drive the system output to the sliding surface. Substituting the augmented control

$$u_k = u_k^{\text{sm}} + u_k^{\text{pc}} \tag{8.42}$$

into Eq. (8.23) and noting Eqs. (8.14) and (8.22) gives

$$s_{k+1} = s_k + K_1\mathbf{C}\mathbf{H}u_k^{\text{pc}} - K_1\mathbf{C}\tilde{\mathbf{P}}_k - K_1K_s\text{sat}(s_k) \tag{8.43}$$

which describes the sliding-mode dynamics and also represents a one-step forward prediction of the sliding function.

Based on Eq. (8.43), an N_h-step forward prediction of the sliding function can be obtained as follows:

$$\begin{aligned} s_{k+N_h} = {} & s_k + K_1\mathbf{C}\mathbf{H}(u_k^{\text{pc}} + u_{k+1}^{\text{pc}} + \cdots + u_{k+N_h-1}^{\text{pc}}) - K_1\mathbf{C}(\tilde{\mathbf{P}}_k + \tilde{\mathbf{P}}_{k+1} + \cdots + \tilde{\mathbf{P}}_{k+N_h-1}) \\ & -K_1K_s[\text{sat}(s_k) + \text{sat}(s_{k+1}) + \cdots + \text{sat}(s_{k+N_h-1})] \end{aligned} \tag{8.44}$$

where the positive integer N_h is called the prediction horizon as well as control horizon in this research.

The N_h equations can be stacked together into the following form:

$$\mathbf{S}_k = \Lambda s_k + \Phi \mathbf{U}_{k-1} - \Gamma \zeta_{k-1} - \mathbf{L}\mathbf{J}_{k-1} \tag{8.45}$$

where the vectors for the future sliding functions, control actions, disturbance estimation errors, and saturation functions are

$$\mathbf{S}_k = \left[s_{k+1},\ s_{k+2},\ \ldots,\ s_{k+N_h}\right]^T \tag{8.46}$$

$$\mathbf{U}_{k-1} = \left[u_k^{\mathrm{pc}},\ u_{k+1}^{\mathrm{pc}},\ \ldots,\ u_{k+N_h-1}^{\mathrm{pc}}\right]^T \tag{8.47}$$

$$\zeta_{k-1} = \left[\tilde{\mathbf{P}}_k^T,\ \tilde{\mathbf{P}}_{k+1}^T,\ \ldots,\ \tilde{\mathbf{P}}_{k+N_h-1}^T\right]^T \tag{8.48}$$

$$\mathbf{J}_{k-1} = \left[\mathrm{sat}(s_k),\ \mathrm{sat}(s_{k+1}),\ \ldots,\ \mathrm{sat}(s_{k+N_h-1})\right]^T. \tag{8.49}$$

Additionally, the four matrices exhibit the following forms:

$$\Lambda = [\mathbf{I},\ \mathbf{I},\ \ldots,\ \mathbf{I}]^T \tag{8.50}$$

$$\Phi = \begin{bmatrix} K_1\mathbf{CH} & 0 & \ldots & 0 \\ K_1\mathbf{CH} & K_1\mathbf{CH} & \ldots & 0 \\ \vdots & \vdots & \ddots & \vdots \\ K_1\mathbf{CH} & K_1\mathbf{CH} & \ldots & K_1\mathbf{CH} \end{bmatrix} \tag{8.51}$$

$$\Gamma = \begin{bmatrix} K_1\mathbf{C} & 0 & \ldots & 0 \\ K_1\mathbf{C} & K_1\mathbf{C} & \ldots & 0 \\ \vdots & \vdots & \ddots & \vdots \\ K_1\mathbf{C} & K_1\mathbf{C} & \ldots & K_1\mathbf{C} \end{bmatrix} \tag{8.52}$$

$$\mathbf{L} = \begin{bmatrix} K_1K_s & 0 & \ldots & 0 \\ K_1K_s & K_1K_s & \ldots & 0 \\ \vdots & \vdots & \ddots & \vdots \\ K_1K_s & K_1K_s & \ldots & K_1K_s \end{bmatrix}. \tag{8.53}$$

Using the aforementioned notations, a cost function for minimization can be expressed by

$$f = \mathbf{S}_k^T\mathbf{S}_k + w\mathbf{U}_{k-1}^T\mathbf{U}_{k-1} \tag{8.54}$$

where w is the weight value to tune the magnitude of the control action.

The optimal control sequence is obtained by minimizing the cost function f. Substituting Eq. (8.45) into Eq. (8.54) and applying the optimality condition $\frac{\partial f}{\partial \mathbf{U}_{k-1}} = 0$ [5] yield

$$\mathbf{U}_{k-1} = -(\Phi^T\Phi + w\mathbf{I})^{-1}\Phi^T(\Lambda s_k - \Gamma\zeta_{k-1} - \mathbf{L}\mathbf{J}_{k-1}) \tag{8.55}$$

where the future disturbance values in ζ_{k-1} and saturation function values in $\mathbf{J}_{k-1}$ are unknown. Hence, they are estimated as follows:

$$\hat{\zeta}_{k-1} = [\tilde{\mathbf{P}}_{k-1}^T,\ \tilde{\mathbf{P}}_{k-1}^T,\ \ldots,\ \tilde{\mathbf{P}}_{k-1}^T]^T \tag{8.56}$$

$$\hat{\mathbf{J}}_{k-1} = [\text{sat}(s_k),\ \text{sat}(s_k),\ \ldots,\ \text{sat}(s_k)]^T. \tag{8.57}$$

Because only the first value of the predicted control sequence is used, the optimal control action can be obtained:

$$u_k^{\text{pc}} = -\mathbf{v}(\Phi^T\Phi + w\mathbf{I})^{-1}\Phi^T(\Lambda s_k - \Gamma\hat{\zeta}_{k-1} - \mathbf{L}\hat{\mathbf{J}}_{k-1}) \tag{8.58}$$

where the selection vector $\mathbf{v} = [1, 0, 0, \ldots, 0]$.

Therefore, in view of Eq. (8.42) along with Eqs. (8.22) and (8.58), the global control action can be derived as follows

$$\begin{aligned} u_k = {} & (K_1\mathbf{CH})^{-1}(-K_3e_{k-1} - K_2e_k + K_1r_{k+1} - K_1\mathbf{CGX}_k - K_1\mathbf{CQV}_k - K_1\mathbf{CP}_{k-1}) \\ & -(\mathbf{CH})^{-1}K_s\text{sat}(s_k) - \mathbf{v}(\Phi^T\Phi + w\mathbf{I})^{-1}\Phi^T(\Lambda s_k - \Gamma\hat{\zeta}_{k-1} - \mathbf{L}\hat{\mathbf{J}}_{k-1}). \end{aligned} \tag{8.59}$$

It is observed from Eq. (8.59) that the one-step forward reference position r_{k+1} is required to realize the controller. In micro-/nanopositioning applications, the trajectory to be tracked is usually predefined. Hence, it is reasonable to assume that r_{k+1} is known. The block diagram of the DSMPC control scheme is depicted in Fig. 8.1.

8.4.2 Stability Analysis

Theorem 8.2 *For the system described by Eqs. (8.12) and (8.13) along with the sliding function (8.18), if the controller (8.59) is employed, then the quasi-sliding mode will occur within a finite number of steps.*

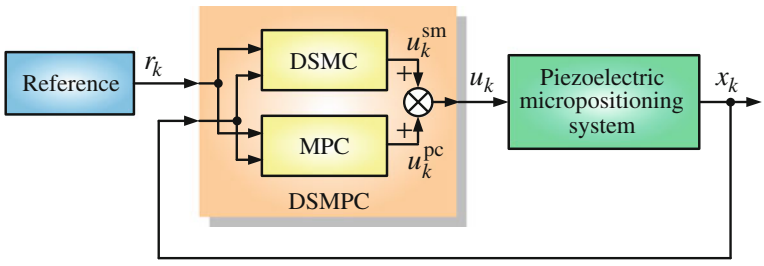

Fig. 8.1 Block diagram of the DSMPC control scheme

Proof Substituting Eq. (8.55) along with Eqs. (8.56) and (8.57) into the stacked equation (8.45) yields

$$\mathbf{S}_k = \Lambda s_k - \Phi(\Phi^T\Phi + w\mathbf{I})^{-1}\Phi^T(\Lambda s_k - \Gamma\hat{\zeta}_{k-1} - L\hat{\mathbf{J}}_{k-1}) - \Gamma\zeta_{k-1} - \mathbf{L}\mathbf{J}_{k-1} \tag{8.60}$$

where the switching control term $\mathbf{L}\mathbf{J}_{k-1}$ takes effect initially in the reaching phase. For a steady-state analysis, the transient switching control action is not considered.

For the convenience of analysis, it is assumed that there is no penalty for the partial control action u_k^{pc}, i.e., $w = 0$. Therefore, Eq. (8.60) further reduces to

$$S_k = \Gamma(\hat{\zeta}_{k-1} - \zeta_{k-1}). \tag{8.61}$$

Next, considering only the first value of the predicted sliding hyperplane vector (8.61) and taking into account Eqs. (8.46) and (8.56), it is derived that

$$\begin{aligned} s_{k+1} &= K_1\mathbf{C}(\tilde{\mathbf{P}}_{k-1} - \tilde{\mathbf{P}}_k) \\ &= K_1\mathbf{C}(\mathbf{P}_k - 2\mathbf{P}_{k-1} + \mathbf{P}_{k-2}) = O(T^3) \end{aligned} \tag{8.62}$$

which indicates that the magnitude of s_{k+1} is of the order $O(T^3)$ in consideration of Property 4.1.

Therefore, the ultimate magnitude of s_{k+1} is limited:

$$|s_{k+1}| \leq \lambda_s \tag{8.63}$$

where λ_s is defined as the quasi-sliding mode band width.

According to Definition 1 and Definition 2 in [1], it can be concluded that the system described by Eqs. (8.12) and (8.13) satisfies the reaching condition of the quasi-sliding mode in λ_s vicinity of the sliding surface in a finite number of steps. Therefore, the closed-loop control system is stable.

Remark 8.2 The essence of the presented DSMPC scheme is to force the system trajectory to reach a quasi-sliding mode in an optimal manner which is enabled by the predictive control action u_k^{pc} as well as u_k^{sm}. One advantage of this quasi-sliding model lies in that it does not require the system state to cross the sliding hyperplane in each successive control step. Therefore, the chattering phenomenon is eliminated. As a consequence, the control action is reduced and the control performance is improved [1].

8.4.3 Error Bound Analysis

Substituting Eq. (8.59) into the one-step forward error equation (8.33) yields

$$\begin{aligned} e_{k+1} = \mathbf{C}(\mathbf{P}_k - \mathbf{P}_{k-1}) - K_1^{-1}(K_2 e_k + K_3 e_{k-1}) \\ -\mathbf{vCH}(\Phi^T\Phi + wI)^{-1}\Phi^T(\Lambda s_k - \Gamma\hat{\zeta}_{k-1} - \mathbf{L}\hat{\mathbf{J}}_{k-1}). \end{aligned} \tag{8.64}$$

As mentioned earlier, the ultimate tracking error is analyzed without considering the transient switching control action $\mathbf{L}\hat{\mathbf{J}}_{k-1}$. Additionally, for the sake of simplicity, it is assumed that there is no penalty for the predictive control action, i.e., $w = 0$. Thus, Eq. (8.64) reduces to

$$e_{k+1} = -K_1^{-1}s_k - K_1^{-1}(K_2 e_k + K_3 e_{k-1}). \tag{8.65}$$

In view of Property 4.2 as well as $s_k = O(T^3)$, it can be derived from (8.65) that

$$e_k = O(T^2). \tag{8.66}$$

Hence, the ultimate bound of the output tracking error e_k is of the order $O(T^2)$, which is much lower than the $O(T)$ tracking error obtained by DSMC as shown in Eq. (8.35).

Remark 8.3 It is observed from Eq. (8.62) that s_{k+1} has the magnitude of order $O(T^3)$. Therefore, the DSMPC controller (8.59) drives the system trajectory to slide in the vicinity of the sliding surface with an ultimate bound of $O(T^3)$ thickness, whose magnitude is much lower than the $O(T)$ thickness achieved by DSMC controller as shown in Eq. (8.32). As a consequence, a much lower control error of order $O(T^2)$ is produced by the DSMPC as indicated in Eq. (8.66).

8.5 Experimental Studies and Discussion

In this section, the performance of the developed controllers is verified by carrying out a series of experimental studies.

8.5.1 Experimental Setup

The experimental setup of a piezo-actuated micropositioning system is shown in Fig. 7.1. A custom-built flexure-based microgripper is actuated by a piezoelectric stack actuator (PSA). For the measurement of the gripper tip position, four strain gages (model: SGD-3/350-DY13, from Omega Engineering Ltd.) are adopted to

construct a full Wheatstone bridge circuit. The control hardware is realized using a National Instruments (NI) cRIO-9022 real-time (RT) controller combined with cRIO-9118 reconfigurable chassis which contains a field-programmable gate array (FPGA) core. Additionally, the chassis is equipped with NI-9263 D/A module and NI-9237 A/D module. The analog excitation signal is amplified by a high-voltage amplifier before being fed into the PSA. LabVIEW™ software is employed to implement a real-time control. After calibrating using a laser displacement sensor (model: LK-H055, from Keyence Corporation), the strain gage sensor offers a three-standard-deviation resolution of 0.34 μm.

8.5.2 Plant Model Identification

The plant model of the system is identified by means of frequency response approach. Specifically, swept sine waves with the amplitude of 0.1 V and frequency range of 1–500 Hz are used to drive the PSA. The position response is measured by the strain gage sensor using a sampling rate of 4 kHz. Then, a spectral analysis is conducted to obtain the frequency responses as depicted in Fig. 8.2. The system exhibits a resonant peak around 244 Hz. Based on the experimental data, a forth-order plant model G_p is identified with MATLAB®. Using a sampling time of $T = 0.00025$ s, the model G_p is discretized and the parameters of models (8.2) and (8.3) are obtained.

It is observed that the forth-order model is able to capture the system dynamics behavior up to 300 Hz. To describe the dynamics at frequencies higher than 300 Hz, a higher-order model is needed. In this work, a lower-order model is used to make a compromise between model complexity and accuracy, and to reveal the efficiency of the developed control scheme.

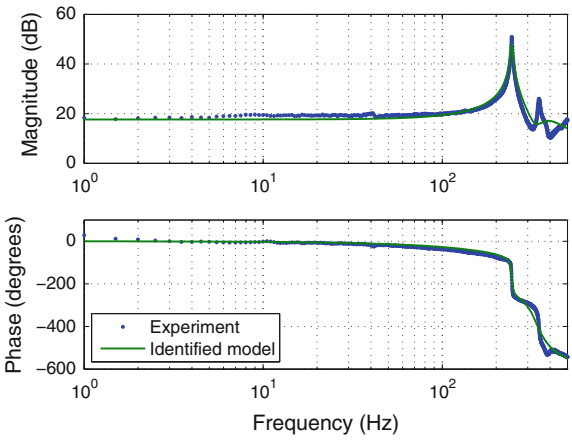

Fig. 8.2 Bode diagrams of the open-loop system obtained by experiment and the identified model

8.5.3 Controller Parameter Design

For comparison purpose, an incremental PID control is implemented due to its popularity. The controller can be expressed by Eq. (8.17) with s_k replaced by u_k^{pid}. The PID gains K_p, K_i, and K_d are optimally tuned through intensive tests. The gains are $K_p = 0.001$, $K_i = 0.0055$, and $K_d = 0.001$ in the present work. The suitability of these gains have been confirmed because other PID gains either produce larger tracking errors or result in oscillatory responses.

The tuned PID gains are adopted to calculate the DSMC and DSMPC gains K_1, K_2, and K_3 in Eq. (8.18). In addition, $K_s = 1.5$ and $\varepsilon = 5.0$ are selected for the DSMC and DSMPC. The DSMPC has two extra parameters, i.e., the prediction horizon N_h and weighting parameter w. In this work, $N_h = 10$ and $w = 5 \times 10^5$ are chosen by the trial-and-error approach to achieve better result. It is notable that the selected controller parameters satisfy the conditions in Eqs. (8.36)–(8.37) and (8.39)–(8.40).

8.5.4 Experimental Studies

8.5.4.1 Sinusoidal Positioning Testing

First, the motion tracking of a 10 Hz, 40 μm amplitude sinusoidal reference input as shown in Fig. 8.3a is examined. The tracking errors of the PID, DSMC, and DSMPC controllers are illustrated in Fig. 8.3b.

It is observed that the PID control produces the maximum error (MAXE) and root-mean-square error (RMSE) of 7.327 and 4.523 μm, i.e., 18.3 % and 11.3 % of the motion range, respectively. In contrast, the DSMC scheme leads to the MAXE of 1.748 μm and RMSE of 0.668 μm, which account for 4.4 % and 1.7 % of the total range, respectively. As compared with PID, the DSMC controller reduces the MAXE and RMSE by 76.1 % and 85.2 %, respectively. Furthermore, the DSMPC mitigates the MAXE and RMSE to 0.868 and 0.243 μm, i.e., 2.2 % and 0.6 % of the positioning range, respectively. Thus, as compared with DSMC, the DSMPC substantially reduces the MAXE and RMSE by 50.3 % and 63.6 %, respectively. The experimental results agree well with the ultimate tracking error bounds as predicted earlier.

Moreover, the sliding function values of the DSMC and DSMPC controllers are illustrated in Fig. 8.3c. It is seen that the sliding functions of both control schemes are well constrained by the thickness parameter of $\varepsilon = 5.0$. Specifically, the DSMC drives the sliding function to the range of ± 2.52 μm. In contrast, the sliding function has been further suppressed within ± 0.90 μm by the DSMPC scheme. In comparison with DSMC, the DSMPC mitigates the sliding surface boundedness by 64.3 % substantially. The experimental results are consistent with the ultimate bound analyses of the sliding surfaces for DSMC and DSMPC schemes as conducted earlier, respectively.

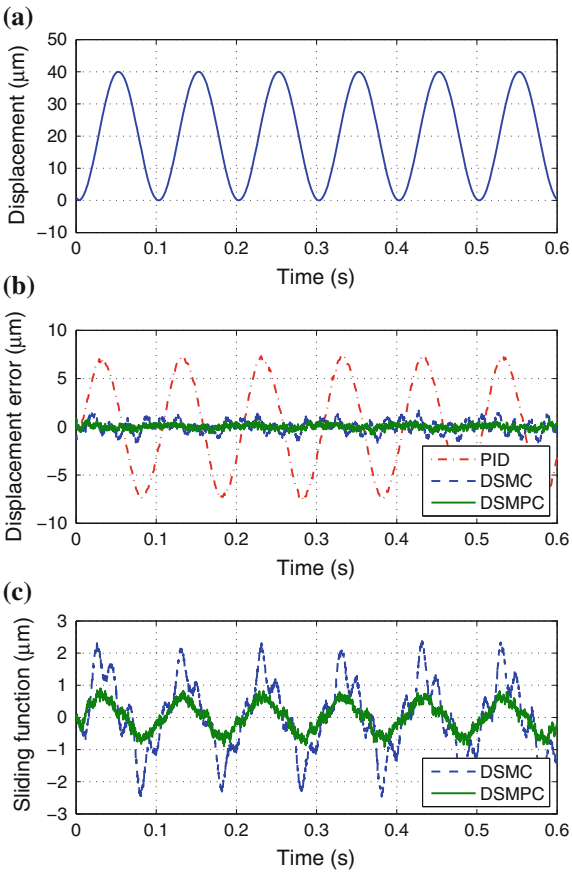

Fig. 8.3 Comparison of PID, DSMC, and DSMPC sinusoidal tracking results. **a** The reference input. **b** PID, DSMC, and DSMPC tracking errors. **c** Sliding functions of DSMC and DSMPC controllers

For a better understanding of the DSMPC scheme, the three components of the control action in terms of equivalent control, switching control, and predictive control are depicted in Fig. 8.4a, b, and c, respectively. It is seen that no chattering phenomenon exists in the DSMPC control action. Furthermore, it is found that the equivalent control is the dominant control action of the DSMPC and DSMC controllers. As compared with DSMC scheme, the DSMPC has an extra control action of predictive control as shown in Fig. 8.4c, whose magnitude is similar to that of the switching control as plotted in Fig. 8.4b. This extra predictive control action explains the reason why the DSMPC performs better than the conventional DSMC control strategy.

However, as compared with the DSMC tracking results, there is a significant amount of noise in the DSMPC results as shown in Fig. 8.3b. The spectra of the switching control, predictive control, and tracking errors of the DSMPC scheme are depicted in Fig. 8.5a, b, and c, respectively. Figure 8.5c shows that the high-frequency noise occurs at 230 Hz, which is close to the resonant frequency of the system. The

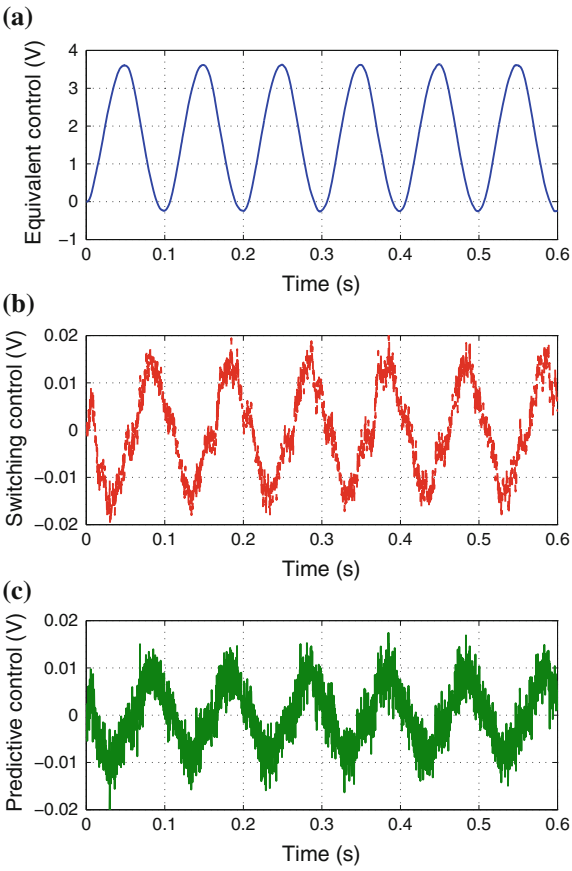

Fig. 8.4 Control action components of the DSMPC controller. **a** Equivalent control action. **b** Switching control action. **c** Predictive control action

noise level can be alleviated by reducing the magnitude of predictive control, which leads to a larger tracking error as the cost. In practice, a tradeoff between the noise and tracking error is required to adjust the predictive control action.

In addition, the motion tracking experiments for the 40-μm amplitude sinusoidal reference input with higher frequencies of 20 and 40 Hz have also been carried out. The tracking results of the three controllers are compared in Table 8.1. Evidently, the DSMPC outperforms both PID and DSMC schemes.

8.5.4.2 Control Bandwidth Testing

To further explore the performance of the control schemes, the control bandwidth of the piezoelectric micropositioning system is examined. Specifically, the motion tracking of the sinusoidal signal with the amplitude of 10 μm and frequency varying

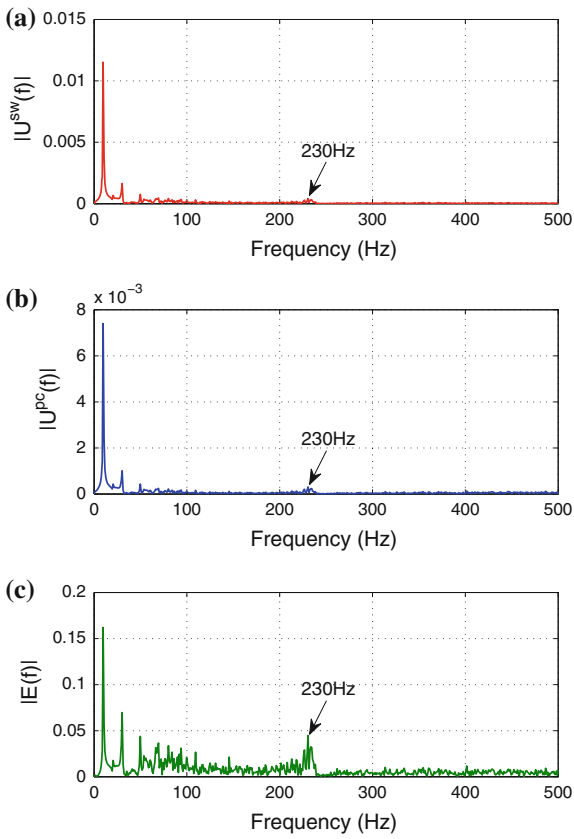

Fig. 8.5 Amplitude spectra of **a** switching control u^{sw}, **b** predictive control u^{pc}, and **c** tracking error of DSMPC

Table 8.1 Sinusoidal positioning results achieved by PID, DSMC, and DSMPC controllers

Frequency	Performance	PID	DSMC	DSMPC
10 Hz	MAXE (μm)	7.327	1.748	0.868
	RMSE (μm)	4.523	0.668	0.243
20 Hz	MAXE (μm)	8.344	3.463	1.647
	RMSE (μm)	13.486	1.392	0.494
40 Hz	MAXE (μm)	12.988	5.323	3.843
	RMSE (μm)	18.942	3.164	2.142

from 1 to 500 Hz has been undertaken. The closed-loop frequency responses of the system are shown in Fig. 8.6.

In this work, the closed-loop control bandwidth is defined as the frequency at which the phase is lagged 30° [8]. With the PID, DSMC, and DSMPC controllers, the 30°-lag bandwidths of 17.1, 47.4, and 53.9 Hz are achieved, which are equivalent to 7.0, 19.4, and 22.1 % of the resonant frequency, respectively. These cutoff frequencies

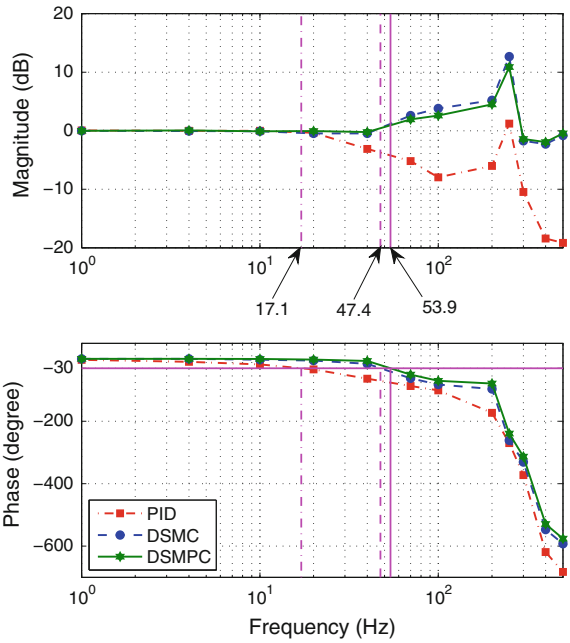

Fig. 8.6 Closed-loop Bode diagrams of the micropositioning system obtained with PID, DSMC, and DSMPC controllers

correspond to small magnitude errors of −0.27, 0.48, and 0.92 dB of the closed-loop responses of PID, DSMC, and DSMPC, respectively. Hence, as compared with PID and DSMC, the DSMPC enables an improvement of 215 and 14 % on the control bandwidth, respectively.

8.5.5 Further Discussion

Figure 8.6 indicates a peak value of about 10 dB in the magnitude response around the resonant frequency of the system. It means that the closed-loop system does not damp the system significantly. This behavior is similar for the DSMC and DSMPC schemes. The resonant peak induces high-frequency noise as depicted in Fig. 8.5c. In the future work, the control scheme can be further enhanced to address the deficiencies.

As the frequency of the reference input increases, the performances of PID and DSMC controllers drop more quickly than that of DSMPC as indicated by Fig. 8.6. Actually, the reason why the PID and DSMC achieve worse positioning results is mainly attributed to their bandwidth limits and the inherent piezoelectric hysteresis effect. In contrast, the fact that a precise high-speed positioning is achieved by the reported DSMPC indicates the robustness of the DSMPC scheme under the influence of piezoelectric nonlinearities and other disturbances. As compared with DSMC, the

DSMPC enables a wider control bandwidth which is dominantly contributed by the predictive control action.

Unlike the existing observer-based DSMC algorithms [7, 9, 10], the DSMPC does not require a state observer because it is developed on the basis of an input/output data-based model. It is known that a state observer is capable of estimating the full states from noisy output signals. Instead, the presented observer-free approach uses the output directly, and it is not able to suppress the noise. Hence, the DSMPC scheme is preferable to be adopted for the situations where the sensor noise is not a critical issue. Otherwise, the implementation of an observer or a filter is desirable.

Although the MPC control action of the DSMPC scheme has been optimized, other control gains have not been optimally tuned. An optimum tuning of the controller parameters is a potential solution to further enhance the positioning performance. In addition, the motion tracking of sinusoidal trajectories has been carried out in this work to show the superiority of DSMPC over PID and DSMC control algorithms. Other type of trajectories (e.g., square and triangle waves) can also be employed for such purpose. Even so, the improvement of positioning accuracy for the micropositioning system over the conventional PID and DSMC as demonstrated by the conducted experiments validates the effectiveness of the DSMPC scheme and exhibits a potential for the future work.

8.6 Chapter Summary

A DSMPC control algorithm has been developed in this chapter dedicated to precision positioning control of a piezoelectric micro-/nanopositioning system without hysteresis modeling and state observer design. Theoretical analyses of the tracking accuracy and stability under the influence of disturbances have been carried out. Experimental results show that the DSMPC scheme produces a smaller tracking error bound than DSMC, thanks to an optimal predictive control action. Moreover, the DSMPC affords an enlarged control bandwidth than PID and DSMC, which is the reason why DSMPC performs better in terms of high-speed tracking accuracy. In the future, further work deserves to extend the control scheme to the nonminimum-phase system control.

References

1. Bartoszewicz, A.: Discrete-time quasi-sliding-mode control strategies. IEEE Trans. Ind. Electron. **45**(5), 633–637 (1998)
2. Elmali, H., Olgac, N.: Implementation of sliding mode control with perturbation estimation (SMCPE). IEEE Trans. Control Syst. Technol. **4**(1), 79–85 (1996)
3. Gao, W., Wang, Y., Homaifa, A.: Discrete-time variable structure control systems. IEEE Trans. Ind. Electron. **42**(2), 117–122 (1995)

4. Mitic, D., Antic, D., Milojkovic, M., Nikolic, S., Peric, S.: Input-output based quasi-sliding mode control of DC-DC converter. Facta Univ. Ser.: Elec. Energ. **25**(1), 69–80 (2012)
5. Neelakantan, V.A., Washington, G.N., Bucknor, N.K.: Model predictive control of a two stage actuation system using piezoelectric actuators for controllable industrial and automotive brakes and clutches. J. Intell. Mater. Syst. Struct. **19**(7), 845–857 (2008)
6. Sarpturk, S., Istefanopulos, Y., Kaynak, O.: On the stability of discrete-time sliding mode control systems. IEEE Trans. Automat. Contr. **32**(10), 930–932 (1987)
7. Xu, J.X., Abidi, K.: Discrete-time output integral sliding-mode control for a piezomotor-driven linear motion stage. IEEE Trans. Ind. Electron. **55**(11), 3917–3926 (2008)
8. Xu, Q., Jia, M.: Model reference adaptive control with perturbation estimation for a micropositioning system. IEEE Trans. Contr. Syst. Technol. **22**(1), 352–359 (2014)
9. Xu, Q., Li, Y.: Micro-/nanopositioning using model predictive output integral discrete sliding mode control. IEEE Trans. Ind. Electron. **59**(2), 1161–1170 (2012)
10. Xu, Q., Li, Y.: Model predictive discrete-time sliding mode control of a nanopositioning piezostage without modeling hysteresis. IEEE Trans. Contr. Syst. Technol. **20**(4), 983–994 (2012)

Chapter 9
Model-Reference Adaptive Control with Perturbation Estimation

This chapter presents the design and testing of a model-reference adaptive control (MRAC) scheme to compensate for the hysteresis effect of a class of piezo-actuated systems, which possess a second-order nominal model. Specifically, by treating the uncertainties as a lumped perturbation to the nominal system model, a scheme of MRAC with perturbation estimation (MRACPE) is developed and validated on a micropositioning system. As compared with existing works, the reported scheme allows the predesign of the maximum tracking error. It is capable of estimating the unmodeled perturbation of the system online.

9.1 Introduction

The idea of adaptive control is to adjust the system response by using a closed-loop controller whose parameters can be updated online. Unlike robust control approach, the adaptive control does not require a prior knowledge about the bounds on uncertain or time-varying items. Hence, adaptive control paves a more straightforward way to the precision control of micro-/nanopositioning systems. Nevertheless, only limited works have been made toward the extension of adaptive controllers to micro-/nanopositioning system control. In the previous work [6], a MRAC strategy is reported to compensate for the hysteresis effect of a micropositioning stage. Even though the adaptive controller has been realized without modeling the hysteresis effect nor acquiring the uncertainty bounds, a Prandtl–Ishlinskii hysteresis model is required to convert the desired motion trajectory into a voltage input. More recently, a MRAC scheme based on the hyperstability theory is presented for a piezo-actuated system [7]. Nonetheless, a Bouc–Wen hysteresis model is still employed to identify the dynamics equation of the system.

From a practical point of view, it is preferable to develop a MRAC scheme without modeling the complicated nonlinear effects. By considering the nonlinearity as perturbations to the system, several perturbation estimation methods have been reported,

© Springer International Publishing Switzerland 2016

Q. Xu and K.K. Tan, *Advanced Control of Piezoelectric Micro-/Nano-Positioning Systems*, Advances in Industrial Control,
DOI 10.1007/978-3-319-21623-2_9

which can be integrated with MRAC schemes. To name a few, a scheme of MRAC with disturbance rejection strategy is presented for the systems, which can be represented by parabolic or hyperbolic partial differential equations along with known disturbance model or constant disturbance [5]. However, these scenarios are different from the situation in a piezo-actuated system, where the disturbance involving hysteresis nonlinearity is not constant. In addition, an adaptive perturbation approximator is outlined to estimate the structured perturbations of second-order systems online [2], and a perturbation estimation mechanism is proposed to design a MRAC controller for a class of MIMO dynamic systems [1]. The aforementioned two methods have been implemented based on the assumption that the system states are all measurable. Nevertheless, this assumption does not always hold for micropositioning systems which typically only offer the displacement feedback. Moreover, the reference signals as used in the preceding literature are all given in terms of voltage. For practical applications, a desired motion trajectory instead of voltage signal is predefined.

This chapter presents a scheme of MRACPE for the precision motion control of a piezoelectric actuation micropositioning system. One advantage of the proposed scheme lies in that the size of the tracking error can be predesigned, which is desirable in practice. A second-order nominal system is assumed and the unmodeled dynamics and nonlinearity effect are treated as a lumped perturbation, which is approximated by a perturbation estimation technique. A dead-zone modification of the adaptive rules is introduced to mitigate the parameter drifts and to speed up the parameter convergence process. Moreover, the MRACPE scheme employs a desired displacement trajectory rather than a voltage signal as the reference input. The stability of the closed-loop control system is proved through Lyapunov stability analysis. Experimental studies show that the MRACPE is superior to conventional PID control in terms of positioning accuracy for both set-point and sinusoidal positioning tasks, which is enabled by a significantly enlarged control bandwidth.

9.2 Dynamics Modeling and Perturbation Estimation

9.2.1 Dynamics Modeling

Considering the micropositioning stage as a mass–spring–damper system, the dynamics model, which integrates the components of the stage and PSA, can be developed as follows:

$$M\ddot{x}(t) + B\dot{x}(t) + Kx(t) = Du(t) + P(t) \tag{9.1}$$

where t is the time variable, x denotes the output displacement, M, B, K, and D represent the equivalent mass, damping parameter, output stiffness, and displacement-voltage coefficient, respectively. In addition, the perturbation term $P(t)$ describes

the lumped effect of hysteresis, model parameter uncertainties, unmodeled high-frequency dynamics, and other disturbances. It is assumed that $P(t)$ is bounded.

The system model (9.1) can be rewritten into the form:

$$\ddot{x}(t) + \alpha_1 \dot{x}(t) + \alpha_0 x(t) = \beta_0 u(t) + f(t) \tag{9.2}$$

where $\alpha_1 = \frac{B}{M}$, $\alpha_0 = \frac{K}{M}$, $\beta_0 = \frac{D}{M}$, and $f(t) = \frac{P(t)}{M}$.

The dynamics model (9.2) indicates that the piezo-actuated system is represented by a second-order linear model, and the hysteresis effect is contained in the unknown perturbations $f(t)$ to the nominal system. The unmodeled nonlinearity and disturbances need to be compensated for in order to achieve a precise control of the position x. In the subsequent section, a perturbation estimation technique is employed for the online estimation of the unmodeled perturbation involving the hysteresis nonlinearity.

9.2.2 Perturbation Estimation

A brief review of the perturbation estimation method is outlined here. More details can be found in the literature [3].

Consider a general nonlinear system given by:

$$\mathbf{x}^{(n)} = \mathbf{f}(\mathbf{X}) + \Delta\mathbf{f}(\mathbf{X}) + [\mathbf{B}(\mathbf{X}) + \Delta\mathbf{B}(\mathbf{X})]\mathbf{u}(t) + \mathbf{d}(t) \tag{9.3}$$

where the vector $\mathbf{x}^{(n)} = [x_1^{(n_1)}, x_2^{(n_2)}, \ldots, x_m^{(n_m)}]^T \in \Re^m$ with $x_i^{(n_i)} \in \Re$, the global state vector $\mathbf{X} = [\mathbf{X}_1^T, \ldots, \mathbf{X}_m^T]^T \in \Re^r$ $(r = \sum_{i=1}^m n_i)$ with the state sub-vector $\mathbf{X}_i = [x_i, \dot{x}_i, \ldots, x_i^{(n_i-1)}]^T \in \Re^{n_i}$ and x_i $(i = 1, \ldots, m)$ denoting m independent coordinates. In addition, the superscript in $x_i^{(n_i)}$ refers to the n_ith order of time derivative.

The bounded perturbations in the system (9.3) can be combined together to form a perturbation vector:

$$\begin{aligned} \boldsymbol{\Psi}(t) &= \Delta\mathbf{f} + \Delta\mathbf{B}\mathbf{u}(t) + \mathbf{d}(t) \\ &= \mathbf{x}^{(n)} - \mathbf{f} - \mathbf{B}\mathbf{u}(t). \end{aligned} \tag{9.4}$$

The estimation for the perturbation $\boldsymbol{\Psi}$ is approximated as:

$$\boldsymbol{\Psi}_{est}(t) = \mathbf{x}_{cal}^{(n)} - \mathbf{f} - \mathbf{B}\mathbf{u}(t - T) \tag{9.5}$$

where $\mathbf{x}_{cal}^{(n)}$ denotes a calculated state vector because the measurement values of the higher order states of the system are not always available. Additionally, T is the sampling time interval and $\mathbf{u}(t - T)$ represents the control input in the previous

time step. In practice, a high enough sampling frequency is selected to ensure that $\mathbf{u}(t) \approx \mathbf{u}(t-T)$.

In order to obtain the state vector $\mathbf{x}_{cal}^{(n)}$, various types of state observers can be employed, e.g., Luenberger observer. In this work, the state vector is computed based on a backward difference equation:

$$\mathbf{x}_{cal}^{(n)}(t) = \frac{\mathbf{x}_{cal}^{(n-1)}(t) - \mathbf{x}_{cal}^{(n-1)}(t-T)}{T}. \tag{9.6}$$

The above approach is employed due to its advantage in terms of computational efficiency.

Given the system model (9.2), the perturbation f can be expressed by:

$$f(t) = \ddot{x}(t) + \alpha_1 \dot{x}(t) + \alpha_0 x(t) - \beta_0 u(t). \tag{9.7}$$

Based on the perturbation estimation strategy, f is estimated as follows:

$$\hat{f}(t) = \ddot{x}(t) + \alpha_1 \dot{x}(t) + \alpha_0 x(t) - \beta_0 u(t-T). \tag{9.8}$$

It is observed from (9.8) that the full states (x, $\dot{x}$, and $\ddot{x}$) of the system are required to implement the perturbation estimation. In a typical positioning system, only the position information x is provided by displacement sensors. Hence, the other states $\dot{x}$ and $\ddot{x}$ are estimated by the aforementioned state calculator (9.6).

In practice, the dynamics model parameters α_1, α_0, and β_0 can only be estimated with some degree of uncertainty. In the subsequent section, a MRACPE control scheme is devised to achieve a precise position control in the presence of model uncertainties.

9.3 MRACPE Control Design

The basic idea of MRACPE lies in the establishment of a closed-loop controller with parameters updated online to change the response of the system. The control error is defined as the deviation of the system output from the desired response of a reference model. Based on this error, the controller parameters are adaptively adjusted. The control objective is to drive the parameters to converge to ideal values for matching the reference model response.

9.3.1 MRACPE Controller Design

Using the estimated perturbation (9.8), the system model (9.2) becomes

$$\ddot{x}(t) + \alpha_1 \dot{x}(t) + \alpha_0 x(t) = \beta_0 u(t) + \hat{f}(t). \tag{9.9}$$

For the purpose of motion tracking control, a reference model is defined as follows:

$$\ddot{x}_m(t) + a_1\dot{x}_m(t) + a_0 x_m(t) = b_0 u_d(t) \tag{9.10}$$

where x_m is the reference model output, u_d is the input to the model, and a_1, a_0, and b_0 are positive parameters. For brevity, the time variable t is omitted hereafter in this section.

Defining the tracking error as

$$e = x - x_m. \tag{9.11}$$

Then, subtracting Eq. (9.10) from Eq. (9.9) leads to an error dynamics equation:

$$\ddot{e} + a_1\dot{e} + a_0 e = \beta_0 u - b_0 u_d + (a_1 - \alpha_1)\dot{x} + (a_0 - \alpha_0)x + \hat{f}. \tag{9.12}$$

Assigning a vector of state error $\mathbf{E} = [e \ \ \dot{e}]^T$, Eq. (9.12) can be expressed into the state-space form:

$$\dot{\mathbf{E}} = \mathbf{A}\mathbf{E} + \beta_0 \mathbf{B}u + \boldsymbol{\Delta} \tag{9.13}$$

where

$$\mathbf{A} = \begin{bmatrix} 0 & 1 \\ -a_0 & -a_1 \end{bmatrix}, \ \mathbf{B} = \begin{bmatrix} 0 \\ 1 \end{bmatrix}, \ \boldsymbol{\Delta} = \begin{bmatrix} 0 \\ \delta \end{bmatrix} \tag{9.14}$$

with $\delta = (a_1 - \alpha_1)\dot{x} + (a_0 - \alpha_0)x - b_0 u_d + \hat{f}$.

It has been shown that if all the eigenvalues of the matrix $\mathbf{A}$ have negative real parts, then all solutions of $\mathbf{E}$ to Eq. (9.13) will tend to zero as $t \to \infty$ [4]. Moreover, the system (9.13) is asymptotically stable. Because given any symmetric positive definite matrix $\mathbf{Q}$, there exists a symmetric positive definite matrix $\mathbf{P}$, which is the unique solution to the linear equation:

$$\mathbf{A}^T\mathbf{P} + \mathbf{P}\mathbf{A} = -\mathbf{Q}. \tag{9.15}$$

In addition, an auxiliary control item is defined as follows:

$$\hat{e} = \mathbf{E}^T\mathbf{P}\mathbf{B}. \tag{9.16}$$

Theorem 9.1 *For the system described by Eq. (9.9) with a reference model (9.10), the tracking error e defined by Eq. (9.11) satisfies* $\lim_{t\to\infty} e(t) = 0$ *if the MRACPE control law is given by*

$$u = k_0 u_d + k_1 x + k_2 \dot{x} + k_3 \hat{f} \tag{9.17}$$

where the adaptive laws for the control parameters k_0, k_1, k_2, and k_3 are chosen as:

$$\dot{k}_0 = -\eta_0 \hat{e}\, u_d \tag{9.18}$$
$$\dot{k}_1 = -\eta_1 \hat{e}\, x \tag{9.19}$$
$$\dot{k}_2 = -\eta_2 \hat{e}\, \dot{x} \tag{9.20}$$
$$\dot{k}_3 = -\eta_3 \hat{e}\, \hat{f} \tag{9.21}$$

where η_0, η_1, η_2, and η_3 are all positive constants.

Proof To demonstrate the stability of the controller, a Lyapunov candidate function is defined as follows:

$$V = \frac{1}{2}\mathbf{E}^T\mathbf{P}\mathbf{E} + \frac{1}{2\eta_0\beta_0}(\beta_0 k_0 - b_0)^2 + \frac{1}{2\eta_1\beta_0}(\beta_0 k_1 + a_0 - \alpha_0)^2 + \frac{1}{2\eta_2\beta_0}(\beta_0 k_2 + a_1 - \alpha_1)^2 + \frac{1}{2\eta_3\beta_0}(\beta_0 k_3 + 1)^2. \tag{9.22}$$

In view of Eqs. (9.13) and (9.16), the time derivative of the first item in Eq. (9.22) can be expressed as

$$\begin{aligned}\dot{V}_1 &= \mathbf{E}^T\mathbf{P}\dot{\mathbf{E}} \\ &= \mathbf{E}^T\mathbf{P}\mathbf{A}\mathbf{E} + \mathbf{E}^T\mathbf{P}(\beta_0\mathbf{B}u + \boldsymbol{\Delta}) \\ &= \frac{1}{2}\mathbf{E}^T(\mathbf{A}^T\mathbf{P} + \mathbf{P}\mathbf{A})\mathbf{E} + \mathbf{E}^T\mathbf{P}\mathbf{B}(\beta_0 u + \delta) \\ &= -\frac{1}{2}\mathbf{E}^T\mathbf{Q}\mathbf{E} + \hat{e}(\beta_0 u + \delta).\end{aligned} \tag{9.23}$$

Hence, the time derivative of the Lyapunov function is derived:

$$\dot{V} = -\frac{1}{2}\mathbf{E}^T\mathbf{Q}\mathbf{E} + \hat{e}(\beta_0 u + \delta) + \frac{\dot{k}_0}{\eta_0}(\beta_0 k_0 - b_0) + \frac{\dot{k}_1}{\eta_1}(\beta_0 k_1 + a_0 - \alpha_0) + \frac{\dot{k}_2}{\eta_2}(\beta_0 k_2 + a_1 - \alpha_1) + \frac{\dot{k}_3}{\eta_3}(\beta_0 k_3 + 1). \tag{9.24}$$

Next, substituting Eq. (9.17) into Eq. (9.24) and rearranging the items leads to

$$\dot{V} = -\frac{1}{2}\mathbf{E}^T\mathbf{Q}\mathbf{E} + (\hat{e}u_d + \frac{\dot{k}_0}{\eta_0})(\beta_0 k_0 - b_0) + (\hat{e}x + \frac{\dot{k}_1}{\eta_1})(\beta_0 k_1 + a_0 - \alpha_0) + (\hat{e}\dot{x} + \frac{\dot{k}_2}{\eta_2})(\beta_0 k_2 + a_1 - \alpha_1) + (\hat{e}\hat{f} + \frac{\dot{k}_3}{\eta_3})(\beta_0 k_3 + 1). \tag{9.25}$$

Then, substituting the adaptive laws (9.18)–(9.21) into Eq. (9.25) and considering Eq. (9.15), allows the derivation:

$$\dot{V} = -\frac{1}{2}\mathbf{E}^T\mathbf{Q}\mathbf{E} \leq 0. \tag{9.26}$$

Therefore, the stability of the closed-loop control system is proved.

9.3.2 Dead-Zone Modification of Adaptive Laws

In practice, due to the noises in the tracking error, the control parameters (k_0, k_1, k_2, and k_3) drift as demonstrated by the experiments as conducted later. In order to alleviate the drift issue, a dead-zone modification scheme [8] is adopted to turn off the adaptation processes once the tracking error attains the predefined small value.

Specifically, the adaptive laws (9.18)–(9.21) are revised as follows:

$$\dot{k}_0 = \begin{cases} -\eta_0 \hat{e}\, u_d, & \text{if } |e| > \varepsilon \\ 0, & \text{if } |e| \leq \varepsilon \end{cases} \tag{9.27}$$

$$\dot{k}_1 = \begin{cases} -\eta_1 \hat{e}\, x, & \text{if } |e| > \varepsilon \\ 0, & \text{if } |e| \leq \varepsilon \end{cases} \tag{9.28}$$

$$\dot{k}_2 = \begin{cases} -\eta_2 \hat{e}\, \dot{x}, & \text{if } |e| > \varepsilon \\ 0, & \text{if } |e| \leq \varepsilon \end{cases} \tag{9.29}$$

$$\dot{k}_3 = \begin{cases} -\eta_3 \hat{e}\, \hat{f}, & \text{if } |e| > \varepsilon \\ 0, & \text{if } |e| \leq \varepsilon \end{cases} \tag{9.30}$$

where ε is the assigned dead-zone size, which enables the restriction of the tracking error e. Generally, the smaller the ε, the lower the tracking errors. The ε value can be tuned by the trial-and-error approach through experimental studies.

9.3.3 Overview of Control Scheme

Recalling the expression for the estimated perturbation in Eq. (9.8), the control law (9.17) can be further written into the form:

$$u(t) = k_0 u_d(t) + (k_1 + k_3\alpha_0)x(t) + (k_2 + k_3\alpha_1)\dot{x}(t) + k_3\ddot{x}(t) - k_3\beta_0 u(t-T). \tag{9.31}$$

The block diagram of the control scheme is illustrated in Fig. 9.1. It is observed that the controller has two inputs, i.e., the desired control voltage u_d and the displacement x of the system. The output of the controller is the voltage u that will be used to drive the piezoelectric actuator.

By using a voltage signal as the reference input, several MRAC schemes have been realized in the previous work [1, 2]. However, for practical applications, a desired displacement trajectory instead of the voltage is predefined for the stage. Thus, once

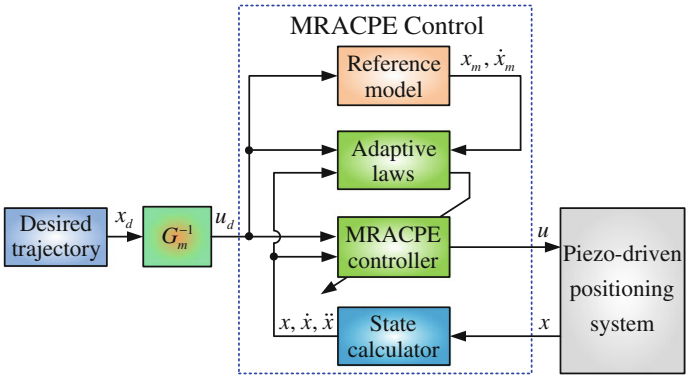

Fig. 9.1 Block diagram of the MRACPE control scheme

a displacement is given, the corresponding desired voltage needs to be determined. Here, this mapping is implemented by resorting to an inverse model of the reference model (9.10), which is expressed by the following transfer function:

$$G_m^{-1}(s) = \frac{U_d(s)}{X_m(s)} = \frac{1}{b_0}(s^2 + a_1 s + a_0) \tag{9.32}$$

where U_d and X_m represent the Laplace transform of u_d and x_m, respectively.

9.4 Experimental Setup and Controller Setup

In this work, the effectiveness of the MRACPE control scheme is verified by conducting a series of experimental studies on a piezo-driven micropositioning system.

9.4.1 Experimental Setup

As illustrated in Fig. 9.2a, the employed micropositioning stage is composed of flexure hinges. The stage is actuated by a piezoelectric stack actuator (PSA) through a bridge-type displacement amplifier, which employs right circular flexure hinges. The linear displacement of the output platform is guided by four leaf springs which are connected to the mounting frame. When the PSA is driven by a voltage amplifier, the stage delivers an amplified displacement along the x-axis direction without parasitic motions, which has been validated by the simulation result of the finite-element analysis (FEA) as shown in Fig. 9.2b. More details about the working principle and analytical modeling of the displacement amplifier can be found in [12].

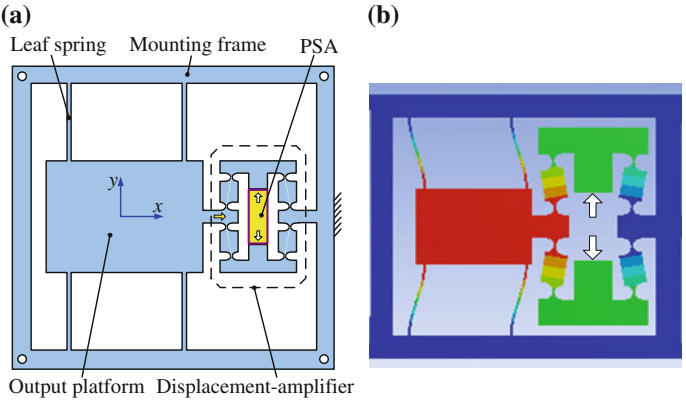

Fig. 9.2 **a** A micropositioning stage driven by a piezoelectric stack actuator through displacement amplifier. **b** Deformed shape obtained by FEA simulation

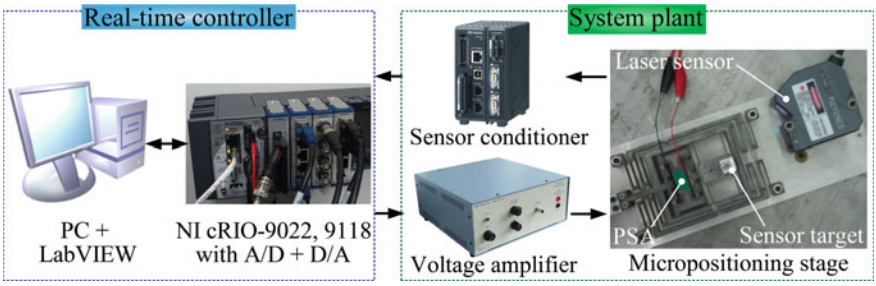

Fig. 9.3 Experimental setup of a piezo-driven micropositioning system

The experimental setup of the custom-built micropositioning system is depicted in Fig. 9.3. Actually, a PSA and a voice coil motor are used to construct a dual-stage micropositioning system as detailed in [10]. In this work, the PSA-driven inner flexure stage is employed to verify the proposed control scheme. The PSA is connected to a high-voltage amplifier (model: EPA-104, from Piezo Systems, Inc.) with an adjustable gain value of then. The output position of the stage is measured by a laser displacement sensor (model: LK-H055, from Keyence Corp.). In addition, a Natural Instruments (NI) cRIO-9022 real-time controller combined with cRIO-9118 reconfigurable chassis is adopted to implement the control algorithm. The chassis is equipped with NI-9215 A/D and NI-9263 D/A modules for the acquisition of sensor readings and production of excitation voltage signals, respectively.

The NI cRIO-9118 chassis contains a field-programmable gate array (FPGA) core, and the associated cRIO-9022 real-time controller communicates with a personal computer (PC) via Ethernet port. The control algorithm is programmed using the LabVIEW™ software. With the MRACPE control algorithm, the control hard-

ware enables a maximal closed-loop sampling frequency of 100 kHz. In this work, a sufficient sampling frequency of 5 kHz is adopted.

9.4.2 Statics Testing and Dynamics Model Identification

First, the motion range of the micropositioning system is tested by applying a sinusoidal voltage signal with the amplitude of 10 V and frequency of 0.2 Hz. The results are illustrated in Fig. 9.4, which shows that a motion range over 94 μm is obtained. In addition, the open-loop output versus input curve exhibits a hysteresis width of 17.4 %. The presence of the significant hysteresis nonlinearity necessitates the control scheme development in order to achieve a precise positioning.

Next, the dynamics model parameters α_1, α_0, and β_0 of the nominal plant model (9.2) are identified by means of frequency response approach. Specifically, swept sine waves with the amplitude of 0.5 V and frequency range of 1–650 Hz are produced to drive the PSA via the high-voltage amplifier. Both the excitation voltage and the displacement output signals are acquired to generate the frequency response of the system, as shown in Fig. 9.5. From the experimental data, a second-order model is identified and the model parameters are tabulated in Table 9.1.

It is observed from Fig. 9.5 that the second-order model is capable of approximating the frequency response up to 600 Hz, which covers the resonant frequency of 470 Hz. In order to capture the system dynamics at frequencies higher than 600 Hz, a model of higher order is needed. In the current work, a simple second-order model is employed to demonstrate the effectiveness of the control scheme, and the residual modes at higher frequencies are considered as disturbances, which will be suppressed by the MRACPE controller.

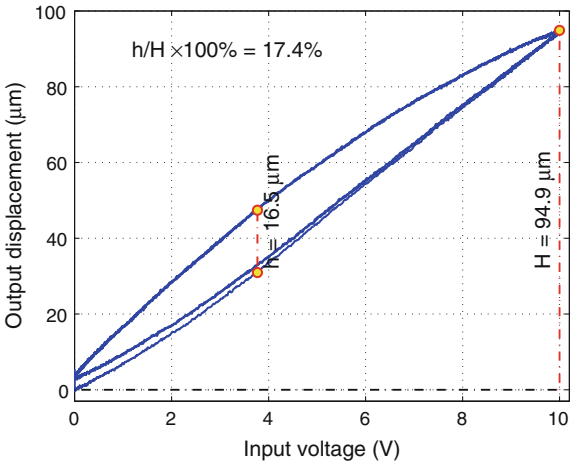

Fig. 9.4 Open-loop hysteresis loop obtained with a 0.2-Hz sinusoidal reference input

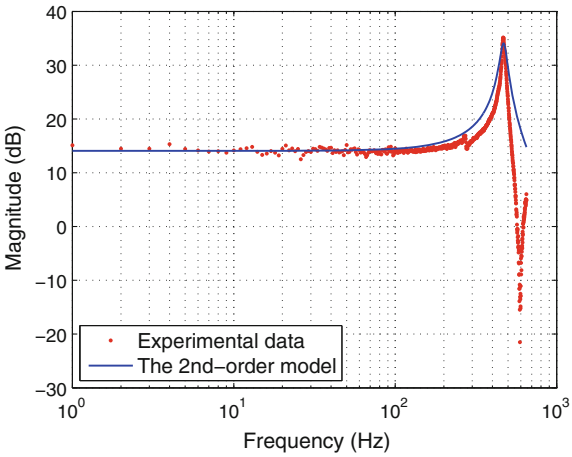

Fig. 9.5 Frequency responses obtained by experiment and the identified second-order model

Table 9.1 Parameters of the plant model and designed controller

Parameter	Value
α_0	8.721×10^6
α_1	2.953×10^2
β_0	4.404×10^7
a_0	8.721×10^6
a_1	1.477×10^3
b_0	4.404×10^7
η_0	1×10^{-2}
η_1	1×10^{-4}
η_2	1×10^{-9}
η_3	1×10^{-17}
ε	0.7
$\mathbf{Q}$	$\text{diag}\{3 \times 10^5, 1 \times 10^{-3}\}$

9.4.3 Controller Setup

For experimental investigations, the reference model is chosen with parameters a_0, a_1, and b_0 as described in Table 9.1. The assigned parameters of the MRACPE controller are also shown in Table 9.1. As depicted in Fig. 9.1, by passing the desired position trajectory x_d through the reference model inverse G_m^{-1}, a reference voltage signal u_d is generated. Excited by u_d, an output $x_m = x_d$ is then produced by the reference model.

For a comparative study, the popular PID controller is also implemented. A digital PID control strategy is employed as follows:

$$u_k = K_p e_k + K_i \sum_{j=0}^{k} e_k + K_d (e_k - e_{k-1}) \tag{9.33}$$

with the positioning error $e_k = x_{d_k} - x_k$, where x_{d_k} and x_k represent the desired and actual system output at the kth time step, and K_p, K_i, and K_d denote the proportional, integral, and derivative gains, respectively. The PID gains are initially tuned by simulation studies using the Ziegler–Nichols (Z–N) method. The gains are then finely adjusted through experimental studies to eliminate the overshoot, i.e., $K_p = 0.01$, $K_i = 0.0023$, and $K_d = 0.029$. A sampling time of $T = 0.0002$ s is adopted for both MRACPE and PID controllers.

9.5 Experimental Results and Discussion

9.5.1 Set-Point Positioning Testing

First, the set-point positioning capability of the micropositioning system is examined. By commanding the output platform from home position to 20 μm, the positioning results using PID and MRACPE controllers are depicted in Fig. 9.6. Both controllers are tuned to achieve a quick response without overshoot. For a quantitative comparison, the performances are shown in Table 9.2.

It is observed that the PID scheme produces a slightly quicker response because its 5 % settling time is 0.006 s smaller than that of SMCPE. Even so, the MRACPE delivers a more accurate positioning as it creates a steady-state root-mean-square (RMS) error which is 7 % lower than the PID result.

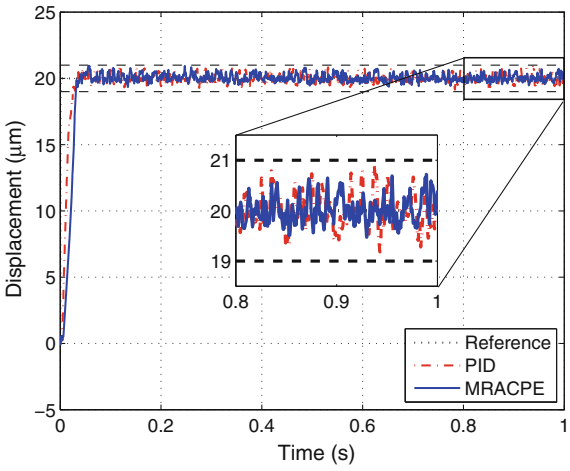

Fig. 9.6 Experimental results of set-point positioning using PID and MRACPE controllers

Table 9.2 Positioning results of PID and MRACPE controllers

Performance	PID	MRACPE
Set-point positioning (20 μm)		
5 % settling time (s)	0.025	0.031
RMS steady-state error (μm)	0.275	0.256
Sinusoidal positioning (10 Hz)		
Maximum steady-state error (%)	39.20	6.51
RMS steady-state error (%)	25.60	2.96

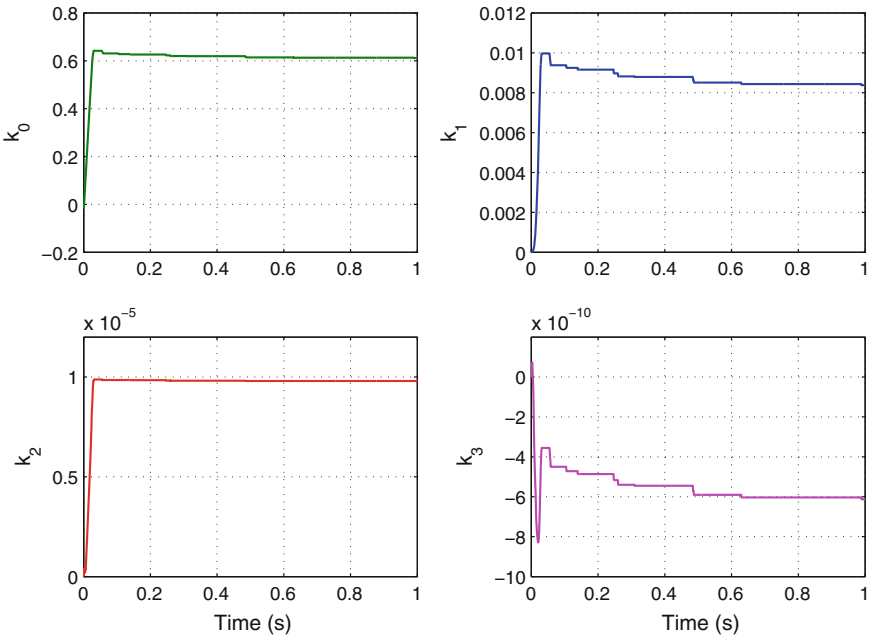

Fig. 9.7 Adaptation processes of the MRACPE control parameters with $\varepsilon = 0.7$ for the set-point positioning

Additionally, the adaptation processes of the four control parameters of the MRACPE scheme are depicted in Fig. 9.7. The dead-zone parameter is assigned as $\varepsilon = 0.7$ to limit the positioning errors within ± 0.7 μm, which is the noise level of the displacement sensor. It is seen that as the response approaches the steady state, the controller parameters converge to the corresponding ideal values, respectively. It is notable that a quicker response speed of MRACPE can be obtained by optimally tuning the control gains η_0, η_1, η_2, and η_3.

9.5.2 Sinusoidal Positioning Testing

Next, a 10-Hz, 20 μm-amplitude sinusoidal positioning control is performed by employing the two controllers, and the results are shown in Fig. 9.8. It is found that the PID algorithm leads to identical responses in each cycle. Concerning the MRACPE, after the transient progress within the first few cycles, it gives identical responses afterwards. Additionally, the PID control produces the maximum and RMS steady-state positioning errors of 7.840 and 5.119 μm, which account for 39.20 and 25.60 % of the positioning range, respectively. In contrast, the MRACPE leads to the maximum and RMS steady-state errors of 1.302 and 0.591 μm, i.e., 6.51 and 2.96 % of the positioning range, respectively. The sinusoidal positioning results are summarized in Table 9.2. As compared with PID control, the MRACPE scheme improves the positioning accuracy by 83 and 88 % in terms of the maximum and RMS errors, respectively.

The sinusoidal positioning results are generated by the same controllers as used in the aforementioned set-point positioning tests, except that $\varepsilon = 1.3$ is reassigned in MRACPE. By optimally tuning the PID gains, the PID 2 controller is generated, which creates the results as shown in Fig. 9.8. It is observed that the maximum and RMS errors of 25.96 and 14.44 % are produced, respectively, which are about four times worse than the MRACPE results. Hence, the superiority of MRACPE over PID control is evident from the experimental results.

Furthermore, to discover the influence of the dead-zone selection on the MRACPE performance, the positioning results with three different dead-zones, i.e., 2.3, 1.6 and 1.3 μm, are examined. The MRACPE positioning errors and the parameter adaptation procedures are shown in Figs. 9.9 and 9.10, respectively. Figure 9.9 indicates that the maximum steady-state positioning errors are restricted by the assigned dead-zone values. The smaller the dead-zone, the better the positioning accuracy.

Figure 9.10 reveals that the controller parameters k_0, k_1, k_2, and k_3 arrive at the steady states quickly in two of the three case studies ($\varepsilon = 2.3$ and 1.6). Concerning the case with a smaller dead-zone value ($\varepsilon = 1.3$), the convergence speed of the controller parameters is slower due to the parameter drift. Further experimental testings show that the parameters get saturated finally. Hence, a tradeoff between the tracking accuracy and parameter convergence speed is needed to assign the dead-zone value.

9.5.3 Control Bandwidth Testing

In addition, the control bandwidth of the PSA-actuated system is tested by applying the 20-μm sinusoidal signal with the frequency varying from 1 to 100 Hz. The closed-loop frequency responses are shown in Fig. 9.11. It is observed that there are large phase lags (over 90°) within the ordinary −3 dB bandwidth, which lead to large

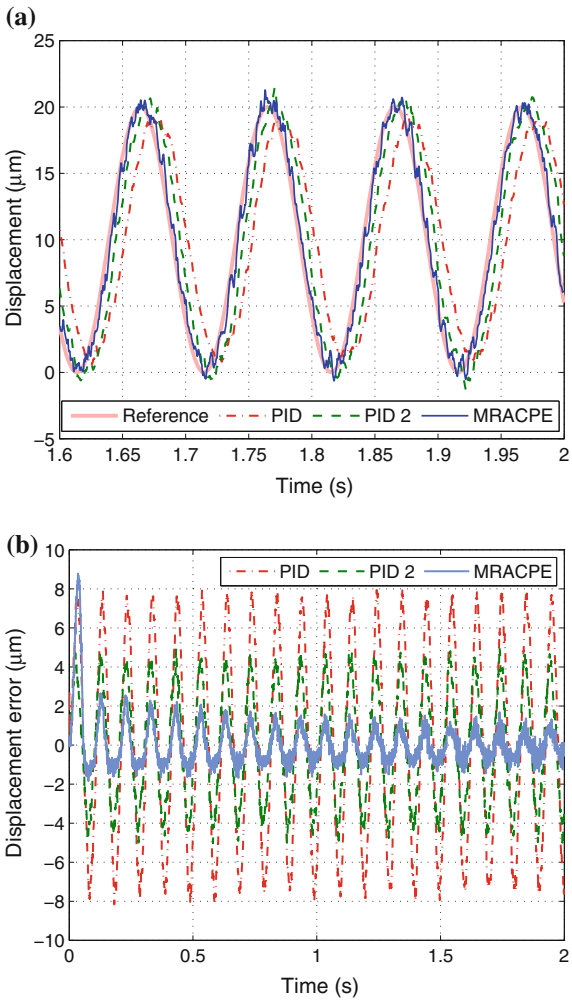

Fig. 9.8 **a** The 10-Hz sinusoidal motion tracking results of PID and MRACPE ($\varepsilon = 1.6$) controllers. **b** Positioning errors

tracking errors. Hence, the closed-loop control bandwidth is defined as the frequency at which the phase is lagged 30° [11]. With the PID and MRACPE controllers, the 30°-lag bandwidths of 12.8 and 79.3 Hz are achieved, which are equivalent to 2.7 and 16.9 % of the resonant frequency, respectively. These cutoff frequencies correspond to small errors of 0.43 and 1.72 dB for the magnitude responses of the PID and MRACPE controllers, respectively. As compared with PID algorithm, the MRAPCE scheme improves the control bandwidth by over six times.

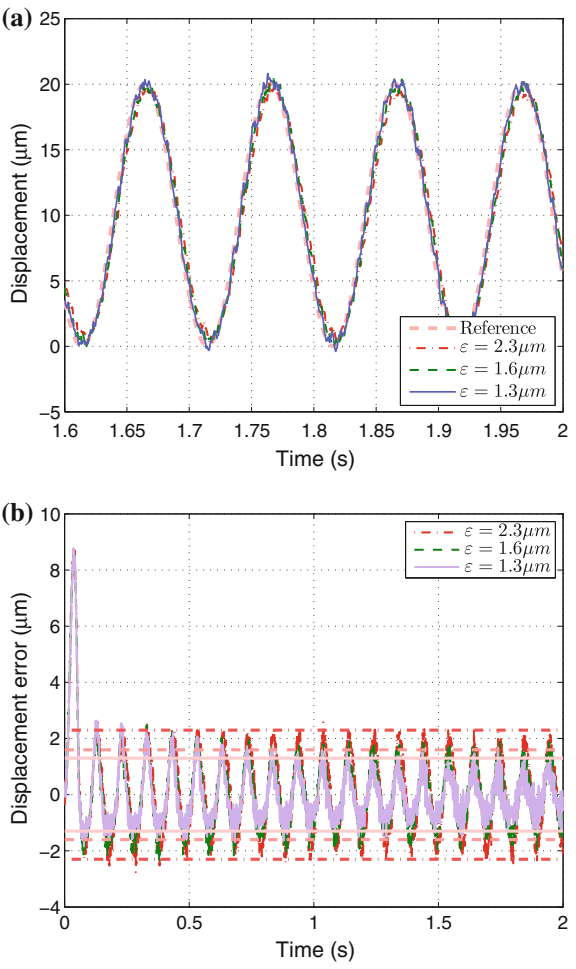

Fig. 9.9 **a** The sinusoidal positioning results of MRACPE with different dead-zones ε. **b** Positioning errors

9.5.4 Discussion

The obtained experimental results confirm the effectiveness of the MRACPE control scheme for a PSA-actuated micropositioning system. Because the scheme is implemented without modeling the hysteresis nonlinearity, the results demonstrate the efficiency of the reported idea for the disturbance suppression. Considering that the nominal plant model is used to develop the perturbation estimator for the estimation of the unmodeled dynamics and uncertainties in the control design, the results also reveal the feasibility of the identified second-order model for the positioning application.

Figure 9.11 indicates that the performance of PID control drops quicker than that of the MRACPE control as the increasing of the reference input frequency.

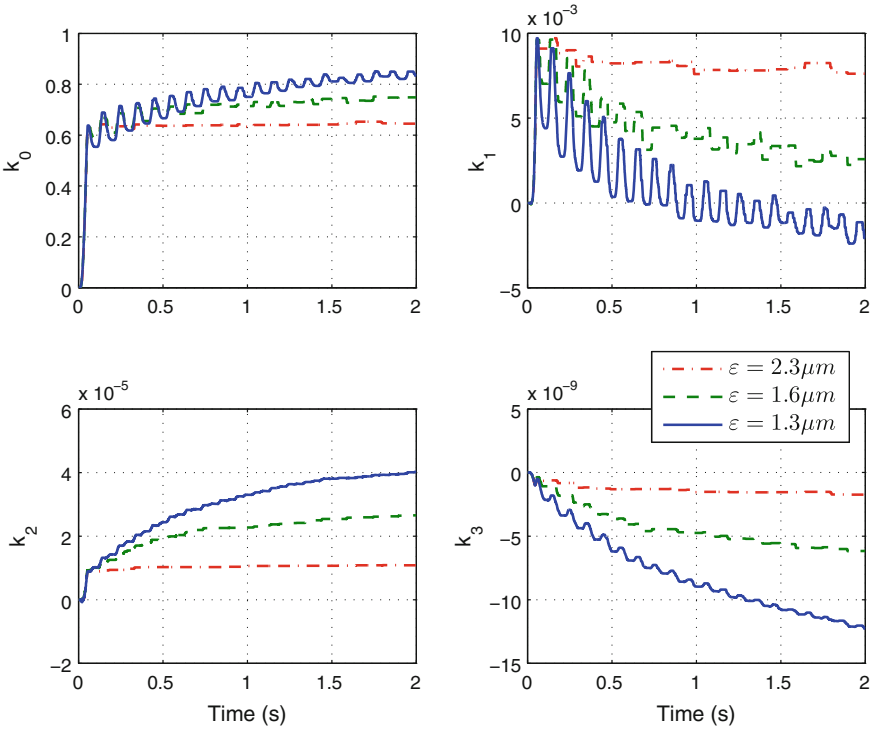

Fig. 9.10 Adaptation processes of the control parameters of MRACPE with different dead-zones ε for sinusoidal positioning

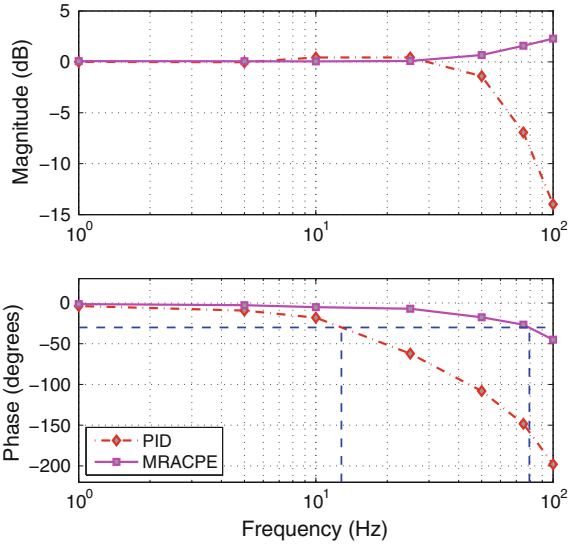

Fig. 9.11 Control bandwidth test results of the micropositioning system with PID and MRACPE controllers

This is one of the reasons why a 10-Hz sinusoidal reference input is adopted in the aforementioned comparative study. Actually, the MRACPE achieves a RMSE less than 10 % of positioning range for a higher speed tracking of reference input with the frequency of 40 Hz.

It is notable that although the MRACPE produces a slightly lower transient response than PID control, it achieves more accurate positioning in both set-point and sinusoidal tracking tasks. Another advantage of the MRACPE is that its positioning error size can be predefined by assigning the dead-zone (ε) value. Experimental results reveal that the smaller the dead-zone, the slower the convergence speed of controller parameters. Even so, the convergence speed of the parameters does not affect the steady-state tracking error because the latter is restricted by the assigned ε value. The smaller the ε, the more accurate the positioning result. However, too small ε produces the maximum positioning error exceeding the ε value, or even causes instability of the system due to the drift of the controller parameters, which are mainly induced by the noises of the displacement sensor. Hence, a tradeoff between the tracking accuracy and the stability is required to choose the dead-zone value. The tracking errors can be reduced by employing displacement sensors with a lower noise level. Alternatively, a state observer may be adopted to estimate the state values. Unavoidably, the employment of state observer complicates the control design process at the same time.

In addition, the control gains of the MRACPE are not optimally tuned. An optimal tuning of the four control gains is a possible solution to further improve the positioning results. Moreover, the robust controller design procedure [9] can be employed to achieve high positioning accuracy at higher speeds.

9.6 Chapter Summary

This chapter provides the design procedure of the MRACPE control scheme for a PSA-actuated micropositioning system without modeling the hysteretic nonlinearity effect. The controller is designed based on Lyapunov stability analysis, and its performance is verified by a series of experimental studies. Results show that the MRACPE with dead-zone modification of the adaptive parameters is capable of further suppressing the disturbances and substantially mitigating the positioning errors as compared with conventional PID control. The MRACPE enables over six times increase of control bandwidth versus the PID algorithm. Moreover, the dead-zone allows the specification of the maximum tracking error for the MRACPE scheme, which is attractive for practical applications. Owing to a not complicated structure, the proposed control scheme can also be extended to position control of other types of micro-/nanopositioning systems.

References

1. Cheng, C.C., Chang, C.C., Su, T.M.: Design of model reference adaptive tracking controllers for mismatch perturbed nonlinear systems with input nonlinearity. In: Proceedings of 17th IFAC World Congress, pp. 5974–5979. Seoul, Korea (2008)
2. Demetriou, M.A., Fahroo, F.: Model reference adaptive control of structurally perturbed second-order distributed parameter systems. Int. J. Robust Nonlinear Control **16**(16), 773–799 (2006)
3. Elmali, H., Olgac, N.: Implementation of sliding mode control with perturbation estimation (SMCPE). IEEE Trans. Control Syst. Technol. **4**(1), 79–85 (1996)
4. Ioannou, P.A., Sun, J.: Robust Adaptive Control. Prentice Hall, New Jersey (1996)
5. Kim, J.Y., Bentsman, J.: Disturbance rejection in robust model reference adaptive control of parabolic and hyperbolic systems. In: Proceedings of 45th IEEE Conference on Decision and Control, pp. 3083–3088. San Diego, CA, USA (2006)
6. Li, Y., Xu, Q.: Hysteresis modeling and compensation for an XY micropositioning stage with model reference adaptive control. In: Proceedings of 48th IEEE Conference on Decision and Control, pp. 5580–5585. Shanghai, China (2009)
7. Liu, Y.T., Chang, K.M., Li, W.Z.: Model reference adaptive control for a piezo-positioning system. Precis. Eng. **34**(1), 62–69 (2010)
8. Narendra, K.S., Annaswamy, A.M.: Stable Adaptive Systems. Prentice Hall, New Jersey (1989)
9. Tuma, T., Haeberle, W., Rothuizen, H., Lygeros, J., Pantazi, A., Sebastian, A.: A dual-stage nanopositioning approach to high-speed scanning probe microscopy. In: Proceedings of 51st IEEE Conference on Decision and Control, pp. 5079–5084. Maui, HI, USA (2012)
10. Xu, Q.: Design and development of a flexure-based dual-stage nanopositioning system with minimum interference behavior. IEEE Trans. Autom. Sci. Eng. **9**(3), 554–563 (2012)
11. Xu, Q., Jia, M.: Model reference adaptive control with perturbation estimation for a micropositioning system. IEEE Trans. Control Syst. Technol. **22**(1), 352–359 (2014)
12. Xu, Q., Li, Y.: Analytical modeling, optimization and testing of a compound bridge-type compliant displacement amplifier. Mech. Mach. Theory **46**(2), 183–200 (2011)

Part IV
Applications to Micromanipulation

Chapter 10
Adaptive Impedance Control of Piezoelectric Microgripper

Delicate interaction control is a crucial issue for automated microsystems dedicated to micromanipulation of microobjects. This chapter presents a framework of digital sliding mode generalized impedance control with adaptive switching gain to regulating both the position and contact force of a piezoelectric-bimorph microgripper for micromanipulation and microassembly applications. Based on a second-order dynamics model, its implementation does not require a state observer and a hysteresis/creep model. The stability of the control system is proved in theory, which ensures the tracking performance in the presence of model uncertainties and disturbances. The effectiveness of the scheme is validated by experimental investigations on the grasp operation of a microgear.

10.1 Introduction

Microassembly is an important approach to producing complex micro-/nanosystems which are composed of microparts fabricated from different materials [2, 26]. As a crucial device to realize the grasp-hold-release operation in the aforementioned application, microgripper has gained intensive attention in the literature. Various types of microgrippers have been proposed in terms of electrostatic [3], electrothermal [15], and piezoelectric microgrippers [24], etc. In particular, smart material-based piezoelectric actuators offer the merits of subnanometer positioning resolution and rapid response speed. Hence, constructed by a pair of piezoelectric unimorph or bimorph actuators, the piezoelectric microgrippers have been popularly applied in micromanipulation and microassembly tasks [6, 22].

To avoid damaging the fragile microobjects and microgripper arms which contact each other during microassembly process, the interaction control is critical to regulate the desired position and contact force simultaneously [20]. Generally, there are two basic approaches to interaction control, i.e., hybrid position/force control and impedance control. The first method generates a compliant motion by controlling

© Springer International Publishing Switzerland 2016

Q. Xu and K.K. Tan, *Advanced Control of Piezoelectric Micro-/Nano-Positioning Systems*, Advances in Industrial Control,
DOI 10.1007/978-3-319-21623-2_10

the end-effector position in position subspace and the interaction force in force subspace, whose implementation relies on a switching of the control law. However, this approach suffers from the robustness problem during the transition between unconstrained and constrained motions [30]. Alternatively, the impedance control enables a compliant motion of the end-effector in a unified framework for both constrained and unconstrained directions [13]. The goal of impedance control is to regulate a desired dynamics relation between the position and contact force. That is, both position and force are indirectly controlled by regulating the predefined dynamics response, i.e., the desired impedance.

Impedance control emerges as a promising approach to interaction control in micro-/nanoscales [11, 18]. For example, a position-based impedance control of a piezoelectric-bimorph microgripper is reported in [29], where a state-feedback position controller and a low-pass filtered force feedback controller are implemented. However, the impedance control usually requires an exact dynamics model of the system. Due to the uncertainties in dynamics model, it is practically difficult to achieve the desired impedance. To remedy this shortcoming, adaptive [17] and robust [19] impedance control algorithms have been developed to tolerate the dynamics parameter uncertainties. Nevertheless, the conventional impedance control framework has a drawback of inability of tracking the reference force input. Several schemes have been exploited to overcome this disadvantage. Typically, a generalized impedance control (GIC) scheme is established based on a generalized desired impedance [5]. It integrates both the position and force errors, and enables the force tracking ability. Recently, intensive efforts have been made toward force tracking impedance control, which is robust to parameter uncertainties in both dynamics and environment models [14]. Although this robustness property appears attractive, it is at the expense of implementation complication. Considering that the impedance control possesses some inherent robustness to environment model errors [1, 28], a GIC with robustness to dynamic model uncertainties is desirable for a precise interaction control.

Regarding piezoelectric microgrippers, in addition to the model uncertainties, further challenges to achieve a delicate interaction control come from the nonlinear hysteresis and creep effects of the piezoelectric actuators. Thus, control strategies need to be well developed to achieve a precise position and force control. Usually, a feedforward control based on an inverse hysteresis model and an inverse creep model is adopted to compensate for the piezoelectric nonlinearities. Nevertheless, modeling the hysteresis and creep effects is a time-consuming work and the tracking result is very sensitive to the model accuracy [34]. Hence, by treating the nonlinearities as disturbances, the robust feedback control is more attractive owing to its merit of easy implementation [32, 35]. In the literature, a state-of-the-art robust GIC algorithm is presented in [16], where the desired motion and force trajectories are tracked simultaneously. It has demonstrated the potential of sliding-mode control (SMC) in precise interaction control in the presence of model uncertainties and disturbances. However, the reported SMC-based GIC is realized in the continuous-time form. Its implementation needs a state observer and prior knowledge on the uncertainty bounds of the dynamics model parameters.

In practice, the control scheme of a microassembly system is usually realized on a computer or a DSP apparatus, i.e., a sampled-data system. As it is known that applying a continuous-time controller directly to a digital system can induce instability due to the computational delays [4]. This is true for a microassembly system, e.g., a visual servoing system [25], which typically has a low sampling rate, e.g., in the order of 10 Hz. Hence, to deploy a reliable interaction control to a sampled-data system, a discrete-time impedance controller is more preferable.

In this chapter, an adaptive digital sliding-mode generalized impedance control (ADSMGIC) is reported to realize an interaction control of a piezoelectric microgripper dedicated to micromanipulation and microassembly. Unlike the continuous-time and discrete-time SMC algorithms which are developed based on the system state [16, 35], the presented one is established by using a discrete-time second-order dynamics model of the system. Hence, it eliminates the use of a state observer and enables a substantial simplification of practical implementation procedures. Moreover, the unmodeled piezoelectric nonlinearities and other uncertainties as well as disturbances are treated as a lumped perturbation. This perturbation term is estimated by resorting to a perturbation estimation technique, which allows the relief of burden on hysteresis and creep modeling. Furthermore, the chattering phenomenon is suppressed by employing an adaptive law for the switching gain. The stability of the closed-loop system is proved theoretically and the effectiveness of the reported interaction control scheme is validated by conducting several experimental studies.

10.2 Problem Formulation

A piezoelectric microgripper is illustrated in Fig. 10.1a. It is constructed by a pair of piezoelectric bimorphs for the microobject grasping. Owing to the symmetry of the microgripper, one gripper arm, i.e., a piezoelectric cantilever as shown in Fig. 10.1b is selected for a detailed analysis. The cantilever suffers from an excitation voltage and a contact force which is exerted by the microobject. In order to guarantee a successful assembly of the microobject, both the position x and the contact force F need to be controlled.

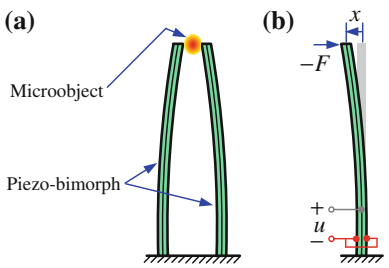

Fig. 10.1 **a** Schematic depiction of grasping a microobject by a piezoelectric microgripper constructed by two piezoelectric cantilevers. **b** Illustration of output displacement x of a piezoelectric cantilever under an excitation of input voltage u and contact force F

10.2.1 Dynamics Modeling and Perturbation Estimation

The dynamics model of a piezoelectric cantilever under the actions of an excitation voltage and an external force $(-F)$ can be established as follows:

$$\hat{m}\ddot{x}(t) + \hat{b}\dot{x}(t) + \hat{k}x(t) = \hat{d}u(t) + P(t) - F(t) \tag{10.1}$$

where t is the time variable, parameters $\hat{m}$, $\hat{b}$, $\hat{k}$, and $\hat{d}$ represent the estimated values of mass, damping coefficient, stiffness, and piezoelectric coefficient of the gripper arm, respectively. In addition, u is the input voltage, x is the output position, and F denotes the interaction force exerted on the microobject. The bounded lumped perturbation term P describes the combined effect of the unmolded piezoelectric nonlinearities (hysteresis and drift), the uncertainties of dynamic model parameters ($\hat{m}$, $\hat{b}$, $\hat{k}$, and $\hat{d}$), and other disturbances.

By adopting a small sampling time T, the following approximations are valid [31]:

$$\dot{x}(t) \approx \frac{1}{T}(x_k - x_{k-1}) \tag{10.2}$$

$$\ddot{x}(t) \approx \frac{1}{T^2}(x_k - 2x_{k-1} + x_{k-2}) \tag{10.3}$$

where $x_k = x(kT)$, $x_{k-1} = x(kT - T)$, and $x_{k-2} = x(kT - 2T)$ with k representing the kth time step.

Then, the continuous-time dynamics model (10.1) is converted into an equivalent discrete-time form:

$$\bar{m}x_{k-2} + \bar{b}x_{k-1} + \bar{k}x_k = \bar{d}u_k + P_k - F_k \tag{10.4}$$

where the parameters are

$$\bar{m} = \frac{\hat{m}}{T^2},\ \bar{b} = -\frac{2\hat{m}}{T^2} - \frac{\hat{b}}{T},\ \bar{k} = \frac{\hat{m}}{T^2} + \frac{\hat{b}}{T} + \hat{k},\ \bar{d} = \hat{d}. \tag{10.5}$$

By employing the perturbation estimation technique [7], the lumped perturbation term P_k can be derived by its one-step delayed estimation:

$$\hat{P}_k = -\bar{d}u_{k-1} + \bar{m}x_{k-3} + \bar{b}x_{k-2} + \bar{k}x_{k-1} + F_{k-1}. \tag{10.6}$$

Hence, the dynamics model (10.4) can be rewritten into:

$$\bar{m}x_{k-2} + \bar{b}x_{k-1} + \bar{k}x_k = \bar{d}u_k + \hat{P}_k - \tilde{P}_k - F_k \tag{10.7}$$

where $\tilde{P}_k = \hat{P}_k - P_k$ is the perturbation estimation error.

10.2.2 Impedance Control Problem

The objective of impedance control is to regulate the position and contact force simultaneously by achieving a desired impedance behavior.

Assume that the output position and predefined reference position of the gripper arm are x and x_r, respectively. By adopting the impedance control algorithm [10], the desired impedance behavior between the output position error $e_x = x - x_r$ and the contact force F can be specified by a second-order dynamics equation:

$$M\ddot{e}_x(t) + B\dot{e}_x(t) + Ke_x(t) = -F(t) \tag{10.8}$$

where M, B, and K represent the target mass, damping, and stiffness parameters, respectively. However, the major limitation of this kind of impedance control is the inability of achieving explicit force tracking control.

To formulate an impedance behavior to track the desired force F_r as exerted on the object, the GIC scheme can be adopted. The GIC combines the position and force errors by using a generalized impedance equation [5]:

$$M\ddot{e}_x(t) + B\dot{e}_x(t) + Ke_x(t) = -K_f e_f(t) \tag{10.9}$$

where $e_f = F - F_r$ is the force error, and M, B, K, and K_f are the target parameters for the generalized impedance.

It is observed from Eq. (10.9) that by introducing the reference force F_r to the desired impedance behavior, the interaction force can be explicitly controlled by using the GIC approach.

Taking into account the approximations (10.2) and (10.3), the differential equation (10.9) is equivalently converted into a difference equation:

$$\bar{M}e_{x,k-2} + \bar{B}e_{x,k-1} + \bar{K}e_{x,k} = -\bar{K}_f e_{f,k} \tag{10.10}$$

where $e_{x,k-2} = e_x(kT - 2T)$ and $e_{f,k} = e_f(kT)$.

In addition, the relationships between the target parameters of the continuous-time impedance (M, B, K, and K_f) and discrete-time impedance ($\bar{M}$, $\bar{B}$, $\bar{K}$, and $\bar{K}_f$) are derived below

$$\bar{M} = \frac{M}{T^2},\ \bar{B} = -\frac{2M}{T^2} - \frac{B}{T},\ \bar{K} = \frac{M}{T^2} + \frac{B}{T} + K,\ \bar{K}_f = K_f. \tag{10.11}$$

However, it is difficult to obtain precise values for the parameters of dynamics model (10.7) in practice. Additionally, the perturbation estimation error $\tilde{P}_k$ always exists, especially when the sampling time T is large and the variation rate of the perturbation P_k is high. Hence, the presence of model uncertainties and disturbances poses a great challenge for the achievement of the desired impedance behavior described by Eq. (10.10). In the following section, a control scheme is developed to overcome this issue.

10.3 ADSMGIC Scheme Design

An ADSMGIC scheme is designed to guarantee the achievement of the desired impedance behavior (10.10) so that both the position and contact force of the micrograpper can be regulated. In particular, a digital sliding mode control (DSMC) scheme is established as follows.

10.3.1 Sliding Function Definition

First, a sliding function is defined and then converted into the discrete-time form.

Based on the position error $e_{x,k} = x_k - x_{r,k}$ and the force error $e_{f,k} = F_k - F_{r,k}$, an incremental PID type of sliding function is defined below

$$s_k = K_P(e_{x,k} - e_{x,k-1}) + K_I e_{x,k} + K_D(e_{x,k} - 2e_{x,k-1} + e_{x,k-2}) + K_4 e_{f,k} + K_5 s_{k-1} \tag{10.12}$$

where K_P, K_I, and K_D denote the proportional, integral, and derivative gains, respectively. In addition, K_4 and K_5 are also positive control gains. Actually, the last term in Eq. (10.12) represents a momentum term which is defined by the momentum constant K_5 ($0 < K_5 < 1$).

Next, through a fundamental algebra operation, the sliding function (10.12) is expressed into the following form

$$s_k = K_1 e_{x,k-2} + K_2 e_{x,k-1} + K_3 e_{x,k} + K_4 e_{f,k} + K_5 s_{k-1} \tag{10.13}$$

where

$$K_1 = K_D \tag{10.14}$$
$$K_2 = -K_P - 2K_D \tag{10.15}$$
$$K_3 = K_P + K_I + K_D. \tag{10.16}$$

Then, by setting the following parameters

$$K_1 = \bar{M} \tag{10.17}$$
$$K_2 = \bar{B} \tag{10.18}$$
$$K_3 = \bar{K} \tag{10.19}$$
$$K_4 = \bar{K}_f \tag{10.20}$$

the sliding function (10.13) can be further written into:

$$s_k = \bar{M} e_{x,k-2} + \bar{B} e_{x,k-1} + \bar{K} e_{x,k} + \bar{K}_f e_{f,k} + K_5 s_{k-1}. \tag{10.21}$$

It is observed that the sliding function (10.21) becomes the desired impedance behavior (10.10) if $s_k = 0$ and $s_{k-1} = 0$ are assigned. Motivated by this observation, the sliding-mode control technique is applied here. That is, if the system impedance trajectory is maintained on the sliding surface $s_k = 0$ and $s_{k-1} = 0$, the desired impedance behavior (10.10) will be achieved. In the following discussions, an ADSMGIC scheme with adaptive gain is developed to ensure that the discrete sliding mode is reached and maintained, i.e., the desired impedance behavior is achieved.

10.3.2 ADSMGIC Design

First, substituting Eq. (10.6) into Eq. (10.7) allows the calculation of the position:

$$x_k = \frac{1}{\bar{k}}[\bar{d}(u_k - u_{k-1}) + \bar{m}x_{k-3} + (\bar{b} - \bar{m})x_{k-2} + (\bar{k} - \bar{b})x_{k-1} - (F_k - F_{k-1}) - \tilde{P}_k]. \tag{10.22}$$

Then, taking into account that the equivalent control u_k^{eq} is the solution to $\Delta s_k = s_k - s_{k-1} = 0$ [8], the following deduction is derived:

$$\bar{M}e_{x,k-2} + \bar{B}e_{x,k-1} + \bar{K}e_{x,k} + \bar{K}_f e_{f,k} + K_5 s_{k-1} = s_{k-1}. \tag{10.23}$$

In view of the definition $e_{x,k} = x_k - x_{r,k}$, Eq. (10.23) becomes

$$\bar{M}e_{x,k-2} + \bar{B}e_{x,k-1} + \bar{K}(x_k - x_{r,k}) + \bar{K}_f e_{f,k} + K_5 s_{k-1} = s_{k-1}. \tag{10.24}$$

It is notable that the equivalent control u_k^{eq} is the control action without considering the perturbation estimation error $\tilde{P}_k$. The error $\tilde{P}_k$ will be compensated for by the switching control action u_k^{sw} derived later. Thus, substituting the x_k expression (10.22) into (10.24), gives

$$\begin{aligned} u_k^{eq} = u_{k-1} &+ \frac{\bar{k}}{\bar{K}\bar{d}}\left[(1 - K_5)s_{k-1} - \bar{M}e_{x,k-2} - \bar{B}e_{x,k-1} - \bar{K}_f e_{f,k}\right] \\ &- \frac{1}{\bar{d}}\left[\bar{m}x_{k-3} + (\bar{b} - \bar{m})x_{k-2} + (\bar{k} - \bar{b})x_{k-1} - \bar{k}x_{r,k} - (F_k - F_{k-1})\right]. \end{aligned} \tag{10.25}$$

The equivalent controller (10.25) takes effect in the sliding phase when the impedance trajectory is kept on the sliding surface (i.e., $s_k = 0$). However, if the initial state of the trajectory does not lie on the sliding surface or a large perturbation estimation error $\tilde{P}_k$ emerges owing to large uncertainties and disturbances during the sliding phase, the stand-alone equivalent control cannot drive the impedance trajectory towards the sliding surface. Under such situation, a switching control action u_k^{sw} is necessary.

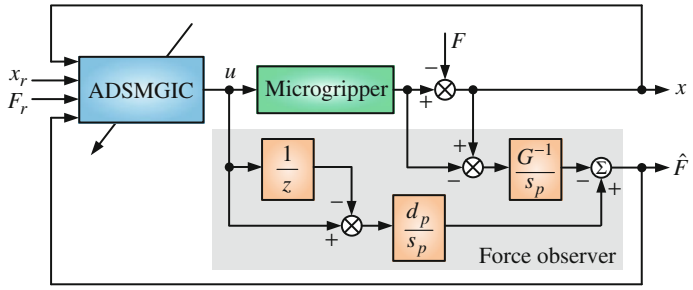

Fig. 10.2 Block diagram of the ADSMGIC control scheme

Hence, the equivalent control is augmented by the switching control to create the total control action:

$$u_k = u_k^{eq} + u_k^{sw}. \tag{10.26}$$

That is

$$\begin{aligned} u_k = u_{k-1} &+ \frac{\bar{k}}{\bar{K}\bar{d}}\left[(1-K_5)s_{k-1} - \bar{M}e_{x,k-2} - \bar{B}e_{x,k-1} - \bar{K}_f e_{f,k}\right] \\ &- \frac{1}{\bar{d}}\left[\bar{m}x_{k-3} + (\bar{b}-\bar{m})x_{k-2} + (\bar{k}-\bar{b})x_{k-1} - \bar{k}x_{r,k} - (F_k - F_{k-1})\right] \\ &- \frac{K_S}{\bar{d}}\text{sign}(s_{k-1}) \end{aligned} \tag{10.27}$$

where the last term is the switching control action. In addition, sign$(\cdot)$ denotes the signum function and K_S is a positive control gain.

A block diagram of the ADSMGIC control scheme is shown in Fig. 10.2. It is observed that both the desired position and force are controlled at the same time. A force observer is employed to estimate the contact force during the grasp operation. Alternatively, a force sensor can be used to provide the force signal.

10.3.3 Stability Analysis

Theorem 10.1 *For the system (10.7) with the sliding function (10.12), if the controller (10.27) is employed, then the discrete sliding mode will occur in a finite number of steps.*

Proof Substituting Eq. (10.27) along with the control gains (10.14)–(10.20) into the sliding function (10.12), a necessary algebra operation gives

$$
\begin{aligned}
s_k &= \bar{K}(x_k - x_{r,k}) + \bar{M}e_{x,k-2} + \bar{B}e_{x,k-1} + \bar{K}_f e_{f,k} + K_5 s_{k-1} \\
&= \bar{K}\left\{\frac{1}{\bar{k}}\left[\bar{d}(u_k - u_{k-1}) + \bar{m}x_{k-3} + (\bar{b} - \bar{m})x_{k-2} + (\bar{k} - \bar{b})x_{k-1} - (F_k - F_{k-1}) - \tilde{P}_k\right]\right. \\
&\quad \left. - x_{r,k}\right\} + \bar{M}e_{x,k-2} + \bar{B}e_{x,k-1} + \bar{K}_f e_{f,k} + K_5 s_{k-1} \\
&= s_{k-1} - \frac{\bar{K}K_S}{\bar{k}}\text{sign}(s_{k-1}) - \frac{\bar{K}}{\bar{k}}\tilde{P}_k \\
&= s_{k-1} - \frac{\bar{K}}{\bar{k}}\left[K_S \text{sign}(s_{k-1}) + \tilde{P}_k\right]
\end{aligned} \tag{10.28}
$$

where the parameters of $\bar{k}$ and $\bar{K}$ are positive.

If $s_{k-1} \geq 0$, it is derived that

$$
s_k \leq s_{k-1} \quad \text{if} \quad K_S \geq |\tilde{P}_k|. \tag{10.29}
$$

Otherwise, in the case of $s_{k-1} < 0$, then

$$
s_k \geq s_{k-1} \quad \text{if} \quad K_S \geq |\tilde{P}_k|. \tag{10.30}
$$

Hence, combining Eqs. (10.29) and (10.30), the following deduction can be derived

$$
|s_k| \leq |s_{k-1}| \quad \text{if} \quad K_S \geq |\tilde{P}_k| \tag{10.31}
$$

which indicates that s_k decreases monotonously, and the discrete sliding mode is reached within a finite number of steps.

Remark 10.1 It has been shown that the relation (10.31) describes a sufficient condition for the existence of discrete sliding mode [27]. Owing to the discontinuity of the signum function sign(·), chattering effects may occur in the control action. To reduce the chattering phenomenon, the boundary layer technique is employed by replacing the signum function in (10.27) with the saturation function:

$$
\text{sat}(s_k) = \begin{cases} \text{sign}(s_k) & \text{if} \quad |s_k| > \delta \\ \frac{s_k}{\delta} & \text{if} \quad |s_k| \leq \delta \end{cases} \tag{10.32}
$$

where a tradeoff between the chattering effect and tracking error is needed to assign the parameter δ.

Remark 10.2 Even though the boundary layer technique is capable of alleviating the chattering effect, the fixed gain K_S is not feasible for some scenarios in practice. In this work, an adaptive rule for the switching gain K_S is employed to adjust the gain value of the saturation function (10.32) online [21]:

$$
K_{S,k} = |K_{S,k-1} + \gamma \text{sign}(s_k s_{k-1})| \tag{10.33}
$$

where the positive adaptation parameter γ determines the rate of adaptation of the control gain.

By resorting to the adaptive rule (10.33), it is deduced that if the impedance trajectory has not yet reached the sliding surface, then $\text{sign}(s_k s_{k-1}) = +1$. Hence, the control gain is increased. Once the impedance trajectory crosses the sliding surface, $\text{sign}(s_k s_{k-1}) = -1$ holds. Consequently, the control gain is decreased accordingly. Therefore, the purpose of the adaptation law (10.33) is to produce an optimal switching gain at each time step so that the discrete sliding mode is reached and maintained, i.e., the desired impedance behavior is achieved.

10.3.4 Evaluation of Steady-State Errors

The developed control scheme is based on the framework of GIC in conjunction with adaptive DSMC. In order to evaluate the steady-state position and force errors, the contact environment of the micrograpper is modeled as follows:

$$F = K_e(x - x_e) \tag{10.34}$$

where K_e describes the stiffness of the environment and x_e represents the equilibrium position of the environment in the absence of contact force.

Combing Eqs. (10.9) and (10.34) allows the generation of an equation of the closed-loop impedance control system interacting with the environment:

$$M\ddot{x} + B\dot{x} + (K + K_f K_e)x = M\ddot{x}_r + B\dot{x}_r + Kx_r + K_f(F_r + K_e x_e) \tag{10.35}$$

which is stable if positive target parameters are chosen for the desired impedance [5].

In order to achieve a satisfactory manipulation with desired position and force behavior, the relationships between the desired position (x_r) and force (F_r) trajectories and the target impedance parameters (M, B, K, and K_f) demand a careful design in compliance with the environment. Based on the assembly/manipulation strategy as given in [5, 16], a tradeoff between the position control and force control can be generated by varying the impedance parameters $\{M, B, K\}$ and $\{K_f\}$, which are associated with the position and force, respectively.

For instance, in the case of a soft environment with a low stiffness K_e, e.g., in the air, the contact force F is negligible and the reference force trajectory can be selected as $F_r = 0$. It follows that the desired generalized impedance (10.9) is simplified into a position trajectory (x_r) defined by parameters M, B, and K. Thus, a position control framework is established. On the contrary, in the presence of a rigid environment with a large stiffness K_e, the motion terms in the generalized impedance (10.9) are neglected and the impedance control becomes a force control problem. Otherwise, if a simultaneous position and force tracking is required, a tradeoff between the position control and force control can be realized by adjusting the target impedance parameters as detailed below.

At the steady state, the response of the closed-loop system (10.35) can be derived as follows:

$$(K + K_f K_e)x = Kx_r + K_f(F_r + K_e x_e) \tag{10.36}$$
$$\Rightarrow K(x - x_r) = K_f[F_r + K_e(x_e - x)] \tag{10.37}$$
$$\Rightarrow K(x - x_r) = K_f(F_r - F) \tag{10.38}$$
$$\Rightarrow K(x - x_r) = K_f\{F_r + K_e[(x_e - x_r) - (x - x_r)]\}. \tag{10.39}$$

In view of Eqs. (10.38) and (10.39), the following steady-state position and force errors are calculated:

$$e_x^{ss} = \frac{F_r + K_e(x_e - x_r)}{K_e + \frac{K}{K_f}} \tag{10.40}$$

$$e_f^{ss} = -\frac{K}{K_f} e_x^{ss}. \tag{10.41}$$

It is deduced that if K_e is relatively small and $K >> K_f$ is assigned, then the steady-state position error e_x^{ss} is relatively small and the steady-state force error e_f^{ss} is relatively large. Thus, the position control is emphasized. In contrast, if K_e is relatively large and $K << K_f$ is assigned, then the force control is emphasized and the desired force is tracked more precisely than the position. Therefore, a compromise between the position and force tracking control can be realized by adjusting the relative values of K and K_f.

Additionally, other target impedance parameters (M and B) can be chosen to produce a required transient response for the closed-loop system (10.35).

10.4 Experimental Setup and Controller Setup

In this section, the experimental setup is presented and the controller parameters are selected for the subsequent experimental investigations.

10.4.1 Experimental Setup

The experimental setup of a prototype piezoelectric microgripper system is depicted in Fig. 10.3. The gripper is composed of two four-layer piezoelectric bimorphs with brass reinforced inner layers. Each actuator has the dimension of $26 \times 5 \times 0.86\,\text{mm}^3$ and is driven by a high-voltage amplifier (model: EPA-104, from Piezo Systems, Inc.). The end-point position of each gripper arm is measured by a laser displacement sensor (model: LK-H055, from Keyence Corp.). The laser sensor provides a

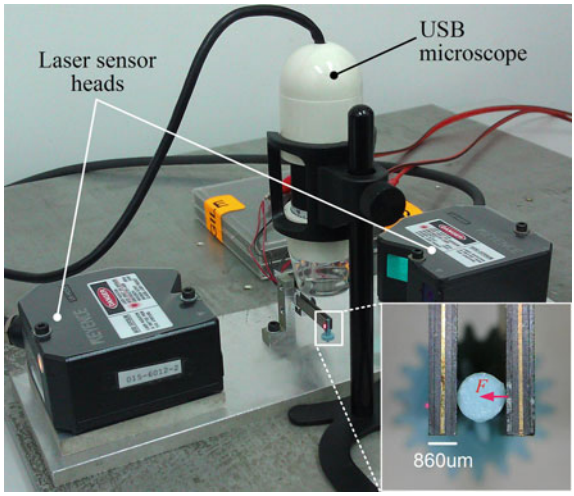

Fig. 10.3 Experimental setup of a piezoelectric microgripper system for a microgear grasping. The *close-up view* shows a snapshot of the micrograpping experiment

resolution of 25 nm within a measuring range of 20 mm around the reference distance of 50 mm, which endows a large free space for micromanipulation/microassembly tasks. A digital microscope (magnification rate: 200x) is mounted above the microgripper for the assembly process monitoring. In addition, a National Instruments (NI) cRIO-9075 real-time controller (from National Instruments Corp.) equipped with NI-9263 D/A module and NI-9870 A/D module is adopted to produce the excitation signals and acquire the sensor readings, respectively. The NI cRIO-9075 combines a real-time processor and a reconfigurable field-programmable gate array (FPGA) within the same chassis, which is connected to a computer via the Ethernet port for communication. Moreover, LabVIEW™ software is employed to implement a real-time control of the microgripper system.

The microobject to be grasped is a plastic microgear with the diameter of 1450 μm, as shown in the close-up view in Fig. 10.3. Due to the symmetry of the microgripper, only the right gripper arm is employed to demonstrate the effectiveness of the reported control scheme, whereas the left one acts as a passive arm in the experiments.

10.4.2 Force Observer Design

Regarding the force sensing issue, diverse methods have been presented to generate the force signal [36, 37], and various types of force sensors have been used to detect the contact force in piezoelectric cantilevers. For example, the strain-gage sensors are widely adopted in the piezoelectric microgripper [12, 29]. Nevertheless, such sensors are inclined to produce noisy signal output, and it is difficult to integrate a suitable sensor into the microgripper.

In view of the limitation of force sensors, the force estimation approach has been studied extensively. For instance, a linear force estimator is reported in [9] based on a linear dynamics model of the system. However, this linear estimator offers a low accuracy due to the influences of piezoelectric hysteresis and creep effects. Later, a nonlinear force estimator was presented in [23, 24], which was constructed by modeling the nonlinear hysteresis and creep effects. Nevertheless, the modeling processes are time-consuming and model errors always exist. Hence, a more effective force estimation method for a piezoelectric microgripper has been developed in recent work [33]. It is implemented without modeling the complicated hysteresis and drift effects. This force observer is employed here to reconstruct the force signal. A brief description is given below, and more details can be found in [33], where a fourth-order model is identified and used in the force estimation. Alternatively, a simple second-order dynamic model is employed in this work.

Basically, two position signals $x(t)$ and $x_1(t)$, i.e., with and without the force applied, are required to estimate the force signal. Specifically, the force that is applied on the microobject can be estimated in the time domain:

$$\hat{F}(t) = \frac{d_p}{s_p}[u(t) - u(t-T)] - \frac{1}{s_p}\mathscr{L}^{-1}\{G^{-1}(s)\}[x(t) - x_1(t)] \tag{10.42}$$

where $u(t)$ and $u(t-T)$ denote the excitation voltages at the time instances t and $t-T$, respectively. x is the position output under the actions of both excitation voltage u and applied force F, whereas x_1 denotes the position output excited by the voltage u alone. Additionally, $\mathscr{L}^{-1}$ represents the inverse Laplace transform operator, and $G(s)$ with unity DC gain is the plant model under the excitation of input voltage. In addition, d_p and s_p are the piezoelectric constant and elastic constant of the piezoelectric bimorph, respectively.

When an excitation voltage u is applied to the high-voltage amplifier with $F = 0$, the plant model G_p is identified below by the frequency response method.

$$G_p(s) = \frac{1.1292 \times 10^8}{s^2 + 126.8\,s + 5.9430 \times 10^6}. \tag{10.43}$$

The piezoelectric constant d_p is calculated as the DC gain of G_p, i.e., $d_p = 19.0\,\mu\text{m/V}$. Then, the plant model G is derived as $G = G_p/d_p$. In addition, by hanging a known weight and recording the induced displacement, the elastic constant of the piezo-bimorph is determined as $s_p = 0.46\,\mu\text{m/mN}$.

To verify the performance of the force observer, an input voltage signal as shown in Fig. 10.4a is applied to the voltage amplifier to drive the gripper arm while without the external force applied. The position response is illustrated in Fig. 10.4b, and the force observer output is shown in Fig. 10.4d. It is seen that the force is accurately estimated with a RMSE of 0.25 mN. In addition, Fig. 10.4c illustrates an open-loop hysteresis loop of the piezoelectric gripper arm, which poses a challenge to the precise interaction control.

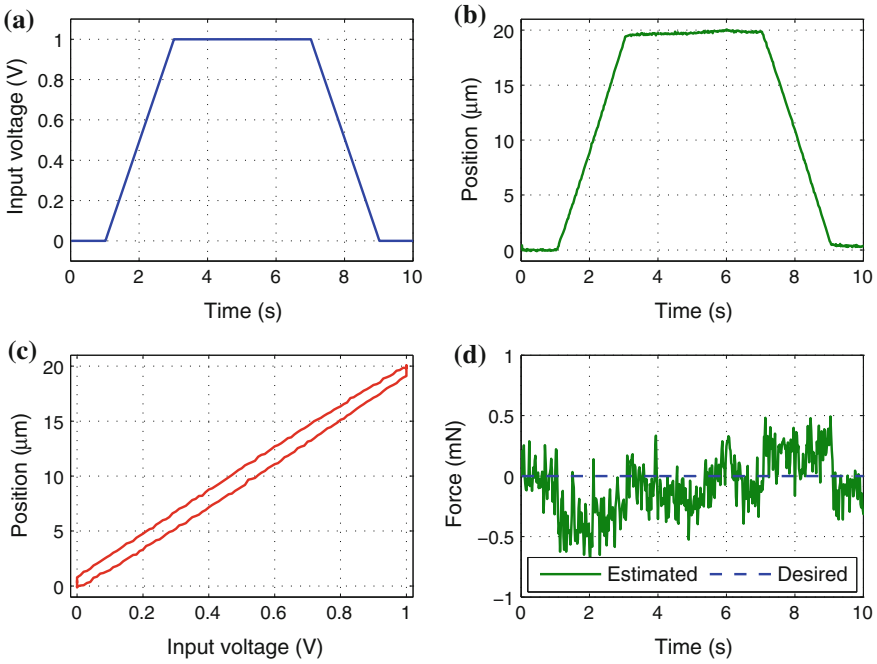

Fig. 10.4 Force estimation result of the force observer without applied force. **a** Input voltage. **b** Output position. **c** Position-voltage hysteresis loop. **d** Force signal

Using the force signal provided by the force observer, experiments on interaction control of the microgripper for micromanipulation/microassembly are conducted by grasping a microgear in the subsequent section.

10.4.3 Controller Setup

10.4.3.1 Trajectory Planning

Initially, the microgear to be grasped is in contact with the gripper arms. To realize an interaction control, a position trajectory x_r and a corresponding force trajectory F_r need to be planned concurrently.

By applying the excitation voltage as given in Fig. 10.5a accompanied with an interaction force to the gripper arm, the resulted position and force signals are acquired as shown in Fig. 10.5b, c (solid lines). Based on the actual position and force outputs, the trajectories are planned as shown in Fig. 10.5b, c (dashed lines). Figure 10.5d depicts the errors between the planned position and force trajectories and the actual ones, respectively. The trajectories are planned to realize a typical grasp-hold-release operation in microassembly tasks.

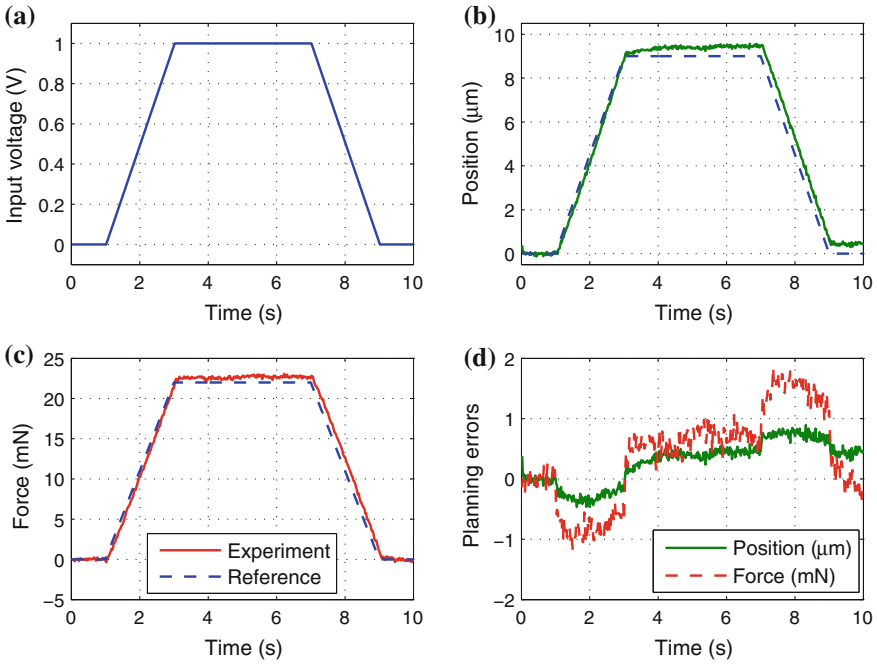

Fig. 10.5 Force estimation result of the force observer with applied force. **a** Input voltage. **b** Output position. **c** Signal of the force applied to microobject. **d** Errors between the planned position/force trajectories and the actual ones

10.4.3.2 Controller Parameters Setup

Concerning the dynamics model parameters, the mass of one piezoelectric bimorph ($\hat{m}$) is chosen as the nominal value. Moreover, by comparing model (10.1) with the inverse Laplace transform of the plant model G_p as shown in Eq. (10.43), other parameters ($\hat{b}$, $\hat{k}$, and $\hat{d}$) are obtained as shown in Table 10.1.

Because the left gripper arm is passive, this arm together with the microgear to be grasped act as the environment in this work. In view of the compliance of the bimorph indicated by s_p, the stiffness is calculated as 2.17×10^3 N/m. Considering that the rigidity of the plastic microgear is much higher than that of the gripper arm, the environment stiffness of $K_e \approx 2 \times 10^3$ N/m is assumed. Other target parameters in the desired impedance (10.9) are selected as: $M = 1$, $B = 2\zeta\omega_n$, and $K = \omega_n^2$, where $\zeta = 1$ is set to achieve a critical damping. In addition, $\omega_n = 1000\pi$ rad/s is chosen to give the target parameters as shown in Table 10.1.

In view of the relationship (10.41) of the steady-state errors, K_f should be chosen to constrain the maximum force to ensure that the gripper arms and the microobject will not be damaged. For illustration, K_f is selected as $K_f = \frac{K}{5}$. Thus, $K > K_f$, which indicates that the position control is emphasized in the impedance control.

Table 10.1 Parameters of dynamics model, target impedance, and ADSMGIC controller

Parameter	Value
$\hat{m}$	1.8×10^{-3} kg
$\hat{b}$	126.8 Ns/μm
$\hat{k}$	5.943×10^{6} N/μm
$\hat{d}$	1.129×10^{8} μm/V
M	1 kg
B	6.2832×10^{3} Ns/m
K	9.8696×10^{6} N/m
K_f	2000 mN/μm
K_P	3.1416×10^{5}
K_I	9.8696×10^{6}
K_D	2500
K_4	2000
K_5	0.5
K_S	3000
γ	5
δ	10^{5}

In addition, with a sampling time $T = 0.02$ s, the discrete-time dynamics model and the target impedance parameters are calculated by Eqs. (10.5) and (10.11), respectively.

10.5 Experimental Results and Discussion

Experimental studies on the prototype microassembly system is carried out to verify the effectiveness of the developed interaction control scheme.

10.5.1 Interaction Control Results

Regarding the developed ADSMGIC controller, the control gains K_P, K_I, K_D, and K_4 are shown in Table 10.1, which are calculated by Eqs. (10.14)–(10.20). Other controller parameters are tuned by several trials as given in Table 10.1. To investigate the effects of the parameter tuning, three case studies are carried out below.

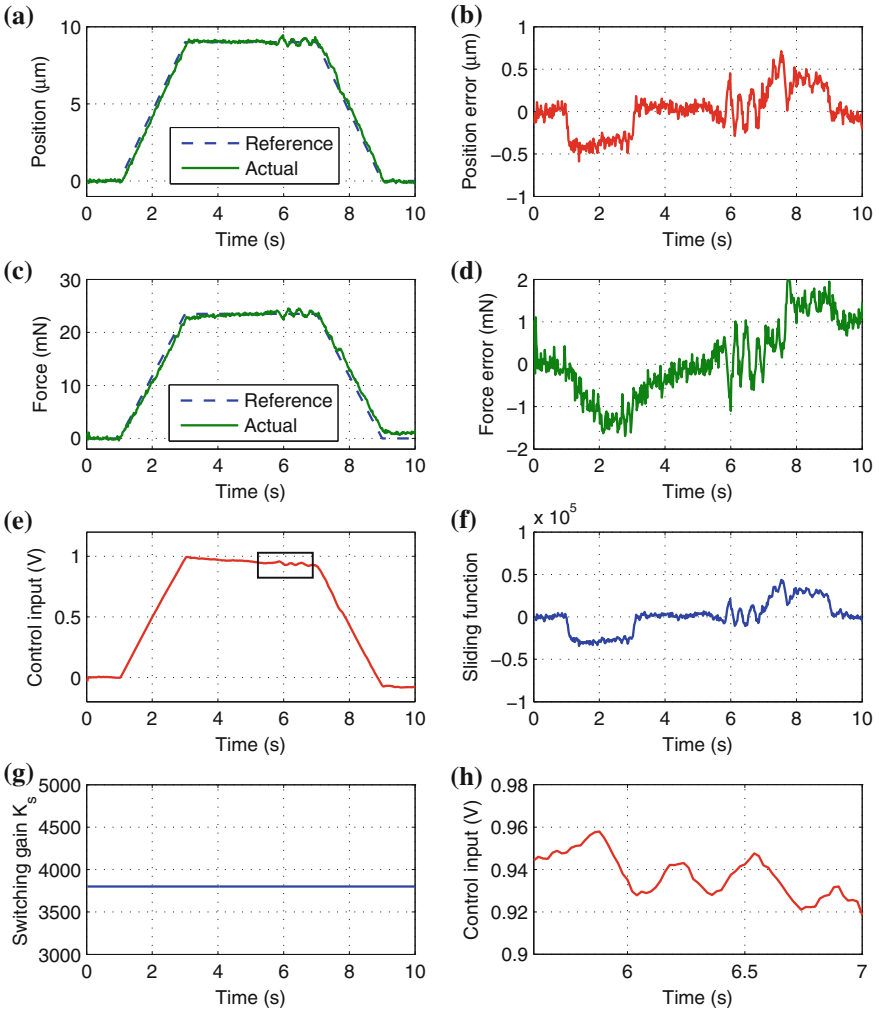

Fig. 10.6 Tracking results of ADSMGIC with fixed control gain $K_S = 3800$. **a** Position trajectory. **b** Position error. **c** Force trajectory. **d** Force error. **e** Control input. **f** Sliding function. **g** Switching gain. **h** Close-up view of control input

10.5.1.1 Case Study I

First, the effectiveness of the adaptive switching gain is examined. For the planned trajectories, the tracking results of the control algorithm with a fixed switching gain $K_S = 3800$ and an adaptive switching gain $K_{S,k}$ are shown in Figs. 10.6 and 10.7, respectively. The position and force RMSEs of the two controllers are summarized in Table 10.2. The position and force relative RMSEs are calculated as the ratios of RMSEs to the peak-to-peak magnitudes of the position and force trajectories,

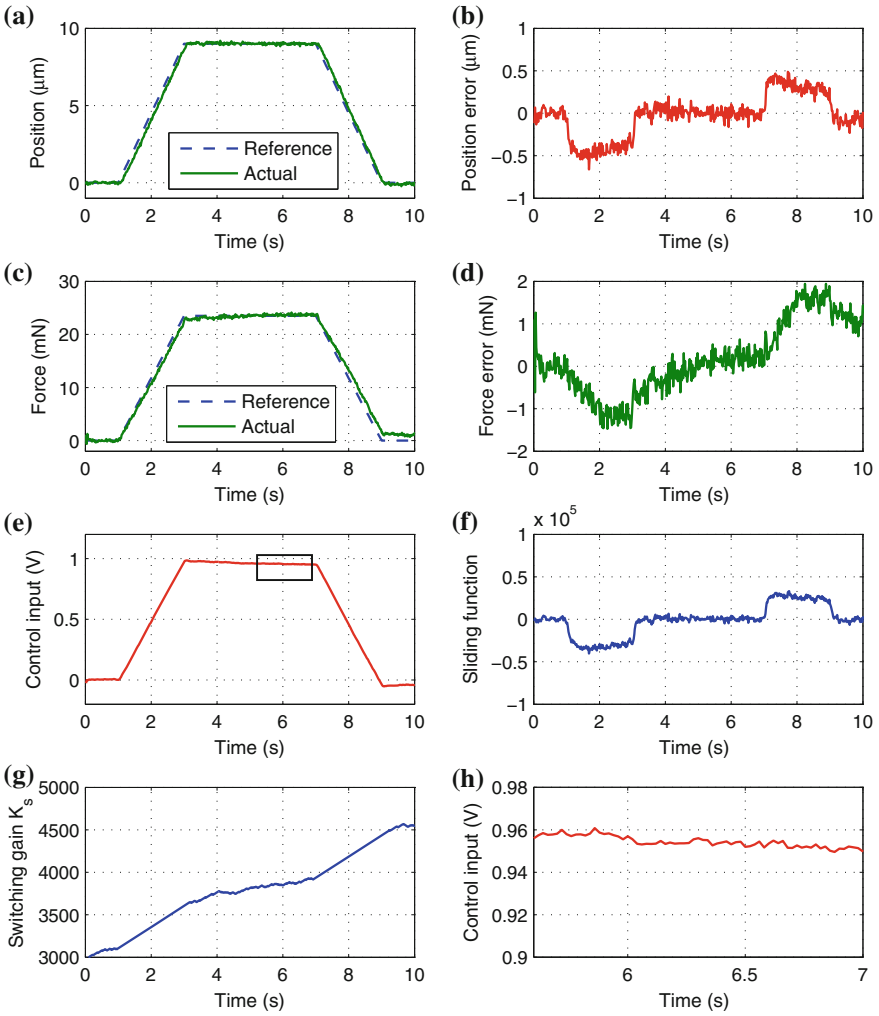

Fig. 10.7 Tracking results of ADSMGIC with adaptive control gain $K_{S,k}$. **a** Position trajectory. **b** Position error. **c** Force trajectory. **d** Force error. **e** Control input. **f** Sliding function. **g** Switching gain. **h** Close-up view of control input

respectively. In addition, Figs. 10.6f and 10.7f indicate that the sliding function is well constrained by the boundary layer parameter $\delta = 10^5$ in both cases.

As compared with the fixed gain, the adaptive gain produces an improvement on the position and force tracking accuracy. The close-up view of the control input as shown in Fig. 10.6h indicates that the fixed switching gain in Fig. 10.6g causes oscillation phenomenon. On the contrary, the oscillation is eliminated by the employment of adaptive gain in Fig. 10.7g as implied by Fig. 10.7h. Hence, the dominant role of the adaptive law for the switching gain is to alleviate the chattering phenomenon of ADSMGIC control action.

Table 10.2 Interaction control results of ADSMGIC for three case studies

		Position error		Force error	
Case study	Control option	RMSE (μm)	Relative (%)	RMSE (μm)	Relative (%)
I	Fixed gain K_S	0.252	2.80	0.88	3.75
	Adaptive gain K_S	0.250	2.77	0.86	3.66
II	Control gain $K_5 = 0.43$	0.30	3.33	0.77	3.28
III	Impedance parameter $K_f = 0$	0.29	3.22	0.78	3.32

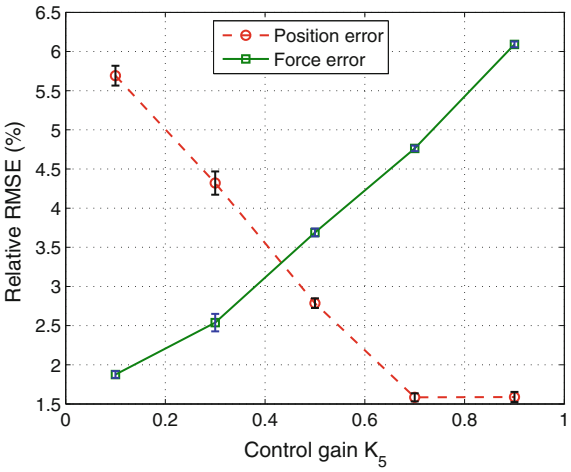

Fig. 10.8 Error bars of position and force tracking relative RMSEs versus the control gain K_5

10.5.1.2 Case Study II

Next, to demonstrate the influence of the control gain on the interaction control, the tracking performance is tested as the gain K_5 varies from 0.1 to 0.9. For each K_5 value, the experiment is conducted five times. The error bars of the position and force tracking results are depicted in Fig. 10.8.

It is found that the position and force errors vary in opposite tendencies as the control gain K_5 changes. Specifically, as K_5 increases from 0.1 to 0.9, the position error is reduced whereas the force error is increased gradually. Hence, a good position tracking is obtained at the sacrifice of force error, and vice versa. It is further observed that a balance between the position and force tracking is achieved with the gain $K_5 =$ 0.43. It leads to almost identical relative RMSEs (3.3 %) for both trajectories, as shown in Table 10.2.

The experimental results indicate that the position and force tracking accuracy can be compromised by adjusting the control gain K_5 for the proposed ADSMGIC scheme.

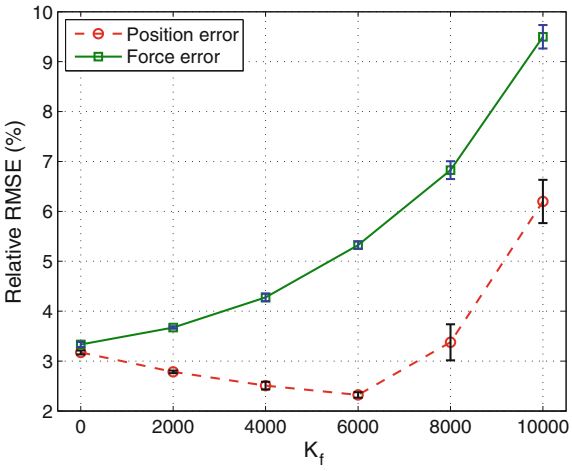

Fig. 10.9 Error bars of position and force tracking relative RMSEs versus the target impedance parameter K_f

10.5.1.3 Case Study III

To illustrate the effect of selection of the target impedance parameters K and K_f on the tracking performance, the control scheme with K_f varying from 0 to 10^4 is tested. For each K_f value, the experiment has been repeated by five times and experimental data are obtained. The error bars of the relative RMSEs for both position and force tracking results versus K_f are plotted in Fig. 10.9.

It is observed that the magnitude of the relative RMSE of the position is lower than that of the force. The reason arises from the fact that the relationship of $K > K_f$ holds. Thus, the position control is more emphasized in the impedance control as predicted by Eqs. (10.40) and (10.41). As a result, a relative small position tracking error is achieved. Moreover, it is found that as K_f increases from 0 to 6000, the position error is reduced gradually. Whereas the force error is increased as the rising of K_f, which is consistent with the tendency as evaluated by Eq. (10.41).

In addition, Fig. 10.9 also illustrates how to select a balance point of the position and force control by adjusting the target impedance parameter. It is evident that in the case of $K_f = 0$, a better balance between the position and force tracking accuracy is achieved in that the ADSMGIC produces similar position and force relative RMSEs, as shown in Table 10.2.

Furthermore, it is found that a too large K_f induces oscillation of the control action. For instance, as K_f increases greater than 8000, a moderate oscillation in the interaction control is produced. The oscillation deteriorates both the position and force tracking accuracy as depicted in Fig. 10.9.

In the aforementioned case studies, the effects of the parameters are intuitively illustrated to have a better understanding of the controller performance under the tuning of control parameters and target parameters. These processes provide a guideline for the extension of the control scheme to other applications.

10.5.2 Discussion on Control Performance

The fact that the controller works well for different values of the target impedance parameter reveals that the control scheme is robust to the target stiffness. In addition, the impedance parameters B and K are determined by the parameter ω_n. Regarding the selection of ω_n, additional experimental testings reveal that, the larger the ω_n value, the smaller the achievable position and force tracking errors for the control scheme.

Generally, in order to overcome the disturbances and uncertainties of the system model, the upper bounds of the perturbation terms need to be acquired in SMC robust control [16], which complicates the control design process. Alternatively, only an upper bound K_S [see Eq. (10.31)], i.e., the switching control gain, of perturbation estimation error is required by the reported robust control framework. Moreover, by adopting the adaptive rule (10.33), the switching gain can be set as zero initially because it is automatically adjusted online. Thus, the burden of specifying the perturbation bounds is relieved in the presented approach. On the other hand, because the perturbation estimation error is usually much lower than the actual perturbation and the switching gain is adjusted to adapt to the sliding function, a much smaller control gain is resulted as compared with conventional SMC algorithms. As a consequence, the reported control framework achieves an improvement on the tracking performance by suppressing the chattering phenomenon.

It is notable that the lumped perturbation term P_k is calculated by the one-step delayed estimation (10.6). Thus, a good calculation accuracy can be obtained by employing a high sampling rate T and a low variation rate of P_k. Due to the controller hardware limit, a sampling time of $T = 0.02\,\mathrm{s}$ is implemented for the prototype microgripper in this work. Even so, a reasonable accuracy for both the position and force tracking has been achieved as illustrated by the experimental results. With such a sampling rate, the conventional continuous-time impedance control may even not work if directly deployed to the sampled-data system. Hence, the experimental results confirm the feasibility of the digital control scheme. The tracking errors can be further reduced by adopting a smaller sampling time.

Additionally, the gain parameters of the ADSMGIC controller are not optimally designed in the preceding experiments. The performance of the control scheme may be improved to further enhance the tracking accuracy. Moreover, the precise micromanipulation is affected by the external disturbances including external vibrations, temperature, etc. The fact that a precise position and force control can be simultaneously achieved demonstrates the robustness of the control scheme in the presence of noise and temperature disturbances. Further work includes the investigation of grasping more microobjects to accomplish complex microassembly tasks. The adhesive forces will also be taken into account during the assembly of smaller microscopic objects.

10.6 Chapter Summary

This chapter reports on a control scheme for position/force control of a piezoelectric-bimorph microgripper dedicated to micromanipulation and microassembly. The presented digital sliding mode-based scheme is easy to implement in that only a second-order dynamic model is used, whereas neither the state estimation nor hysteresis modeling is needed. The stability of the control system has been proved theoretically and the effectiveness of the scheme has been validated by a series of experimental studies on typical grasp operation. The superiority of the adaptive switching gain over fixed one in terms of chattering suppression has been confirmed. Moreover, results indicate that the scheme is capable of achieving satisfactory interaction control results. A tradeoff between the position and force tracking accuracy can be realized by varying the relative values of control gains or target impedance parameters. As a future work, adaptive rules for the model parameters may be devised to eliminate the procedure of dynamic model identification. Moreover, the extension of the proposed methodology to interaction control of microgrippers driven by other types of actuators will also be explored for micromanipulation and microassembly tasks.

References

1. Almeida, F., Lopes, A., Abreu, P.: Force-impedance control: A new control strategy of robotic manipulators. In: Kaynak, O., Tosunoglu, S., Ang, M. (eds.) Recent Advances in Mechatronics, pp. 126–137. Springer, Singapore (1999)
2. Bargiel, S., Rabenorosoa, K., Clévy, C., Gorecki, C., Lutz, P.: Towards micro-assembly of hybrid MOEMS components on a reconfigurable silicon free-space micro-optical bench. J. Micromech. Microeng. **20**(4), 045012 (2010)
3. Beyeler, F., Neild, A., Oberti, S., Bell, D.J., Sun, Y., Dual, J., Nelson, B.J.: Monolithically fabricated microgripper with integrated force sensor for manipulating microobjects and biological cells aligned in an ultrasonic field. J. Microelectromech. Syst. **16**(1), 7–15 (2007)
4. Bonitz, R.G., Hsia, T.C.: Internal force-based impedance control for cooperating manipulators. IEEE Trans. Robot. Autom. **12**(1), 78–89 (1996)
5. Chan, S.P., Liaw, H.C.: Generalized impedance control of robot for assembly tasks requiring compliant manipulation. IEEE Trans. Ind. Electron. **43**(4), 453–461 (1996)
6. Chonan, S., Jiang, Z.W., Koseki, M.: Soft-handling gripper driven by piezoceramic bimorph strips. Smart Mater. Struct. **5**, 407–414 (1996)
7. Elmali, H., Olgac, N.: Implementation of sliding mode control with perturbation estimation (SMCPE). IEEE Trans. Control Syst. Technol. **4**(1), 79–85 (1996)
8. Furuta, K.: Sliding mode control of a discrete system. Syst. Control Lett. **14**(2), 145–152 (1990)
9. Haddab, Y., Chaillet, N., Bourjault, A.: A microgripper using smart piezoelectric actuators. In: Proceedings of the IEEE/RSJ International Conference on Intelligent Robots and Systems, pp. 659–664. Takamatsu, Japan (2000)
10. Hogan, N.: Stable execution of contact tasks using impedance control. In: Proceedings of the IEEE International Conference on Robotics and Automation, pp. 1047–1054. Raleigh, North Carolina, USA (1987)
11. Huang, H.B., Sun, D., Mills, J.K., Cheng, S.H.: Robotic cell injection system with position and force control: toward automatic batch biomanipulation. IEEE Trans. Robot. **25**(3), 727–737 (2009)

12. Huang, X., Cai, J., Wang, M., Lv, X.: A piezoelectric bimorph micro-gripper with micro-force sensing. In: IEEE International Conference on Information Acquisition, pp. 145–149. Hong Kong and Macau, China (2005)
13. Jung, S., Hsia, T.C., Bonitz, R.G.: Force tracking impedance control for robot manipulators with an unknown environment: theory, simulation, and experiment. Int. J. Robot. Res. **20**(9), 765–774 (2001)
14. Jung, S., Hsia, T.C., Bonitz, R.G.: Force tracking impedance control of robot manipulators under unknown environment. IEEE Trans. Control Syst. Technol. **12**(3), 474–483 (2004)
15. Kim, K., Liu, X., Zhang, Y., Sun, Y.: Nanonewton force-controlled manipulation of biological cells using a monolithic MEMS microgripper with two-axis force feedback. J. Micromech. Microeng. **18**(5), 055013 (2008)
16. Liaw, H.C., Shirinzadeh, B.: Robust generalised impedance control of piezo-actuated flexure-based four-bar mechanisms for micro/nano manipulation. Sens. Actuator A-Phys. **148**(2), 443–453 (2008)
17. Lu, W.S., Meng, Q.H.: Impedance control with adaptation for robotic manipulations. IEEE Trans. Robot. Autom. **7**(3), 408–415 (1991)
18. Lu, Z., Chen, P.C.Y., Lin, W.: Force sensing and control in micromanipulation. IEEE Trans. Syst. Man Cybern. Part C, Appl. Rev. **36**(6), 713–724 (2006)
19. Lu, Z., Kawamura, S., Goldenberg, A.A.: An approach to sliding-mode based control. IEEE Trans. Robot. Autom. **11**(5), 754–759 (1995)
20. Menciassi, A., Eisinberg, A., Carrozza, M.C., Dario, P.: Force sensing microinstrument for measuring tissue properties and pulse in microsurgery. IEEE/ASME Trans. Mechatron. **8**(1), 10–17 (2003)
21. Monsees, G., Scherpen, J.M.A.: Adaptive switching gain for a discrete-time sliding mode controller. Int. J. Control **75**(4), 242–251 (2002)
22. Qiu, L., Cui, Y., Feng, F.: Design of a new micro-gripper based on piezoelectric bimorphs. Appl. Mech. Mater. **101–102**, 173–177 (2011)
23. Rakotondrabe, M., Haddab, Y., Lutz, P.: Nonlinear modeling and estimation of force in a piezoelectric cantilever. In: Proceedings of the IEEE/ASME International Conference on Advanced Intelligent Mechatronics, pp. 1–6. Zurich, Switzerland (2007)
24. Rakotondrabe, M., Ivan, I.A.: Development and force/position control of a new hybrid thermo-piezoelectric microgripper dedicated to micromanipulation tasks. IEEE Trans. Autom. Sci. Eng. **8**(4), 824–834 (2011)
25. Reddy, A.N., Maheshwari, N., Sahu, D.K., Ananthasuresh, G.K.: Miniature compliant grippers with vision-based force sensing. IEEE Trans. Robot. **26**(5), 867–877 (2010)
26. Sariola, V., Jaaskelainen, M., Zhou, Q.: Hybrid microassembly combining robotics and water droplet self-alignment. IEEE Trans. Robot. **26**(6), 965–977 (2010)
27. Sarpturk, S., Istefanopulos, Y., Kaynak, O.: On the stability of discrete-time sliding mode control systems. IEEE Trans. Autom. Control **32**(10), 930–932 (1987)
28. Schutter, J.D., Bruyninckx, H., Zhu, W.H., Spong, M.W.: Force control: A bird's eye view. In: Siciliano, B. (ed.) Control Problems in Robotics and Automation: Future Directions, pp. 1–17. Springer, Berlin (1998)
29. Seki, H.: Modeling and impedance control of a piezoelectric bimorph microgripper. In: Proceedings of the IEEE/RSJ International Conference on Intelligent Robots and Systems, vol. 2, pp. 958–965. Raleigh, USA (1992)
30. Seraji, H., Colbaugh, R.: Force tracking in impedance control. Int. J. Robot. Res. **16**(1), 97–117 (1997)
31. Tarokh, M.: A discrete-time adaptive control scheme for robot manipulators. J. Robot. Syst. **7**(2), 145–166 (1990)
32. Wu, J., Shieh, L.S., Zhang, Y., Song, G.: Digital controller design for Bouc-Wen model with high-order hysteretic nonlinearities through approximated scalar sign function. Int. J. Sys. Sci. **42**(10), 1581–1599 (2011)
33. Xu, Q.: A new method of force estimation in piezoelectric cantilever-based microgripper. In: Proceedings of the IEEE/ASME International Conference on Advanced Intelligent Mechatronics, pp. 574–579. Kaohsiung, Taiwan (2012)

34. Xu, Q.: Identification and compensation of piezoelectric hysteresis without modeling hysteresis inverse. IEEE Trans. Ind. Electron. **60**(9), 3927–3937 (2013)
35. Xu, Q., Li, Y.: Model predictive discrete-time sliding mode control of a nanopositioning piezostage without modeling hysteresis. IEEE Trans. Control Syst. Technol. **20**(4), 983–994 (2012)
36. Zhang, L., Dong, J.: High-rate tunable ultrasonic force regulated nanomachining lithography with an atomic force microscope. Nanotechnology **23**(8), 085303 (2012)
37. Zhang, Y., Zou, Q.: High-speed force load in force measurement in liquid using scanning probe microscope. Rev. Sci. Instrum. **83**(1), 013707 (2012)

Chapter 11
Position/Force Switching Control of a Miniature Gripper

This chapter presents the design and implementation of combined position and force control of a piezoelectrically actuated compliant gripper. The challenge of achieving a smooth transition between the position and force switching control is addressed by means of an incremental control scheme. Precision control under the influence of hysteretic nonlinearity is guaranteed by a digital sliding-mode control (DSMC) algorithm. The scheme is implemented with an FPGA platform. Experimental investigations are undertaken to verify the effectiveness of the gripper system by executing grasp-hold-release operations of a micro copper wire.

11.1 Introduction

As a key device in microhandling system, miniature gripper plays an important role dedicated to micromanipulation and microassembly tasks. Typically, the gripper is employed to execute an automated grasp-hold-release operation for such applications as material characterization, biological sample pick-and-place, and micro-object assembly. Diverse miniature grippers have been reported using different actuation principles [15]. In particular, piezoelectric actuators are prevailing in many industrial applications owing to their ultrahigh position resolution and quick response capabilities [13, 23].

To grasp an object gently without impairing the object and the gripper, it is important to regulate both the relative position and touch force between the gripper and object [14, 19]. In addition, a gripper with integrated position and force sensing is able to characterize the stiffness and viscosity properties of various materials, such as biological tissues [2]. However, it is challenging to implement a position and force control for a PSA-driven gripper.

One of the major challenges stems from the combination of the position and force control. Intuitively, a position/force switching control can be adopted to adjust the gripper tip position and gripping force in an alternate manner [17]. The concerned

© Springer International Publishing Switzerland 2016

Q. Xu and K.K. Tan, *Advanced Control of Piezoelectric Micro-/Nano-Positioning Systems*, Advances in Industrial Control,
DOI 10.1007/978-3-319-21623-2_11

dominant issue lies in how to achieve a smooth transition when different control variables are switched [12]. Similar problem resides in the hybrid position/force control scheme [4, 16], which calls for a stable switch to accomplish the position and force control in different subspaces. Even though the switching control problem can be avoided by employing the compliance [10] or impedance control framework [8, 20], care must be taken for the position and force trajectory planning to ensure a desired performance. To achieve a smooth transition of the position and force control, an intermediate brake mode can be added between the two control modes [6, 18]. Furthermore, to accomplish a rapid intermediate control and to reduce the force overshoot in the initial contact, an optimal velocity profile can be used [1]. However, an extra control mode is required, whose execution increases the overall operation time of the gripper. More recently, fuzzy control has been proposed to smooth the transition [5, 11]. However, the membership functions have to be readjusted to adapt to different objects, which complicates the practical implementation process. Hence, a simple yet efficient approach is desirable to realize a smooth transition between the position and force control. Another challenge is organized from the piezoelectric actuator which exhibits strong nonlinearities in terms of hysteresis and drift effects once driven by a voltage source [9].

To this end, a scheme of incremental control is reported in this chapter to achieve a smooth transition of the position/force switching control for the gripper system. Specifically, in the closing and opening phases, an incremental DSMC is devised to cater for the position control. During the contact phase, an incremental-type digital PID force control is adopted. The incremental controller solves the change value of the control action in each time step. At the moment of switching between two consecutive control phases, the controller adopts the control action in the previous phase as the base value for the next one. In this way, a smooth transition between two adjacent phases is easily achieved. The proposed control algorithm is deployed to an FPGA-based digital control platform. The feasibility of the scheme is examined by a typical grasp-hold-release operation of a micro copper wire through experimental studies. Moreover, its superiority over the conventional approach is demonstrated via comparison studies.

11.2 Experimental Setup and Calibration

11.2.1 Working Principle of the Gripper

The mechanical structure of the employed gripper is shown in Fig. 11.1. The compliant gripper consists of a bridge-type displacement amplifier, a rotary bearing mechanism, and two gripper arms/tips. The stroke ($2S$) of PSA is magnified by the bridge-type amplifier, which provides an amplification ratio of A_1. Figure 11.1b exhibits a pseudo-rigid-body (PRB) model of the amplifier. The amplified displacement ($A_1 S$) at the output end of the amplifier is transmitted to the two gripper arms

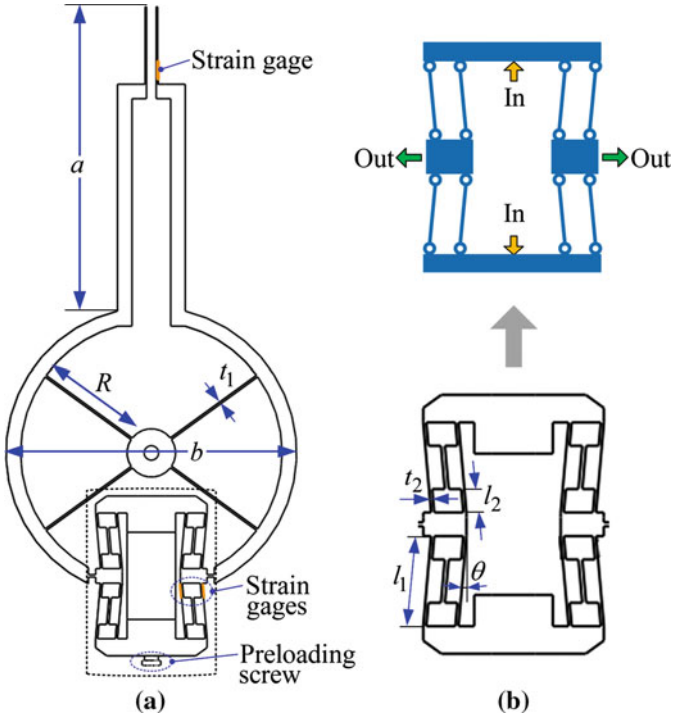

Fig. 11.1 Schematic diagram of a miniature gripper. **a** The gripper structure. **b** Bridge-type displacement amplifier

through two sets of rotary guiding flexures, respectively. With a distance a away from the bearing mechanism, the displacement of each gripper tip is further magnified by a factor of $A_2 = 1 + 2a/b$, where b is the diameter of the rotary bearing mechanism. Hence, the overall displacement at each tip of the gripper can be expressed as $A_1 A_2 S$, and the gripping range of the gripper is $2A_1 A_2 S$. In contrast to a parallelogram-based gripper, the employed one reduces the number of guiding flexures and simplifies the gripper structure, which indicates a reduction of the fabrication cost.

To measure the displacement of the gripper tips and the contact force during the gripping operation, a vision-based sensing approach can be employed [14]. Nevertheless, the relative low sensing resolution and sampling rate are the major disadvantages of such approach. Recently, it has been shown that strain gages provide a straightforward way to measure the position and gripping force of a PSA-driven monolithic gripper [19]. In this work, two groups of strain gages are adopted and surface-bonded on the flexures as the position and force sensors, respectively. Due to a symmetric architecture, the measurement for a single gripper arm is sufficient. To generate a high sensitivity and high signal-to-noise ratio (SNR) for the measurement, the strain-gage position sensor is glued on the bridge amplifier and the strain-gage force sensor is attached on the base end of the gripper tip, as indicated in Fig. 11.1. A preloading screw is used to adjust the amplification ratio A_1 of the bridge amplifier

Table 11.1 Main parameters of a compliant gripper

Parameter	Symbol	Value
Length of arm	a	62.0 mm
Diameter of rotary bearing	b	60.0 mm
Length of guiding flexure	R	22.0 mm
Width of guiding flexure	t_1	0.4 mm
Length of amplifier arm	l_1	11.5 mm
Length of amplifier flexure	l_2	3.0 mm
Width of amplifier flexure	t_2	0.4 mm
Incline angle of amplifier	θ	5.0°
Thickness of material	h	5.0 mm

and the initial gap between the two gripper tips. The entire gripper can be mounted on a support base through the central fixing hole of the rotary bearing.

The structural parameters are designed as shown in Table 11.1 to enable a gripping range of 200 μm using a PSA of 14.5-μm stroke.

11.2.2 Experimental Setup

A prototype gripper is shown in Fig. 11.2, which is fabricated from a piece of Al-7075 material by the wire-EDM process. A PSA (model: TS18-H5-202, from Piezo

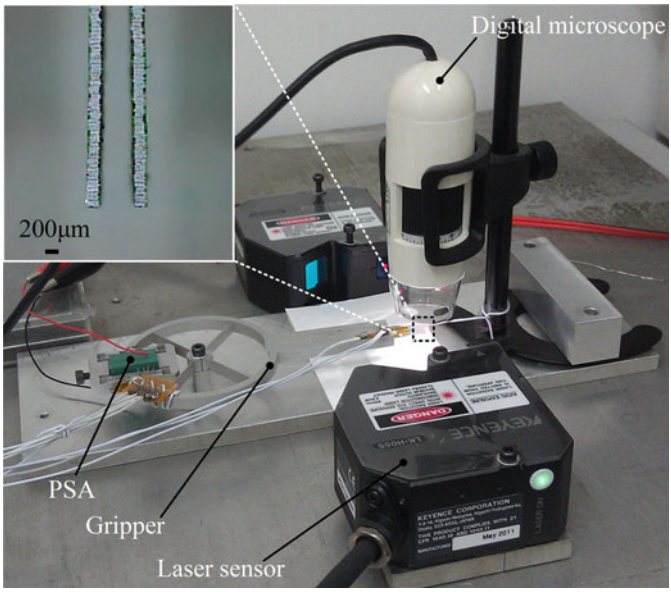

Fig. 11.2 Experimental setup of a prototype gripper system

Systems, Inc.) is chosen to actuate the gripper. The PSA is driven through a commercial high-voltage amplifier to deliver a maximal stroke of 14.5 μm. For the measurement of the gripper tip position, four strain gages (model: SGD-3/350-DY13, from Omega Engineering Ltd.) are employed to construct a full-bridge circuit. Due to the space limit, another strain gage (model: SGD-3/350-LY13, from Omega Engineering Ltd.) is adopted to form a quarter bridge for the gripping force measurement. In addition, a Natural Instruments (NI) cRIO-9022 real-time (RT) controller combined with cRIO-9118 reconfigurable chassis (from National Instruments Corp.) is adopted to implement the control algorithm. The NI-9263 D/A and NI-9237 A/D modules are adopted for producing the analog excitation signals and acquiring the strain-gage sensor signals, respectively. The NI cRIO-9118 chassis contains a FPGA core, and the associated cRIO-9022 RT controller communicates with a personal computer (PC) via the 10/100 Mbit/s Ethernet port.

For the calibration of strain-gage position sensor, the tip position of the gripper is also measured by a laser displacement sensor (model: LK-H055, from Keyence Corp.), which provides a 25-nm resolution within a 20-mm measuring range. Additionally, a digital microscope (model: AM2011 Dino-Lite Basic, from AnMo Electronics Corp.) with a magnification ratio of 200 is employed to monitor the gripper tips and grasped objects during the gripping process.

The control algorithms are programmed using LabVIEW™ software to realize a deterministic RT control for the gripper system. Specifically, the algorithm is developed and debugged in PC with LabVIEW. Afterward, the program is compiled to generate FPGA codes automatically. When the compilation is completed, the codes are downloaded into cRIO platform through the Ethernet connection. Once downloaded completely, the cRIO system can work independently.

11.2.3 Calibration of Position and Force Sensors

The purpose of calibration is to determine the position and force gains so as to convert the position and force strain-gage outputs into the position and force values, respectively. The position and force gains can be derived by comparing the strain-gage outputs with the known position and force values under the assumption that there is a constant linear relationship between the strain-gage outputs and the measured values. It has been shown that the strain-gage gains can be calibrated by using different input signals such as sinusoidal and square waves [7]. In this work, the step signals are adopted for the calibration of the position and force sensors.

To calibrate the strain-gage position sensor, a step signal with a 3-V amplitude is used to drive the PSA. By comparing the strain-gage output and the laser sensor readings, a gain of η_d = 185.541 μm/mV is derived to calibrate the position sensor. The output of the two sensors are plotted in Fig. 11.3a. The root-mean-square error (RMSE) of the strain-gage position sensor output with respect to the laser sensor output is calculated as 0.154 μm. With a zero input, the noise signal of the

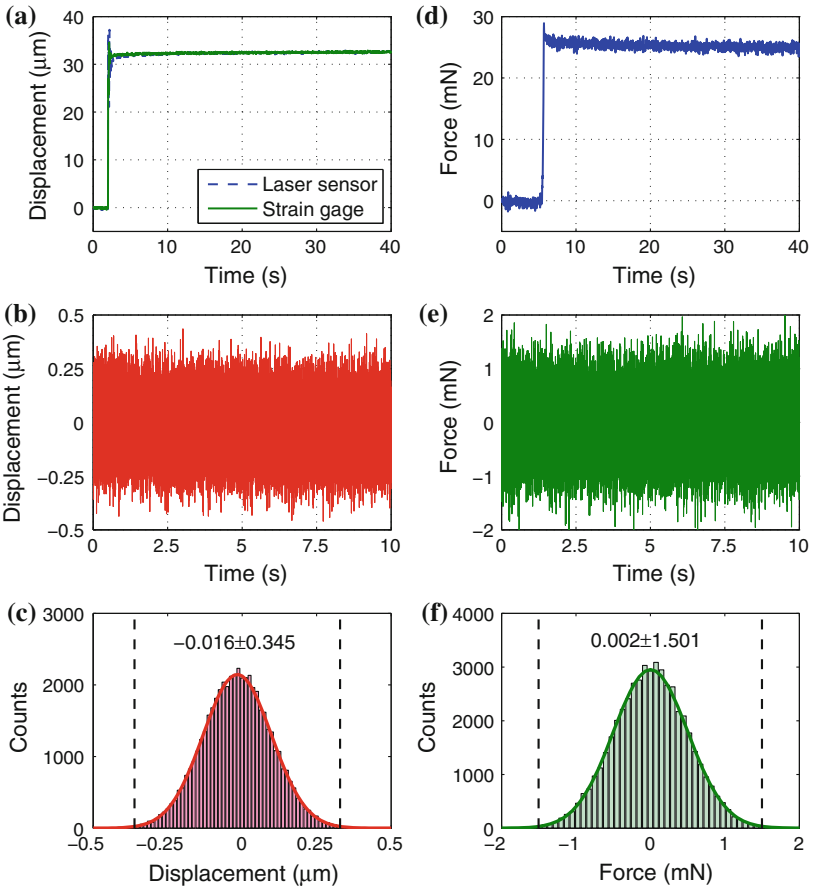

Fig. 11.3 Calibration results of strain-gage position and force sensors. **a** The output of laser sensor and strain-gage position sensor. **b** Strain-gage position sensor noise. **c** Histogram of strain-gage position sensor noise. **d** The output of strain-gage force sensor. **e** Strain-gage force sensor noise. **f** Histogram of strain-gage force sensor noise

strain-gage position sensor is acquired as shown in Fig. 11.3b and the histogram is given in Fig. 11.3c, which reveals that the white noise follows a normal distribution (solid curve). The limit of three standard deviations (3σ) from the mean ($-0.016\,\mu$m) is obtained as $0.345\,\mu$m, which indicates that 99.7 % of the sensor readings fall within the interval of $-0.016 \pm 0.345\,\mu$m. In addition, a slight drift is observed in Fig. 11.3a, which is caused by the PSA with a constant voltage input.

Additionally, the strain-gage force sensor is calibrated by hanging a known weight (25 mN) and acquiring the caused sensor output voltage. The force sensor gain is then calculated as $\eta_f = 658.345$ mN/mV, which is employed to convert the voltage into the force value as plotted in Fig. 11.3d. In addition, Fig. 11.3e, f display the noise and its histogram of the force sensor without a force exerted. It indicates a 3σ limit

of 1.501 mN. Hence, 99.7 % of force sensor readings lie within the range of 0.002 ± 1.501 mN around the mean value.

11.2.4 Gripping Range Testing

Using the strain-gage position sensor, the gripping range of the gripper is examined experimentally. By applying a sinusoidal signal of 0.5-Hz frequency and 10-V amplitude to drive the PSA through the high-voltage amplifier, the gripping range is tested as shown in Fig. 11.4. It is found that displacement of one gripper tip is 138 μm, indicating a gripping range of 276 μm for the gripper. As compared with the simulation result (200 μm), the experimental result of the gripping range is larger, which is caused by adjusting the preloading screw.

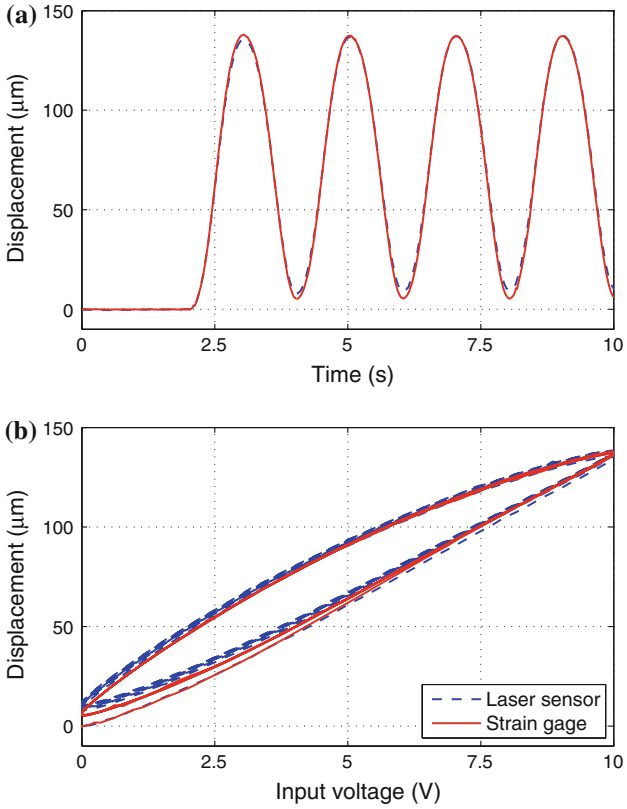

Fig. 11.4 Test result of gripping range by applying a 0.5-Hz, 10-V amplitude sinusoidal input. **a** Time history results. **b** Hysteresis curves

Figure 11.4b exhibits a significant hysteresis effect which calls for a control technique for the precision control of the gripper tips. It is also observed that there is a slight discrepancy between the strain-gage position sensor and laser sensor outputs. The discrepancy is mainly caused by different dynamic properties of the two types of sensors. In addition, the results indicate that the strain-gage gain, which is determined by using a step signal input, applies to the sinusoidal input as well. This fact verifies the assumption that there is a constant linear relationship between the strain-gage outputs and the measured values.

11.2.5 Frequency Response Testing

The dynamics characteristics of the gripper system are examined by means of frequency response. Particularly, a sweep sine wave with a 0.1-V amplitude and frequency ranging from 1 to 500 Hz is used to drive the PSA. The position response is measured by the strain-gage position sensor. Spectral analysis is then conducted to derive the frequency responses of the gripper, which are shown in Fig. 11.5. A resonant peak at the frequency of 244 Hz is observed. The resonance limits the usable bandwidth of the system [22]. The reason lies in that the input signals with high-frequency components will excite the resonance vibration. Hence, a high resonant frequency is desirable to obtain a large control bandwidth.

Based on the experimental data, a fourth-order model of the plant is obtained. Figure 11.5 indicates that the identified model well approximates the system dynamics behavior up to 300 Hz. It is notable that a higher order model can be generated

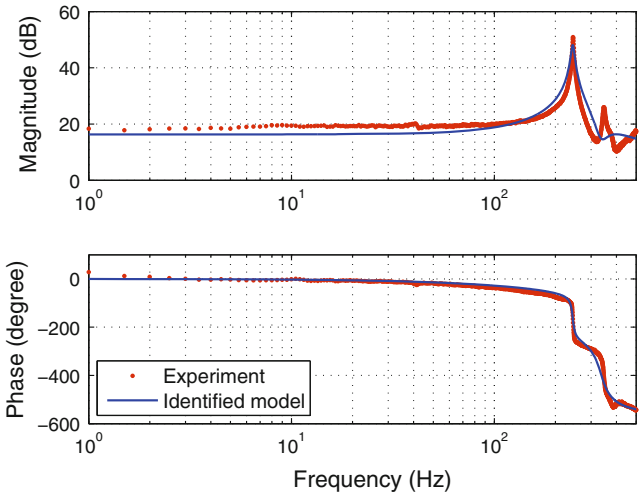

Fig. 11.5 Open-loop frequency response of the gripper system

to better describe the dynamics at higher frequencies. In this work, a model of lower order is adopted to make a compromise between the accuracy and complexity of the plant model.

11.3 Position/Force Switching Control Scheme Design

11.3.1 Event-Based Switching Control Framework

For a precision microhandling task, the grasp process of the gripper can be classified into three stages in terms of closing phase (I), contact phase (II), and opening phase (III). Here, an event-based switching control strategy between the three phases is employed to regulate the position and force alternately, which is depicted in Fig. 11.6. The closing phase occurs before the contact of gripper tips and object, and opening phase runs after the said contact procedure. In the closing and opening phases, a precise position control of the gripper tips is sufficient. Depending on different treatments of the contact phase, two control approaches can be developed in terms of position control with force monitoring and position/force switching control.

The first method realizes only the position control in the closing and opening phases. It applies a constant control voltage during the contact phase once a desired force magnitude is attained. In contrast, the second method implements a position control in the closing and opening phases and a force control in the contact phase, respectively. Considering that only the position control is needed in the first approach, any precision position control strategy can be employed. Regarding the position/force switching control scheme, the system exhibits one input variable, i.e., the driving voltage, and two output variables, i.e., the position and force. Because the three phases adopt the same control input, the switching between different controllers may cause instability and unwanted response of the position and force outputs. Therefore,

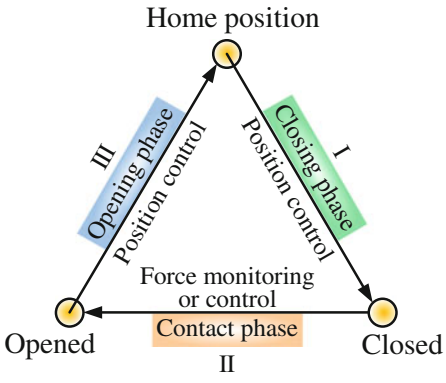

Fig. 11.6 An event-based switching control framework of the gripper system with three phases of operation

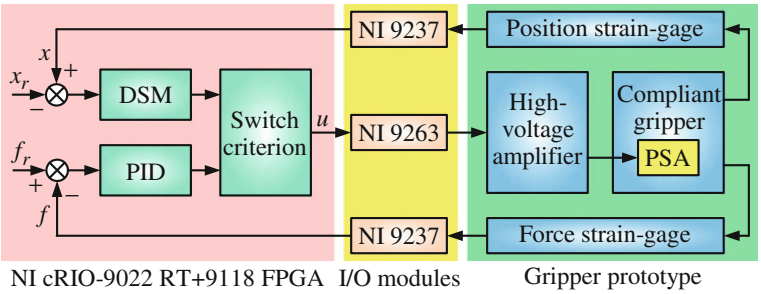

Fig. 11.7 Block diagram of position/force switching control for the gripper system

it is essential to guarantee a stable and smooth transition between two consecutive phases so that a satisfactory response is accomplished.

To achieve such goal, an incremental control framework is presented in this work. Specifically, in both the closing and opening phases, an incremental DSMC position control is proposed. During the contact phase, an incremental-type digital PID force control is used. The incremental control algorithm only solves the change value of the control action in each time step. During the switching between two consecutive control phases, the incremental controller adopts the control action in the previous phase as the base value for the next one. In this way, a smooth transition between the two phases is accomplished. Moreover, a switching criterion of the position/force control is assigned based on a threshold of the contact force.

The framework of the position/force switching control is described in Fig. 11.7. In the following discussions, an incremental DSMC and an incremental PID control are designed to regulate the position and contact force, respectively.

11.3.2 Incremental DSMC Position Controller

It is known that the dynamics model of the piezo-actuated system can be represented as follows [3]:

$$x(k) = \sum_{i=1}^{n} a_i x(k-i) + \sum_{i=0}^{m} b_i u(k-i) + d(k) \tag{11.1}$$

where $x(k)$ and $u(k)$ represent the output position and input voltage at the time step k, respectively. a_i and b_i are the model coefficients. In addition, $d(k)$ describes the lumped effect of piezoelectric hysteresis, drift, external force, parameter uncertainties, and other model disturbances.

By expressing $e(k) = x(k) - x_r(k)$ as the position error, where $x_r(k)$ is the desired position trajectory, a PI-type sliding function is defined below

$$s(k) = \lambda_P e(k) + \lambda_I \varepsilon(k) \tag{11.2}$$

where λ_P and λ_I are the positive gains. Additionally, the integral error is calculated by $\varepsilon(k) = \sum_{i=1}^{k} e(i)$. Hence,

$$\varepsilon(k) = \varepsilon(k-1) + e(k). \tag{11.3}$$

The equivalent control action $u_{\text{eq}}(k)$ is solved from the relationship of $s(k) = 0$, which gives

$$\begin{aligned} u_{\text{eq}}(k) = -(b_0^{-1})\Bigg[\sum_{i=1}^{n} a_i x(k-i) + \sum_{i=1}^{m} b_i u(k-i) + \hat{d}(k) - \tilde{d}(k) - x_r(k)\Bigg] \\ -(\lambda b_0)^{-1}\lambda_I \varepsilon(k-1) \end{aligned} \tag{11.4}$$

where $\lambda = \lambda_P + \lambda_I$, $\tilde{d}(k) = \hat{d}(k) - d(k)$ represents the estimation error of the disturbance, and $\hat{d}(k) = d(k-1)$ denotes the estimated value of the disturbance term $d(k)$. That is,

$$\hat{d}(k) = x(k-1) - \sum_{i=1}^{n} a_i x(k-i-1) - \sum_{i=0}^{m} b_i u(k-i-1). \tag{11.5}$$

It is notable that the disturbance estimation error can be expressed into the form:

$$\tilde{d}(k) = d(k-1) - d(k) \approx -\dot{d}(t)T \tag{11.6}$$

where T is the sampling time.

Assume that $\dot{d}(t)$ is bounded, i.e., $|\dot{d}(t)| \leq \Lambda$. It is then derived that $\tilde{d}(k)$ is also bounded, i.e., $|\tilde{d}(k)| \leq \Lambda T$.

Substituting Eq. (11.5) into Eq. (11.4) and assigning $\tilde{d}(k) = 0$ results in

$$\begin{aligned} u_{\text{eq}}(k) = u(k-1) - (b_0^{-1})\Bigg\{x(k-1) - x_r(k) + \sum_{i=1}^{n} a_i[x(k-i) - x(k-i-1)] \\ + \sum_{i=1}^{m} b_i[u(k-i) - u(k-i-1)]\Bigg\} - (\lambda b_0)^{-1}\lambda_I \varepsilon(k-1). \end{aligned} \tag{11.7}$$

The equivalent control (11.7) represents the control action for the case of perfect disturbance estimation, i.e., $\tilde{d}(k) = 0$. It acts during the sliding phase in which the position trajectory is maintained on the sliding hyperplane. Otherwise, if the initial position of the system is not resident on the sliding hyperplane or a large estimation error $\tilde{d}(k)$ is caused, the trajectory cannot be kept on sliding hyperplane by the stand-alone equivalent control. Thus, a nonlinear control action $u_{\text{sw}}(k)$ is required.

Here, a nonlinear switching control action is employed to enhance the equivalent control. The overall control action is given by:

$$u_{\mathrm{DSM}}(k) = u_{\mathrm{eq}}(k) + u_{\mathrm{sw}}(k) \tag{11.8}$$

i.e.,

$$\begin{aligned} u_{\mathrm{DSM}}(k) = u(k-1) - (b_0^{-1})\Big\{ & x(k-1) - x_r(k) + \sum_{i=1}^{n} a_i[x(k-1) - x(k-i-1)] \\ & + \sum_{i=1}^{m} b_i[u(k-i) - u(k-i-1)]\Big\} \\ & -(\lambda b_0)^{-1}\lambda_I \varepsilon(k-1) - \lambda_S b_0^{-1}\mathrm{sgn}\{(s(k-1)\} \end{aligned} \tag{11.9}$$

where λ_S represents a positive control gain and $\mathrm{sgn}\{\cdot\}$ denotes the signum function.

To evaluate the stability of the control system, the relation (11.9) is substituted into dynamics model (11.1). Then, some fundamental algebra operation gives

$$\begin{aligned} x(k) &= \sum_{i=1}^{n} a_i x(k-i) + b_0 u(k) + \sum_{i=1}^{m} b_i u(k-i) + d(k) \\ &= x_r(k) - \tilde{d}(k) - (\lambda)^{-1}\lambda_I \varepsilon(k-1) - \lambda_S \mathrm{sgn}\{(s(k-1)\}. \end{aligned} \tag{11.10}$$

Substituting Eq. (11.10) into the equation of sliding function (11.2) yields

$$\begin{aligned} s(k) &= \lambda[x(k) - x_r(k)] + \lambda_I \varepsilon(k-1) \\ &= -\lambda[\lambda_S \mathrm{sgn}\{s(k-1)\} + \tilde{d}(k)]. \end{aligned} \tag{11.11}$$

It is notable that the parameters λ and λ_S are selected as positive values.

Assigning $\lambda_S = |\tilde{d}(k)| + \delta$ where δ represents an arbitrary positive constant, the following deduction can be drawn:

$$\lambda\delta \le |s(k)| \le 2\lambda|\tilde{d}(k)| + \lambda\delta. \tag{11.12}$$

Recalling that $\tilde{d}(k)$ is bounded by $|\tilde{d}(k)| \le \Lambda T$, it is deduced from Eq. (11.12) that the discrete sliding mode in the vicinity of the sliding hyperplane $s(k) = 0$ is attained in finite steps.

Remark 11.1 In practice, chattering phenomenon may be induced by the discontinuous signum function $\mathrm{sgn}\{\cdot\}$. To alleviate the chattering effect, the technique of boundary layer is adopted by using the saturation function instead of $\mathrm{sgn}\{\cdot\}$ in Eq. (11.9):

$$\mathrm{sat}\{s(k)\} = \begin{cases} \mathrm{sgn}\{s(k)\} & \text{for} \quad |s(k)| > \varepsilon \\ s(k)/\varepsilon & \text{for} \quad |s(k)| \le \varepsilon \end{cases} \tag{11.13}$$

where the thickness parameter ε of the boundary layer guarantees that the sliding function is bounded within $\pm\varepsilon$. In practice, a compromise between control error and chattering is considered in the selection of parameter ε.

It is notable that the presented control scheme is easy to implement in that a single linear plant model is needed. Whereas neither a state observer nor a hysteresis model is required for the control realization.

11.3.3 Incremental PID Force Controller

In the contact phase, the touch force f between the gripper tips and the object is controlled to follow a desired force trajectory f_r by employing an incremental PID controller. Defining $e(k) = f_r(k) - f(k)$ as the force error, the incremental PID controller equation is expressed as follows:

$$\begin{aligned} u_{\mathrm{PID}}(k) = u(k-1) + K_P[e(k) - e(k-1)] + K_I e(k) \\ + K_D[e(k) - 2e(k-1) + e(k-2)] \end{aligned} \tag{11.14}$$

where $u(k-1)$ represents the control command in the previous time step. K_P, K_I, and K_D are the positive control gains.

Generally, the PID control parameters can be adjusted with Ziegler–Nichols (Z–N) method by simulation studies, and then finely tuned through experimental investigations. Due to the lack of an accurate force response model, the PID gains are directly determined by the trial-and-error approach via experimental studies in this work.

11.3.4 Switching Criterion

In the grasp process, the two gripper tips initially move from their home positions toward the object at a velocity of v_r (μm/s). During this closing phase, the DSMC position control is employed. Once the gripper tips touch the object and the force sensor indicates a contact force exceeding the threshold value f_0, the control system switches to force control. In the duration of the contact phase, the regulation of the contact force f_{grip} is implemented by the incremental PID force control. After a cumulative number of time steps k_{contact}, the grasped object can be moved to the destination in microhandling tasks. Then, the gripper tips start to move away from the object at the velocity of v_r. In the opening phase, no force profile is required and the controller switches back to the DSMC position control again. The switching process between the position and force control is given below

$$
\begin{aligned}
&\text{if} \quad |f(k)| < f_0 \\
&\qquad x_r(k) = v_r k; \\
&\qquad u(k) = u_{\text{DSM}}(k); \\
&\qquad u(k-1) = u(k); \\
&\text{else if } |f(k)| \geq f_0 \text{ and } k \leq k_{\text{contact}} \\
&\qquad f_r(k) = f_{\text{grip}}; \\
&\qquad u(k) = u_{\text{PID}}(k); \\
&\qquad u(k-1) = u(k); \\
&\text{else} \\
&\qquad x_r(k) = x|_{k=k_{\text{contact}}} - v_r(k - k_{\text{contact}}); \\
&\qquad u(k) = u_{\text{DSM}}(k); \\
&\qquad u(k-1) = u(k); \\
&\text{end.}
\end{aligned}
\tag{11.15}
$$

11.4 Experimental Investigations and Discussion

The developed control schemes have been validated on the gripper system by conducting several experimental studies. In particular, the gripping and releasing testing of a copper wire with the diameter of 300 μm has been implemented to verify the effectiveness of the presented incremental control strategy.

11.4.1 Controller Setup

The scheme of the position control with force monitoring adopts the DSMC control algorithm, and the position/force switching control involves both DSMC and PID algorithms. Table 11.2 shows the control parameters of DSMC position controller and PID force controller, which are tuned by the trial-and-error method via experimental studies. Moreover, a force threshold of f_0 = 3.5 mN and a 2.7 s duration of the

Table 11.2 Parameters of the DSMC position controller and PID force controller

Controller	Parameter	Value
DSMC	λ_P	4000
	λ_I	1
	λ_S	0.4
	ε	7000
PID	K_P	0.0010
	K_I	0.0030
	K_D	0.0006

gripping force $f_{\text{grip}} = 20$ mN are selected as the first and second switching criteria, respectively. In addition, the sampling rate is chosen as 2 kHz.

11.4.2 Position/Force Switching Control Results

Concerning the scheme of the position control with force monitoring, the reference trajectories for the position and force tracking are assigned in Fig. 11.8a, b, respectively. Figure 11.8c depicts the control action, and the position and force errors are shown in Fig. 11.9a, b, respectively. The operation procedures are described below:

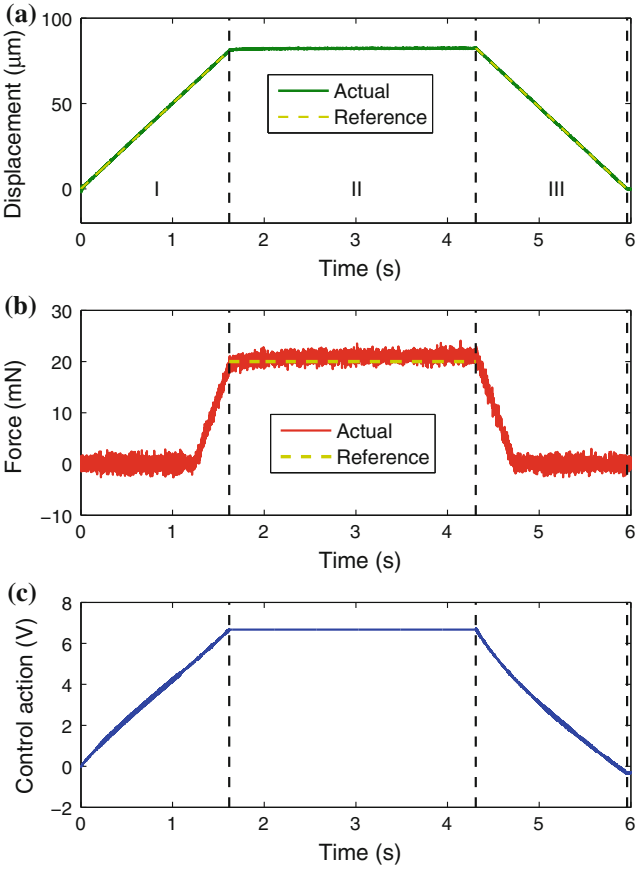

Fig. 11.8 The results of position control with force monitoring for gripping a copper wire. **a** Position control results, **b** grasp force control results, **c** control action

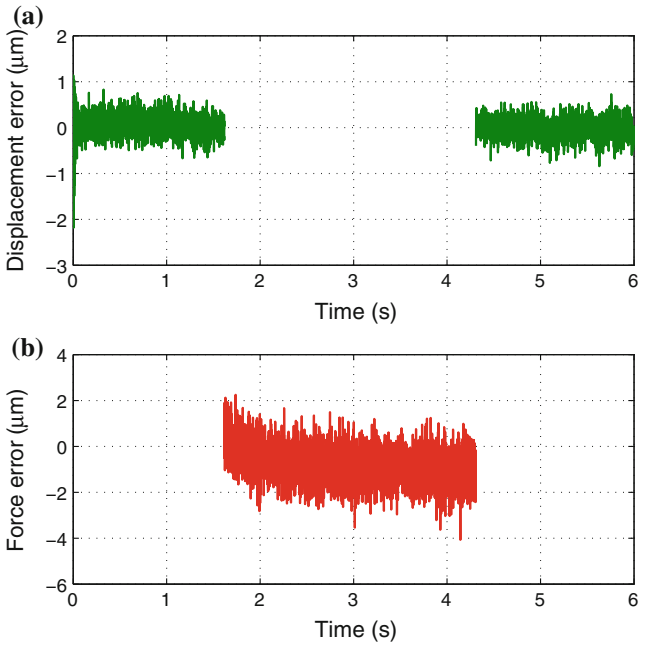

Fig. 11.9 Tracking errors of the position control with force monitoring approach. **a** Position errors. **b** Force errors

1. First, the gripper tips move at a constant velocity of $v_r = 50\,\mu$m/s as commanded by the DSMC position controller. The griper tip closes when the touch force arrives at the desired force f_{grip} and the corresponding driving voltage u_1 is recorded.
2. Second, the constant control voltage u_1 is applied aiming to maintain a constant gripping force of 20 mN for a specified duration of time of 2.7 s.
3. Third, the DSMC position control is switched on again to open the gripper at the constant velocity of v_r to release the copper wire.

Regarding the scheme of the position/force switching control, the reference position and force trajectories are planned as depicted in Fig. 11.10a, b, respectively. In addition, Fig. 11.11a, b display the control errors. The operation processes are shown as follows:

1. Initially, the gripper tip is controlled by the DSMC position controller to close at a velocity of $v_r = 50\,\mu$m/s until the contact force arrives at the threshold f_0.
2. Then, the DSMC position controller is switched off and PID force control is switched on to hold a constant gripping force of 20 mN for a specified duration of 2.7 s.
3. Afterward, the PID force control is switched off and DSMC position control is turned on again to open the gripper at the velocity of v_r to release the copper wire.

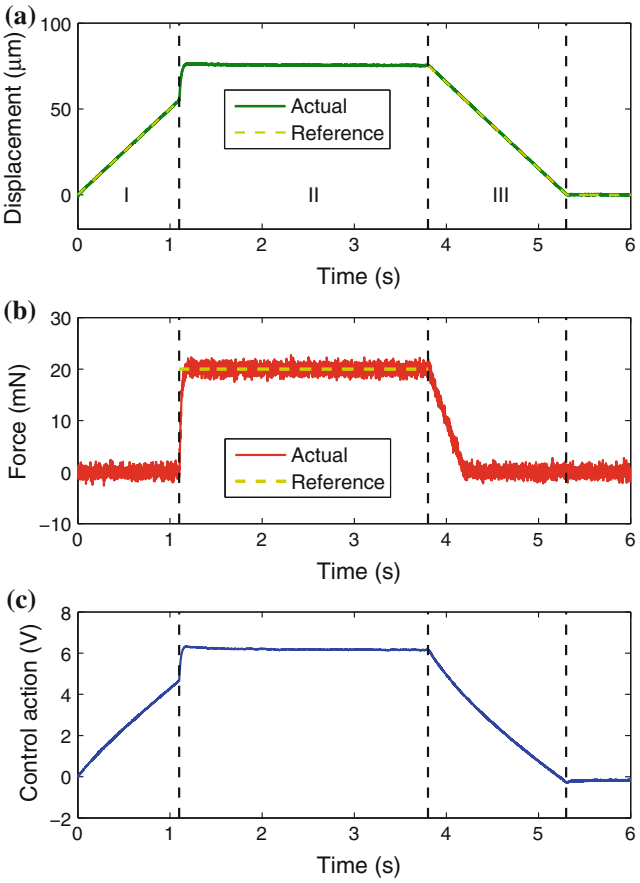

Fig. 11.10 The results of position/force switching control for gripping a copper wire. **a** Position control results. **b** Grasp force control results. **c** Control action

The controller output is exhibited in Fig. 11.10c. Moreover, the snapshots of the grasp process are shown in Fig. 11.12. These sequences represent the closing (Fig. 11.12a–c), contact (Fig. 11.12d–e), and opening (Fig. 11.12f– h) phases of the grasp-hold-release operation, respectively.

11.4.3 Further Discussion

For comparison purpose, the experimental results of the two implemented control schemes are tabulated in Table 11.3, where RMSE describes the steady-state position/force tracking errors. It is observed that both of the two schemes offer a precision positioning without chattering phenomenon. It benefits from the nice tracking capa-

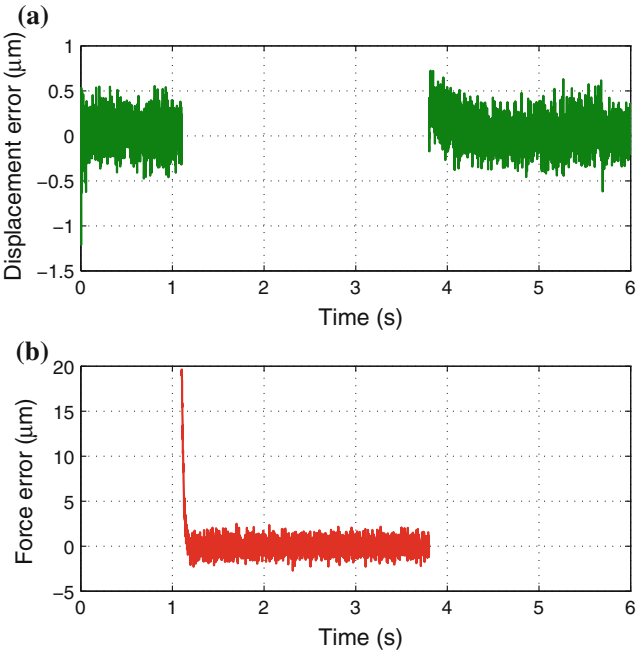

Fig. 11.11 Tracking errors of the position/force switching control scheme. **a** Position errors. **b** Force errors

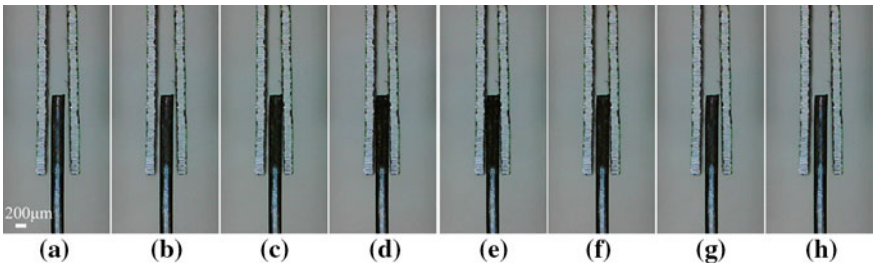

Fig. 11.12 Snapshots of **a**–**c** grasp, **d**–**e** hold, and **f**–**h** release operations for a copper wire of 300-μm diameter

Table 11.3 Position and force control results of the two schemes

Control scheme	Position RMSE (μm)	Force RMSE (mN)	Overall time (s)
Position control with force monitoring	0.214	1.135	5.96
Position/Force switching control	0.202	0.747	5.29

bility of the DSMC control algorithm in front of piezoelectric nonlinearities. As compared with the first scheme of the position control with force monitoring [21], the second approach of the position/force switching control has reduced the position and force tracking RMSE by 5.6 and 34.2 %, respectively. The accurate force control is vital for some demanding applications such as biological sample handling.

The first method is relatively easy to implement because no force control is applied. However, during the contact phase, an obvious drift phenomenon occurs in the gripping force, as shown in Fig. 11.8b. The drift effect stems from the PSA with a constant voltage applied. As a result, a constant gripping force cannot be maintained exactly. On the contrary, the second control strategy is capable of regulating both the position and gripping force precisely, as indicated in Fig. 11.10. Moreover, because a force control is adopted in the contact phase, the step response as shown in Fig. 11.10b is much quicker than the ramp tracking response as depicted in Fig. 11.8b. Consequently, the second scheme has reduced the overall execution time of the three-phase grasp process by 11 % as compared with the first approach.

In view of the position trajectories as shown in Figs. 11.8a and 11.10a, it is observed that the opening and closing phases are implemented within a large motion range due to a large initial gap between the gripper tips and the copper wire. In addition, the trajectories consist of both rising and falling curves. Hence, the opening and closing phases exhibit a significant hysteretic nonlinearity. By contrast, the contact phase is realized within a smaller gripping range. In such a small motion range, the hysteresis effect is not dominant while the drift phenomenon requires an explicit treatment. Therefore, the advanced DSMC controller is adopted for the hysteresis suppression in the position control during the opening and closing phases. Whereas the force control in the contact phase is realized using the PID control, whose objective is to maintain a desired touch force by alleviating the drift phenomenon. Another reason of using PID controller for the force control lies in that a force response model of the gripper is not needed in that PID is a model-free control technique. Applying DSMC control strategy in force control requires the identification of a force response model, which complicates the practical implementation procedure. On the other hand, the stand-alone PID control is not able to produce a satisfactory suppression of the hysteresis effect in the opening and closing phases. Hence, DSMC instead of PID is employed in the position control regime.

Additionally, the slopes of the position and force trajectories in the closing or opening phases can be calculated to determine the combined stiffness of the gripper tips and grasped object. For instance, similar stiffness values of 1.104 and 1.092 mN/μm are obtained from the opening phase trajectories of the first and second control methods, respectively. The similarity arises from the reason that the same DSMC position control is applied in the opening phase in both of the two methods, hence similar performance is expected.

The fact that satisfactory tracking results in the closing and opening phases have been achieved reveals the robustness property of the implemented DSMC control strategy under the influence of contact force. Moreover, Figs. 11.8 and 11.10 indicate that a smooth transition between the position and force control has been achieved.

The experimental results demonstrate the effectiveness of the presented incremental control scheme dedicated to smooth position/force switching control.

It is notable that a velocity of 50 μm/s is employed in both closing and opening phases in the gripping operations. Actually, different velocities can be realized in the two phases. Moreover, other trajectory types and velocity values can also be used. Further experiments indicate that a faster positioning velocity of 300 μm/s can be implemented with an RMSE less than 0.5 μm.

11.5 Chapter Summary

This chapter reports on the position and force control of a compliant gripper, which possesses integrated strain-gage position and force sensors. The gripper provides a gripping range of 276 μm along with the position and force sensing resolutions of 0.345 μm and 1.501 mN, respectively. In addition, the gripping range and initial gap between the gripper tips can be adjusted to accommodate different sizes of objects. An incremental-based smooth position/force switching control framework is proposed to demonstrate a grasp-hold-release operation of a copper wire of 300-μm diameter. Furthermore, the reported DSMC control algorithm simplifies the control design and implementation procedures. Experimental results confirm that the presented incremental control scheme makes it easy to realize a smooth transition during the switching control. Moreover, the position/force switching control performs better than the conventional approach of position control with force monitoring, as the former allows an exact delivery of the desired position and contact force.

In view of the promising accuracy for both the position and gripping force regulation of the presented incremental switching controller, it will be employed for handling deformable biological materials in the future. Moreover, an architectural optimization of the gripper structure will be performed to adapt to the manipulation and assembly of more micrometer-sized objects dedicated to industrial automation.

References

1. Alkkiomaki, O., Kyrki, V., Kalviainen, H., Liu, Y., Handroos, H.: Smooth transition from motion to force control in robotic manipulation using vision. In: Proceeding 9th International Conference on Control, Automation, Robotics and Vision, pp. 1–6 (2006)
2. Beyeler, F., Neild, A., Oberti, S., Bell, D.J., Sun, Y., Dual, J., Nelson, B.J.: Monolithically fabricated microgripper with integrated force sensor for manipulating microobjects and biological cells aligned in an ultrasonic field. J. Microelectromech. Syst. **16**(1), 7–15 (2007)
3. Cao, Y., Cheng, L., Chen, X.B., Peng, J.Y.: An inversion-based model predictive control with an integral-of-error state variable for piezoelectric actuators. IEEE/ASME Trans. Mechatron. **18**(3), 895–904 (2013)
4. Capisani, L.M., Ferrara, A.: Trajectory planning and second-order sliding mode motion/interaction control for robot manipulators in unknown environments. IEEE Trans. Ind. Electron. **59**(8), 3189–3198 (2012)

5. Gao, B., Shao, J., Han, G., Sun, G., Yang, X., Wu, D.: Using fuzzy switching to achieve the smooth switching of force and position. Appl. Mech. Mater. **274**, 638–641 (2013)
6. Hara, S., Yamada, Y.: A control method switching from servo automatic transfer to force sensorless impedance control manual positioning. In: Proceeding IECON 2007—33rd Annual Conference of the IEEE Industrial Electronics Society, pp. 292–298 (2007)
7. Leang, K.K., Shan, Y., Song, S., Kim, K.J.: Integrated sensing for IPMC actuators using strain gages for underwater applications. IEEE/ASME Trans. Mechatron. **17**(2), 345–355 (2012)
8. Liaw, H.C., Shirinzadeh, B.: Robust adaptive constrained motion tracking control of piezo-actuated flexure-based mechanisms for micro/nano manipulation. IEEE Trans. Ind. Electron. **58**(4), 1406–1415 (2011)
9. Minase, J., Lu, T.F., Cazzolato, B., Grainger, S.: A review, supported by experimental results, of voltage, charge and capacitor insertion method for driving piezoelectric actuators. Precis. Eng. **34**(10), 692–700 (2010)
10. Motoi, N., Shimono, T., Kubo, R., Kawamura, A.: Task realization by a force-based variable compliance controller for flexible motion control systems. IEEE Trans. Ind. Electron. **61**(2), 1009–1021 (2014)
11. Navarro, C., Treesatayapun, C., Baltazar, A.: Determination of the instantaneous initial contact point on a parallel gripper using a multi input fuzzy rules emulated network controller with feedback from ultrasonic and force sensors. In: Batyrshin I., Gonzalez Mendoza M. (eds.) Advances in Artificial Intelligence, Lecture Notes in Computer Science, vol. 7629, pp. 261–272. Springer, Berlin (2013)
12. Niksefat, N., Wu, Q., Sepehri, N.: Stable control of an electro-hydraulic actuator during contact tasks: Theory and experiments. In: Proceeding of American Control Conference, pp. 4114–4118 (2000)
13. Rakotondrabe, M., Ivan, I.A.: Development and force/position control of a new hybrid thermo-piezoelectric microgripper dedicated to micromanipulation tasks. IEEE Trans. Automat. Sci. Eng. **8**(4), 824–834 (2011)
14. Reddy, A.N., Maheshwari, N., Sahu, D.K., Ananthasuresh, G.K.: Miniature compliant grippers with vision-based force sensing. IEEE Trans. Robot. **26**(5), 867–877 (2010)
15. Sakaino, S., Sato, T., Ohnishi, K.: Multi-DOF micro-macro bilateral controller using oblique coordinate control. IEEE Trans. Ind. Inform. **7**(3), 446–454 (2011)
16. Sakaino, S., Sato, T., Ohnishi, K.: Precise position/force hybrid control with modal mass decoupling and bilateral communication between different structures. IEEE Trans. Ind. Inform. **7**(2), 266–276 (2011)
17. Shimada, N., Yoshioka, T., Ohishi, K., Miyazaki, T.: Novel force-sensor-less contact motion control for quick and smooth industrial robot motion. In: Proc. IECON 2011 - 37th Annual Conf. on IEEE Industrial Electronics Society, pp. 4238–4243 (2011)
18. Takahashi, T., Tsuboi, T., Kishida, T., Kawanami, Y., Shimizu, S., Iribe, M., Fukushima, T., Fujita, M.: Adaptive grasping by multi fingered hand with tactile sensor based on robust force and position control. In: Proceeding International Conference on Robotics and Automation, pp. 264–271 (2008)
19. Wang, D.H., Yang, Q., Dong, H.M.: A monolithic compliant piezoelectric-driven microgripper: Design, modeling, and testing. IEEE/ASME Trans. Mechatron. **18**(1), 138–147 (2013)
20. Xu, Q.: Adaptive discrete-time sliding mode impedance control of a piezoelectric microgripper. IEEE Trans. Robot. **29**(3), 663–673 (2013)
21. Xu, Q.: New robust position and force regulation for a compliant microgripper. In: Proceeding 9th IEEE International Conference on Automation Science and Engineering, pp. 801–806 (2013)
22. Yong, Y.K., Moheimani, S.O.R., Kenton, B.J., Leang, K.K.: High-speed flexure-guided nanopositioning: Mechanical design and control issues. Rev. Sci. Instrum. **83**(12), 121101 (2012)
23. Zhou, Q., Korhonen, P., Laitinen, J., Sjovall, S.: Automatic dextrous microhandling based on a 6-DOF microgripper. J. Micromechatronics **3**(3–4), 359–387 (2006)

Index

A
Actuators, 2
Adaptive control, 9
Adaptive digital sliding-mode generalized impedance control (ADSMGIC), 211
Adaptive laws, 192
Adaptive rule, 217
Adhesive force, 229
Artificial neural networks (ANN), 8, 23

B
Backlash operator, 30
Backward difference equation, 190
Bayesian inference, 35
Bouc–Wen hysteresis, 58
Bouc–Wen model, 28
Boundary layer technique, 88, 133

C
Calibration, 237
Capacitive sensors, 3
Chattering, 88, 147
Compliant gripper, 234
Compliant mechanisms, 1
Control bandwidth, 161, 181, 200
Controllability, 116
Controllable canonical form, 149, 168
Convergence condition, 133

D
Dead-zone modification, 193
Dead-zone operator, 31
Digital microscope, 237
Digital PID control, 73, 197
Digital signal processor (DSP), 10, 25, 211
Digital sliding-mode control (DSMC), 15, 127, 170, 214, 234
Digital sliding-mode prediction control (DSMPC), 167
Digital systems, 14
Discrete sliding mode, 216
Discrete-time model, 129, 148, 168, 212
Discrete-time sliding-mode control (DTSMC), 10, 127
Discretization, 129
Discretization noise, 129
Displacement amplifier, 194, 234
Displacement sensor, 3
Disturbance, 148
Disturbance estimation, 150, 169
Disturbance observer, 13
Dual formulation, 34, 61
Dynamics model, 58, 81, 212

E
E-beam lithography, 3
Eigenvalue, 86
Electrical discharge machining (EDM), 94, 236
Environment interaction, 218
Equivalent control, 84, 131, 152, 215, 243
Euler backward difference, 129
Event-based switching, 241

F
Feedback control, 9
Feedforward compensation, 71

© Springer International Publishing Switzerland 2016

Q. Xu and K.K. Tan, *Advanced Control of Piezoelectric Micro-/Nano-Positioning Systems*, Advances in Industrial Control,
DOI 10.1007/978-3-319-21623-2

Feedforward control, 5, 47
Feedforward plus feedback control, 8, 49, 73
Field-programmable gate array (FPGA), 134, 195, 234
Finite-element analysis (FEA), 194
Flexure hinge, 2
Force control, 245
Force observer, 220
Frequency response, 63, 95, 240
Fuzzy logic control, 9

G
Generalized impedance control (GIC), 14, 210
Generalized minimum variance control (GMVC), 11
Genetic algorithm (GA), 36

H
H_∞ control, 9
Hammerstein model, 5
High-order model, 147
Hybrid position/force control, 14
Hysteresis, 4
Hysteresis models, 6, 28

I
Impedance control, 14, 210, 213
Incremental control, 15, 242
Incremental PID control, 49, 158, 234, 245
Inductance sensors, 3
Input–output-based DSMC (IODSMC), 147
Integral error, 131
Intelligent hysteresis model, 59
Interaction control, 13, 209, 224
Inverse hysteresis model, 8
Inverse MPI model, 32
Iterative learning control, 13

K
Kernel trick, 34, 61

L
Lagrangian function, 33
Laser displacement sensor, 3, 62, 195, 237
Laser interferometer, 3
Least squares support vector machines (LSSVM), 8, 24, 57
Linear time-invariant (LTI) model, 106, 148
LSSVM model, 33
Luenberger observer, 92
Lyapunov candidate, 192

M
Matching condition, 81, 148
Metal strain gauges, 3
Micro-/nano-positioning, 1
Micro-/nano-positioning system, 1
Microassembly, 13, 209
Microgripper, 13, 209, 233
Micromanipulation, 13, 209
Model generalization, 44, 66
Model predictive control (MPC), 11, 173
Model predictive discrete-time sliding-model control (MPDTSMC), 80
Model predictive output integral discrete-time sliding-mode control (MPOIDSMC), 105
Model-reference adaptive control (MRAC), 12
Modified Prandtl–Ishlinskii (MPI) model, 29
Momentum term, 214
Motion tracking, 159, 179
MRAC with perturbation estimation (MRACPE), 187, 190
Multivalued mapping, 58

N
Neural network control, 9
Noise, 48, 57, 88, 114, 180, 204
Nonlinear regression, 60
Normalization transformation, 41

O
Observability, 116
Optical microscopes, 3
Optical sensors, 3
Optimization, 28, 33, 39, 58
Output integral discrete-time sliding-mode control (OIDSMC), 105

P
Parameter optimization, 36
Particle swarm optimization (PSO), 24, 36, 64
Perturbation estimation, 189
PID control, 135
PID sliding function, 151, 170

Piezo benders, 2
Piezo diaphragms, 2
Piezoelectric actuators, 2
Piezoelectric bimorph, 62, 128, 209
Piezoelectricity, 4
Piezoelectric stack actuator (PSA), 194, 233
Piezoresistive strain gauges, 3
Piezo stacks, 2
PI sliding function, 84, 107, 130, 242
Pole placement, 93
Position and force control, 13
Position/force switching control, 15, 233
Prandtl–Ishlinskii model, 30
Precision alignment, 3
Proportional-integral-derivative (PID) control, 9
Pseudo-rigid-body (PRB) model, 234
PZT, 4

Q
Quadratic programming (QP), 8, 24
Quasi-sliding domain, 132

R
Rate dependency, 33, 40
Rate-dependent hysteresis, 7, 23
Rate-independent hysteresis, 7
Reaching law, 131, 152
Regression, 32
Regression model, 60
Repetitive control, 13
Robust control, 154
Robustness, 143, 162

S
Sampled-data system, 10
Sampling time, 134
Scanning electron microscopes, 3
Scanning probe microscopes, 3
Second-order model, 129, 188
Sensitivity, 3, 235
Sensor calibration, 237
Sensors, 3
Set-point positioning, 159, 198
Signal-to-noise ratio (SNR), 235
Singular value, 116
Sinusoidal tracking, 200
SISO, 107
Sliding condition, 133
Sliding-mode control (SMC), 10
Sliding-mode observer, 113
Sliding surface, 133
Smart actuators, 2, 209
Smooth transition, 15, 234
Spectral analysis, 157, 240
Spillover, 79
Stability, 91, 108, 112, 152, 175, 216
State observer, 11, 92
State-space model, 81
Strain gage, 156, 237
Strain sensors, 3
Support vector, 34, 61
Support vector machines (SVM), 8, 23
Switching control, 86, 131, 154, 215
System identification, 63, 134, 157

T
Target impedance, 213
Trajectory planning, 222
Tustin approximation, 83

W
White noise, 238

Z
Zero-order-hold (ZOH), 148
Ziegler–Nichols (Z–N) method, 73, 198